

Electronic Thesis and Dissertation Repository

6-27-2024 10:30 AM

The transition from used fuel container corrosion under oxic conditions to corrosion in an anoxic environment

Elham Salehi Alaei,

Supervisor: Noël, James J., *The University of Western Ontario*

A thesis submitted in partial fulfillment of the requirements for the Doctor of Philosophy degree in Chemistry

© Elham Salehi Alaei 2024

Follow this and additional works at: <https://ir.lib.uwo.ca/etd>

Recommended Citation

Salehi Alaei, Elham, "The transition from used fuel container corrosion under oxic conditions to corrosion in an anoxic environment" (2024). *Electronic Thesis and Dissertation Repository*. 10213.
<https://ir.lib.uwo.ca/etd/10213>

This Dissertation/Thesis is brought to you for free and open access by Scholarship@Western. It has been accepted for inclusion in Electronic Thesis and Dissertation Repository by an authorized administrator of Scholarship@Western. For more information, please contact wlsadmin@uwo.ca.

Abstract

Used nuclear fuel poses significant risks to human health and the environment, necessitating its safe and permanent disposal. The universally proposed plan for this is to bury the fuel-containing containers in a multi-barrier system known as a deep geological repository (DGR) at least 500 metres underground. These containers, crucial for withstanding long-term mechanical loads and a corrosive environment, vary in design across countries, with some featuring copper (Cu) shells on nodular cast iron insert (Sweden, Finland) or Cu-coated carbon steel vessels (Canada). Upon emplacement, the containers undergo evolving conditions underground, transitioning from warm, humid, and oxidizing to cool, dry, and anoxic environments over time.

During the initial oxidizing phase, oxygen entrapped upon sealing the DGR and water-radiolysis will lead to the formation of an oxide/hydroxide film on the Cu container surface. Subsequently, as anoxic conditions prevail, bisulfide (SH^-) ions produced by the action of sulfate-reducing bacteria (SRB) remote from the container will become the primary oxidant.

While considerable efforts have been devoted to investigating exclusively either the oxic or anoxic periods, the current study has addressed the gap in understanding how early oxide growth impacts later stages, particularly in the presence of SH^- ions. In a series of experiments, various methods were employed to create copper oxide/hydroxide layers with known compositions and structures to investigate their role in bisulfide-induced corrosion of the Cu substrate under de-aerated conditions. The morphology of the oxide film and the concentration of bisulfide species influence potential interaction mechanisms, including chemical conversion, galvanic coupling, and direct corrosion of Cu by bisulfide species.

Our findings have shown that regardless of the composition or structure of the oxide film, it underwent partial conversion to copper sulfide via chemical and/or galvanic processes. Moreover, an unreacted remnant of the oxide layer detected on the surface was non-protective and permitted direct Cu corrosion by bisulfide species.

Electrochemically- and radiolytically-grown oxides exhibited quick conversion to copper sulfide, whereas hydrothermally-grown oxides, thicker in nature, underwent slower conversion, with regions remaining unreacted. These results highlight the importance of electrochemical pathways in facilitating rapid oxide-to-sulfide conversion, contrasting with slower chemical pathways.

Keywords: Copper, Corrosion, Electrochemistry, Conversion, Oxide, Sulfide, Nuclear Waste Management

Summary for Lay Audience

The safe disposal of used nuclear fuel is crucial to protect both people and the environment from chemical and radiological hazard. One widely accepted method is to bury the used fuel container (UFC) underground in a DGR, at least 500 m below the surface. In Canada, UFCs are made of a strong carbon steel vessels coated with a 3-mm-thick layer of Cu. Copper has been chosen as the main corrosion barrier for the container in Finland, Sweden, Canada, and some other countries (e.g., Switzerland, South Korea, and Japan) are considering Cu coating due to its known corrosion resistance under anoxic conditions. Over time, the conditions around the container will change from warm and humid to cool and dry. Initially, oxygen trapped in the repository causes an oxide film to form on the container surface. Eventually, as the environment becomes anoxic, bisulfide ions produced by sulfate-reducing bacteria will become the main threat for Cu corrosion.

The current research aims to understand how the early growth of oxide layers on copper containers affects their later corrosion when exposed to bisulfide ions. Through experiments, different types of oxide layers have been created via a variety of methods to study how the oxide interacts with bisulfide ions under specific conditions. This interaction can lead to chemical conversion of copper oxide to copper sulfide, galvanic processes between oxide reduction and copper oxidation by sulfide, or direct corrosion of copper by bisulfide. Understanding the conversion process is crucial for ensuring the long-term integrity of the containers storing nuclear fuel.

The mechanism and extent of conversion of different types of copper (hydr)oxides with known compositions and thicknesses have been analyzed using various electrochemical and corrosion measurements such as corrosion potential, cyclic voltammetry (CV), and cathodic stripping voltammetry. Additionally, a range of surface analytical techniques including Raman spectroscopy, scanning electron microscopy (SEM) and focused ion beam (FIB) milling were used to figure out the chemical composition, surface film morphology and thickness measurement at the film/Cu interface.

Dedication

Whole-heartedly, and gratefully so, I dedicate this work

To

My caring parents

(بانو) Banoo and (داوود) Davood

&

My loving sister

(لیکا) Elica

Who have all offered me unconditional love and support and made it possible for me to complete this work.

To

All Iranian women who fight for their dreams

&

All victims of downed flight PS752, especially my dear friends

Hadis Hayatdavoodi (Chemistry PhD Candidate at Western University)

Paniz Soltani (Material Science PhD Candidate at Max Plank Institute)

Co-Authorship Statement

In **Chapters 4** and **5** of this thesis, you will find published data (DOI: 10.1002/maco.202313757). As the main investigator and author, I conducted all the experiments for this research project with assistance from:

Chapter 4: Mr. Brad Kobe and Ms. Claire Samantha Tully assisted with SEM analysis, Dr. Thalia Standish assisted with laser Raman spectroscopy, Dr. Sina Matin assisted with FE-SEM/EDX analysis, Dr. James J. Noël and Dr. David W. Shoesmith assisted with editing.

Chapter 5: Dr. Todd Simpson assisted with SEM/FIB analysis, Dr. Sina Matin assisted with FE-SEM/EDX analysis, Dr. Thalia Standish assisted with laser Raman spectroscopy, Dr. James J. Noël and Dr. David W. Shoesmith assisted with editing.

Chapter 6: Dr. Todd Simpson assisted with SEM/FIB analysis, Dr. James J. Noël and Dr. David W. Shoesmith assisted with editing.

Chapter 7: Dr. Vahid Dehnavi assisted with SEM/EDX analysis, Dr. Todd Simpson assisted with SEM/FIB analysis, Ms. Jijo Joseph assisted with experimental design, Dr. Jonas Hedberg assisted with laser Raman spectroscopy, Dr. David W. Shoesmith and Dr. James J. Noël assisted with editing.

Chapter 8: Dr. Vahid Dehnavi assisted with powder XRD analysis, Dr. James J. Noël and Dr. David W. Shoesmith assisted with editing.

Acknowledgments

I would like to express my deepest gratitude to my supervisor, Dr. James J. Noël, whose unwavering support, guidance, and friendship have been a beacon of light throughout both the ups and downs of my academic journey. His expertise and mentorship have been invaluable in shaping my research. Beyond providing invaluable assistance with scientific endeavors, Dr. Noël has been a source of strength and solace, offering emotional support during challenging times. He has not only imparted invaluable scientific knowledge but has also shared invaluable life lessons, nurturing personal growth and resilience. His willingness to lend a compassionate ear and offer words of encouragement has been a constant source of inspiration. Moreover, Dr. Noël has played an integral role in introducing me to Canadian culture, fostering a sense of belonging and understanding in a new environment.

Furthermore, I extend my heartfelt gratitude to Dr. David W. Shoesmith, for his exceptional mentorship, expertise, and valuable insights. Not only his generosity and kindness have left an indelible mark on my journey but also his willingness to share resources, provide feedback, and engage in fruitful discussions have been crucial in overcoming various challenges and achieving meaningful outcomes. Although he has been retired, supervision is in his blood.

I am also thankful to my thesis committee members for their insightful feedback and constructive criticism.

I am profoundly grateful to grant providers and research collaborators, Nuclear Waste Management Organization (NWMO, Toronto, Canada) and Swedish Nuclear Fuel and Waste Management Company (SKB, Solna, Sweden) for their financial support, which made this research possible. Their investment in my work has allowed me to pursue my academic aspirations and contribute to the field of nuclear waste management. Their collaborative spirit and camaraderie have made this journey both productive and enjoyable. I am deeply thankful for the invaluable support and knowledge shared by our national and international collaborators throughout the duration of this research endeavor. Their

expertise and collaborative efforts have significantly enriched the scope and depth of our work. I also want to thank the Western University-Chemistry department for providing a conducive environment for learning and research. I would like to acknowledge the personnel at Western Nanofabrication Facility and Surface Science Western, especially Dr. Todd Simpson, Mr. Brad Kobe, Dr. Thalia Standish, Dr. Jonas Hedberg, and Dr. Vahid Dehnavi, for assisting with FIB, SEM, laser Raman, and XRD.

I would like to express my sincere gratitude to the dedicated research assistants, Dr. Jian Chen and Dr. Dmitrij Zagidulin, who have contributed to the success of this project. Their expertise, diligence, and commitment to excellence have been invaluable in conducting lab experiments, troubleshooting technical challenges, and ensuring the smooth progression of our research efforts.

I am fortunate to have had the opportunity to work alongside such talented individuals, and I extend my appreciation to each member of Dr. Noël's research team for their meaningful contributions.

I am deeply indebted to my parents, Banoo and Davood, whose unconditional love, encouragement, and sacrifices have been the cornerstone of my academic journey. Their endless support, both emotionally and financially, has enabled me to pursue my dreams and overcome numerous challenges along the way. I am forever grateful for their guidance and belief in my abilities.

I also want to express my sincere appreciation to my close friends, for their support and care throughout this journey. Their friendship, understanding, and words of encouragement have been a source of strength during challenging times. Their belief in my potential has been priceless, and I am truly fortunate to have them in my life.

Table of Contents

Abstract.....	ii
Summary for Lay Audience.....	iv
Dedication	v
Co-Authorship Statement	vi
Acknowledgments	vii
Table of Contents	ix
List of Acronyms, Abbreviations, and Symbols.....	xv
List of Tables	xxi
List of Figures.....	xxii
1 Introduction.....	1
1.1 Background and motivation.....	1
1.2 Thesis objectives.....	5
1.3 Thesis outline	5
1.4 References.....	7
2 Technical Background.....	10
2.1 Used nuclear fuel containers.....	10
2.1.1 Used fuel container design.....	10
2.2 Buffer materials and sealing systems.....	13
2.3 Natural analogues.....	14
2.4 Evolution of the repository environment	16
2.4.1 Temperature and heat transfer	17
2.4.2 Redox conditions	18
2.5 Impact of environmental evolution on Cu corrosion in a DGR environment.....	21
2.5.1 Oxidic corrosion.....	21

2.5.2	Radiation-influenced corrosion (RIC)	22
2.5.3	Dissolved bisulfide and microbiologically-influenced corrosion (MIC)..	24
2.5.4	Conversion of copper oxides/hydroxides or other forms of Cu (II) to copper sulfide.....	25
2.6	Formation of copper complexes over time under DGR conditions	28
2.6.1	Copper oxides	28
2.6.2	Cu (II) hydroxide	30
2.6.3	Cu sulfides	31
2.6.4	Other Cu salts.....	33
2.7	Literature review of Cu corrosion.....	35
2.7.1	Relevant thermodynamic data for Cu under disposal conditions	35
2.7.2	The destabilization of Cu in the presence of bisulfide.....	37
2.8	The electrochemical behaviour of Cu in alkaline environments	41
2.9	Raman spectroscopy of Cu oxides, hydroxides, and sulfides.....	43
2.10	Conversion of Cu oxide to Cu sulfide.....	46
2.11	References.....	51
3	Experimental and Instrumentation	67
3.1	Specimen preparation.....	67
3.2	Formation of an oxide layer on Cu specimens.....	68
3.2.1	Electrochemical method.....	68
3.2.2	Hydrothermal method	69
3.2.3	Radiation method.....	69
3.3	Exposure of grown oxide to sulfide-containing solution.....	71
3.3.1	Solution preparation.....	71
3.4	Electrochemical techniques	72
3.4.1	Corrosion potential measurement	72

3.4.2	Potentiostatic polarization.....	72
3.4.3	Cyclic voltammetry.....	72
3.4.4	Linear sweep voltammetry.....	74
3.5	Specimen analysis.....	75
3.5.1	Microscopy	75
3.5.2	Spectroscopy	82
3.6	References.....	90
4	Investigating the Electrochemical Behaviour of Copper in Alkaline Solution and the Effect of Electrochemically-grown Single-Phase Copper (I) Oxide on Bisulfide-induced Corrosion	93
4.1	Introduction.....	93
4.2	Experimental.....	95
4.2.1	Specimen preparation.....	95
4.2.2	Solution preparation.....	95
4.2.3	Electrochemical cell design and instrumentation	96
4.2.4	Electrochemical/corrosion experiments.....	96
4.2.5	Surface analyses.....	97
4.3	Results and Discussion	97
4.3.1	Oxidation of copper in alkaline solution.....	97
4.3.2	Exposure of oxidized Cu to bisulfide-containing solutions under two different conditions	103
4.4	Conclusions.....	112
4.5	References.....	113
5	Investigating the Electrochemical Behaviour and Surface Properties of the Electrochemically-grown Mixed Oxide in an Aqueous Bisulfide Solution.....	116
5.1	Introduction.....	116
5.2	Experimental.....	117

5.2.1	Specimen preparation.....	117
5.2.2	Solution preparation.....	117
5.2.3	Electrochemical cell design and instrumentation	117
5.2.4	Electrochemical/corrosion experiments.....	117
5.2.5	Surface analyses.....	119
5.3	Results and Discussion	119
5.3.1	Voltammetric behaviour of Cu in de-aerated 0.1 M NaOH solution.....	119
5.3.2	Formation of a duplex Cu_2O – CuO ($\text{Cu}(\text{OH})_2$) film.....	119
5.3.3	Conversion of $\text{Cu}_2\text{O}/\text{CuO}/\text{Cu}(\text{OH})_2$ to Cu_2S	122
5.4	Conclusions.....	133
5.5	References.....	135
6	Assessment of the Electrochemical Behaviour and Surface Properties of Hydrothermally-grown Mixed Oxide in the Presence of Bisulfide-containing Solution	137
6.1	Introduction.....	137
6.2	Experimental	139
6.2.1	Specimen preparation.....	139
6.2.2	Solution preparation.....	139
6.2.3	Electrochemical cell design and instrumentation	139
6.2.4	Electrochemical/corrosion experiments.....	139
6.2.5	Surface analyses.....	140
6.3	Results and Discussion	140
6.3.1	Characterization of hydrothermally-grown mixed oxide.....	140
6.3.2	Characterization of sulfidized grown oxide	145
6.3.3	Mechanistic understanding of localized corrosion	157
6.4	Conclusions.....	157

6.5	References.....	158
7	Assessment of the Electrochemical Behaviour and Surface Properties of Radiolytically-formed Mixed Oxide in the Presence of Bisulfide-containing Solution	162
7.1	Introduction.....	162
7.2	Experimental	164
7.2.1	Specimen preparation.....	164
7.2.2	Solution preparation.....	165
7.2.3	Specimen irradiation	165
7.2.4	Electrochemical cell design and instrumentation	165
7.2.5	Electrochemical/corrosion experiments.....	165
7.2.6	Surface analyses.....	166
7.3	Results and Discussion	167
7.3.1	Characterization of radiolytically-grown oxide film	167
7.3.2	Characterization of the sulfidized grown oxide	175
7.3.3	Mechanistic understanding	185
7.4	Conclusions.....	187
7.5	References.....	188
8	Investigating the Role of Cu in the Conversion of Copper Oxide to Copper Sulfide.....	194
8.1	Introduction.....	194
8.2	Experimental.....	196
8.2.1	Specimen preparation.....	197
8.2.2	Solution preparation.....	197
8.2.3	Cell design	197
8.2.4	Analytical characterization	198

8.3 Results and Discussion	198
8.3.1 Characterization of the pristine Cu ₂ O and CuO powders	198
8.3.2 Characterization of the sulfidized Cu ₂ O, CuO, and mixed Cu/CuO powders	199
8.4 Conclusions.....	203
8.5 References.....	205
9 Summary and Future Work.....	208
9.1 Summary	208
9.2 Future Work	211
Curriculum Vitae	213

List of Acronyms, Abbreviations, and Symbols

Acronyms, Abbreviations

BWR	Boiling water reactor
BCC	Body-centred cubic
BSE	Backscattered electron
BSD	Backscattered electron detector
CSV	Cathodic stripping voltammetry
CV	Cyclic voltammetry
CANDU	Canada Deuterium Uranium
CE	Counter electrode
CCD	Charge-coupled device
DGR	Deep geological repository
DFT	Density functional theory
EDX	Energy dispersive X-ray spectroscopy
EDZ	Excavation damaged zone
EXAFS	Extended X-ray absorption fine structure
FIB	Focused ion beam
FE-SEM	Field emission-scanning electron microscopy
FSW	Friction stir welding

FCC	Face-centred cubic
FEG-SEM	Field-emission gun scanning electron microscope
HCB	Highly compacted bentonite
ICDD	International centre of diffraction data
JCPDS	Joint committee on powder diffraction standards
LSV	Linear sweep voltammetry
MIC	Microbiologically-induced corrosion
NWMO	Nuclear Waste Management Organization
OFF	O-free P-doped
OER	Oxygen evolution reaction
PWR	Pressurized water reactor
PTFE	Polytetrafluoroethylene
RH	Relative humidity
RIC	Radiation-induced corrosion
RE	Reference electrode
SRB	Sulfate-reducing bacteria
SEM	Scanning electron microscopy
SKB	Swedish Nuclear Fuel and Waste Management Company
SHE	Standard hydrogen electrode

SCE	Saturated calomel electrode
SE	Secondary electron
SED	Secondary electron detector
UFC	Used fuel container
WE	Working electrode
XRD	X-ray diffraction
XPS	X-ray photoelectron spectroscopy
XANES	X-ray absorption near-edge structure spectroscopy
XAS	X-ray absorption spectroscopy

Symbols

Ar	Argon gas
Cu	Copper
Cl ⁻	Chloride ion
CuCl ₂ ⁻	Copper-chloro complex
CuO	Cupric oxide/Tenorite
Cu ₂ O	Cuprous oxide/Cuprite
Cu(OH) ₂	Cupric hydroxide
Cu ₂ Cl(OH) ₃	Atacamite
Cu ₃ (CO ₃) ₂ (OH) ₂	Azurite

$\text{Cu}_2(\text{CO}_3)(\text{OH})_2$	Malachite
$\text{Cu}_3(\text{NO}_3)(\text{OH})_3$	Gerhardtite
$\text{Cu}_2(\text{NO}_3)(\text{OH})_3$	Rouaite
Cu_2S	Chalcocite
CuS	Covellite
$\text{Cu}_{1.12}\text{S}$	Varrowite
$\text{Cu}_{1.4}\text{S}$	Spionkopite
$\text{Cu}_{1.6}\text{S}$	Geerite
$\text{Cu}_{1.75}\text{S}$	Anilite
$\text{Cu}_{1.8}\text{S}$	Digenite
$\text{Cu}_{1.96}\text{S}$	Djurleite
CaSO_4	Gypsum
CaCO_3	Calcite
CO_2	Carbon dioxide gas
$\text{Cu}_4(\text{SO}_4)(\text{OH})_6$	Brochantite
^{60}Co	Cobalt-60
E	Potential (V)
e^-	Electron
E_e	Equilibrium electrode potential (V)

E_{corr}	Corrosion potential (V)
$E_{Initial}$	The initially applied potential (V)
E_{Final}	The final applied potential (V)
E_{Switch}	The switch applied potential (V)
FeS	Mackinawite
FeS ₂	Pyrite
F	Faraday's constant (96485 C mol ⁻¹)
Ga	Gallium
H ₂ O ₂	Hydrogen peroxide
HNO ₃	Nitric acid
H ₂ S	Hydrogen sulfide
H	Henry's Law constant
I_{corr}	Corrosion current (A)
i_{corr}	Corrosion current density (A cm ⁻²)
K _{sp}	Solubility product constant
n	Number of electron transfer
O ₂	Oxygen gas
Q	Coulomb charge (C)
q	Coulomb charge density (C m ⁻³)

R	Universal gas constant ($\text{J mol}^{-1} \text{K}^{-1}$)
SH^-	Bisulfide ion
S^{2-}	Sulfide ion
SO_4^{2-}	Sulfate ion
Si	Silicon
S	Sulfur
T	Temperature (K)
t	Time (s)
V_m	Molar volume ($\text{m}^3 \text{mol}^{-1}$)
α	Alpha
β	Beta
γ	Gamma
λ	Wavelength (nm)
δ	Nernst diffusion layer thickness (m)
ΔG°	Standard Gibbs free-energy change (kJ mol^{-1})
ν	The scan rate (V s^{-1})

List of Tables

Table 4.1: Absolute charge densities calculated by integration of the current density–time curves in Figure 4.4 (b).....	103
Table 4.2: Elemental composition at the selected areas of the oxidized Cu specimen exposed to Ar-sparged 0.1 M NaCl + 10 ⁻⁴ M SH ⁻ solution.	109
Table 5.1: Atomic percentage of different elements corresponding to Figure 5.9	130
Table 6.1: Atomic percentage of different elements corresponding to Figure 6.3	143
Table 6.2: Composition (wt. %) at selected regions shown in Figure 6.4	144
Table 7.1: Composition (wt. %) of the surface oxides (shown in Figure 7.2) formed during corrosion in the absence and presence of γ -radiation in aerated pure water (400 μ L). ..	170
Table 7.2: Composition (wt. %) of the surface films (shown in Figure 7.8) after 20 h-immersion in a 0.1 M Cl ⁻ + 5 \times 10 ⁻⁵ M SH ⁻ solution.	178
Table 7.3: Composition (wt. %) of the surface films (shown in Figure 7.12) after 20 h-immersion in a 0.1 M Cl ⁻ + 5 \times 10 ⁻⁵ M SH ⁻ solution.	183

List of Figures

Figure 1.1: Schematic of (a) a DGR and (b) a multi-barrier system to be used for long-term storage of used nuclear fuel [5]. Image courtesy of NWMO.....	2
Figure 1.2: A prototype of the NWMO Mark II container and the bentonite clay buffer box for the disposal of used CANDU fuel bundles [13,14].....	3
Figure 2.1: SKB’s reference canister with an outer corrosion barrier of copper and an insert of nodular cast iron (With permission of SKB) [4,5].	11
Figure 2.2: Exploded view of a Swedish KBS-3 canister and its major components (from the left: copper base, copper tube, insert, steel lid for insert, and copper lid). Image courtesy of SKB (TR-10-14 [4]).	11
Figure 2.3: Cross-section view of BWR and PWR type fuel assemblies (all dimensions given in millimetres, unless otherwise indicated). Image courtesy of SKB [4,5].	11
Figure 2.4: Comparison of the (a) KBS-3, (b) the original NWMO reference (NWMO Mark I) and (c) the current Canadian reference (NWMO Mark II) used fuel container designs [17]......	13
Figure 2.5: An illustration of a UFC within a bentonite clay buffer box [1]......	14
Figure 2.6: A cross-sectional view of the Cigar Lake uranium ore body in Saskatchewan (Cramer and Smellie 1994) reveals that the uranium ore, enclosed by a clay layer at a depth of 430 meters, has been isolated from the surface environment for more than 1.3 billion years [1].	15
Figure 2.7: A qualitative illustration showing the evolution of exposure conditions anticipated in a Canadian DGR as a function of time [29]. The temperature plot is for a specific repository design while the oxygen and radiation dose curves are purely illustrative.	16

Figure 2.8: The predicted time-dependent container surface temperature for the current Canadian DGR design [25].	17
Figure 2.9: (a) Bisulfide flux at container surface (based on the modelling approach described in Briggs et al. [31]) and (b) Estimated O ₂ consumption and surface absorbed radiation dose rate (based on the observed rate of O ₂ consumption from Müller et al. [32] and the maximum absorbed dose rates from Marco et al. [33] and an assumed half-life of 30 years).	19
Figure 2.10: Predicted time dependence of the corrosion potential of a copper canister in a KBS-3V repository at the Olkiluoto site [61].	27
Figure 2.11: The fcc packing of Cu atoms, bcc packing of O atoms and cubic structure of Cu ₂ O. The schematics were adapted from Chen et al. and redrawn for this thesis [71]...	29
Figure 2.12: Schematic showing the different shapes of single Cu ₂ O crystals with increasing growth time [71].	29
Figure 2.13: The fcc structure of Cu, cubic structure of Cu ₂ O and monoclinic structure of CuO [71].	30
Figure 2.14: Pourbaix diagram of the Cu–O–S system, showing a number of stable regions for stoichiometric and non-stoichiometric Cu _x S species [82]. [Cu] _{tot} =1 mmol/L, [SH ⁻] _{tot} = 2 mmol/L, and [Na ⁺] = [NO ₃ ⁻] = 10 mmol/L [84].	31
Figure 2.15: Crystal structures of (a) the low-chalcocite (monoclinic), (b) high-chalcocite (hexagonal), (c) cubic-chalcocite (cubic), (d) djurleite, (e) digenite, and (f) anilite [89].	33
Figure 2.16: Optical images of basic cupric carbonate minerals (a,b) and basic cupric nitrate minerals (c,d). (a) Azurite, Cu ₃ (CO ₃) ₂ (OH) ₂ , (b) Malachite, Cu ₂ (CO ₃)(OH) ₂ , (c) Gerhardtite, Cu ₃ (NO ₃)(OH) ₃ , and (d) Rouaite, Cu ₂ (NO ₃)(OH) ₃ [97].	34
Figure 2.17: Pourbaix diagrams for Cu in pure H ₂ O at (a) 25 °C and (b) 100 °C. [Cu(aq)] _{tot} = 10 ⁻⁶ mol/kg [98].	35

Figure 2.18: Pourbaix diagrams of Cu in chloride solutions at 25 °C, (a) $[\text{Cl}^-] = 10^{-3} \text{ mol/L}$ and (b) $[\text{Cl}^-] = 1 \text{ mol/L}$ [80].	36
Figure 2.19: Pourbaix diagram for copper at 25 °C in H_2O containing $[\text{SH}^-] = 0.2 \text{ mmol/kg}$ ($2 \times 10^{-4} \text{ mol/L}$) and $[\text{Cu}]_{\text{tot}} = 10^{-6} \text{ mol/kg}$ [104].	38
Figure 3.1: Wrought copper microstructure [3].	67
Figure 3.2: Schematic of the three-compartment electrochemical cell (solution volume of 700 mL).	69
Figure 3.3: (a) Picture of ^{60}Co gamma cell irradiator [7] and (b) custom-designed sample holder [8].	71
Figure 3.4: The relationship between different possible potential programs and the corresponding electroanalytical technique: (a) chronoamperometry, (b) cyclic voltammetry, and (c) linear sweep voltammetry [11].	73
Figure 3.5: Optical microscope representation [15].	76
Figure 3.6: Schematic of a scanning electron microscope (With permission of the Nanoscience) [18].	77
Figure 3.7: Schematic of electron beam interaction [19].	78
Figure 3.8: Schematic diagram of the generation of backscattered electrons (BSEs) vs. secondary electrons (SEs) (With permission of the Nanoscience) [18].	79
Figure 3.9: SEM images of (a) tungsten filament source, (b) solid-state crystal electron source, and (c) FEG electron source [18].	80
Figure 3.10: Schematic illustration of a dual-beam FIB/SEM instrument. Expanded view shows the electron and ion beam sample interactions [21].	81
Figure 3.11: Schematic representation of (a) Rayleigh scattering (elastic), Stokes and anti-Stokes Raman scattering (inelastic) occurring during Raman spectroscopy and (b) intensity	

of Stokes Raman (red) scattering with regards to anti-Stokes Raman (blue) scattering (With permission of the Thermo Fisher scientific) [23]. 83

Figure 3.12: Schematic diagram of a dispersive Raman microscope: 1–optical microscope; 2–spectrograph; 3–laser source; 4–microscope objective; 5–sampling stage with a sample; 6–beam splitter or dichroic mirror; 7–Rayleigh filter; 8–microscope-to-spectrograph coupling optics; 9–spectrograph entrance aperture; 10–collimating mirror; 11–diffraction grating; 12–focusing mirror; 13–array detector (With permission of the Thermo Fisher scientific) [23]. 84

Figure 3.13: Schematic illustration of the constructive interference obeying Bragg's law ($[hkl]$, the plane normal, is the vector drawn from the origin of the unit cell to intersect the crystallographic plane (hkl) at a 90° angle. Additionally, the plane normal $[hkl]$ must be parallel to the diffraction vector (s) [25]. 87

Figure 3.14: Schematic diagram of X-ray tube [25]. 88

Figure 3.15: A schematic showing the Bragg-Brentano geometry in an XRD analysis [26]. 88

Figure 4.1: Proposed mechanism for copper corrosion in $[Cl^-]$ containing groundwater under oxic conditions (With permission of the Swedish Nuclear Fuel and Waste Management Company) [10]. 94

Figure 4.2: Cyclic voltammetry scans recorded on a Cu specimen immersed in 0.1 M NaOH (pH 13) solution under (a) aerated and (b) de-aerated conditions at 2 mV/s, (c) de-aerated conditions at 1 mV/s. Regions A and B represent different oxidation processes. 99

Figure 4.3: Current density-time plot recorded during potentiostatic oxidation of Cu at -0.3 V in 0.1 M NaOH solution for 30 min under aerated and de-aerated conditions. 101

Figure 4.4: Plots recorded during potentiostatic oxidation at different potentials in de-aerated 0.1 M NaOH for 30 min: (a) i -time and (b) Log i -time..... 102

- Figure 4.5: E_{corr} -time curves of oxidized Cu specimens exposed to 0.1 M NaCl solutions containing different concentrations of bisulfide inside the glove-box..... 104
- Figure 4.6: Raman Spectra collected on (a) an oxidized Cu specimen in 0.1 M NaOH (30 min, -0.3 V/SCE) and oxidized Cu specimens exposed to 0.1 M NaCl containing (b) 5×10^{-5} M SH^- and (c) 10^{-4} M SH^- inside the glove-box..... 105
- Figure 4.7: Morphologies of films on (a) a Cu specimen oxidized in 0.1 M NaOH and oxidized specimens exposed to 0.1 M NaCl containing (b) 5×10^{-5} M SH^- and (c) 10^{-4} M SH^- , inside the glove-box. 106
- Figure 4.8: E_{corr} -time transients recorded on Cu electrodes, oxidized for 30 min at -0.3 V in Ar-sparged 0.1 M NaOH, on exposure to 0.1 M NaCl solution containing various bisulfide concentrations. 107
- Figure 4.9: SEM micrographs of (a) the oxide layer formed on a Cu specimen in Ar-sparged 0.1 M NaOH, and sulfide layers on oxidized specimens exposed to 0.1 M NaCl containing, (b) 5×10^{-5} M SH^- and (c) 10^{-4} M SH^- 108
- Figure 4.10: Selected regions on the oxidized Cu specimen exposed to Ar-sparged 0.1 M NaCl + 10^{-4} M SH^- solution for EDX. 109
- Figure 4.11: (a) E_{corr} recorded on Cu specimens oxidized at -0.3 V/SCE in 0.1 M NaOH after immersion in anaerobic solutions containing 0.1 M Cl^- + 5×10^{-5} M SH^- (variations show the inherent irreproducibility of transition times and reproducibility of potentials) and (b) the respective CSVs, performed at a scan rate of 1 mV/s, after the surface was exposed to the bisulfide solution for different time periods, as indicated. 111
- Figure 4.12: Anodic charge densities for specimens oxidized at -0.3 V/SCE in 0.1 M NaOH and the corresponding cathodic charges, with standard deviation, after immersion for different periods of time in a solution containing 0.1 M Cl^- + 5×10^{-5} M SH^- 112
- Figure 5.1: (a) Cathodic stripping voltammograms on Cu specimens after anodic polarization at different potentials in 0.1 M NaOH, (b) CSVs recorded after oxide growth at -0.24 , -0.27 and -0.3 V/SCE on an enhanced current density scale. 120

- Figure 5.2: FE-SEM micrographs (a,b) showing the surface morphology of an oxide film anodically grown at -0.22 V/SCE in 0.1 M NaOH and (c) a FIB-cut cross-section of the film..... 121
- Figure 5.3: Raman spectrum recorded on a Cu specimen oxidized at -0.22 V/SCE in de-aerated 0.1 M NaOH..... 122
- Figure 5.4: (a) E_{corr} recorded on Cu specimens oxidized at -0.22 V/SCE in 0.1 M NaOH after immersion in an anaerobic 0.1 M $\text{Cl}^- + 5 \times 10^{-5}$ M SH^- solution; and (b) the respective CSVs performed at a scan rate of 1 mV/s after the surface was exposed to the bisulfide for different time periods, as indicated..... 123
- Figure 5.5: Anodic charge densities for specimens oxidized at -0.22 V/SCE in 0.1 M NaOH and the corresponding cathodic charges, with standard deviation, after immersion for different periods of time in a solution containing 0.1 M $\text{Cl}^- + 5 \times 10^{-5}$ M SH^- 125
- Figure 5.6: SEM micrographs (a,b) showing the surface morphology of an oxide film grown at -0.22 V/SCE in 0.1 M NaOH after 45 min exposure (stage B in E_{corr} plot vs. time, Figure 5.4 (a)) to a solution containing 0.1 M $\text{Cl}^- + 5 \times 10^{-5}$ M SH^- : (c) a FIB-cut cross-section of the film. 127
- Figure 5.7: SEM micrograph and respective EDX maps of an oxide film grown at -0.22 V/SCE in 0.1 M NaOH after 45 min exposure (stage B in E_{corr} plot vs. time, Figure 5.4 (a)) to a solution containing 0.1 M $\text{Cl}^- + 5 \times 10^{-5}$ M SH^- 127
- Figure 5.8: FE-SEM micrographs (a,b) showing the surface morphology of an oxide grown at -0.22 V/SCE in 0.1 M NaOH after 24 h exposure (stage D in E_{corr} plot vs. time, Figure 5.4 (a)) to solution containing 0.1 M $\text{Cl}^- + 5 \times 10^{-5}$ M SH^- and (c,d) a FIB-cut cross-section of the film..... 129
- Figure 5.9: FE-SEM micrograph and respective EDX maps of an oxide grown at -0.22 V/SCE in 0.1 M NaOH after long-term exposure (stage D in E_{corr} plot vs. time, Figure 5.4 (a)) to solution containing 0.1 M $\text{Cl}^- + 5 \times 10^{-5}$ M SH^- 129

Figure 5.10: Raman spectra recorded on a Cu surface that was oxidized at -0.22 V/SCE in 0.1 M NaOH before and after exposure to a solution containing 0.1 M Cl^- + 5×10^{-5} M SH^- for different periods.	131
Figure 5.11: Schematic illustration of the stages of conversion of a $\text{Cu}_2\text{O}/\text{CuO}/\text{Cu}(\text{OH})_2$ film on a Cu surface to Cu_2S in a chloride solution containing 5×10^{-5} M SH^- : (a) the $\text{Cu}_2\text{O}/\text{CuO}/\text{Cu}(\text{OH})_2$ layer before exposure to the SH^- solution; (b) the partially converted film after a short exposure period with E_{corr} in region B (Figure 5.4 (a)); (c) the film after an extended period of exposure to the SH^- solution with E_{corr} in region D (Figure 5.4 (a)).	133
Figure 6.1: SEM images of hydrothermally-grown copper oxide on SKB copper.	141
Figure 6.2: Raman spectrum of hydrothermally-grown copper oxide.....	142
Figure 6.3: SEM/FIB cross-sections of hydrothermally-grown copper oxide (a) outer layer, (b) inner layer, and (c) EDX selected spots.	143
Figure 6.4: SEM images on the surface of an oxidized Cu specimen after film removal via a chemical method (Red boxes show the selected regions for EDX).	144
Figure 6.5: E_{corr} recorded on Cu during the growth of oxide in 0.57 M KClO_3 and 0.1 M Na_2CO_3 solution at 50 °C.....	145
Figure 6.6: E_{corr} of oxidized Cu in 0.1 M NaCl + 10^{-4} M Na_2S	145
Figure 6.7: SEM images and FIB cross-section on oxidized Cu after 1 h-exposure to 0.1 M NaCl + 10^{-4} M Na_2S (E_{corr} : -260 mV).	147
Figure 6.8: EDX maps of a FIB cross-section on oxidized Cu after exposure to 0.1 M NaCl + 10^{-4} M Na_2S (E_{corr} : -260 mV).	147
Figure 6.9: Raman spectra obtained on oxidized Cu after exposure to 0.1 M NaCl + 10^{-4} M Na_2S at different E_{corr} , as indicated on the figure.	148

Figure 6.10: SEM images and FIB cross-section on oxidized Cu after exposure to 0.1 M NaCl + 10^{-4} M Na ₂ S (E_{corr} : -385 mV).	149
Figure 6.11: EDX maps of FIB cross-section on oxidized Cu after exposure to 0.1 M NaCl + 10^{-4} M Na ₂ S (E_{corr} : -385 mV).	150
Figure 6.12: SEM images and FIB cross-section on oxidized Cu after exposure to 0.1 M NaCl + 10^{-4} M Na ₂ S (E_{corr} : -598 mV).	151
Figure 6.13: EDX maps of FIB cross-section on oxidized Cu after exposure to 0.1 M NaCl + 10^{-4} M Na ₂ S (E_{corr} : -598 mV).	152
Figure 6.14: E_{corr} of oxidized Cu in 0.1 M NaCl + 10^{-4} M Na ₂ S.	154
Figure 6.15: Raman Spectrum obtained on oxidized Cu after exposure to 0.1 M NaCl + 10^{-4} M Na ₂ S at -760 mV.	154
Figure 6.16: SEM images and FIB cross-section on oxidized Cu after exposure to 0.1 M NaCl + 10^{-4} M Na ₂ S (E_{corr} : -760 mV).	155
Figure 6.17: Oxidized Cu in 0.1 M NaCl + 2×10^{-4} M Na ₂ S: E_{corr} (left) and cathodic stripping voltammograms (right) recorded after immersion for various periods.	156
Figure 7.1: Optical images during copper corrosion after exposure to 400 μ L of aerated pure water (pH ₀ 9) in the presence of γ -radiation.	167
Figure 7.2: SEM images of the copper surface in 400 μ L of aerated pure water solutions (pH ₀ = 9) in the absence (a) and presence of γ -radiation (b) 24 h, (c) 48 h, and (d) 70 h (Red boxes show the selected locations for EDX).	169
Figure 7.3: Image and Raman spectrum (a,c) of a Cu surface corroded for 70 h in 400 μ L of aerated pure water in the absence of γ -radiation and image and Raman spectra (b,d) of a Cu surface corroded for 70 h in 400 μ L of aerated pure water in the presence of γ -radiation (Selected locations are shown with red x and numbers).	171

- Figure 7.4: SEM images (a) BSE and (b) SE of the surface and (c) the metal-oxide cross-section (cut using focused Ga-ion beam) after 70 h corrosion in 500 μL aerated pure water solution in the presence of γ -radiation. 173
- Figure 7.5: EDX map of a circular feature and the surrounding colloidal patches on a Cu surface after 70 h-corrosion in 500 μL of aerated pure water (pH_0 9) in the presence of γ -radiation. 174
- Figure 7.6: Images and Raman spectra of the base layer (top row) and a circular feature (bottom row) on the surface oxide after 70 h-corrosion in 500 μL of aerated pure water (pH_0 9) in the presence of γ -radiation (Selected locations are shown with red x and numbers). 175
- Figure 7.7: Optical images of the grown oxide in 400 μL of pure water in the presence of γ -radiation; 24 h, 48 h, and 70 h after 20 h-immersion in a 0.1 M $\text{Cl}^- + 5 \times 10^{-5}$ M SH^- solution..... 176
- Figure 7.8: SEM images of the grown oxide in 400 μL of pure water in the absence of γ -radiation (a) and in the presence of γ -radiation (b) 24 h, (c) 48 h, and (d) 70 h after 20 h-immersion in a 0.1 M $\text{Cl}^- + 5 \times 10^{-5}$ M SH^- solution (Red boxes show the selected locations for EDX). 177
- Figure 7.9: Optical image and Raman spectra recorded at selected locations on the grown oxide (70 h-radiation in 400 μL pure water) after 20 h-immersion in a 0.1 M $\text{Cl}^- + 5 \times 10^{-5}$ M SH^- solution (Selected locations are shown with red numbers). 179
- Figure 7.10: E_{CORR} measurement as a function of time for a grown oxide (70 h-radiation in 500 μL pure water) after immersion in a 0.1 M $\text{Cl}^- + 5 \times 10^{-5}$ M SH^- solution. 180
- Figure 7.11: Cathodic stripping voltammograms of grown oxide (70 h-radiation in 500 μL pure water) after transfer to a (a) 0.1 M Cl^- , and (b) 0.1 M $\text{Cl}^- + 5 \times 10^{-5}$ M SH^- solution at 10 mV/min. 181
- Figure 7.12: SEM images (top and middle rows) and FIB cross-sections (bottom row) of the grown oxide corroded for 70 h in a 500 μL of pure water in the presence of γ -radiation

after immersion in a $0.1 \text{ M Cl}^- + 5 \times 10^{-5} \text{ M SH}^-$ solution (Red boxes show the selected locations for EDX).....	183
Figure 7.13: Images and Raman spectra of selected spots on the grown oxide (70 h-radiation in 500 μL pure water) after 20 h-immersion in a $0.1 \text{ M Cl}^- + 5 \times 10^{-5} \text{ M SH}^-$ solution (x and the red numbers show the selected locations for Raman).....	184
Figure 8.1: Cell used in the immersion tests; (a) pre-purging with Ar gas, (b) adding powder to the bisulfide solution (continuously stirring), and (c) retrieving the resulting powder	197
Figure 8.2: XRD patterns (Red) of the pristine (a) CuO powder and (b) Cu ₂ O powder, together with standards (Blue) obtained from the Rigaku SmartLab XRD database.	199
Figure 8.3: XRD patterns collected on CuO powder exposed to $0.1 \text{ M Cl}^- + 5 \times 10^{-5} \text{ M SH}^-$ solutions for different durations of immersion, together with standard obtained from the Rigaku SmartLab XRD database.	200
Figure 8.4: XRD patterns of (a) a mixed Cu/CuO powder (1:1 ratio) exposed to bisulfide solutions ($0.1 \text{ M Cl}^- + 5 \times 10^{-5} \text{ M SH}^-$) for different immersion times, together with (b) standards obtained from the Rigaku SmartLab XRD database fitted to the selected pattern for sulfidized Cu/CuO powder after 1 h.	201
Figure 8.5: XRD patterns collected on (a) a Cu ₂ O powder exposed to $0.1 \text{ M Cl}^- + 5 \times 10^{-5} \text{ M SH}^-$ solutions for different durations of immersion, together with (b) standard obtained from the Rigaku SmartLab XRD database fitted to the selected pattern for sulfidized Cu ₂ O powder after 24 h.	202
Figure 8.6: XRD pattern collected on CuO powder exposed to $0.1 \text{ M Cl}^- + 5 \times 10^{-3} \text{ M SH}^-$ solution for 24 h, together with standards obtained from the Rigaku SmartLab XRD database.....	203

1 Introduction

1.1 Background and motivation

Internationally, nuclear power is recognized as the second-largest contributor to low-carbon energy, generating 10% of the global electricity supply [1]. Particularly, in Canada, 15% of the nationwide electricity and 60% of the Ontario electricity is produced by nuclear power plants [2,3]. In Canada, almost 99.9% of the used nuclear fuel, a by-product of this process, has been produced by Canada Deuterium Uranium (CANDU) nuclear power reactors located in Ontario, Quebec, and New Brunswick. There are also very small quantities of used fuel from research, demonstration, and isotope-producing reactors, in particular at the Chalk River Laboratories site in Ontario [4].

When CANDU fuel is removed from the reactor at the end of its useful life, it is considered to be a waste product. Used fuel is highly radioactive and releases energy primarily as thermal radiation (heat) and as alpha (α), beta (β), gamma (γ), and neutron radiation, therefore, it requires careful management. Although its initial radioactivity level decreases very quickly with time, residual radioactivity persists, and the used fuel remains a potential hazard to human health and the environment for an extended period of time. It is estimated to take about one million years for the radioactivity level to reach about that of an equivalent amount of natural uranium [5,6].

For the first 7-10 years after removal, the used fuel is stored at the reactor site in fuel bays (enclosed water pools) which provide radiation shielding and cooling. After this time, the used fuel can be stored in air-cooled concrete containers, commonly known as dry storage. These highlight how several metres of water or tens of centimetres of concrete and steel provide shielding from the radiation emitted by used fuel stored at the surface [4].

The Government of Canada assigned the Nuclear Waste Management Organization (NWMO) to be responsible for the safe and long-term management of Canada's used nuclear fuel. The NWMO led the development of a long-term approach, known as Adaptive Phased Management (APM), which is both a technical method (what is planned to build)

and a management system (how the organization will work with Canadian and Indigenous people to get it done) [7].

The plan is consistent with the long-term management strategy adopted by other countries with nuclear power programs, such as Finland, Sweden, Switzerland, the United Kingdom and France [8,9]. The project will contain and isolate used nuclear fuel inside a DGR, at a depth of approximately 500 to 800 m in a stable geological formation [10,11]. The key components of the repository, shown in **Figure 1.1 (a)** are: A- the main surface facilities, where fuel is received, packaged, and transferred underground; B- the underground repository facilities, notably the shafts, and main services area; C- the placement rooms connected by access tunnel including the engineered barrier system, notably the used fuel container, buffer and sealing materials; and D- the excavated host rock. The concept also incorporates the transportation system for moving fuel from interim storage sites to the repository site [10].

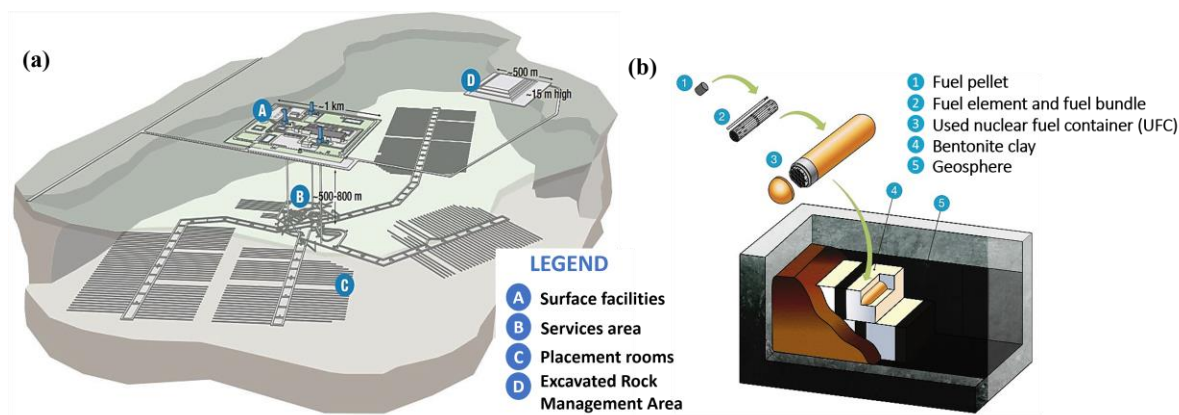


Figure 1.1: Schematic of (a) a DGR and (b) a multi-barrier system to be used for long-term storage of used nuclear fuel [5]. Image courtesy of NWMO.

Within a DGR, a series of engineered and natural barriers will work together to permanently contain used nuclear fuel, as shown in **Figure 1.1 (b)**. Each of these barriers provides a distinct and stand-alone level of protection. In the event of any barrier's deterioration, the next one comes into play [10,12].

Used nuclear fuel bundles will be placed into durable UFCs. Together with the bentonite clay buffer box (barrier 4), the container is a principal part of the engineered barrier system. The container prevents radionuclides in the fuel from escaping into the underground environment. It is engineered to remain intact and keep the used nuclear fuel completely isolated until the fuel's radioactivity has decreased to the level of natural uranium [13,14].

In 2014, the NWMO refined its container design to one that is optimized for the used CANDU fuel (referred as the Mark II, shown in **Figure 1.2**). This modification also streamlines the handling and emplacement in the DGR. Each container, with a length of 2.5 m, accommodates 48 used CANDU fuel bundles (four layers of 12 bundles) in a steel basket within a carbon steel pipe.

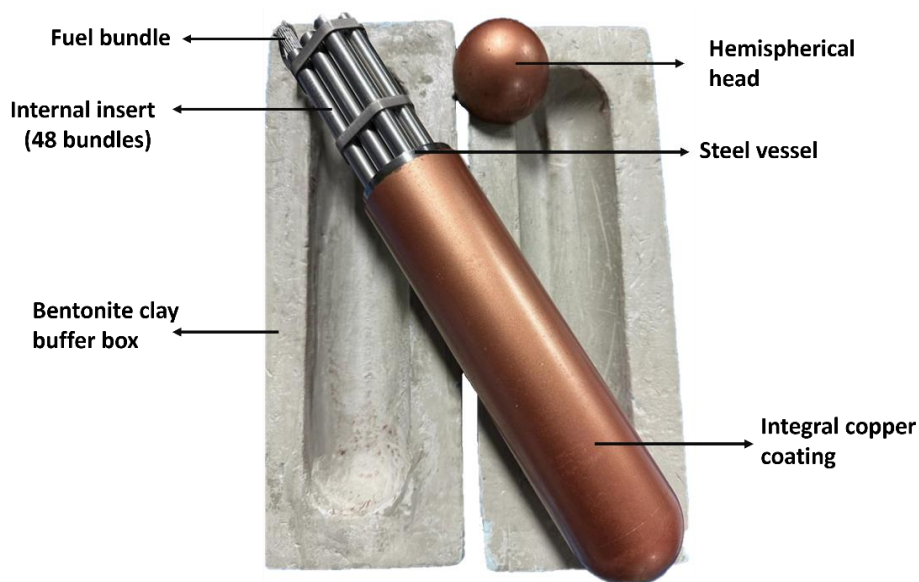


Figure 1.2: A prototype of the NWMO Mark II container and the bentonite clay buffer box for the disposal of used CANDU fuel bundles [13,14].

This steel vessel has the mechanical strength to withstand pressures up to 45 megapascals caused by swelling of the bentonite clay buffer surrounding the container, the overlying rock and three-kilometre-thick glaciers during a future ice age. The pipe is protected by a 3-millimetre corrosion-resistant copper coating. The container has two hemi-spherical heads that are welded to the core of the container. This hemi-spherical design is specially engineered to withstand significant pressure [15,16]. This design significantly decreases

the amount of Cu required (3 mm compared to 25–50 mm in designs employing separately manufactured copper shells over iron/steel inserts, referred as the Mark I) and adopts modern coating technologies to apply the Cu directly to the steel, eliminating the necessity for the Cu to be self-supporting during fabrication [14].

The choice of copper as the main corrosion barrier for the container, widely adopted in many countries (e.g., Finland, Sweden, Canada) was originally grounded in its thermodynamic stability under predicted DGR conditions. Subsequently, this choice has been supported by decades of corrosion research and by preservation of archaeological and natural copper samples that have remained intact in the earth for hundreds/thousands or millions/billions of years, respectively [5,10,17,18].

Cu containers emplaced in a DGR will experience an evolution of exposure conditions. Initially, the environment in the vicinity of the container will be oxidizing and warm due to limited amounts of oxygen (O_2) trapped during the construction phase and heat from radioactive decay within the fuel matrix. Under these conditions, corrosion will lead to the formation of oxide layers on the Cu surface [19,20]. Presently available information indicates the maximum depth of container corrosion due to O_2 consumption will be limited to 298 μm , as calculated using mass balance, conservatively assuming the corrosion product to be Cu_2O only. Additionally, oxidants produced by water (H_2O) radiolysis could result in a further 10-30 μm penetration of the Cu coating [21,22]. Once anoxic conditions are established, SH^- ions produced by the action of SRB, could diffuse through the sealing system and cause Cu corrosion [23-25]. In Swedish/Finnish and Canadian DGRs, the groundwater SH^- concentrations are expected to be up to 10^{-4} M, and $<10^{-6}$ M, respectively. Predictions of corrosion due to bisulfide could vary from a few micrometres to nearly 1 mm [26,27].

Considering the thickness of the copper layer in the new UFC design, there is a considerably smaller tolerance for uncertainty in the copper corrosion allowance compared to Mark I. Hence, it is imperative to have a good understanding of the corrosion behaviour of the copper layer in the unique and changing DGR conditions over time to build sufficient confidence in this design.

1.2 Thesis objectives

The repository environment is anticipated to evolve from early oxic conditions to later anoxic conditions. Likewise, degradation processes of the UFCs should transition from the initial oxygen-driven processes to those governed by the availability of bisulfide as oxidant. This transition may involve the conversion of accumulated (hydr)oxide-type corrosion products produced during the brief oxic phase to copper sulfide compounds during the long anoxic phase. During this conversion, bisulfide species could interact with the UFC surface in several ways depending on the type of (hydr)oxide corrosion products present, the nature and concentration of the bisulfide species, and other factors:

- i. Chemical conversion of copper oxide to copper sulfide
- ii. Galvanically-coupled processes between the copper oxide reduction and Cu oxidation by bisulfide
- iii. Direct corrosion of Cu by bisulfide species arriving at the metal surface

So far, considerable efforts have been devoted to investigating exclusively either the oxic period or the anoxic period. However, the significant gap that the current research aims to address is how the early period of oxide growth affects the evolution of the container surface under anoxic conditions at which the primary threat to the integrity of the Cu container would be bisulfide ions within the groundwaters.

The objectives of this thesis project were to create different types of copper oxide/hydroxide layers via various methods, with known compositions and distinct structures, to investigate their role in the subsequent bisulfide-induced corrosion of the underlying Cu under de-aerated conditions. The morphology of the surface oxide film and the nature and concentration of bisulfide species will influence the possible conversion scenarios that have been mentioned above, thereby determining the depth of copper corrosion.

1.3 Thesis outline

In **Chapter 1**, background information on the project and the thesis motivation, objective, and outline were presented. In **Chapter 2**, materials background, literature review, and

theoretical background were presented on the properties of copper and its corrosion under oxic and anoxic conditions. Additionally, the possible theories on the conversion of copper oxide to sulfide were discussed in detail. In **Chapter 3**, the experimental methods used in Chapters 4 – 8 were described. In **Chapter 4**, the best condition for growing Cu (I) oxide was optimized and the effect of various conditions and bisulfide concentrations on the conversion of Cu (I) oxide to sulfide was studied. The kinetics of oxide-to-sulfide conversion in the presence of various bisulfide concentrations was the focus of this chapter. In **Chapter 5**, the influence of electrochemically-grown dual-layer oxide ($\text{Cu}_2\text{O}/\text{CuO}$) in alkaline solution on the bisulfide-induced corrosion of copper was explored. This was obtained by measuring corrosion potential followed by cathodic stripping voltammetry to evaluate the extent to which the conversion processes took place after different immersion periods and analyzing the surface corrosion products (films) to determine the film properties and the morphology of the corrosion damage. In **Chapter 6**, the influence of hydrothermally-grown copper oxide ($\text{Cu}_2\text{O}/\text{CuO}$) with different structure than that of electrochemically-grown oxide on the bisulfide-induced corrosion was studied. Experiments were performed by measuring corrosion potential at different concentrations of bisulfide and analyzing the surface corrosion products (films) to determine the film properties and corrosion damage. In **Chapter 7**, the corrosion products analogous to those formed during the initial repository oxic period were created, and the possibility that such films can subsequently inhibit the reaction of copper with bisulfide was determined. Surface morphologies of corrosion products and corrosion damage were examined using SEM/EDX/FIB. The comparison between different types of copper oxide enabled us to better understand the effect of the nature of the oxide film on the bisulfide-induced corrosion and to consider all the possible scenarios. In **Chapter 8**, the role of copper metal in the conversion of copper oxide to sulfide was investigated. For this purpose, in the absence and presence of metallic copper, different copper oxides in the form of powder samples were exposed to aqueous bisulfide solutions. The purity of powder samples and the effect of the bisulfide ions on the conversion of copper oxides were studied using XRD method. In **Chapter 9**, the summary and major conclusions of this thesis were presented along with a brief discussion on future work.

1.4 References

- [1] S. Sadekin, S. Zaman, M. Mahfuz, R. Sarkar, Nuclear power as foundation of a clean energy future: A review, *Energy Procedia*, 160, 513-518, 2019.
- [2] B.W. Brook, A. Alonso, D.A. Meneley, J. Misak, T. Blee, J.P. van Erp, Why nuclear energy is sustainable and has to be part of the energy mix, *Sustainable Materials and Technologies* 1-2, 8-16, 2014.
- [3] The Canadian nuclear factbook 2020, Canadian Nuclear Association, 2020.
- [4] P. Gierszewski, A. Parmenter, Confidence in safety – Revell site, TR-2022-14, NWMO, 2022.
- [5] D.S. Hall, M. Behazin, W.J. Binns, P.G. Keech, An evaluation of corrosion processes affecting copper-coated nuclear waste containers in a deep geological repository, *Progress in Materials Science*, 118, 100766, 2021.
- [6] F. Garisto, Sixth case study: Features, events and processes, TR-2017-08, NWMO, 2017.
- [7] NWMO (S. Briggs, ed.), Technical program for long-term management of Canada's used nuclear fuel – Annual Report 2022, TR-2023-01, NWMO, 2023.
- [8] Inventory of radioactive waste in Canada, Natural Resources Canada, 2016.
- [9] Programs around the world for managing used nuclear fuel, NWMO, 2020.
- [10] D.S. Hall, P.G. Keech, An overview of the Canadian corrosion program for the long-term management of nuclear waste, *Corrosion Engineering, Science and Technology*, 52, 2-5, 2017.
- [11] T. Standish, J. Chen, R. Jacklin, P. Jakupi, S. Ramamurthy, D. Zagidulin, P.G. Keech, D.W. Shoemith, Corrosion of copper-coated steel high level nuclear waste containers under permanent disposal conditions, *Electrochimica Acta*, 211, 331-342, 2016.

- [12] L. Abrahamsen-Mills, J. Small, State of science review: Modelling microbial effects to assess long-term performance of a DGR, NWMO, 2019.
- [13] M. Wu, M. Behazin, J. Nam, P. Keech, Internal corrosion of used fuel container, TR-2019-02, NWMO, 2019.
- [14] J. Chen, M. Behazin, W.J. Binns, K. Birch, C. Boyle, Technical program for long-term management of Canada's used nuclear fuel – Annual report 2017, TR-2018-01, NWMO, 2018.
- [15] Morco, R.P. "Gamma-radiolysis kinetics and its role in the overall dynamics of materials degradation" Doctor of Philosophy, The University of Western Ontario, Electronic Thesis and Dissertation Repository, 7248, 2020.
- [16] Description of a deep geological repository and centre of expertise for Canada's used nuclear fuel, NWMO, 2015.
- [17] Implementing adaptive phased management 2020 to 2024, TR-2020-01, NWMO, 2020.
- [18] F. King, Critical review of the literature on the corrosion of copper by water, SKB, 2010.
- [19] F. King, L. Ahonen, C. Taxen, U. Vourinen, L. Werme, Copper corrosion under expected conditions in a deep geologic repository, TR-01-23, SKB, 2001.
- [20] R. Wu, R. Sandström, L.Z. Jin, Creep crack growth in phosphorus alloyed oxygen free copper, *Materials Science and Engineering: A*, 583, 151-160, 2013.
- [21] D.S. Hall, T.E. Standish, M. Behazin, P.G. Keech, Corrosion of copper-coated used nuclear fuel containers due to oxygen trapped in a Canadian deep geological repository, *Corrosion Engineering, Science and Technology*, 53, 309-315, 2018.
- [22] F. King, M. Behazin, A Review of the effect of irradiation on the corrosion of copper-coated used fuel containers, *Corrosion and Materials Degradation*, 2, 678-707, 2021.

[23] J. Chen, Z. Qin, D.W. Shoesmith, Rate controlling reactions for copper corrosion in anaerobic aqueous sulphide solutions, *Corrosion Engineering, and Science Technology*, 46, 138-141, 2011.

[24] F. King, A review of the properties of pyrite and the implications for corrosion of the copper canister, TR-13-19, SKB, 2013.

[25] L. Duro, V. Montoya, E. Colàs, David García, Groundwater equilibration and radionuclide solubility calculations, TR-2010-02, NWMO, 2010.

[26] F. King, D.S. Hall, P.G. Keech, Nature of the near-field environment in a deep geological repository and the implications for the corrosion behaviour of the container, *Corrosion Engineering, and Science Technology*, 52, 25-30, 2017.

[27] Long-term safety for the final repository for spent nuclear fuel at Forsmark, TR-11-01, SKB, 2011.

2 Technical Background

The focus of this chapter is on the engineered barrier system that can guarantee the safe isolation of used nuclear fuel. The integrity of this system strongly depends on environmental parameters that will evolve over time; therefore, it is imperative to discuss the relevant effects in more detail.

2.1 Used nuclear fuel containers

As previously stated, the used fuel will be placed inside a durable UFC. The primary purpose of this container is to confine and isolate the used fuel from the subterranean surroundings, preventing groundwater from contacting the used fuel and, consequently, preventing the release of radionuclides from the fuel into the underground environment [1].

2.1.1 Used fuel container design

2.1.1.1 Scandinavian design

The Swedish (SKB) [2] and Finnish (Posiva) [3] programs have collaboratively developed a cylindrical container for light water reactor fuel, measuring nearly 5 m in length and just over 1 m in diameter, featuring an inner metallic core made of nodular cast iron for structural integrity, with steel channel tubes accommodating the fuel assemblies (**Figure 2.1**).

The outer layer is constructed from a 5-cm thick O-free P-doped (OFP) copper for corrosion protection, including a tube, lid, and base, all joined using friction stir welding (FSW). The canister components include a cast iron insert with a steel tube cassette, a steel lid, a copper tube, a copper lid, and a copper base, as shown in **Figure 2.2**.

The canister design includes two inserts, one for 12 boiling water reactor (BWR) fuel assemblies and another for 4 pressurized water reactor (PWR) fuel assemblies, with the canisters having uniform external dimensions for efficient handling (**Figure 2.3**) [4].



Figure 2.1: SKB's reference canister with an outer corrosion barrier of copper and an insert of nodular cast iron (With permission of SKB) [4,5].

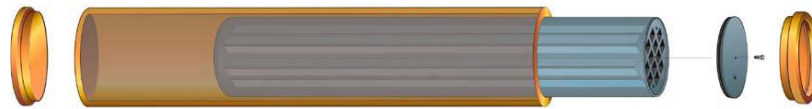


Figure 2.2: Exploded view of a Swedish KBS-3 canister and its major components (from the left: copper base, copper tube, insert, steel lid for insert, and copper lid). Image courtesy of SKB (TR-10-14 [4]).

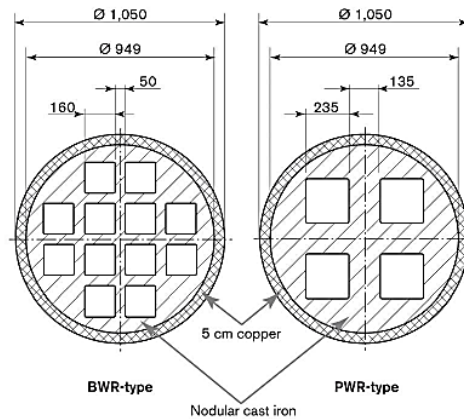


Figure 2.3: Cross-section view of BWR and PWR type fuel assemblies (all dimensions given in millimetres, unless otherwise indicated). Image courtesy of SKB [4,5].

The specifications for OFP copper (>99.99%) include some requirements to meet the desired creep ductility, prevent embrittlement during manufacturing, and avoid corrosion coupled to grain boundary corrosion. To achieve the necessary creep ductility, phosphorus content should be within the range of 30–100 wt. ppm, and sulfur content should be kept below 12 wt. ppm. To prevent embrittlement in the manufacturing process, the hydrogen content should be maintained at less than 0.6 wt. ppm. Additionally, to prevent corrosion coupled to grain boundary corrosion, the oxygen content is recommended to be below some tens of wt. ppm [4,6-8].

2.1.1.2 Canadian design

In Canada, the design of the reference container incorporates distinctive elements, yet it aligns with the fundamental similarities and best practices being explored and applied by other prominent international waste management organizations.

For several years, the NWMO considered a modified version of the KBS-3 'dual vessel' UFC design, incorporating a large cast-iron inner vessel for structural strength and a 25-mm-thick cylindrical copper 'overpack' for corrosion resistance [9]. However, since 2010, Korean and Canadian researchers have been exploring methods to directly apply metallic copper coatings onto steel substrates using gas dynamic cold spray [10-13] and electrodeposition [10,14]. In 2011, the NWMO engineering team conducted a significant re-evaluation, leading to the adoption of the 'Mark II' UFC as the current Canadian reference design, as demonstrated in **Figure 2.4**. This design optimizes coatings for CANDU fuel bundles, utilizing modern coating technologies like electrodeposition for empty containers and lids before fuel loading and cold spray over closure welds of filled containers [10,13]. Despite a thinner coating (3 mm), the copper layer exceeds the current conservative corrosion allowance (< 1.3 mm) for the first 1,000,000 years [15,16]. The mechanical requirements, specifically the creep ductility, for copper-coated steel UFCs differ significantly from those of dual-vessel designs. The direct deposition of copper onto the steel container eliminates the need for dopants to enhance creep ductility or weldability.

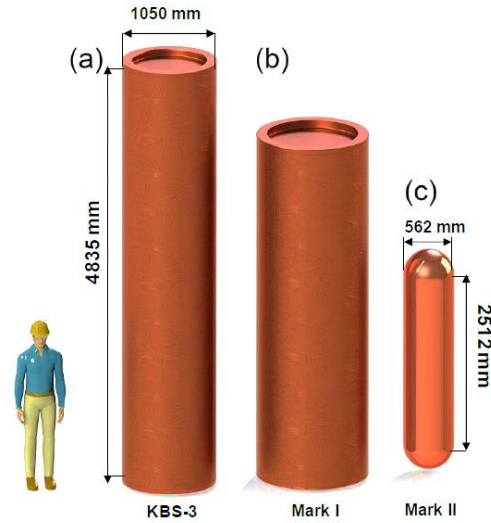


Figure 2.4: Comparison of the (a) KBS-3, (b) the original NWMO reference (NWMO Mark I) and (c) the current Canadian reference (NWMO Mark II) used fuel container designs [17].

While ongoing efforts focus on understanding the microstructure and fracture mechanics of the copper coatings, the integrally bonded coating in the Canadian UFC concept addresses concerns related to creep ductility and stress corrosion cracking seen in dual-vessel designs [10,18]. The assumption that the corrosion behaviour of NWMO copper coatings (i.e. electrodeposited and cold spray) matches that of wrought copper (i.e. SKB OFP) is under investigation through research programs, including long-term electrochemical tests, materials characterization, and surface analysis. While metals deposited through cold spray methods may sometimes exhibit porosity, the NWMO methods limit porosity to less than 1%, and preliminary results indicate that the copper coatings exhibit behaviour similar to wrought copper under various solution conditions [19,20].

2.2 Buffer materials and sealing systems

The waste disposal strategy involves surrounding each container with a swelling clay-based buffer material to create a low-permeability and chemically benign environment. The clay buffer will serve multiple purposes it will: impede water flow, increase the time for water to reach the container; minimize microbiologically-influenced corrosion by suppressing

microbial activity; slow radionuclide movement in case of container failure; and mechanically support and protect the container [1]. Bentonite, a naturally occurring clay, is the primary component of the buffer, containing the stable mineral montmorillonite. Montmorillonite's unique property of swelling in water is harnessed to seal fractures and gaps, rendering the saturated clay nearly impermeable. The clay is compressed into two solid halves of a box, known as a buffer box, surrounding the waste container, as illustrated in **Figure 2.5**. This buffer box, arranged with thermal spacing bentonite blocks and gap fill material (to fill the gap spaces in the engineered barrier system), ensures safe handling, emplacement, and thermal isolation of the waste containers in the repository. The bentonite stability, swelling ability, and impermeability contribute to the overall containment strategy for long-term waste disposal.

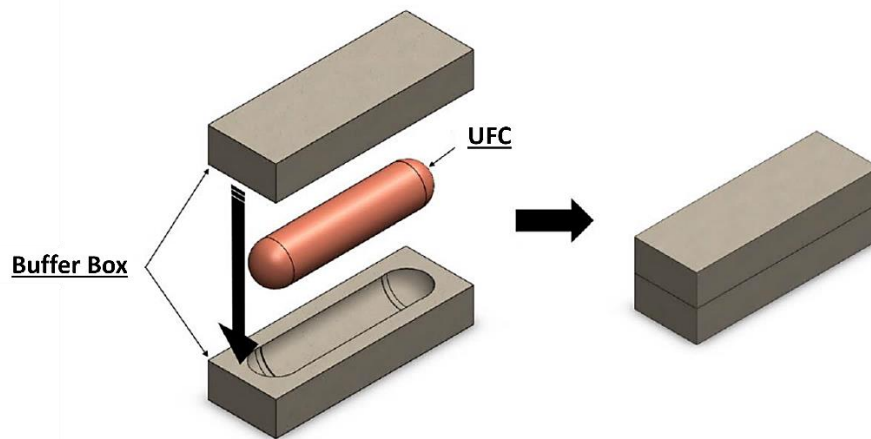


Figure 2.5: An illustration of a UFC within a bentonite clay buffer box [1].

2.3 Natural analogues

The long-term stability of engineered barrier materials is crucial for the safe management of used nuclear fuel, alongside the stability of the geosphere. These materials are chosen based on the proven durability of analogous natural materials in deep geological conditions. Cigar Lake uranium ore body in Saskatchewan serves as a natural analogue for the repository (**Figure 2.6**).

Geological evidence from Cigar Lake reveals that uraninite ore, a natural uranium oxide, remained stable underground for over 1.3 billion years [1]. The combination of uranium

oxide ore, surrounded by natural clay, effectively contained uranium, preventing any surface indication of the ore deposit. This natural stability is predictive of the effectiveness of uranium oxide used fuel containment in a repository, ensuring long-term confinement of radionuclides.

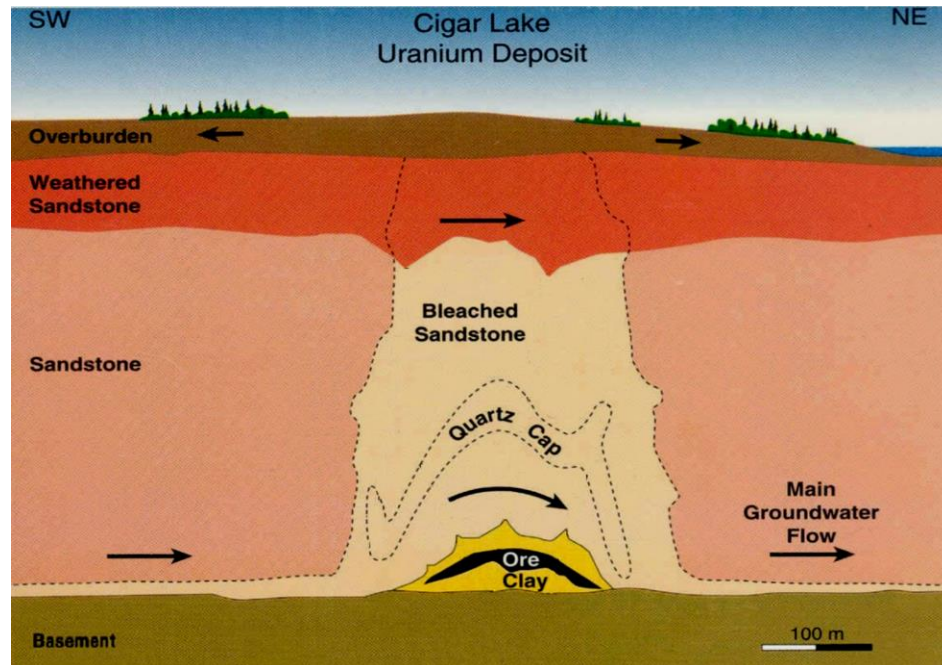


Figure 2.6: A cross-sectional view of the Cigar Lake uranium ore body in Saskatchewan (Cramer and Smellie 1994) reveals that the uranium ore, enclosed by a clay layer at a depth of 430 meters, has been isolated from the surface environment for more than 1.3 billion years [1].

The selection of copper as a container material is primarily based on its stability under conditions commonly encountered underground, characterized by water-saturated rock and chemically reducing environments with low to no oxygen. Various lines of evidence, including thermodynamic calculations, experimental studies, and observations from natural analogues, support the long-term stability of copper under such conditions. Studies suggest that a relatively thin layer of copper can endure for over one million years in the Canadian repository, reinforcing confidence in its long-term performance [21]. Copper durability is also evidenced by the presence of naturally occurring, pure metallic copper deposits around the Great Lakes, historically utilized by First Nations people and

understood to be ~1 billion years old. Natural occurrences of copper, such as those in the Keweenaw Peninsula in northern Michigan and the Permian Littleham Mudstone in southwest England, further underscore its inherent stability [22-24].

In Dunarobba forest, Italy, sequoia-like trees buried in naturally occurring clay for 1½ million years have been remarkably preserved. The clay impeded water flow to the trees, preventing decomposition, and the trees, composed of wood, did not fossilize [1].

2.4 Evolution of the repository environment

In the context of a DGR for used nuclear fuel, an understanding of the evolution of environmental conditions over time, especially at the external UFC surface and within the surrounding bentonite clay (near-field) is crucial for predicting container corrosion behaviour confidently. Over the past four decades, consensus has emerged that the DGR environment undergoes a transition from initially warm, dry, and oxidizing conditions to a long-term state of cool, wet, and anoxic conditions, as generally shown in **Figure 2.7** [25].

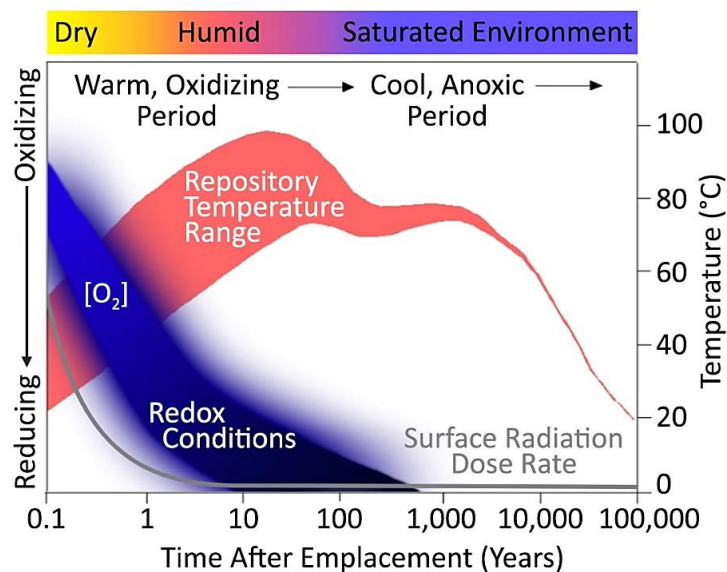


Figure 2.7: A qualitative illustration showing the evolution of exposure conditions anticipated in a Canadian DGR as a function of time [29]. The temperature plot is for a specific repository design while the oxygen and radiation dose curves are purely illustrative.

This evolution has significant implications for corrosion types, rates, and the overall performance of used nuclear fuel containers. The design of the DGR includes constraints on environmental parameters, with anoxic deep groundwaters limiting available oxygen for corrosion to that trapped in the repository at closure and that generated by water radiolysis. Additionally, factors such as buffer and backfill properties, including volume, porosity, and saturation, determine the inventory of trapped oxygen and play a role in determining initial porewater compositions and transport rates of reactants and corrosion products near the container surface [26-28].

2.4.1 Temperature and heat transfer

The nature of the near-field environment is significantly influenced by the thermal behaviour of the UFCs. This thermal behaviour, in turn, is determined by the layout of the DGR and the decay characteristics of the radionuclide inventory within the used nuclear fuel bundles. **Figure 2.8** illustrates a thermal calculation specific to the Canadian nuclear fuel waste management program.

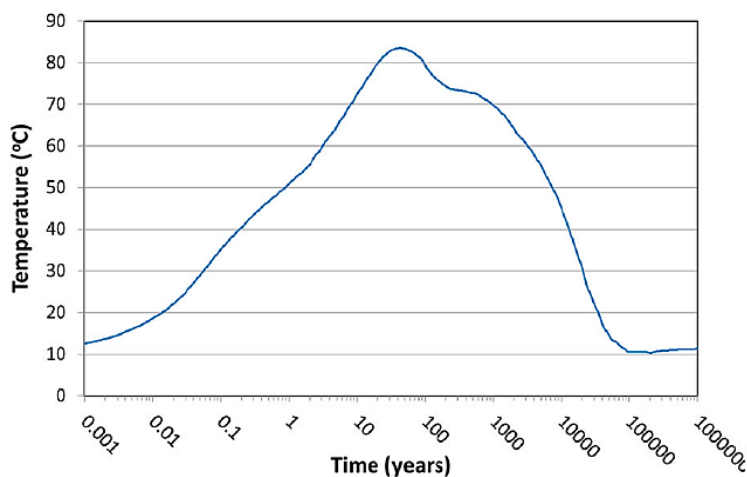


Figure 2.8: The predicted time-dependent container surface temperature for the current Canadian DGR design [25].

It depicts a temperature elevation peaking within a few decades, followed by a gradual return to ambient temperature. In addition, the container surface temperature affects the thermal conductivity of the buffer materials. The temperature gradient through the buffer

materials could also influence the corrosion behaviour, impacting reaction rates and solubility variations [30]. The far-field, representing the host rock, is defined by site geology, placement depth, and remains relatively stable over the lifetime of the DGR.

2.4.2 Redox conditions

The redox conditions in the DGR are influenced by the inventory of trapped O_2 during closure and by the radiolysis of the porewater. The former is heavily dependent on the DGR design and the buffer and backfill properties. The consumption of oxygen in the DGR might be counteracted by the radiolytic production of oxidants from the interaction of gamma radiation with water and humid air, especially for thin-walled containers. Although the amounts of oxidants produced are modest, trace quantities have been observed, as indicated by previous studies [26].

In the DGR, the initially trapped O_2 will eventually be completely consumed, and the gamma radiation field will have decayed. Following this, the corrosion of the container can only occur if bisulfide is present in the repository. While microbial activity within the bentonite is suppressed, bisulfide could be generated by sulfate-reducing bacteria in regions where microbial activity is not constrained by low water activity, such as in the host rock or at the rock-highly compacted bentonite (HCB) interface. The predicted time dependence of the interfacial flux of SH^- for various locations on the UFC surface in a Canadian DGR placement room is shown in **Figure 2.9 (a)**. In mass-transfer simulations with a constant concentration of SH^- (10^{-6} mol/L) assumed at the wall of the placement room, the bisulfide flux profiles in **Figure 2.9 (a)** reveal that significant amounts of SH^- do not reach any part of the container surface until several years after the commencement of bisulfide production.

Based on the O_2 profiles in **Figure 2.9 (b)**, a sulfide film will not be present on the container while O_2 is available, eliminating concerns about the catalysis of the O_2 reduction reaction by Cu_2S . The supply of SH^- will vary across different parts of the container surface, with maximum flux to the hemispherical end caps due to geometrical reasons, while interior surfaces shielded from the bisulfide source will experience the lowest flux. Exterior

surfaces closest to the bisulfide source will have an intermediate flux. Despite these variations, the SH^- fluxes will be small, with an interfacial flux of $10^{-6} \text{ mol/m}^2\text{yr}^1$.

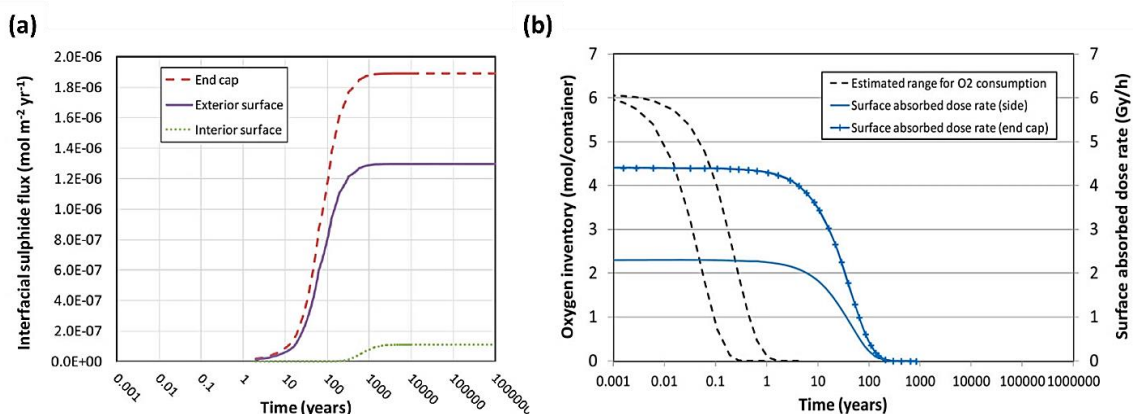


Figure 2.9: (a) Bisulfide flux at container surface (based on the modelling approach described in Briggs et al. [31]) and (b) Estimated O_2 consumption and surface absorbed radiation dose rate (based on the observed rate of O_2 consumption from Müller et al. [32] and the maximum absorbed dose rates from Marco et al. [33] and an assumed half-life of 30 years).

In general, the evolution of the repository near-field environment can be broadly categorized into four stages, with each stage's duration dependent on host rock properties (especially for crystalline vs. sedimentary host rock) and associated with specific forms of corrosion [25]:

2.4.2.1 Immediate post-placement period (stage I)

Trapped oxygen and moisture will be present in the early stage of the DGR, contributing to potential aqueous corrosion. The radiation dose rate will be at its peak, dominated by γ -radiation, with negligible contributions from α - and β -particles, as they are stopped by the Zircaloy cladding. The γ -radiation dose rate evolution over time is assessed for the Canadian UFC design, showing higher rates than with other designs, like KBS-3, due to a thinner steel body [33,34]. The neutron dose rate is anticipated to be significantly lower than that of γ -radiation and can be considered negligible. Stage I will last for a few days to several months, dependent on factors such as the thermal gradient from the UFCs, the

drying of the HCB buffer material, and the consumption of oxygen through corrosion or other processes [25]. A brief period with uneven distribution of moisture may occur during the drying process of the HCB material.

2.4.2.2 Dry-out period (stage II)

The UFC surface will become sufficiently dry to prevent aqueous corrosion. Atmospheric corrosion may still occur, due to the presence of deliquescent salt deposits on the UFC surface and driven by any remaining trapped oxygen. This stage will last until the repository becomes saturated with groundwater from its surroundings. The duration is highly dependent on site-specific characteristics such as the initial moisture content in the HCB, the magnitude of the thermal gradient, and, particularly, the hydraulic conductivity of the host rock. NWMO estimates this period to extend to approximately 50 years in crystalline host rock and around 5000 years in sedimentary host rock [25].

2.4.2.3 Container re-wetting and buffer saturation period (stage III)

This stage represents a transition during which humidity at the UFC surface progressively increases until full wetting is achieved. The increasing relative humidity (RH) leads to the progressive deliquescence of salt species, which may result in non-uniform wetting of the UFC exterior surfaces. If trace oxygen remains, it will be consumed during this stage in the DGR evolution. Non-uniform corrosion is highly unlikely due to the low expected oxygen concentration but may be possible. If the radiation dose rate is still high, especially for the crystalline host rock scenario, which will allow water to enter earlier, non-uniform radiation-influenced corrosion (RIC) may also be possible, in principle. The composition of the groundwater entering the repository during this stage will depend heavily on the host rock type, geographical setting and the buffer properties [35].

2.4.2.4 Long-term anoxic period (stage IV)

The final stage will begin once the near field reaches full saturation. The long-term near-field environment is characterized by continued cooling and anoxic conditions. There is no evidence in Canada that the injection of dilute and possibly aerated, glacial meltwaters to repository depth will be possible, making issues associated with buffer erosion extremely

improbable. The steady production of SH^- at the repository boundaries, sustained by ongoing microbial activity, particularly that involving SRB, will become the dominant source of microbiologically-influenced corrosion (MIC) during this stage [25].

2.5 Impact of environmental evolution on Cu corrosion in a DGR environment

To provide a comprehensive understanding of corrosion behaviour and potential mechanisms impacting the UFC service life over time in a DGR environment, one approach that can be applied, involves considering various types of corrosion based on the different oxidants present, produced, or transported into the DGR [36]. Each corrosion type is evaluated separately to determine a corrosion allowance for each. This assessment utilizes either a simple rate-based model or an inventory-based model to address the specific characteristics and potential reactions associated with different oxidants within the repository environment.

Four corrosion sub-allowances are examined: oxic corrosion attributed to trapped oxygen, radiation-influenced corrosion, anoxic aqueous corrosion, and microbiologically-influenced corrosion. The corrosion allowances for copper canisters in a Canadian deep geological repository are contingent upon site-specific geological and groundwater characteristics, particularly the far-field bisulfide concentration. Under generic Canadian site conditions, the total corrosion damage is assessed at 270 μm over 1 million years. By incorporating highly conservative considerations for potential corrosion reactions, one could predict that the maximum estimated corrosion damage would be 1.2 mm within the same timeframe. This corrosion level is notably lower than the 3 mm coating thickness specified in the Canadian used fuel container design and the 25-50 mm thickness of copper in dual-walled vessels (Sweden, Finland), emphasizing the robustness of the corrosion protection measures in place [21].

2.5.1 Oxic corrosion

In a DGR environment after waste emplacement, a finite quantity of molecular oxygen will be trapped, primarily in the pore space of HCB blocks and backfill material. Due to the initial saturation of the HCB with water, a portion of the oxygen will be present in dissolved

form, while the remaining fraction will be in the gaseous state within the unsaturated pore volume [15,37]. The corrosion of copper due to this trapped oxygen is analyzed using an inventory approach, considering factors like porosity, degree of saturation, solubility in water, and the ideal gas law [37]. For the Canadian DGR design, NWMO estimates that 13 mol of O₂ will be present per UFC, corresponding to 2.9 mol/m² of copper surface area. The assumption is made that the entire oxygen inventory reacts solely with the copper coating material, although realistically, a significant fraction is expected to be consumed by microbial activity and mineral oxidation in the bentonite buffer, backfill, and host rock [25,38-41]. The corrosion products are conservatively assumed to be Cu (I) oxide or other Cu (I) salts rather than Cu (II) species. This approach establishes a practical upper limit for oxidic corrosion, providing a conservative estimate of its extent.

For the Canadian UFC and DGR reference designs, the calculated depth of 81 μm for 2.9 mol/m² of oxygen corresponds to the ratio of oxygen to copper surface area. The robustness of this value to potential changes in the reference design parameters is crucial, as modifications may occur based on site conditions. Trapped oxygen impact may range from 36 to 298 μm, depending on design variations and repository depth [37]. The most conservative estimate, accounting for worst-case scenarios in design parameters (e.g. low occupancy of the repository, short rooms, siting at a greater depth, large block-to-wall gaps and large spacer blocks), yields a maximum corrosion depth of 298 μm. The corrosion product composition will depend on the specific environment, with Cu₂O expected to be the primary component [37,38].

2.5.2 Radiation-influenced corrosion (RIC)

The local environment within and around the UFCs will experience ionizing radiation, primarily γ-radiation, emitted by the decay of radionuclides in the bundles of used nuclear fuel. The radiation energy absorbed by the HCB and UFC metal components will mainly dissipate as heat, while inducing ionization and molecular decomposition in the water and gas-phases, which can generate redox-active species [42,43]. High dose rates can lead to γ-radiolysis of water, producing oxidants like H₂O₂, and radiolysis of humid air, yielding compounds such as NO_x and HNO₃ [44,45]. The thinner copper-coated UFC design, especially in the hemispherical heads, offers less radiation shielding than dual-vessel

designs, increasing the need to assess the maximum extent of RIC on the copper exterior of UFCs in a Canadian DGR environment [34]. This concern is generally less relevant for other waste management programs, due to their thicker UFC wall designs and lower penetrating dose rates.

The period of the highest radiation dose rates will occur during the initial post-emplacment stage and the subsequent dry-out period, with a significant decrease in external dose rates over the first few decades and reaching negligible levels after approximately 300 years [26]. The radiation dose rate may remain moderately elevated during the wetting and long-term anoxic stages, depending on local geology, especially in Canadian crystalline host rock [25]. This contrasts with bentonite saturation in Canadian sedimentary host rock, which may take thousands of years.

Morco et al. [26] recently integrated the time-dependent radiation dose rate to assess the accumulated radiation dose at the exterior surface of UFCs. Assuming that all accumulated dose will be absorbed in water droplets at the UFC surface, and using established radiolysis models for humid air and water, the accumulated dose can be converted into a fixed quantity of nitric acid that could be produced. This fixed amount can provide an inventory-based assessment of the maximum depth of RIC in a post-closure DGR environment. The results suggest that less than 9.4 μm of radiation-induced copper corrosion will occur over 1 million years. While this inventory-based approach neglects the effects of bentonite clay, a recent study [46] suggests that highly compacted bentonite has no significant impact on the RIC of copper. In this study, the extent of copper corrosion was assessed by measuring the thickness of the oxide layer grown after irradiation whether in pure anoxic water or within the bentonite-containing system, as number of electrons needed to reduce the layer. Although the increase in number of electrons was more pronounced in the bentonite system, the difference between the two systems fell nearly within the margin of experimental uncertainty [46].

Recent investigations on radiation-induced corrosion of copper indicate that the primary corrosion product is expected to be Cu_2O , influenced by pH, with various other compounds possible depending on the UFC surface environmental conditions [47,48]. Also, surface

characterization revealed local corrosion features exhibited non-uniformity. Therefore, an additional conservative factor for localization during the radiolysis period can be estimated to be around 40–50 μm , with a maximum allowance of 100 μm for RIC [48].

2.5.3 Dissolved bisulfide and microbiologically-influenced corrosion (MIC)

In the context of a DGR environment, dissolved bisulfide generated by anaerobic SRB is proposed as a major contributor to long-term copper corrosion [15,49,50]. Site models, reflecting the geochemical conditions of the low permeability crystalline and sedimentary rock formations in the Canadian DGR concept, indicate extremely low mineralogical sulfide content. Consequently, microbiological activity is considered as the predominant source of bisulfide in the DGR setting.

The assessment of MIC assumes, based on experimental support, that no bisulfide species will be produced in the HCB material, and the formation of biofilms at the bentonite-copper interface will be prevented. However, considering experimental evidence indicating that SRB activity can occur in low-density bentonite materials, such as slurries [51,52], the possibility of some SRB activity at the bentonite-rock boundaries or within the rock near the bentonite within the excavation damaged zone (EDZ) is acknowledged. Additionally, there might be SRB activity in remote cracks and fissures of the host rock, potentially supplying dissolved bisulfide that could diffuse into the repository toward the surfaces of the UFCs [53].

In the context of a post-closure DGR with stagnant water conditions, the transport of bisulfide to the surfaces of UFCs would necessitate diffusion through the HCB material. The diffusion coefficient of aqueous bisulfide in saturated HCB is small, approximately on the order of $10^{-11} \text{ m}^2/\text{s}$ [54]. Additionally, the likelihood of microbial activity in the low-permeability crystalline and sedimentary rock formations, typical in the DGR concepts of Canada and other nations, is deemed to be low.

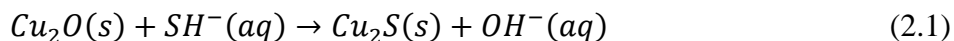
Despite conservative assumptions acknowledging some activity of SRB, a fixed, elevated concentration of bisulfide species at the boundaries of the DGR is considered for further conservative assessment. Notably, iron-rich clays demonstrate the capacity to precipitate

microbially formed bisulfide, converting it into mackinawite (FeS), which could act as a barrier preventing the bisulfide from reaching the container [55].

Predictions of corrosion due to bisulfide in relevant reports vary from a few micrometres to nearly 1 mm [56,57]. Higher estimates are often associated with assumptions of large bisulfide diffusion coefficients, the absence of iron in the bentonite, and microbial activity occurring within the bentonite rather than exclusively at the EDZ or beyond.

2.5.4 Conversion of copper oxides/hydroxides or other forms of Cu (II) to copper sulfide

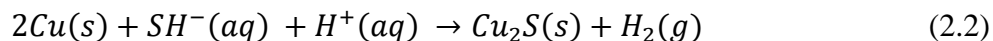
When assessing MIC of the UFCs, it is crucial to note that the flux of bisulfide will only occur once the DGR becomes saturated with water [25]. The expected timescales for repository saturation are greater than the period required for O₂ consumption, indicating that once anoxic period establishes, oxidic corrosion is anticipated to have ceased [32]. This leaves the UFC exteriors covered in a layer of copper oxide/hydroxide. Smith et al. [58] showed that in aqueous bisulfide solutions with concentrations between 3×10^{-5} and 10^{-3} mol/L [SH⁻], containing 0.1 mol/L NaCl, a Cu₂O layer grown on Cu surface spontaneously converts to Cu₂S according to Equation (2.1) [58].



Cathodic stripping voltammetry and Raman spectroscopy measurements suggest that the conversion of copper oxide to copper sulfide is approximately 100% efficient in certain experiments involving electrochemically grown copper oxide [58]. Additionally, density functional theory (DFT) calculations have been employed to investigate the chemical mechanisms and rates on various copper surfaces [59].

Reactions involving dissolved copper species (e.g., Cu⁺, CuCl₂⁻) within the bentonite porewater and dissolved bisulfide ions may lead to the precipitation of copper sulfide before the bisulfide reaches the container surface. These reactions are significant in a DGR context, as incoming bisulfide will interact with previously formed corrosion products, such as copper oxides and dissolved copper, before reaching the copper metal surface.

The exchange reactions, distinct from electrochemical reduction of hydrogen as described in Equation (2.2), do not necessitate such reduction and are therefore competitive in sequestering incoming bisulfide ions.



Consequently, any damage from corrosion processes occurring before bisulfide exposure would mitigate the impact of bisulfide corrosion, as the reacting copper would not be further corroded by bisulfide.

Handling such a process within an assessment of the maximum corrosion damage to a UFC introduces complexity in the overall approach of combining individual values for corrosion (i.e., summation of damage from each process). It becomes crucial to consider the efficiency of the conversion of copper oxide to copper sulfide within the underground environment and over the DGR's lifetime. One reasonable approach is to examine varying concentrations of bisulfide, subsequent damage, and the thickness of the oxide film that the bisulfide will encounter.

In scenarios where bisulfide concentrations are low and the oxide is thin or non-uniform, the efficiency of the conversion of copper oxide to copper sulfide may be low. This is because the probability of aqueous bisulfide encountering copper oxide on its way to the surface would not necessarily be high. In such cases, there would be no consideration for the conversion of copper oxide to sulfide within a conservative corrosion allowance. This is applicable to the Canadian DGR, which is expected to contain minimal dissolved bisulfide and only a thin oxide layer from trapped oxygen.

In analyses with higher concentrations of bisulfide and thicker copper oxides on UFC surfaces, the probability of individual bisulfide ions encountering copper oxide instead of metallic copper is higher. Therefore, the overall effect of copper oxide to copper sulfide conversion becomes more pronounced as the total corrosion damage increases. In this scenario, it is assumed that 50% of the previously oxidized copper will sequester bisulfide within this assessment [21].

2.5.4.1 Mixed-potential modelling

The model effectively predicts the corrosion behaviour throughout the entire service life of the canister [60]. In **Figure 2.10**, the variation of E_{corr} is illustrated as the environment transitions from the early warm, aerobic period to the long-term cool, anoxic phase in the presence of bisulfide. Initially, E_{corr} will be relatively positive due to the aerobic environment. The break in E_{corr} between approximately 1 year and 100 years is attributed to the assumed desiccation of the bentonite closest to the canister, causing the interfacial relative humidity to drop below the necessary value to sustain aqueous corrosion until the repository begins to saturate.

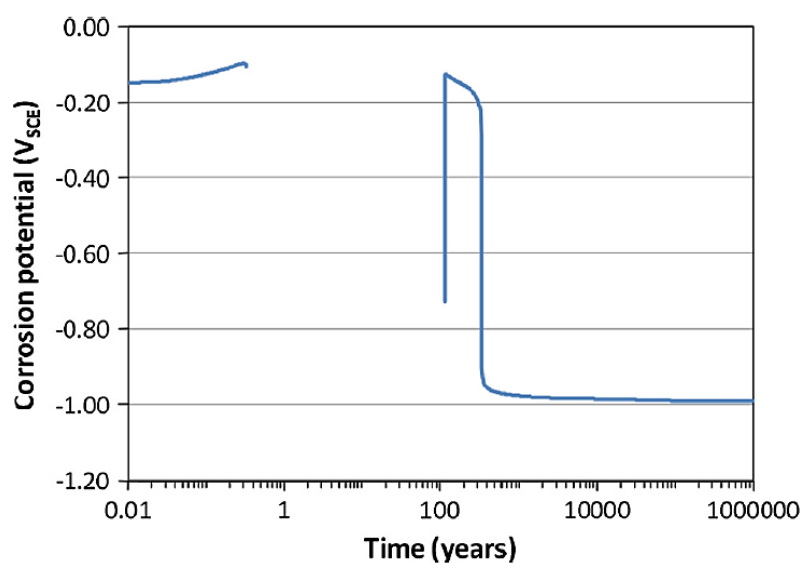


Figure 2.10: Predicted time dependence of the corrosion potential of a copper canister in a KBS-3V repository at the Olkiluoto site [61].

The positive shift in E_{corr} will occur as soon as the canister surface re-wets sufficiently to sustain interfacial reactions. This shift will be a result of the coupling of anodic dissolution to form Cu_2S and the cathodic reduction of both Cu (II) and CuCl_2^- . As the concentrations of Cu (II) and CuCl_2^- decrease, the cathodic reaction will change to the reduction of SH^- or H_2O (Reactions (2.3) and (2.4)), leading to a precipitous drop in E_{corr} by 800 mV. This abrupt decrease in E_{corr} has been experimentally observed both in bulk solution and with

an electrode covered by compacted clay as the environment was progressively deaerated followed by the addition of SH^- [62].



2.6 Formation of copper complexes over time under DGR conditions

2.6.1 Copper oxides

Copper has a face-centred cubic (fcc) crystal structure with an electronic configuration of $[\text{Ar}]3\text{d}^{10}4\text{s}^1$, which is responsible for its ductile nature and excellent electrical and thermal conductivity. Depending on the Cu oxidation state, copper oxides exist as cuprous oxide (Cu_2O) and cupric oxide (CuO) [63-65].

2.6.1.1 Cu (I) oxide

Cu_2O , the primary copper oxide formed during corrosion, is a semiconductor with a bandgap energy range of 2.0–2.2 eV. The colour of Cu_2O varies from pink to deep red based on crystal size. The physical properties of Cu_2O , including its shape and semiconductor type (p or n), depend on growth mechanisms and conditions [66-69].

Cu_2O has a cubic crystallographic structure. This structure consists of four Cu atoms and eight O atoms, forming two inter-penetrating cubic lattices of fcc packing of Cu atoms and body-centred cubic (bcc) packing of O atoms, as shown in **Figure 2.11**. The interatomic distances between Cu–O and Cu–Cu are 1.84 Å and 3.02 Å, respectively, with unit cell parameters $a = b = c = 4.27 \text{ \AA}$ and $\alpha = \beta = \gamma = 90^\circ$ [70].

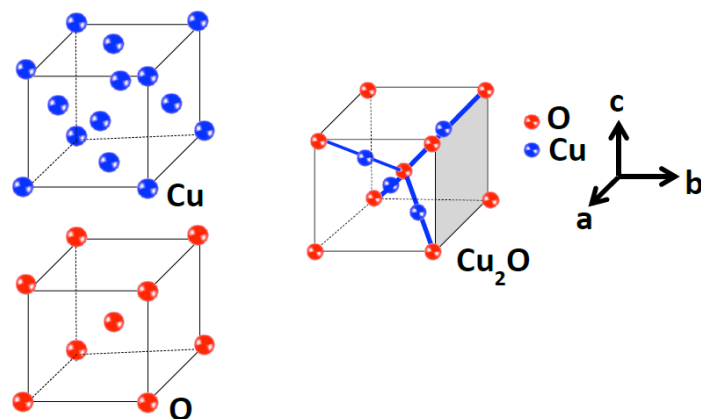


Figure 2.11: The fcc packing of Cu atoms, bcc packing of O atoms and cubic structure of Cu_2O . The schematics were adapted from Chen et al. and redrawn for this thesis [71].

The unit cell of Cu_2O shows various crystallographic planes. The growth of a single Cu_2O crystal is influenced by surface lattice energies, with the $\{113\}$ plane exhibiting the highest growth rate and the $\{111\}$ plane having the lowest growth rate, unless altered by the presence of additives affecting surface reactivity.

Cu_2O single crystals undergo shape evolution during growth. Initially forming cubes with $\{100\}$ planes, they gradually transform into truncated cubes, truncated octahedrons, and finally into octahedrons with $\{111\}$ planes, considered thermodynamically stable, **Figure 2.12**.

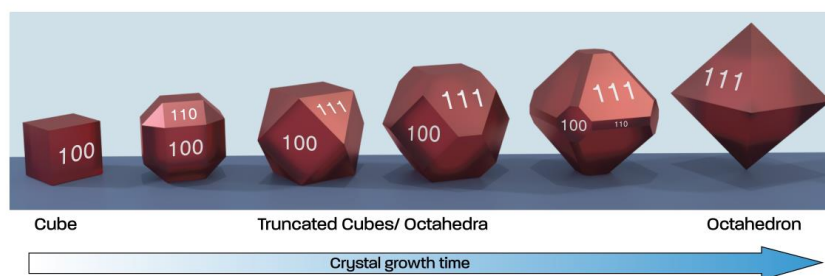


Figure 2.12: Schematic showing the different shapes of single Cu_2O crystals with increasing growth time [71].

Extended growth times result in crystals with multiple faces, possibly leading to spherical shapes. Various shapes, including branching structures and hopper-cubes, are influenced

by the interplay between precipitation/crystallization kinetics and diffusion, highlighting the roles of both kinetics and thermodynamics in shaping Cu_2O crystals [71,72].

2.6.1.2 Cu (II) oxide

CuO , known as tenorite, is a semiconductor with a bandgap of 1.3–1.9 eV and appears black. It has a monoclinic crystallographic structure with Cu coordinated to 4 O atoms, characterized by lattice constants: $a = 4.68 \text{ \AA}$, $b = 3.42 \text{ \AA}$, $c = 5.14 \text{ \AA}$, $\alpha = \gamma = 90^\circ$, and $\beta = 99.6^\circ$. At room temperature, CuO is less stable than Cu_2O [70,73-75].

Figure 2.13 illustrates the face-centred cubic structure of Cu, the cubic structure of Cu_2O , and the monoclinic structure of CuO .

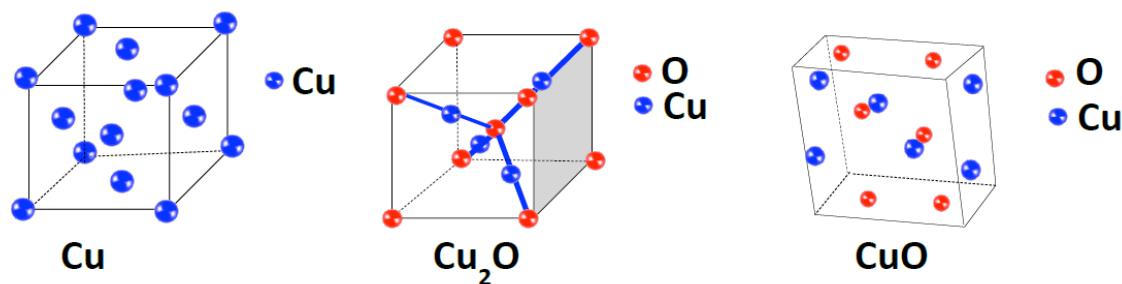


Figure 2.13: The fcc structure of Cu, cubic structure of Cu_2O and monoclinic structure of CuO [71].

2.6.2 Cu (II) hydroxide

Copper (II) hydroxide, $\text{Cu}(\text{OH})_2$, known as cupric hydroxide, is rare but exists naturally as the blue-to-green mineral and is reported to be polymorphic, commonly appearing in fibrous or colloidal forms with an orthorhombic crystal structure, featuring unit cell parameters of $a = 2.951 \text{ \AA}$, $b = 10.592 \text{ \AA}$, $c = 5.257 \text{ \AA}$, and $\alpha = \beta = \gamma = 90^\circ$ [76].

The properties of $\text{Cu}(\text{OH})_2$ vary based on its formation process and the age of the precipitate. At ambient temperatures, $\text{Cu}(\text{OH})_2$ is metastable and often forms during the oxidation of copper, particularly in alkaline environments and in the presence of dissolved chloride anions [77-79].

2.6.3 Cu sulfides

Thermodynamic investigations have identified stability regions for various copper sulfides, including yarrowite ($\text{Cu}_{1.12}\text{S}$), spionkopite ($\text{Cu}_{1.4}\text{S}$), geerite ($\text{Cu}_{1.6}\text{S}$), anilite ($\text{Cu}_{1.75}\text{S}$), digenite ($\text{Cu}_{1.8}\text{S}$), djurleite ($\text{Cu}_{1.96}\text{S}$), chalcocite (Cu_2S), and under more oxidizing conditions, covellite (CuS) [80-82]. The general formula for copper sulfides is often expressed as Cu_{2-x}S due to the commonly observed cation deficiency [83]. Among these phases, chalcocite (Cu_2S) has a stability field that extends to more negative potentials than that of water. This makes chalcocite the expected phase under natural corrosion conditions, particularly in anoxic environments, as illustrated in **Figure 2.14** [84].

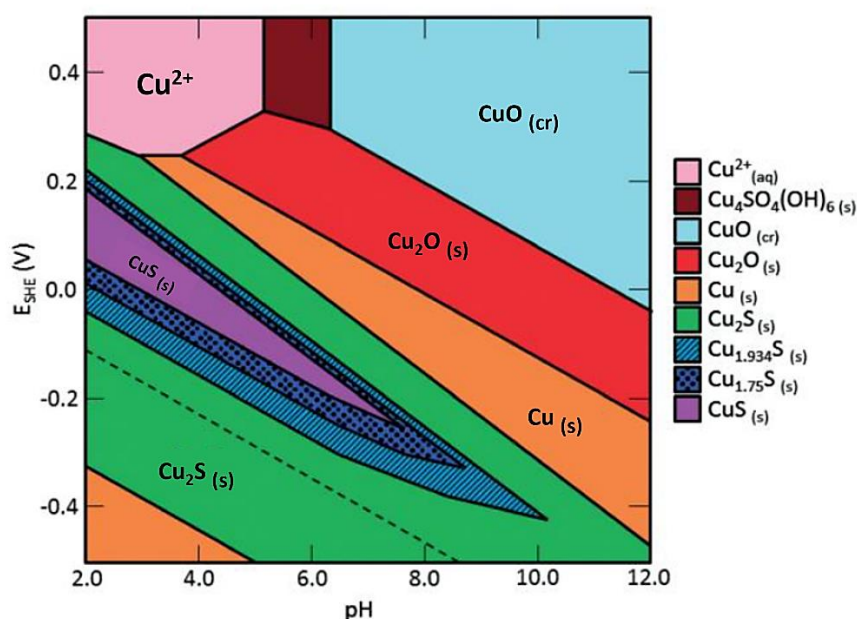


Figure 2.14: Pourbaix diagram of the Cu–O–S system, showing a number of stable regions for stoichiometric and non-stoichiometric Cu_xS species [82]. $[\text{Cu}]_{\text{tot}}=1 \text{ mmol/L}$, $[\text{SH}^-]_{\text{tot}}= 2 \text{ mmol/L}$, and $[\text{Na}^+] = [\text{NO}_3^-] = 10 \text{ mmol/L}$ [84].

Despite the occasional presence of covellite (CuS), various techniques, including XPS and certain X-ray absorption fine structure (EXAFS) analyses, indicate that copper exists predominantly in its monovalent state across different copper sulfide phases [85-87]. This implies that under reducing conditions in the presence of sulfide, Cu chemistry is consistently dominated by Cu (I) [81]. In an XPS study by Folmer and Jellinek [85], the

nearly identical binding energies for Cu (2p) spectra in all Cu_xS compounds confirmed monovalent copper. Additionally, a slight binding energy shift in chalcogen-rich compounds suggested the presence of S_2 pairs, leading to proposed overall CuS stoichiometries:

Recent analysis of Cu X-ray photoelectron spectra by Biesinger supports the challenge of discerning different copper sulfide species solely through Cu (2p) spectra. However, Biesinger demonstrated that distinguishing sulfide phases becomes possible by combining Cu (2p) spectra, Cu LMM Auger spectra, and the modified Auger parameter, emphasizing the need for a comprehensive approach [88].

The crystal structures of copper sulfides exhibit complexity and vary with their stoichiometry. Cu_xS species can be categorized into three types, based on crystal structures: hexagonal close-packed (djurleite and chalcocite), cubic close-packed (anilite and digenite), and hexagonal close-packed with covalently bonded S atoms (covellite). Chalcocite, djurleite, and digenite demonstrate monoclinic crystal structures at ambient temperature. Some of these structures are presented in **Figure 2.15** [89].

Copper sulfides exhibit electronic conductivity, with electrons displaying 1000 times greater mobility than cations [90, 91]. Cu_2S is recognized as a p-type semiconductor, in which conduction is linked to free holes originating from acceptor levels of Cu vacancies [92]. The valence band's highest levels contain additional holes due to Cu vacancies, and the energy band gap increases with rising Cu deficiency in most copper sulfide (Cu_{2-x}S) phases [93]. As the value of x increases, a shift to the lowest occupied energy level and a change in band gap energy occur, leading to hole formation near the valence band. Reported band gap energies for Cu_2S , $\text{Cu}_{1.8}\text{S}$, and CuS are 1.2 eV, 1.5 eV, and 2.0 eV, respectively [94].

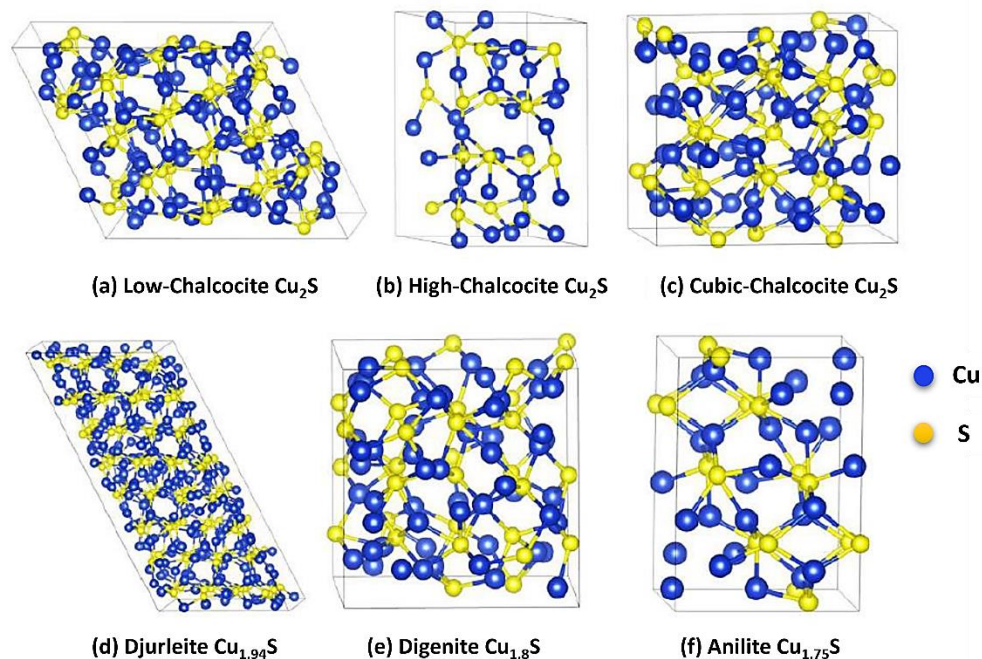


Figure 2.15: Crystal structures of (a) the low-chalcocite (monoclinic), (b) high-chalcocite (hexagonal), (c) cubic-chalcocite (cubic), (d) djurleite, (e) digenite, and (f) anilite [89].

2.6.4 Other Cu salts

In a DGR environment, groundwater is expected to contain various anions, including chloride, sulfate, carbonate [25], and nitrate produced via humid air radiolysis [26]. The dissolution of host rock minerals will contribute to the presence of these anions. While salts like Cu (I) sulfate and Cu (I) chloride ($[\text{CuCl}_3]^{2-}$ and $[\text{CuCl}_2]^-$) may form due to the interaction with these anions, their high solubility makes them unlikely to be main corrosion products. Along with soluble copper complexes, such as $[\text{CuCl}_3]^-$ and $[\text{CuCl}_4]^{2-}$ [95], less soluble basic copper salts may be also formed. Cupric ions in solution readily complex with carbonate, giving rise to CuCO_3 , a solid product, that rapidly reacts with moisture to form basic copper carbonates. Atacamite ($\text{Cu}_2\text{Cl}(\text{OH})_3$), azurite ($\text{Cu}_3(\text{CO}_3)_2(\text{OH})_2$), and malachite ($\text{Cu}_2(\text{CO}_3)(\text{OH})_2$) may be formed. Azurite, a rare, bright blue mineral, contrasts with the more common malachite, a bright green copper corrosion product [96].

Copper nitrates are a common corrosion product in the presence of NO_3^- . Pure $\text{Cu}(\text{NO}_3)_2$ exists in either tri- or hexahydrate forms and is a highly soluble, blue salt. Producing anhydrous cupric nitrate is challenging, as it tends to decompose into basic copper (II) nitrate instead of dehydrating. Basic copper (II) nitrate minerals, like likasite ($\text{Cu}_3\text{NO}_3(\text{OH})_5 \cdot 2\text{H}_2\text{O}$) and gerhardtite and rouaite which are polymorphs ($\text{Cu}_2(\text{NO}_3)(\text{OH})_3$), are rare in nature, often complexed with other anions. Likasite is the most thermodynamically stable among copper nitrates, but its production conditions (highly alkaline and high Cu^{2+} concentrations) are uncommon. The polymorphs form in solutions with near-neutral pH, with gerhardtite being the most stable [95,96]. **Figure 2.16** shows the optical images of basic cupric carbonate minerals and some of basic cupric nitrate minerals.

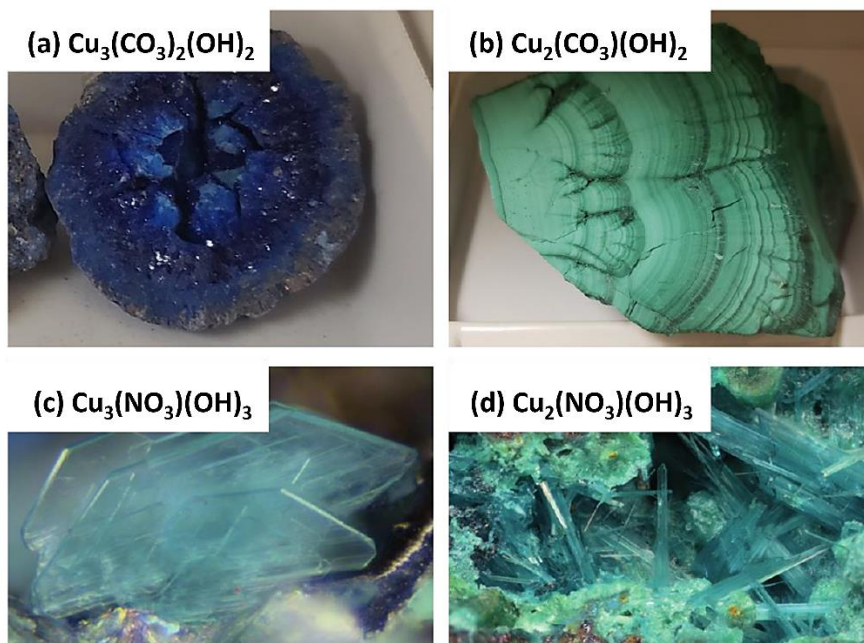


Figure 2.16: Optical images of basic cupric carbonate minerals (a,b) and basic cupric nitrate minerals (c,d). (a) Azurite, $\text{Cu}_3(\text{CO}_3)_2(\text{OH})_2$, (b) Malachite, $\text{Cu}_2(\text{CO}_3)(\text{OH})_2$, (c) Gerhardtite, $\text{Cu}_3(\text{NO}_3)(\text{OH})_3$, and (d) Rouaite, $\text{Cu}_2(\text{NO}_3)(\text{OH})_3$ [97].

2.7 Literature review of Cu corrosion

2.7.1 Relevant thermodynamic data for Cu under disposal conditions

A very useful approach to understand which compositions are thermodynamically stable over a range of conditions in a system containing metal in contact with an aqueous solution is a Pourbaix diagram or potential versus pH plot. The lines for redox reactions in this diagram are defined by the Nernst equation under equilibrium conditions. These lines bound the regions of stability for different species [80].

The thermodynamic data for copper under expected repository conditions have been extensively studied and presented in Pourbaix diagrams. While various groundwater species have been studied, the focus is on the impact of dissolved O_2 , Cl^- , and SH^- on the thermodynamic stability of copper. This section provides details on the relevant thermodynamic data for copper when exposed to these specific species.

Pourbaix diagrams of Cu in pure water are illustrated in **Figure 2.17** [80], revealing that Cu is thermodynamically stable over the entire pH range at both 25 °C and 100 °C in the absence of dissolved O_2 .

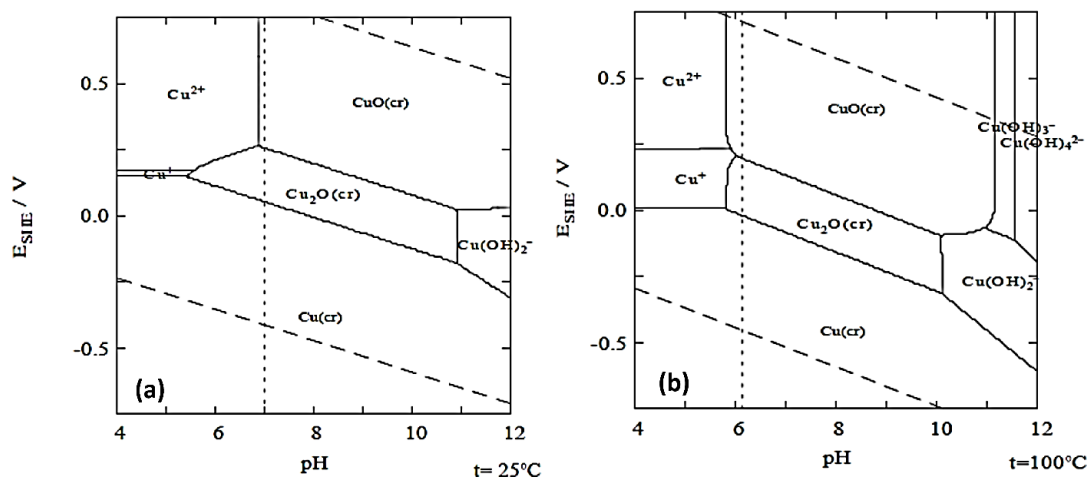


Figure 2.17: Pourbaix diagrams for Cu in pure H_2O at (a) 25 °C and (b) 100 °C.

$$[Cu(aq)]_{tot} = 10^{-6} \text{ mol/kg [98].}$$

The absence of O_2 ensures that metallic copper remains stable. However, it would be probable for metallic Cu to form either soluble ions or oxides in the presence of O_2 . It is noteworthy that there is a slight potential for metallic copper to dissolve as Cu (I) in highly acidic conditions ($pH < 2$) at $100\text{ }^\circ\text{C}$, although such circumstances are not expected in a DGR environment.

The absence of O_2 ensures that metallic copper remains stable. However, it would be probable for metallic Cu to form either soluble ions or oxides in the presence of O_2 . It is noteworthy that there is a slight potential for metallic copper to dissolve as Cu (I) in highly acidic conditions ($pH < 2$) at $100\text{ }^\circ\text{C}$, although such circumstances are not expected in a DGR environment.

Chloride ions, prevalent in groundwater, can impact copper corrosion by forming aqueous complexes and solid phases [99]. **Figure 2.18** illustrates the stability fields of various copper species in aqueous chloride solutions [100].

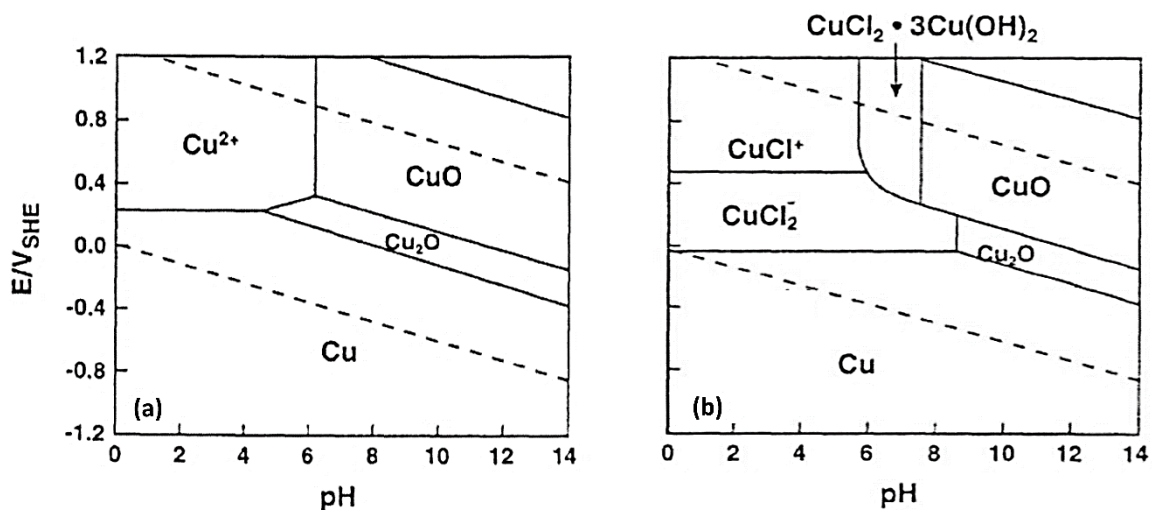


Figure 2.18: Pourbaix diagrams of Cu in chloride solutions at $25\text{ }^\circ\text{C}$, (a) $[\text{Cl}^-] = 10^{-3}\text{ mol/L}$ and (b) $[\text{Cl}^-] = 1\text{ mol/L}$ [80].

In the absence of dissolved O_2 , copper remains thermodynamically stable in chloride-containing environments over most of the pH range. The corrosion of copper by the reduction of H_2O to form soluble copper-chloro complexes (CuCl_2^-) is feasible at a high chloride concentration of 1 mol/L , but only under extremely low pH conditions

(approaching 0), as depicted in **Figure 2.18 (b)**. Such low pH values are unrealistic in a DGR. When dissolved O₂ is present, the formation of various copper compounds, including Cu₂O, copper-chloro complexes, CuO, and CuCl⁺, becomes thermodynamically possible. It is noteworthy that the stability region of CuCl₂·3Cu(OH)₂ becomes distinct with an increase in [Cl⁻] from 10⁻³ to 1 mol/L.

The precipitation of dissolved Cu (II), the latter formed by the homogeneous oxidation of Cu (I) in the presence of O₂, may lead to the formation of botallackite (CuCl₂·3Cu(OH)₂). Additionally, the oxidation of an underlying Cu₂O film on the copper surface has been suggested as a pathway for botallackite formation [100].

2.7.2 The destabilization of Cu in the presence of bisulfide

In addition to O₂ and Cl⁻, bisulfide is identified as a highly detrimental groundwater species affecting Cu stability. Sulfide in the DGR environment may exist in the forms of hydrogen sulfide (H₂S) or the bisulfide ion (SH⁻). The chemical equilibrium between gaseous H₂S and SH⁻, as represented by reaction (2.5), suggests that their concentrations are approximately equal in neutral (pH 7) solutions.



In partially saturated repository-like conditions, sulfide can exist in three chemical forms: gaseous H₂S (H₂S (g)), aqueous H₂S (H₂S (aq)), and the SH⁻. The distribution of sulfide among these forms is influenced by temperature, system pressure, and the pH of the aqueous environment, with Henry's Law providing a means to calculate the solubility of H₂S (g) in water. The Henry's Law constant (H) is approximately 1 × 10⁻³ mol/(m³ Pa) or 0.1 mol/(L bar), makes the determination of sulfide partitioning between the gas phase in bentonite buffer pores and the porewater possible [17].

In the early oxic phase of a repository, sulfides will be rapidly oxidized to sulfate (SO₄²⁻) through abiotic processes [17]. Despite O₂ consumption through sulfide oxidation, aerobic corrosion of the Cu container resulting in Cu oxide formation, microbial and mineral reactions in bentonite clay, and corrosion of structural steel will utilize the initially trapped O₂ [25].

However, these oxides are thermodynamically unstable in bisulfide-containing environments and their conversion to sulfides are highly probable [101-103]. Once this conversion occurs, bisulfide-induced corrosion of Cu is expected to be governed by the mass transport of bisulfide from distant locations to the Cu container surface [17].

The formation of stable and insoluble copper sulfide (Cu_2S) will significantly lower the potential for copper oxidation, making H^+ or H_2O suitable oxidizing agents, as illustrated in **Figure 2.19**, and even without dissolved O_2 , the anodic reaction of copper with bisulfide (reaction (2.6)) can be supported by the cathodic reduction of water (reaction (2.7)) [104].

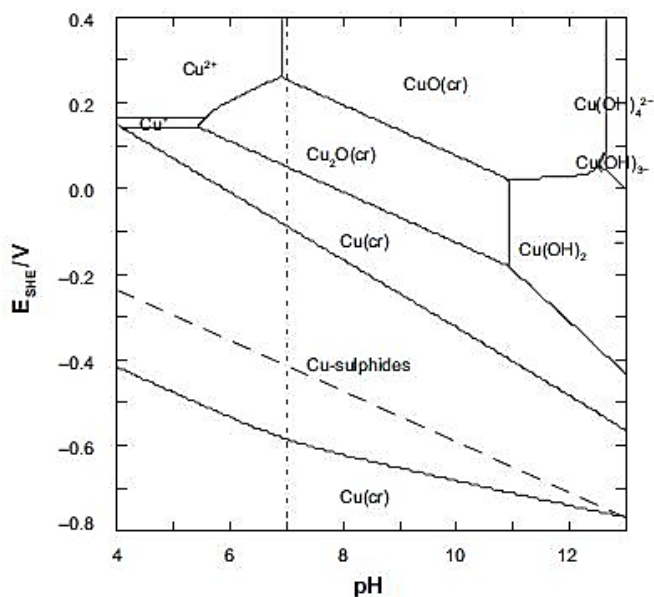
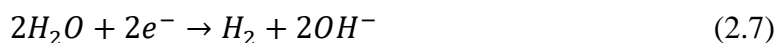
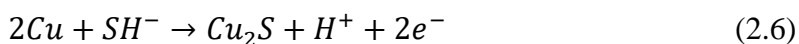


Figure 2.19: Pourbaix diagram for copper at 25°C in H_2O containing $[\text{SH}^-] = 0.2 \text{ mmol/kg}$ ($2 \times 10^{-4} \text{ mol/L}$) and $[\text{Cu}]_{\text{tot}} = 10^{-6} \text{ mol/kg}$ [104].

The copper sulfides formed, namely Cu_2S and CuS , exhibit extremely low solubility product constants of 2×10^{-47} and 8.5×10^{-45} , respectively. The significant thermodynamic driving force for the formation of these copper sulfides makes the corrosion reaction, involving the coupling of Equations 2.15 and 2.16, dominant over all expected pH, redox, and chemical conditions in an anoxic geologic repository [105].

The potential-pH diagram in **Figure 2.19**, while simplified, can be further nuanced under natural corrosion conditions, especially in the presence of elemental sulfur. Additional sulfides such as anilite ($\text{Cu}_{1.75}\text{S}$), dijenite ($\text{Cu}_{1.8}\text{S}$), djurleite ($\text{Cu}_{1.96}\text{S}$), and covellite (CuS) can be formed, each with its own stability range at a given pH (**Figure 2.14**). The redox potential of the environment ultimately determines the stable phase. However, within the range of measured redox potentials in proposed DGR sites (200-400 mV/SHE), stoichiometric Cu_2S remains the only thermodynamically stable phase [17].

The reported E-pH diagrams for copper under repository conditions consider a total sulfide concentration ($[\text{SH}^-]_{\text{tot}}$) of 2×10^{-4} mol/L. Although total sulfur concentrations may be higher, the assumption is that bisulfide concentrations will remain low due to the limited solubility of naturally occurring sulfide minerals (e.g., pyrite, FeS_2) found in fractures of the host rock. However, other pathways for bisulfide production, such as those involving SRB, may exist [106]. The concentration of sulfate is substantial, allowing production of bisulfide by SRB. Observations indicate an increase in sulfate concentration over time in bentonite pore-water; this is attributed to the dissolution of gypsum (CaSO_4) [107].

Considerable efforts have been dedicated to investigating Cu corrosion in SH^- environments under anoxic conditions; however, these have concentrated on determining the kinetics and mechanism of copper sulfide film growth (as Cu_2S) and quantifying the key parameters that influence film formation [108,109]. In addition to $[\text{SH}^-]$, the transport of SH^- ions to the Cu surface also plays a role in determining the morphological and protective properties of the sulfide film formed on the Cu surface [109]. Martino et al. [110] categorized the properties of Cu_2S films formed at different $[\text{SH}^-]$ and $[\text{Cl}^-]$, the latter anion being expected to be particularly important in Canadian groundwaters. The same author showed that, as the $[\text{SH}^-]$ increased, the sulfide film evolved from a single-layer porous film to a partially passivating film. In addition, Cl^- ions were found to influence the Cu corrosion in different ways: (a) Cl^- displaced adsorbed SH^- from the Cu surface, which inhibits the initial step in the sulfide film formation process; (b) Cl^- induced and maintained porosity in the sulfide film; and (c) at very high concentration (i.e., 5.0 M), Cl^- could facilitate Cu transport as CuCl_2^- complexes [110-112].

The results of a study conducted by Escobar et al. [113] on copper corrosion at varying temperatures (15 to 90 °C) in simulated groundwaters containing bisulfide revealed a notable destabilization of copper, as evidenced by low E_{corr} values in the presence of bisulfide. Tafel analyses indicated an escalation in the corrosion rate of copper, with higher bisulfide concentrations and temperatures leading to increased corrosion current density.

King and Stroes-Gascoyne [62] simulated copper corrosion in a solution containing chloride and bisulfide, simulating the evolution of repository redox conditions. The E_{corr} exhibited a shift towards more negative values as conditions transitioned from oxic to anoxic. The addition of bisulfide caused a 500 mV decrease in E_{corr} , which ranged from –0.8 to –1.0 V vs SCE depending on the bisulfide concentration. A similar potential drop was observed on a stationary, clay-covered Cu electrode, albeit with a delayed response, suggesting slower mass transport due to the presence of the clay.

Chen et al. [112,114-116] performed comprehensive studies on the corrosion of Cu in anoxic chloride and bisulfide solutions under stagnant conditions within an anaerobic chamber (glovebox). They explored the properties of Cu sulfide films in solutions with different chloride and bisulfide concentrations using various techniques, including E_{corr} , and scanning electron microscopy (SEM) coupled with focused ion beam (FIB) cross-sectioning, and energy dispersive X-ray spectroscopy (EDX). In these studies, the growth kinetics of copper sulfide films were observed to be influenced by the concentration of bisulfide ions. In an anaerobic solution with 5×10^{-4} mol/L of bisulfide and a chloride concentration of 0.1 mol/L, the film growth exhibited a parabolic pattern, resulting in the formation of a thick, compact, and crystalline Cu_2S film over a period of 1691 hours. The authors suggested that the dominant control mechanism for film growth was Cu (I) diffusion within the film, with a minor contribution from SH^- diffusion from the bulk solution. The proposed mechanism for copper sulfide film growth involved Cu (I) diffusion along the crystalline grain boundaries within the Cu_2S film. However, no supporting evidence was provided for this proposition. In scenarios where the bisulfide concentration was 5×10^{-5} mol/L, corrosion occurred through the development of a cellular and non-protective film. The corrosion rate followed an approximately linear rate law, leading to the formation of a porous morphology, which was influenced by SH^- diffusion within the

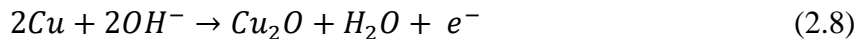
pores of the Cu_2S film. The proposed mechanism suggests that film growth initiates at the film/solution interface through the transport of Cu (I)—potentially as a CuCl_2^- complex—within the cellular film. Later, the process is controlled by SH^- diffusion within the cellular matrix of the Cu_2S film, and eventually by SH^- diffusion from the bulk solution when bisulfide becomes depleted at the film/solution interface.

In an extensive study by Gennero De Chialvo and Arvia [117] on Cu electrochemical behaviour in alkaline solutions with bisulfide, potentiostatic polarization and cyclic voltammetric measurements were employed under stagnant and RDE conditions. The presence of bisulfide shifted the potential for copper oxide formation to more positive values, enabling the electrochemical separation of Cu sulfidation from oxide formation. This facilitated the study of electrochemical copper sulfide formation in aerated aqueous bisulfide solutions. Anodic formation of copper sulfides (Cu_2S , CuS) occurred at potentials close to the equilibrium potentials of $\text{Cu}/\text{Cu}_2\text{S}$ and Cu/CuS , indicating control by the Cu/Cu (I) and Cu/Cu (II) redox couples. In their study, Gennero De Chialvo and Arvia claimed that voltammetric data revealed the initial formation of non-stoichiometric copper sulfide ($\text{Cu}_{1.8}\text{S}$), succeeded by the formation of stoichiometric sulfide (Cu_2S). They proposed a dual-layer film structure with the formation of CuS at the film/solution interface at large overpotentials. However, no chemical compositional analyses were conducted. The authors suggested a two-stage process for anodic sulfide film formation: (i) adsorption of SH^- leading to the growth of a monolayer of Cu_2S through a nucleation and growth mechanism, as indicated by current-time transient measurements; and (ii) subsequent oxidation of Cu resulting in the formation of a thick and homogeneous CuS layer. They also claimed that the electrochemically grown copper sulfide enhanced the properties of the subsequent copper oxide formation, preventing passivation by accumulating sulfur-containing species at surface defects, inhibiting localized corrosion [122].

2.8 The electrochemical behaviour of Cu in alkaline environments

The voltammetric behaviour of copper in alkaline solutions has been extensively studied using various electrochemical and surface analytical techniques [118-124].

1. The anodic voltammetric behaviour can be divided into three distinct regions, with an initial peak observed at $E = -260$ mV (SHE), attributed to the formation of a base-layer of Cu_2O [119,120,125,126].

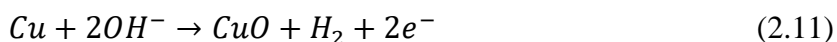
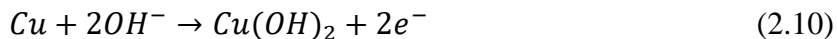


2. At more anodic overpotentials, the nucleation and growth of Cu (II) hydroxide are detected ($E = 40$ mV (SHE)) [119].



The anodic oxidation of Cu_2O into Cu (II) could cause pitting in the Cu_2O base-layer. Subsequently, direct oxidative dissolution of Cu as Cu (II) occurs at the base of the pores. The hydrolysis by OH^- renders the Cu (II) species less soluble ($K_{\text{sp}} = 2.20 \times 10^{-20}$). In the absence of convection, local supersaturation results in the formation and deposition of $\text{Cu}(\text{OH})_2$. The shapes of potentiostatic current transients suggest that this process introduces a degree of passivity [78]. Even at potentials positive enough for Cu (II) formation, Cu_2O continues to grow, potentially through a comproportionation reaction between Cu (II) and Cu to form Cu (I) [127].

3. The formation of a mixed layer comprising $\text{Cu}(\text{OH})_2$ and CuO , which exhibits partial passivation, is noted at considerable positive overpotentials ($E \geq 0.14$ V (SHE)) [124].



Surface passivation is associated with the formation of CuO , and one proposes that CuO initially forms at the base of pores within the Cu_2O base-layer, preventing further dissolution of Cu (II) [125]. Subsequently, CuO continues forming at the interface between Cu_2O and $\text{Cu}(\text{OH})_2$.

XPS analyses conducted by Strehblow [128] reveal the development of an outer layer of $\text{Cu}(\text{OH})_2$ on top of an inner layer of Cu_2O . The Cu_2O base layer grows to a thickness of 10-14 Å, while $\text{Cu}(\text{OH})_2$ continues to thicken linearly with potential. Druska and Strehblow

[128] performed an angle-resolved XPS study on Cu-Ni alloys in alkaline solution that suggests that, unless the potential is highly positive (i.e., ≥ 1.0 V/SHE), CuO forms as a thin layer between the Cu₂O base-layer and a thicker outer layer of Cu(OH)₂. This outcome is expected to be similar for pure copper.

2.9 Raman spectroscopy of Cu oxides, hydroxides, and sulfides

In this thesis, Raman spectroscopy was utilized to identify surface films generated on copper during and after corrosion/electrochemical experiments. This nondestructive technique was employed to monitor the growth and transformation of copper sulfides, oxides, and hydroxides.

Some publications argue that the Raman spectrum of Cu₂O exhibits a broad doublet in the range of 490-650 cm⁻¹, resembling bands reported for both Cu(OH)₂ and Cu₂O by other authors [129-131]. Utilizing a Raman microprobe with 632 nm excitation, Cioffi et al. [129] noted bands at 513 and 602 cm⁻¹ for Cu₂O nanoparticles within a polypyrrole film, while Texier et al. [130] observed similar bands at 500 and 620 cm⁻¹ when studying a standard powder sample of Cu₂O.

During the electrochemical oxidation of copper in alkaline solution, Chan et al. [132, 133] observed a broad doublet (525 and 625 cm⁻¹) associated with Cu₂O and Cu(OH)₂ as a shoulder on this doublet (460 cm⁻¹). However, Niaura [134] performed a SERS study on copper immersed in 0.1 mol/L NaOH under open circuit conditions, attributing the peaks at 460 and 525 cm⁻¹ to 1- and 2-coordinate OH⁻ adsorbed on bare copper, respectively. Under electrochemical conditions, Hartinger et al. [135] observed a SERS signal at 700 cm⁻¹, attributing it to a stretching mode of adsorbed Cu-OH. Ex-situ Raman spectra of CuO recorded on embedded nanoparticles or compressed commercially available powders using various excitations are consistent and show characteristic CuO bands at 303, 350, and 636 cm⁻¹.

The investigation conducted by Turnbull et al. [48] focused on the corrosion behaviour of copper in small volumes of nitric acid (HNO₃) solution, simulating the effects of radiolytic

production of HNO_3 in aerated water vapor. Analysis of the corrosion products, conducted using energy dispersive X-ray and Raman spectroscopies, revealed that, in deaerated HNO_3 , the corrosion process resulted in minor surface roughening. This was initially driven by the rapid reduction of HNO_3 , leading to a surface with marginal reactivity due to the formation of chemisorbed NO_3^- and NO_2^- , and/or a thin Cu_2O layer. Despite the initial corrosion, saturation of the solution volume with dissolved Cu^+ eventually impeded the process, leading to the accumulation of Cu_2O and, to a limited extent, CuO . Raman spectra indicated the characteristic peaks at $525/625/147\text{ cm}^{-1}$ and the faint peak at 220 cm^{-1} for the presence of Cu_2O , and a weak signal at 297 cm^{-1} suggesting the formation of CuO at a later stage.

Deng et al. [136] provided the first comprehensive investigation of the oxygen evolution reaction (OER) on copper and copper oxides surfaces. Various techniques including XRD, SEM, cyclic voltammetry, chronoamperometry, in situ X-ray absorption near-edge structure spectroscopy (XANES), and Raman spectroscopy, were employed. The as-prepared specimens underwent XRD and SEM analyses to characterize their structure and morphology. The electrochemical behaviour of copper surfaces in the OER was studied using cyclic voltammetry and chronoamperometry. Additionally, in situ XANES and Raman spectroscopy were utilized to gain insights into the oxidation states and chemical changes during the OER on copper surfaces. Raman spectroscopy confirmed characteristic bands for Cu_2O and CuO films at $218/523/623\text{ cm}^{-1}$ and $298/347/591\text{ cm}^{-1}$, respectively. The $\text{Cu}(\text{OH})_2/\text{Cu}$ film exhibited a distinct peak at 490 cm^{-1} belonging to $\text{Cu}(\text{OH})_2$, along with minor Cu_2O phase peaks at 523 and 623 cm^{-1} . These findings contribute valuable insights into the OER on copper and copper oxides surfaces.

In the study conducted by Reyter et al. [137] the cyclic voltammetry of a polycrystalline copper electrode in 1 M NaOH solution revealed a complex redox behaviour with different oxidation states, leading to the formation of various mono- or multilayers of Cu_2O , CuO , $\text{Cu}(\text{OH})_2$, or Cu_2O_3 . The growth process of oxide films at different potentials (-200 , -100 , 0 , and $700\text{ mV}/(\text{Hg}/\text{HgO})$) was investigated using chronocoulometry, linear sweep voltammetry, SEM, EDX, XRD (X-ray diffraction), XPS, and in situ Raman spectroscopy.

Notably, $\text{Cu}(\text{OH})_2$ nanoneedles were observed at the oxide/solution interface, except at 700 mV, where a duplex $\text{CuO}/\text{Cu}_2\text{O}$ film was formed.

In situ Raman spectroscopy measurements at the copper/electrolyte interface were conducted during anodic, fast cycling and cathodic treatments in 1 M NaOH to investigate the oxide phase-film formation and removal. The recorded spectrum for the cycled copper electrode exhibited bands at 293 and 488 cm^{-1} , attributed to $\text{Cu}(\text{OH})_2$, along with signals indicating the presence of Cu_2O phase at 525 and 625 cm^{-1} (and a small peak at 400 cm^{-1}). CuO , although it has a small peak at 300 cm^{-1} , was challenging to detect due to its weaker scattering compared to Cu_2O and $\text{Cu}(\text{OH})_2$, with its major feature at 630 cm^{-1} coinciding with the Cu_2O Raman band.

In an electrochemical study of chalcopyrite leaching, Parker et al. [138] recorded Raman reference spectra for potential products, such as Cu_2S and CuS . The chalcocite spectrum exhibited a broad band around 300 cm^{-1} and a narrower signal at approximately 210 cm^{-1} , while the covellite spectrum had a single sharp peak at roughly 475 cm^{-1} . However, spectra for chalcocite from the University of Arizona/California Institute of Technology [139] displayed two major bands at ~ 210 and ~ 300 cm^{-1} but also showed additional peaks between 400 and 700 cm^{-1} , raising concerns about sample purity. SERS studies also identified a peak at around 290 cm^{-1} for copper immersed in Na_2S solutions, attributing it to a Cu-S stretch [140,141].

Various Raman shifts for Cu_2S and CuS have been reported. Wang et al. [142] and Minceva-Sukarova [143] claimed that peaks for Cu_2S and CuS appear at 472 and 474 cm^{-1} , respectively, similar to the values reported by Parker et al. [138] for CuS . Mernagh and Trudu [144] listed CuS as having a Raman shift of 263 cm^{-1} , while de Tacconi et al. [145] observed CuS at approximately 475 cm^{-1} and suggested no Raman signal for Cu_2S . However, it is worth noting that the spectra reported by de Tacconi et al. had a limited spectral window (300-600 cm^{-1}); a broader scan would be needed to support such a claim.

Parker et al. [138] and Smith et al. [58] reported similar Raman peaks for Cu_2S . Smith et al. collected in-situ Raman spectra on a pre-oxidized Cu electrode in a $\text{Na}_2\text{S} + \text{NaCl}$

solution, observing a strong Raman signal at $\sim 300\text{ cm}^{-1}$ after only 5 minutes of exposure, which was attributed to Cu_2S . The intensity of the signal increased marginally over time, suggesting it was associated with the outermost layers of the film [58].

2.10 Conversion of Cu oxide to Cu sulfide

To date, the influence of the initial oxidic phase anticipated in a DGR on the subsequent Cu corrosion by SH^- has not been studied in detail. Kristiansen et al. [146] investigated the sulfidization of copper oxide, both in the form of a layer grown on metallic Cu and as a powder, using soft X-ray spectroscopy. The results demonstrated that the tenorite (CuO) layer on the oxidized Cu surface reacted with the SH^- solution, with the top 100 nm layer of oxide being converted to Cu_2S in a transformation involving the reduction of Cu (II) to Cu (I)-containing species. By contrast, the transformation of CuO powder to Cu (I) species was much less pronounced. Although the mechanism for the reduction of Cu (II) to Cu (I) was not clearly understood, it was proposed that the main mechanism was likely the comproportionation reaction between Cu atoms in the underlying metallic Cu and Cu (II) ions from the corrosion products. If this mechanism prevailed, the absence of Cu metal in the experiments with powdered oxide would prevent the transformation of Cu (II) to Cu (I), consistent with observations.

King et al. [147] conducted a simulation of evolving repository redox conditions, with the focus on the impact of microbiological processes on Cu corrosion. As conditions evolved from oxic to anoxic, a shift in E_{corr} to less noble (less positive) values was observed. As the $[\text{SH}^-]$ was increased, E_{corr} approached a value in the range of -0.8 to -1.0 V/SCE. Experiments conducted on a stationary electrode covered by a clay layer yielded similar results, but with a delayed response of the E_{corr} to the presence of SH^- due to the slow mass transport of SH^- through the clay.

Smith et al. [58] showed that the composition of the electrochemically formed oxide film on Cu varied from a compact Cu_2O film, after short periods of oxidation, to a porous tri-layer film comprised of a Cu_2O base layer, a thin intermediate layer of CuO and an outer scattered deposit of $\text{Cu}(\text{OH})_2$ after longer oxidation periods in highly alkaline solutions. Scanning electron micrographs of specimens indicated that the coherent oxide layer formed

after 0.5 h was converted to a porous layer covered by scattered surface deposits after an additional 2 h. Based on the evolution of the E_{corr} with time, Smith et al. showed that, upon exposure of oxidized Cu specimens to SH^- , conversion of the oxide to sulfide was observed. This was confirmed by in-situ Raman spectroscopy and cathodic stripping voltammetry. Smith et al. claimed that this conversion occurred by a chemical conversion of oxide to sulfide at the oxide/solution interface. The sulfide films on the oxidized Cu surface continued to grow, yielding dendritic sulfide crystals on top of the oxide layer until, at longer times, the surface became covered by a porous sulfide layer.

Haleem et al. [148] investigated the electrochemical behaviour of Cu in SH^- -containing 0.1 M NaOH solutions. Galvanostatic polarization of Cu specimens was performed in solutions containing SH^- in the range of 10^{-6} to 5×10^{-3} M. For $[\text{SH}^-] \leq 5 \times 10^{-5}$ M, potential–time profiles were similar to those measured in the absence of SH^- and, based on reduction potentials, Cu_2O , CuO , and/or $\text{Cu}(\text{OH})_2$ were thought to have been formed. It was proposed that there may be a $[\text{SH}^-]$ threshold below which Cu (I) sulfide formation would be kinetically hindered.

Hollmark et al. [103] grew either Cu (I) or Cu (II) films, exposed them to solutions containing either 10^{-3} or 0.1 M sodium sulfide (Na_2S) for 8 h and then analyzed the surfaces using X-ray absorption spectroscopy (XAS). They observed bisulfide diffusion into the bulk oxide films but suggested that this process proceeded inhomogeneously, since a small amount of oxide film remained unconverted. The findings demonstrated that the sulfide films formed were not coherent layers. In agreement with Smith et al. [58], Hollmark et al. concluded that oxide-to-sulfide conversion could occur by different conversion mechanisms.

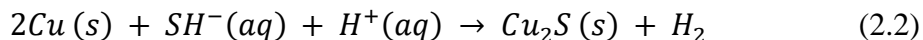
The study conducted by Bojinov et al. [149] investigated the interaction between copper (OFP) and a bisulfide-containing borate buffer solution using electrochemical techniques, microscopic observations, and spectroscopic analyses. The focus was on copper behaviour during direct immersion or de-passivation following oxide film formation. Corrosion layers forming in bisulfide-containing environments relevant to nuclear waste storage typically involve a Cu_2S deposit with a thin inner layer and a thicker disordered outer layer.

The paper aimed to show that copper does not develop a continuous and adherent passive film when exposed to bisulfide. Experiments with varying bisulfide concentrations and oxidation reveal differences in surface film morphology, suggesting that sulfide films formed through a dissolution/precipitation process lack adhesion to the substrate, hindering efficient passivation. Cross-sectional investigations indicate oxygen enrichment at the interface, suggesting electrolyte penetration beneath the sulfide film.

While the previous studies show that Cu oxides will eventually be converted to sulfides, this research work aims to investigate the mechanisms of conversion and the involvement of the metallic Cu substrate which has remained unresolved. A number of possible corrosion scenarios can be envisaged to occur when SH^- contacts an oxidized waste container surface:

1. No conversion of copper oxide to sulfide

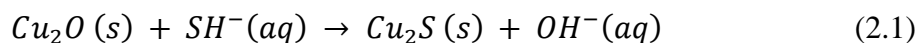
The SH^- ions could cause Cu corrosion, reaction (2.2), by transport through the porous oxide without reacting with it:



This would yield the maximum amount of UFC corrosion, since only the metallic Cu would consume the SH^- ions.

2. Chemical conversion of oxide to sulfide

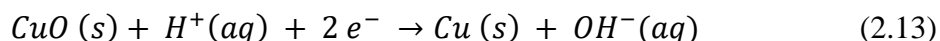
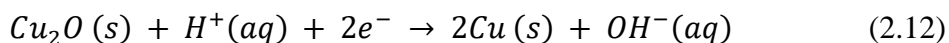
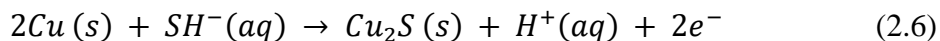
The conversion of Cu_2O to Cu_2S could occur via a chemical substitution reaction, reaction (2.1), between SH^- ions and the oxide, with no redox reaction involved.



Reaction with the oxide would initially consume SH^- ions transported to the UFC surface, thereby delaying further Cu corrosion. This would decrease the extent of corrosion to the container since bisulfide-driven Cu corrosion would only initiate either after the oxide layer was totally consumed by reaction with SH^- or when it became sufficiently porous to allow SH^- transport to the underlying metal.

3. Electrochemical conversion of oxide to sulfide

The transport of SH^- to the container surface through a porous oxide could result in oxidation of the Cu by SH^- , reaction (2.6), galvanically-coupled to the simultaneous reduction of the oxide, reactions (2.12) and (2.13):



In this scenario, the amount of Cu consumed in forming Cu_2S would be the same as that produced by the reduction of the copper oxide. However, the Cu produced by oxide reduction would be expected to be finely particulate and unprotective and eventually converted to Cu_2S via reaction (2.6). Additionally, in the presence of Cu (II) species, the Cu produced could participate in the comproportionation reaction to reduce Cu (II) to Cu (I) via reaction (2.14):



with the Cu (I) leading to Cu_2S formation via reaction (2.6) or to Cu_2O by reaction with H_2O .

4. A combination of all possible interactions

A possibility is that some of the SH^- may be consumed in converting oxide (either chemically or galvanically) to sulfide while the remainder penetrated the porous oxide to directly corrode the underlying Cu substrate. The subsequent amount of Cu corrosion would be decreased by the amount of SH^- consumed in the conversion process, which would depend on the degree of conversion of oxide to sulfide, a reaction that may or may not go to completion.

This range of mechanistic possibilities makes it necessary to evaluate the mechanism and extent of oxide conversion to sulfide and how it influences the maximum depth of corrosion damage to the container. In this study, the mechanism and extent of conversion of different types of copper (hydr)oxides with known compositions, morphologies, and thicknesses

were investigated. This was achieved by oxidizing Cu to form oxide layers with known compositions representative of the oxic period, then exposing them to oxygen-free solutions containing a known concentration of SH^- , simulating the anoxic environment. The extent of oxide to sulfide conversion was then analyzed using cathodic stripping voltammetry and a range of surface analytical techniques.

2.11 References

- [1] P. Gierszewski, R. Parmenter, Confidence in safety – Revell site, TR-2022-14, NWMO, 2022.
- [2] Long-term safety for the final repository for spent nuclear fuel at Forsmark, main report of the SR-Site project, TR-11-01, SKB, 2011.
- [3] Posiva, TKS-2009 nuclear waste management of the Olkiluoto and Loviisa power plants: Programme for research, development and technical design for 2010–2012, Posiva Oy, 2010.
- [4] Design, production and initial state of the canister, TR-10-14, SKB, 2010.
- [5] A. Hedin, Long-term safety for KBS-3 repositories at Forsmark and Laxemar-a first evaluation. Main report of the SR-Can project, TR-06-09, SKB, 2006.
- [6] C.-G. Andersson, P. Eriksson, M. Westman, G. Emilsson, Status report, Canister fabrication, TR-04-23, SKB, 2004.
- [7] R. Sandstrom, H.C.M. Andersson, The effect of phosphorus on creep in copper, *Journal of Nuclear Materials*, 372, 66–75, 2008.
- [8] R. Sandstrom, R. Wu. Influence of phosphorus on the creep ductility of copper, *Journal of Nuclear Materials*, 441, 364–371, 2013.
- [9] Design and production of the KBS–3 repository, SKB, 2010.
- [10] P.G. Keech, P. Vo, S. Ramamurthy, J. Chen, R. Jacklin, D.W. Shoesmith, Design and development of copper coatings for long term storage of used nuclear fuel, *Corrosion Engineering, Science and Technology*, 49, 425–430, 2014.
- [11] H.-J. Choi, M. Lee, J.Y. Lee, Application of a cold spray technique to the fabrication of a copper canister for the geological disposal of CANDU spent fuels, *Nuclear Engineering and Design*, 240, 2714–2720, 2010.

- [12] P. Jakupi, P.G. Keech, I. Barker, S. Ramamurthy, R.L. Jacklin, D.W. Shoesmith, D.E. Moser, Characterization of commercially cold sprayed copper coatings and determination of the effects of impacting copper powder velocities, *Journal of Nuclear Materials*, 466, 1–11, 2015.
- [13] P. Vo, D. Poirier, J.-G. Legoux, P.G. Keech, Application of copper coatings onto used fuel canisters for the Canadian nuclear industry. In: J. Karthikeyan, C. Kay, editors. *High pressure cold spray: principles and applications*, ASM International, 253–276, 2016.
- [14] P.G. Keech, P. Lin, N. Mahalanobis, Electrodeposited copper coatings for used fuel containers. In: *35th Annual CNS Conference Proceedings*. Saint John, Canada: Canadian Nuclear Society, 2015.
- [15] G.M. Kwong, Status of corrosion studies for copper used fuel containers under low salinity conditions, TR-2011-14, NWMO, 2011.
- [16] J.R. Scully, M. Edwards, Review of the NWMO copper corrosion allowance, TR-2013-04, NWMO, 2013.
- [17] Supplementary information on canister integrity issues, TR-19-15, SKB, 2019.
- [18] C.H. Boyle, S.A. Meguid, Mechanical performance of integrally bonded copper coatings for the long-term disposal of used nuclear fuel, *Nuclear Engineering and Design*, 293, 403–412, 2015.
- [19] D. Crusset, V. Deydier, S. Necib, J.-M. Gras, P. Combrade, D. Feron, E. Burger, Corrosion of carbon steel components in the French high-level waste programme: evolution of disposal concept and selection of materials, *Corrosion Engineering, Science and Technology*, 52, 17–24, 2017.
- [20] N. Diomidis, L.H. Johnson, Materials options and corrosion-related considerations in the design of spent fuel and high-level waste disposal canisters for a deep geological repository in opalinus clay, *JOM*, 66, 461–470, 2014.

- [21] D.S. Hall, M. Behazin, J.W. Binns, P.G. Keech, An evolution of corrosion processes affecting copper-coated nuclear waste containers in a deep geological repository, *Progress in Materials Science*, 188, 100766, 2021.
- [22] C.C. Patterson, Native copper, silver, and gold accessible to early metallurgists. *American Antiquity*, 36, 286–321, 1971.
- [23] T.J. Bornhorst, J.B. Paces, N.K. Grant, J.D. Obradovich, N.K. Huber, Age of native copper mineralization, Keweenaw Peninsula, Michigan. *Economic Geology*, 83, 619–25, 1988.
- [24] N.K. Huber, The Portage lake volcanics (Middle Keweenaw) on Isle Royale, Michigan; professional paper; Report USGS 754C; Washington, DC, USA: United States Department of the Interior, 44, 1973.
- [25] F. King, D.S. Hall, P.G. Keech, Nature of the near-field environment in a deep geological repository and the implications for the corrosion behaviour of the container, *Corrosion Engineering, Science and Technology*, 52, 25–30, 2017.
- [26] R.P. Morco, J.M. Joseph, D.S. Hall, C. Medri, D.W. Shoesmith, J.C. Wren, Modelling of radiolytic production of HNO₃ relevant to corrosion of a used fuel container in deep geologic repository environments, *Corrosion Engineering, Science and Technology*, 52, 141–147, 2017.
- [27] R. Guo, Thermal modelling of a mark II container, TR-2015-06, NWMO, 2015.
- [28] R. Guo, Thermal response of a Canadian conceptual deep geological repository in crystalline rock and a method to correct the influence of the near-field adiabatic boundary condition, *Engineering Geology*, 218, 50–62, 2017.
- [29] R. Pusch, The Buffer and Backfill Handbook. Part 1: Definitions, basic relationships and laboratory methods, TR-02-20, SKB, 2002.
- [30] R. Guo, Thermal response of a Mark II conceptual deep geological repository in crystalline rock, TR-2016-03, NWMO, 2016.

- [31] S. Briggs S, J. McKelvie, P.G. Keech, B. Sleep, M. Krol, Transient modelling of sulphide diffusion under conditions typical of a deep geological repository, *Corrosion Engineering, Science and Technology*, 52, 200-203, 2017.
- [32] H.R. Müller, B. Garitte, T. Vogt, S. Köhler, T. Sakaki, H. Weber, T. Spillmann, M. Hertrich, J. K. Becker, N. Giroud, V. Cloet, N. Diomidis, T. Vietor, Implementation of the full scale emplacement (FE) experiment at the Mont Terri rock laboratory, *Mont Terri Rock Laboratory, 20 Years: Two Decades of Research and Experimentation on Claystones for Geological Disposal of Radioactive Waste*, 289-308, 2018.
- [33] R.P. Morco, J.M. Joseph, C. Medri, D.S. Hall, J.C. Wren, Model calculations of radiolytic production of oxidants anticipated under deep geologic repository environments, *Corrosion Engineering, Science and Technology*, 2017.
- [34] L. Werme, C. Lilja, Fuel and canister process report for the safety assessment SR-site, TR-10-46, SKB, 2010.
- [35] OECD, Nuclear Energy Agency. Porewater extraction from argillaceous rocks for geochemical characterization, Paris, France: OECD Publishing, 2000.
- [36] F. King, M. Kolar, Lifetime predictions for nuclear waste disposal containers, *Corrosion*, 75, 309–323, 2018.
- [37] D.S. Hall, T.E. Standish, M. Behazin, P.G. Keech, Corrosion of copper-coated used nuclear fuel containers due to oxygen trapped in a Canadian deep geological repository, *Corrosion Engineering, Science and Technology*, 53, 309–315, 2018.
- [38] C.-C. Hung, Y.-C. Wu, F. King, Corrosion assessment of canister for the disposal of spent nuclear fuel in crystalline rock in Taiwan, *Corrosion Engineering, Science and Technology*, 52, 194–9, 2017.
- [39] D.S. Hall, P.G. Keech, An overview of the Canadian corrosion program for the long-term management of nuclear waste, *Corrosion Engineering, Science and Technology*, 52, 2–5, 2017.

- [40] F. King, C. Lilja, K. Pedersen, P. Pitkanen, M. Vahanen, An update of the state-of-the-art report on the corrosion of copper under expected conditions in a deep geologic repository, TR-10-67, SKB, 180, 2010.
- [41] Long-Term Safety for KBS-3 Repositories at Forsmark and Laxemar – a First Evaluation, TR-06-09, SKB, 2006.
- [42] J.M. Joseph, B. Seon Choi, P. Yakabuskie, J.C. Wren, A combined experimental and model analysis on the effect of PH and $O_2(Aq)$ on γ -radiolytically produced H_2 and H_2O_2 . Radiation Physics and Chemistry, 77, 1009–1020, 2008.
- [43] P.A. Yakabuskie, J.M. Joseph, J.C. Wren, The effect of interfacial mass transfer on steady-state water radiolysis. Radiation Physics and Chemistry, 79, 777–785, 2010.
- [44] D. Dautzenberg, Gamma-radiolysis of hydrogen-oxygen mixtures—II. Influence of the additives H_2O , HNO_3 , CO_2 , ethanol, n-pentane and NO_2 on the reactivity of H_2-O_2 and $H_2-O_2-N_2$ -mixtures, International Journal of Radiation Applications and Instrumentation. Part C. Radiation Physics and Chemistry, 36, 767–770, 1990.
- [45] D.T. Reed, R.A. Van Konynenburg, Effect of ionizing radiation on moist air systems, MRS Online Proceedings Library (OPL), 112, 393, 1987.
- [46] K. Karin Norrfors, A. Bjorkbacka, A. Kessler, S. Wold, M. Jonsson, γ -radiation induced corrosion of copper in bentonite-water systems under anaerobic conditions, Radiation Physics and Chemistry, 144, 8–12, 2018.
- [47] A. Bjorkbacka, S. Hosseinpour, M. Johnson, C. Leygraf, Radiation induced corrosion of copper for spent nuclear fuel storage, Radiation Physics and Chemistry, 92, 80–6, 2013.
- [48] J. Turnbull, R. Szukalo, M. Behazin, D. Hall, D. Zagidulin, S. Ramamurthy, J.C. Wren, D.W. Shoesmith, The effects of cathodic reagent concentration and small solution volumes on the corrosion of copper in dilute nitric acid solutions, Corrosion, 74, 326-336, 2018.

- [49] NWMO, Postclosure safety assessment of a used fuel repository in crystalline rock, TR-2017-02, NWMO, 2017.
- [50] F. King, Microbiologically influenced corrosion of nuclear waste containers, *Corrosion*, 65, 233–251, 2009.
- [51] A.A. Grigoryan, D.R. Jalique, P. Medihala, S. Stroes-Gascoyne, G.M. Wolfaardt, J. McKelvie, D.R. Krober, Bacterial diversity and production of sulfide in microcosms containing uncompacted bentonites, *Heliyon*, 4, 2018.
- [52] A. Sevcu, J. Steinova, K. Burkartova, K. Cerna, Microbiology in nuclear waste disposal: microbial diversity in aged bentonites; MIND 2.07; Microbiology in Nuclear Waste Disposal, 43.
- [53] B. Sherwood Lollar, Far-field microbiology considerations relevant to a deep geological repository – State of science review, TR-2011-09, NWMO, 77, 2011.
- [54] F. King, Microbially influenced corrosion of copper nuclear fuel waste containers in a Canadian disposal vault; AECL-11471, Atomic Energy of Canada Ltd., 1996.
- [55] P. Alt-Epping, P. Wersin, Reactive transport modelling of sulphide fluxes in the near-field: summary of model development and application to a simplified backfill-buffer-rock system in 2014 and 2015, Working Report, WR 2017-50, Posiva Oy.
- [56] F. King, K. Miroslav, Copper Sulfide Model (CSM) – Model improvements, sensitivity analyses, and results from the integrated sulfide project inter-model comparison exercise, TR-18-08, SKB, 2019.
- [57] V. Cloet, M. Pekala, P. Smith, P. Wersin, N. Diomidis, An evaluation of sulphide fluxes in the near field of a HLW repository, Technical Report NTB 17-04, Nagra, 131, 2017.
- [58] J.M. Smith, J.C. Wren, M. Odziemkowski, D.W. Shoesmith, The electrochemical response of preoxidized copper in aqueous sulfide solutions. *Journal of the Electrochemical Society*, 154, C431, 2007.

- [59] J.H. Stenlid, A.J. Johansson, C. Leygraf, T. Brinck, Computational analysis of the early stage of cuprous oxide sulphidation: a top-down process, *Corrosion Engineering, Science and Technology*, 52, 50–53, 2017.
- [60] F. King, M. Kolar, M. Vähänen, C. Lilja, Modelling long term corrosion behaviour of copper canisters in KBS-3 repository, *Corrosion Engineering, Science and Technology*, 46, 217–222, 2011.
- [61] F. King, C. Lilja, M. Vähänen, Progress in the understanding of the long-term corrosion behaviour of copper canisters, *Journal of Nuclear Materials*, 438, 228-237, 2013.
- [62] F. King, S. Stroes-Gascoyne, Predicting the effects of microbial activity on the corrosion of copper nuclear waste disposal containers, in: J.H. Wolfram (Ed.), *Microbial Degradation Processes in Radioactive Waste repository and in Nuclear Fuel Storage Areas*, Kluwer Press, Dordrecht, 149–162, 1997.
- [63] J.R. Davis, *Copper and copper alloys*, ASM International, Materials Park, Ohio, 2001.
- [64] K. Chen, D. Xue, Reaction route to the crystallization of copper oxides, *Applied Science and Convergence Technology*, 23, 14-26, 2014.
- [65] M.B. Gawande, A. Goswami, F.X. Felpin, T. Asefa, X. Huang, R. Silva, X. Zou, R. Zboril, R.S. Varma, Cu and Cu-based nanoparticles: synthesis and applications in catalysis, *Chemical reviews*, 116, 3722-3811, 2016.
- [66] H.W. Gillett, Cuprous hydroxide and cuprous oxide, *The Journal of Physical Chemistry*, 13, 332–340, 1908.
- [67] D. Miller, Electrolytic precipitation of cuprous oxide. *The Journal of Physical Chemistry*, 13, 256–261, 1909.
- [68] R. Restori, D. Schwarzenbach, Charge density in cuprite, Cu_2O , *Acta Crystallographica Section B: Structural Science*, 42, 201–208, 1986.

- [69] Standard test methods for chemical analysis of cuprous oxide and copper pigments; ASTM D283-13, ASTM International, 2013.
- [70] J. Ghijsen, L.H. Tjeng, J. Van Elp, H. Eskes, J. Westerink, G.A. Sawatzky, M.T. Czyzyk, Electronic structure of Cu₂O and CuO, *Physical Review B*, 38, 11322, 1988.
- [71] Jean, Arielle M., "Evolution of Cu₂O morphology during copper corrosion in the presence of gamma-radiation" M.Sc., The University of Western Ontario, Electronic Thesis and Dissertation Repository, 4593, 2017.
- [72] K.S. Choi, Shape control of inorganic materials via electrodeposition, *Dalton Transactions*, 40, 5432-5438, 2008.
- [73] H.W. Richardson, Copper compounds, *Ullmann's encyclopedia of industrial chemistry*, Wiley-VCH Verlag GmbH & Co. KGaA, 2000.
- [74] S. Åsbrink, L.-J. Norrby, A refinement of the crystal structure of copper(II) oxide with a discussion of some exceptional e.s.d's, *Acta Crystallographica Section B: Structural Crystallography and Crystal Chemistry*, 26, 8–15, 1970.
- [75] G. Tunell, E. Posnjak, C.J. Ksanda, Geometrical and optical properties, and crystal structure of tenorite, *Zeitschrift für Kristallographie-Crystalline Materials*, 90, 120–142, 1935.
- [76] H.R. Oswald, A. Reller, H.W. Schmalle, E. Dubler, *Acta Crystallographica Section C: Crystal Structure Communications*, 46, 2279-2284, 1990.
- [77] J.S. Halliday, The anodic behaviour of copper in caustic soda solutions, *Transactions of the Faraday Society*, 50, 171-178, 1954.
- [78] D.W. Shoesmith, T.E. Rummery, D. Owen, W. Lee, Anodic oxidation of copper in alkaline solutions I. Nucleation and growth of cupric hydroxide films, *Journal of the Electrochemical Society*, 123, 790–799, 1976.

- [79] M. Biton, G. Salitra, D. Aurbach, P. Mishkov, D. Ilzyer, On the electrochemical behavior and passivation of copper and brass (Cu70/Zn30) electrodes in concentrated aqueous KOH solutions, *Journal of the Electrochemical Society*, 153, B555, 2006.
- [80] I. Puigdomenech, C. Taxén, Thermodynamic data for copper. Implications for the corrosion of copper under repository conditions, TR-00-13, SKB, 2000.
- [81] B.W. Mountain, T.M. Seward, The hydrosulphide/sulphide complexes of copper (I): Experimental determination of stoichiometry and stability at 22 C and reassessment of high temperature data, *Geochimica et Cosmochimica Acta*, 63, 11–29, 1999.
- [82] S. Sun, P. Li, S. Liang, Z. Yang, Diversified copper sulfide (Cu_{2-x}S) micro-/nanostructures: a comprehensive review on synthesis, modifications and applications, *Nanoscale*, 9, 11357–11404, 2017.
- [83] S. Cassaignon, S. Sanchez, J.-F. Guillemoles, J. Vedel, H.G. Meier, Influence of the composition on the copper diffusion in copper sulfides study by impedance spectroscopy, *Journal of the Electrochemical Society*, 146, 4666–4671, 1999.
- [84] H.-H. Huang, The Eh-pH diagram and its advances, *Metals*, 6, 23, 2016.
- [85] J.C.W. Folmer, F. Jelinek, The valence of copper in sulphides and selenides: an X-ray photoelectron spectroscopy study, *Journal of the Less Common Metals*, 76, 153–162, 1980.
- [86] D.L. Perry, J.A. Taylor, X-ray photoelectron and Auger spectroscopic studies of Cu₂S and CuS, *Journal of Materials Science Letters*, 5, 384–386, 1986.
- [87] D. Li, G.M. Bancroft, M. Kasrai, M.E. Fleet, X.H. Feng, B.X. Yang, K.H. Tan, S K- and L-edge XANES and electronic structure of some copper sulfide minerals, *Physics and Chemistry of Minerals*, 21, 317–324, 1994.
- [88] M.C. Biesinger, Advanced analysis of copper X-ray photoelectron spectra, *Surface and Interface Analysis*, 49, 1325–1334, 2017.

- [89] R.J. Goble, The relationship between crystal structure, bonding and cell dimensions in the copper sulfides, *Canadian mineralogist*, 23, 61–76, 1985.
- [90] A. Adamou, A. Nicolaides, C. Varotsis, Bio-hydrometallurgy dynamics of copper sulfide-minerals probed by micro-FTIR mapping and Raman microspectroscopy, *Minerals Engineering*, 132, 39–47, 2019.
- [91] E.M. Khairy, N.A. Darwish, Studies on copper-semiconducting layer-electrolyte systems—II. Galvanostatic anodic polarization of Cu/Cu₂S/S²⁻ applying stationary and rectangular pulse techniques, *Corrosion Science*, 13, 149–164, 1973.
- [92] S. Pakeva, K. Germanova, Electric and photoelectric properties of polycrystalline copper sulphide, *Journal of Physics D: Applied Physics*, 18, 1371, 1985.
- [93] A.V. Naumov, V.N. Semenov, A.N. Lukin, E.G. Goncharov, Phase composition of copper sulfide films produced from copper salt–thiourea complexes, *Inorganic materials*, 38, 271–273, 2002.
- [94] Y. Zhao, H. Pan, Y. Lou, X. Qiu, J. Zhu, C. Burda, Plasmonic Cu_{2-x}S nanocrystals: optical and structural properties of copper-deficient copper (I) sulfides, *Journal of the American Chemical Society*, 131, 4253–4261, 2009.
- [95] H.-B. Yi, F.-F. Xia, Q. Zhou, D. Zeng, [CuCl₃]⁻ and [CuCl₄]²⁻ hydrates in concentrated aqueous solution: a density functional theory and Ab initio study, *The Journal of Physical Chemistry A*, 115, 4416–4426, 2011.
- [96] B. Bovio, S. Locchi, Crystal structure of the orthorhombic basic copper nitrate, Cu₂(OH)₃NO₃, *Journal of Crystallographic and Spectroscopic research*, 12, 507–517, 1982.
- [97] Grandy, Lindsay J., "Effects of gamma-radiation on the evolution of copper corrosion dynamics in deep geological repository solution environments", The University of Western Ontario, Electronic Thesis and Dissertation Repository. 8257, 2021.
- [98] V.S. Bagotsky, *Fundamentals of electrochemistry*, John Wiley & Sons, 2005.

- [99] F. King, Corrosion of copper in alkaline chloride environments, TR-02-25, SKB, 2002.
- [100] F. King, L. Ahonen, C. Taxén, U. Vuorinen, L. Werme, Copper corrosion under expected conditions in a deep geologic repository, Posiva 2002-01, Posiva Oy, 2001.
- [101] S.R. De Sanchez, D.J. Schiffrin, The use of high speed rotating disc electrodes for the study of erosion-corrosion of copper base alloys in sea water, *Corrosion Science*, 28, 141–151, 1988.
- [102] J. Chen, Z. Qin, L. Wu, J.J. Noël, D.W. Shoesmith, The influence of sulphide transport on the growth and properties of copper sulphide films on copper, *Corrosion Science*, 87, 233–238, 2014.
- [103] H.M. Hollmark, P.G. Keech, J.R. Vegelius, L. Werme, L.-C. Duda, X-ray absorption spectroscopy of electrochemically oxidized Cu exposed to Na₂S, *Corrosion Science*, 54, 85–89, 2012.
- [104] M. Pourbaix, A. Pourbaix, Potential-pH equilibrium diagrams for the system S-H₂O from 25 to 150 C: Influence of access of oxygen in sulphide solutions, *Geochimica et Cosmochimica Acta*, 56, 3157, 1992.
- [105] W. Dale, *CRC Handbook of Chemistry and Physics*; 52nd Edition, B-232, 1971-1972.
- [106] K. Pederson, *Microbial Processes in Radioactive Waste Disposal*, TR-00-04, SKB, 2000.
- [107] A. Muurinen, J. Lehtikoinen, Porewater chemistry in compacted bentonite, Posiva 99-20, Posiva Oy, 1999.
- [108] M. Guo, J. Chen, T. Martino, C. Lilja, J.A. Johansson, M. Behazin, W.J. Binns, P.G. Keech, J.J. Noël, D.W. Shoesmith, The nature of the copper sulfide film grown on copper in aqueous sulfide and chloride solutions, *Materials and Corrosion*, 72, 300-307, 2021.

- [109] T. Martino, J. Smith, J. Chen, Z. Qin, J.J. Noël, D.W. Shoesmith, The properties of electrochemically-grown copper sulfide films, *Journal of The Electrochemical Society*, 166, C9, 2019.
- [110] T. Martino, R. Partovi-Nia, J. Chen, Z. Qin, D.W. Shoesmith, Mechanisms of film growth on copper in aqueous solutions containing sulphide and chloride under voltammetric conditions, *Electrochimica Acta*, 127, 439-447, 2014.
- [111] M. Guo, J. Chen, T. Martino, M. Biesinger, J.J. Noël, D.W. Shoesmith, The susceptibility of copper to pitting corrosion in borate-buffered aqueous solutions containing chloride and sulfide, *Journal of The Electrochemical Society*, 166, C550, 2019.
- [112] J. Chen, Z. Qin, T. Martino, D.W. Shoesmith, Effect of chloride on Cu corrosion in anaerobic sulphide solutions, *Corrosion Engineering, Science and Technology*, 52, 40–44, 2017.
- [113] I.S. Escobar, E. Silva, C. Silva, A. Ubal, Study of the effect of sulfide ions on the corrosion resistance of copper for use in containers for high-level waste, *Journal of the Minerals Metals & Materials Society (JOM)*, 371–386, 1999.
- [114] J. Chen, Z. Qin, D.W. Shoesmith, Kinetics of corrosion film growth on copper in neutral chloride solutions containing small concentrations of sulfide, *Journal of the Electrochemical Society*, 157, C338–C345, 2010.
- [115] J. Chen, Z. Qin, D.W. Shoesmith, Long-term corrosion of copper in a dilute anaerobic sulfide solution, *Electrochimica acta*, 56, 7854–7861, 2011.
- [116] J. Chen, Z. Qin, D.W. Shoesmith, Rate controlling reactions for copper corrosion in anaerobic aqueous sulphide solutions, *Corrosion Engineering, Science and Technology*, 46, 138–141, 2011.
- [117] M.R. Gennero De Chialvo, A.J. Arvia, The electrochemical behaviour of copper in alkaline solutions containing sodium sulphide, *Journal of applied electrochemistry*, 15, 685–696, 1985.

- [118] S.M. Abd El Haleem, B.G. Ateya, Cyclic voltammetry of copper in sodium hydroxide solutions, *Journal of Electroanalytical Chemistry*, 117, 309-319, 1981.
- [119] J. Ambrose, R.G. Barradas, D.W. Shoesmith, Rotating copper disk electrode studies of the mechanism of the dissolution-passivation step on copper in alkaline solutions, *Electroanalytical Chemistry and Interfacial Chemistry*, 47, 65-80, 1973.
- [120] H.-H. Strehblow, V. Maurice, P. Marcus, Initial and later stages of anodic oxide formation on Cu, chemical aspects, structure and electronic properties, *Electrochimica Acta*, 46, 3755-3766, 2001.
- [121] M.R. Gennero de Chialvo, S.L. Marchiano, A.J. Arvia, The Mechanism of oxidation of copper in alkaline solutions, *Journal of applied electrochemistry*, 14, 165-175, 1984.
- [122] M. Shirkhanzadeh, G.E. Thompson, V.A. Ashworth, Study of the initial stages in oxidation of copper in alkaline solutions, *Corrosion Science*, 31, 293-298, 1990.
- [123] H.-H. Strehblow, B. Titze, The investigation of the passive behaviour of copper in weakly acidic and alkaline solutions and the examination of the passive film by ESCA and ISS, *Electrochimica Acta*, 25, 839-850, 1980.
- [124] J. Ambrose, R.G. Barradas, D.W. Shoesmith, Investigation of copper in alkaline solutions by cyclic voltammetry, *Electroanalytical Chemistry and Interfacial Chemistry*, 47, 47-64, 1973.
- [125] D.W. Shoesmith, S. Sunder, M.G. Bailey, G.J. Wallace, F.W. Stanchell, Anodic oxidation of copper in alkaline solutions: Part IV. Nature of the passivating film, *Journal of Electroanalytical Chemistry and Interfacial Electrochemistry*, 143, 153-165, 1983.
- [126] N.S. McIntyre, S. Sunder, D.W. Shoesmith, R.B. Stanchell, Chemical information from XPS application of electrode surfaces, *Journal of Vacuum Science and Technology*, 18, 714, 1981.

- [127] D.W. Shoesmith, T.E. Rummery, D. Owen, W. Lee, Anodic oxidation of copper in alkaline solutions 2 – The open-circuit potential behaviour of electrochemically formed cupric hydroxide films, *Electrochimica Acta*, 22,1403-1409, 1977.
- [128] P. Druska, H.-H. Strehblow, Quantitative determination of the passive layer on Cu-Ni alloys, *Surface and Interface Analysis*, 23, 440-450, 1995.
- [129] N. Cioffi, L. Torsi, I. Losito, C. DiFranco, I. DeBari, L. Chiavarone, G. Scamarcio, V. Tsakova, L. Sabbatini, P.G. Zambonin, Electrosynthesis and analytical characterization of polypyrrole thin films modified with copper nanoparticles, *Journal of Materials Chemistry*, 11, 1434-1440, 2001.
- [130] F. Texier, L. Servant, J.L. Bruneel, F. Argoul, In situ probing of interfacial processes in the electrodeposition of copper by confocal Raman microspectroscopy, *Journal of Electroanalytical Chemistry*, 446, 189-203, 1998.
- [131] B.L. Hurley, R.L. McCreery, Raman spectroscopy of monolayers formed from chromate corrosion inhibitor on copper surfaces, *Journal of the Electrochemical Society*, 150, B367-B373, 2003.
- [132] H.Y.H Chan, C.G. Takoudis, M.J. Weaver, Electrochemical control of gas phase oxidation and reduction of copper by surface-enhanced Raman spectroscopy, *Electrochemical and Solid-State Letters*, 2, 189-191, 1999.
- [133] H.Y.H Chan, C.G. Takoudis, M.J. Weaver, Oxide formation and oxygen adsorption on copper in aqueous media as probed by surface-enhanced Raman spectroscopy, *The Journal of Physical Chemistry B*, 103, 357-365, 1999.
- [134] G. Niaura, Surface-enhanced Raman spectroscopic observation of two kinds of adsorbed OH⁻ ions at copper electrode, *Electrochimica Acta*, 45, 3507- 3519, 2000.
- [135] S. Hartinger, B. Pettinger, K. Doblhofer, Cathodic formation of a hydroxide adsorbate on copper (111) electrodes in alkaline electrolyte, *Journal of Electroanalytical Chemistry*, 397, 335-338, 1995.

- [136] Y. Deng, A.D. Handoko, Y. Du, S. Xi, B. S. Yeo, In situ Raman spectroscopy of copper and copper oxide surfaces during electrochemical oxygen evolution reaction: identification of Cu^{III} oxides as catalytically active species, *Acs Catalysis*, 6, 2473–2481, 2016.
- [137] D. Reyter, M. Odziemkowski, D. Bélanger, L. Roué, Electrochemically activated copper electrodes surface characterization, electrochemical behavior, and properties for the electroreduction of nitrate, *Journal of The Electrochemical Society*, 154, K36-K44, 2007.
- [138] G. Parker, G. Hope, R. Woods, Raman spectroscopic identification of surface species in the leaching of chalcopyrite. *Electrochemistry in Mineral Processing VI*. Doyle, F.M., Kelsall, G.H., Woods, R., Editors PV2003-18, The Electrochemical Society Proceeding Series, Pennington, NJ, 181, 2003.
- [139] University of Arizona & California Institute of Technology, RRUFF Project, Mineralogical Database. <http://rruff.info/index.php>.
- [140] A. Kudelski, Structures of monolayers formed from different HS-(CH₂)₂-X thiols on gold, silver and copper: Comparative studies by surface-enhanced Raman scattering, *Journal of Raman Spectroscopy*, 34, 853-862, 2003.
- [141] R. Woods, G.A. Hope, K. Watling, A SERS spectroelectrochemical investigation of the interaction of 2-mercaptobenzothiazole with copper, silver and gold surfaces, *Journal of applied electrochemistry*, 30, 1209-1222, 2000.
- [142] S.-Y. Wang, W. Wang, Z.-H. Lu, Asynchronous-pulse ultrasonic spray pyrolysis deposition of Cu_xS (x=1,2) thin films, *Materials Science and Engineering: B*, 103, 184-188, 2003.
- [143] B. Minceva-Sukarova, M. Najdoski, I. Grozdanov, C.J. Chunnillall, Raman spectra of thin solid films of some metal sulfides, *Journal of molecular structure*, 410, 267-270, 1997.
- [142] T.P. Mernagh, A.G. Trudu, A laser Raman microprobe study of some geologically important sulphide minerals, *Chemical Geology*, 103, 113-127, 1993.

- [145] N.R. de Tacconi, K. Rajeshwar, R.O. Lezno, Study of copper sulfide film formation by voltammetry combined with electrochemical quartz crystal microgravimetry/coulometry and optical spectroscopy, *The Journal of Physical Chemistry*, 100, 18234-18239, 1996.
- [146] P.T. Kristiansen, F. Massel, L. Werme, C. Lilja, L.C. Duda, Sulfidation of single-phase oxide on copper and as powder studied using soft X-ray spectroscopy, *Journal of Electrochemical Society*, 162, C785, 2015.
- [147] F. King, M. Kolar, S. Stroes-Gascoyne, P. Maak, Model for the microbiological corrosion of copper containers in a deep geologic repository. *MRS Online Proceedings Library (OPL)*, 807, 535, 2003.
- [148] S.M. Abd El Haleem, E.E. Abd El Aal, Electrochemical behavior of copper in alkaline-sulfide solutions, *corrosion*, 62, 121-128, 2006.
- [149] M. Bojinov, T. Ikäläinen, Z. Que, T. Saario, Effect of sulfide on de-passivation and re-passivation of copper in borate buffer solution, *Corrosion Science*, 218, 111201, 2023.

3 Experimental and Instrumentation

This chapter outlines the fundamental concepts behind the experimental methods employed in the research discussed in this thesis. More detailed information about the experiments specific to each chapter can be found within those respective chapters.

3.1 Specimen preparation

Oxygen-free (< 5 wt% ppm), phosphorous-doped (30-100 wt% ppm) wrought Cu provided by SKB, the Swedish Nuclear Fuel and Waste Management Co., was used in all experiments [1]. The addition of phosphorous (P) serves to restrain creep deformation in Cu, which might otherwise arise from the high levels of mechanical stress exerted on the container after emplacement in a DGR [2].

The microstructure of the wrought copper material is shown in **Figure 3.1**. For the rest of this thesis, it will be referred to as SKB Cu.

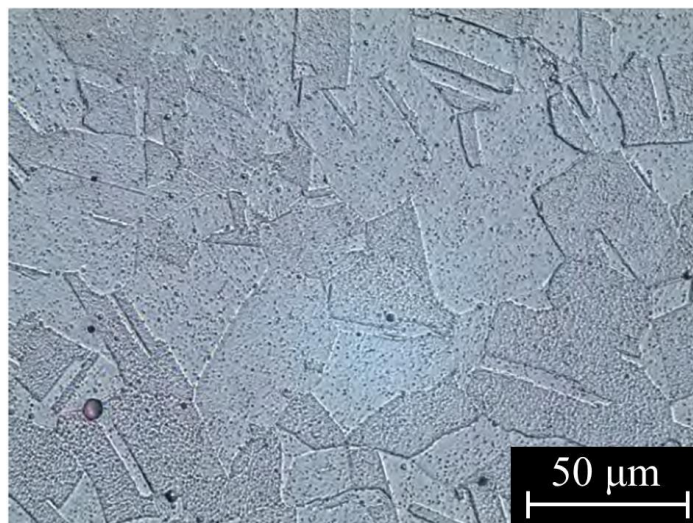


Figure 3.1: Wrought copper microstructure [3].

The Cu specimens were machined into 1 cm diameter disks, each threaded and connected to a Ti rod. Each disk was set in a polytetrafluoroethylene holder using epoxy resin (Hysol EE4190 GAL CZZ 0001 JF, Henkel) with only a single flat circular face with a total surface area of 0.785 cm² left bare to be exposed to the electrolyte. Each disk was ground using a

sequence of SiC papers (800, 1000, 1200, 2500 and 4000 grit), polished to a mirror finish using a 1 μm diamond suspension, rinsed with Type-I water, ultrasonically cleaned with methanol, washed again with Type-I water, and finally dried in a stream of Ar gas.

3.2 Formation of an oxide layer on Cu specimens

In this study, the aim was to create cover layers that replicate natural copper oxides/hydroxides that develop on the copper surface of a container within oxic period. In order to form an oxide layer with desired attributes, including thickness and composition, various approaches were applied.

3.2.1 Electrochemical method

3.2.1.1 Solution preparation

All electrolyte solutions were prepared with Type-I water (resistivity: 18.2 $\text{M}\Omega\cdot\text{cm}$) that was purified using a Barnstead Nano-pure water system. Reagent-grade NaOH (assay 98.9%, Fisher Chemical) was used to make the 0.1 M solutions (pH 13) used in preparing oxide-coated electrodes. The solution pH was measured using an Orion™ Star pH meter (Thermo Fisher Scientific).

3.2.1.2 Electrochemical/corrosion cell design and instrumentation

The electrochemical cell was equipped with three electrodes: the reaction of interest took place at the working electrode (WE), whose potential was measured and controlled via a reference electrode (RE), whereas the current flew between the WE and the counter electrode (CE).

In the three-compartment cell configuration, as shown in **Figure 3.2**, a dense glass frit was used to separate the solution in the WE compartment from that in the RE and CE compartments. A Luggin probe was used to minimize the ohmic potential drop between the RE and WE.

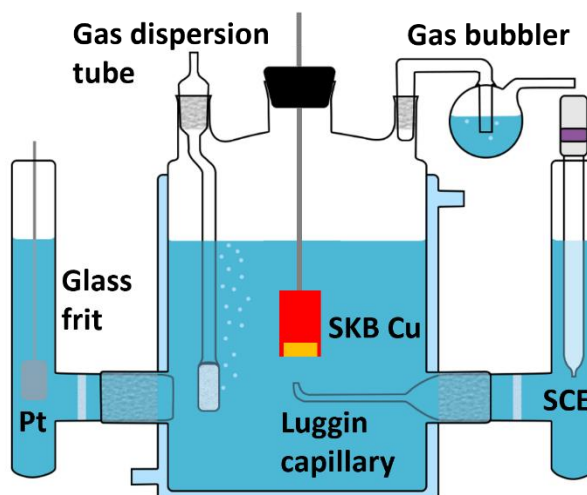


Figure 3.2: Schematic of the three-compartment electrochemical cell (solution volume of 700 mL).

A Pt sheet connected to external circuitry with a Pt wire and a saturated calomel electrode (SCE, 0.242 V/SHE (Standard Hydrogen Electrode)) were used as the counter and reference electrodes, respectively. Periodically, the SCE was checked against a master reference SCE to ensure the electrode remained reliable ($\Delta E = \pm 5$ mV). Electrochemical data were collected using either a Solartron 1287 potentiostat or a Solartron Analytical Modulab equipped with Corrware (Scribner Associates) and XM-Studio-ECS software.

3.2.2 Hydrothermal method

3.2.2.1 Solution preparation

The prepared copper substrates were immersed in a 40 mL solution containing 0.57 M KClO_3 and 0.1 M Na_2CO_3 , maintained at a temperature of 50°C for three days [4].

3.2.3 Radiation method

3.2.3.1 Solution preparation

The test solutions were prepared with aerated Type-1 water. The pH was adjusted to 9.0 by adding a low-concentration solution of high-grade sodium hydroxide (NaOH, assay 98.9%, Fisher Chemical) dropwise.

The pH of the solutions was measured using an Orion™ 9110DJWP Double Junction Micro-pH Electrode (Thermo Scientific) designed for small solution volumes.

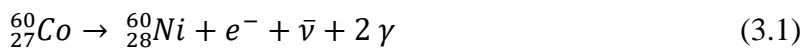
3.2.3.2 Exposure procedure

The copper samples were placed in 20 mL vials and sealed with aluminum crimp caps featuring a silicone septum coated with polytetrafluoroethylene (PTFE) (Thermo Fisher Scientific). Subsequently, the solution was placed on the copper surface using a micro-pipette. The vials were exposed to irradiation using an MDS Nordion Gamma Cell 220 Excel ^{60}Co irradiator, as detailed in the following section.

3.2.3.3 Gamma cell irradiator

Radiation experiments were conducted using a MDS Nordion Gamma Cell 220 Excel ^{60}Co irradiator, depicted in **Figure 3.3 (a)**. The radiation source, ^{60}Co , is encased in a cylindrical array of stainless steel “pencils” surrounded by a lead shell enclosed in steel. Samples are placed into a motorized stage that vertically moves into and out of the irradiation zone, allowing for the safe loading of samples without direct exposure of humans to the radiation source.

With a half-life of 5.3 years, Cobalt-60 undergoes beta decay according to Equation (3.1), emitting two gamma photons with energies measuring 1.17 and 1.33 MeV. Although the emitted beta particle (e^-) has a maximum energy of 0.32 MeV, it is incapable of penetrating the stainless-steel pencils to interact with samples within the gamma cell irradiator [5].



To ensure a uniform radiation dose for all specimens during the irradiation, a custom-designed sample holder, as illustrated in **Figure 3.3 (b)** was used. For the radiation experiments in this thesis, the absorbed radiation dose rate was 1.1 kGy/h, where 1 Gy is equivalent to 1 J of energy absorbed per kg of water. The radiation dose used in these experiments is approximately 500 times higher than the expected dose rate under DGR conditions on the exterior surface of the UFC [6].

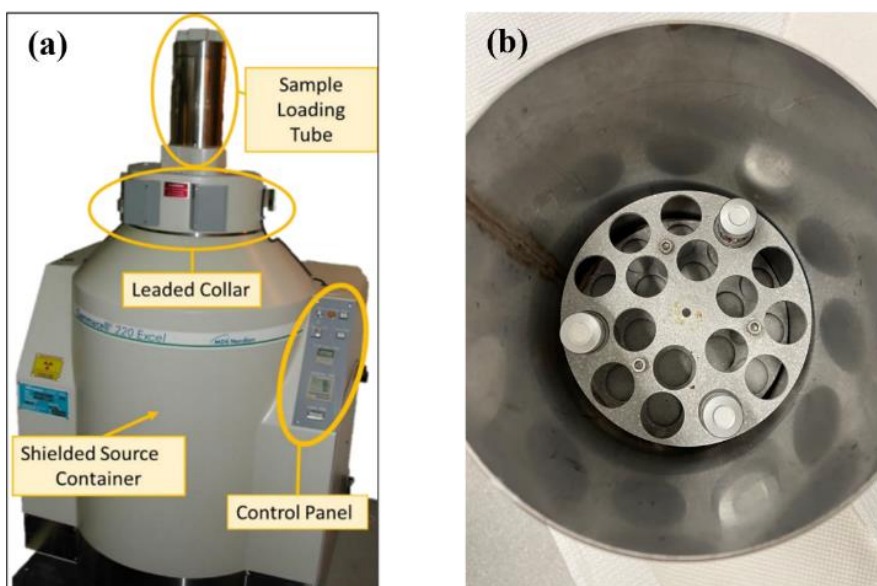


Figure 3.3: (a) Picture of ^{60}Co gamma cell irradiator [7] and (b) custom-designed sample holder [8].

3.3 Exposure of grown oxide to sulfide-containing solution

3.3.1 Solution preparation

Reagent-grade sodium sulfide ($\text{Na}_2\text{S}\cdot 9\text{H}_2\text{O}$, assay $\geq 98.0\%$, Sigma Aldrich) was added to Type-I water to prepare solutions with different $[\text{SH}^-]$. Since Na_2S is stored in hydrated form, it was first dried on a filter paper to minimize errors in calculating concentrations. All SH^- solutions contained 0.1 M NaCl (assay $\geq 99.0\%$, Fisher Chemical) as a supporting electrolyte.

Prior to experiments performed inside either an Ar-purged anaerobic chamber (Canadian Vacuum Systems Ltd.) equipped with an MBraun glove box control system or a Faraday cage, Type-I water was sparged with a stream of ultra-high purity Ar gas for 30 minutes on the benchtop. Following the transfer of water into the glove box, sulfide solutions were prepared inside the glovebox to ensure an anoxic environment. The minimum detectable $[\text{O}_2]$, as indicated by the detection limit of the O_2 sensor in the chamber, was 1 ppm.

3.4 Electrochemical techniques

3.4.1 Corrosion potential measurement

A corrosion potential (E_{corr}) measurement is essentially the potential difference between the test material (WE) and a reference electrode (RE) when zero current flows through an external measuring system [9]. It is important to note that corrosion potential measurement provides qualitative information and does not offer insights into the corrosion rate or kinetics [10].

In this study, corrosion potentials were monitored on oxidized specimens after transfer to a second electrochemical cell containing SH^- solutions, to investigate the effect of SH^- on the preformed oxide films.

3.4.2 Potentiostatic polarization

In a potentiostatic anodic polarization experiment, a constant external potential is imposed on the working electrode and maintained for a specific duration while monitoring the resulting current, as shown in **Figure 3.4 (a)**. This enables the separation of the anodic and cathodic corrosion reactions and facilitates the flow of measurable current through an external circuit. During anodic polarization, oxidation takes place at the working electrode, and the generated electrons travel through the potentiostat circuitry to the counter electrode, where they participate in the reduction reaction [11].

In this thesis, freshly prepared Cu specimens were oxidized at -0.3 V and -0.22 V/SCE in 0.1 M NaOH for 30 minutes, under de-aerated conditions, to form oxides with different compositions.

3.4.3 Cyclic voltammetry

In a cyclic voltammetry (CV) experiment, the potential is systematically swept back and forth between two potential limits at a constant rate, and the resulting current flowing through the circuit is recorded, **Figure 3.4 (b)**. The graphical representation of current versus potential is referred to as a cyclic voltammogram. In a CV scan, the applied potential is scanned from an initial potential (E_{Initial}) to a final potential (E_{Final}) where ($E_{\text{Initial}} < E_{\text{Final}}$).

The potential scan is reversed at E_{Switch} and the current is recorded on the reverse scan. Typically, this graph exhibits distinct anodic and cathodic peaks that correspond to various electrochemical reactions occurring at different potentials at an electrode surface.

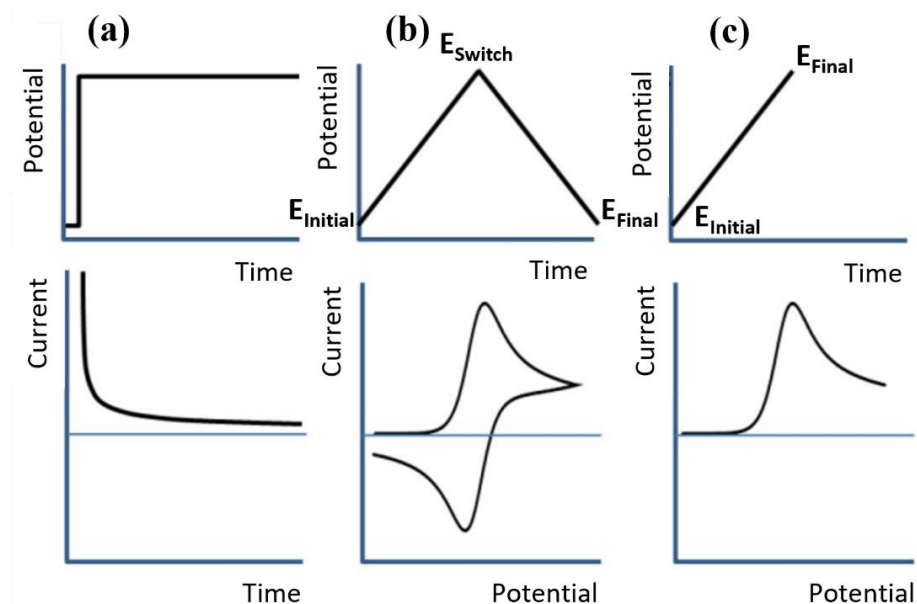


Figure 3.4: The relationship between different possible potential programs and the corresponding electroanalytical technique: (a) chronoamperometry, (b) cyclic voltammetry, and (c) linear sweep voltammetry [11].

The identification of these peaks in the voltammogram can yield valuable insights into the underlying processes since different electrochemical reactions generate unique characteristic peaks [11,12]. Integrating the current density (i) as a function of time (t) yields charge density (q), a measure of the extent of film formation, Equation (3.2) [13].

$$q = \int_0^t i \cdot dt \quad (3.2)$$

In this study, voltammetric experiments were performed to investigate the mechanism of copper (hydr)oxide formation. The potential was scanned from -1.3 to 0.5 V/SCE at a scan rate of 1 mV/s under de-aerated conditions to identify the appropriate potentials to be used in film growth experiments.

3.4.4 Linear sweep voltammetry

In linear sweep voltammetry (LSV), the potential of the working electrode is systematically altered in a linear fashion over time, as depicted in the top plot of **Figure 3.4 (c)**. This alteration commences from a potential where no electrode reaction occurs and progresses towards a potential where either the surface oxidation (at more positive values) or reduction (at more negative values) transpires. Consequently, the potential applied can be expressed as shown in Equation (3.3).

$$E_t = E_i \pm \nu t \quad (3.3)$$

where E_t represents the electrode potential at time t , E_i is the starting potential and ν denotes the scan (or sweep) rate, i.e., the absolute value of the constant rate of the potential change, dE/dt . The sign of ν depends upon the direction of the potential scan (positive for anodic sweeps and negative for cathodic sweeps) [12].

Cathodic stripping voltammetry (CSV) entails a potential scan in which the film previously formed on the sample surface is reduced back into the solution, resulting in the appearance of a peak on a potential–current plot (voltammogram) [14].

In this study, after E_{corr} measurement of various durations were performed in SH^- solutions, the potential was scanned from the final value of E_{corr} to -1.4 V/SCE at a scan rate of 1 mV/s to cathodically strip any oxide and sulfide films present on the electrode surface. The negative potential limit was chosen to minimize the H_2 evolution due to H_2O reduction. From the potentials at which cathodic peaks appeared and the measured charges associated with them, Equation (3.2), the nature and amount of the oxide and sulfide phases present were determined.

Nonetheless, most of the time, to fully interpret data acquired through electrochemical methods often requires supplementation from additional non-electrochemical approaches that offer chemical or structural insights. Specifically, the integration of spectroscopic techniques with electrochemical experiments can provide highly valuable information.

3.5 Specimen analysis

3.5.1 Microscopy

3.5.1.1 Optical microscopy

The optical microscope, commonly known as the “light microscope” is a variety of microscope that uses visible light and an arrangement of lenses to magnify images of minute samples, facilitating the examination of surface features. Conventional optical microscopes are constrained by a resolution dictated by the dimensions of submicrometre particles approaching the wavelength of visible light (400–700 nm) [15,16].

A basic optical microscope comprises an eyepiece and an objective lens. A digital microscope presents images directly on a computer screen, eliminating the need for an eyepiece. In a digital microscope, the image is captured by a charge-coupled device (CCD) camera to create a micrograph, which is then displayed on the screen [17]. **Figure 3.5** shows a schematic illustration of an optical microscope.

Optical microscopy was used in this thesis to gather information about thin hydroxide/oxide layers formed on the surface due to the pronounced reflectance of visible light by copper complexes. That is, the colour can provide chemical information about the solid species on the surface. Optical images were captured using a Keyence VHX-6000 digital microscope, or the 50 x Olympus microscope coupled with a Renishaw InVia Reflex Raman Spectrometer. Only relatively low-resolution micrographs were acquired, with magnifications ranging from 10 x to 120 x.

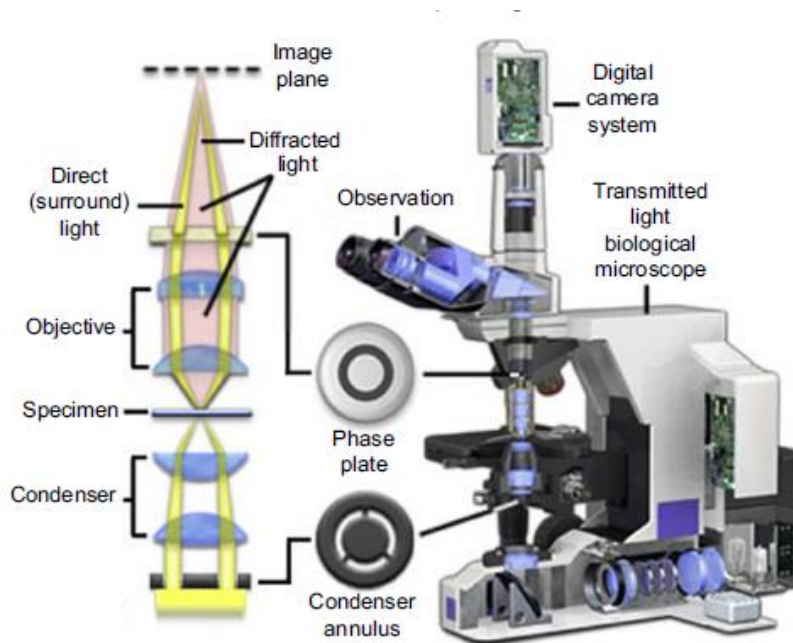


Figure 3.5: Optical microscope representation [15].

3.5.1.2 Scanning electron microscopy

A scanning electron microscope (SEM) is a type of electron microscope that produces images at a much greater resolution than an optical microscope because a focused beam of electrons is used to scan the sample surface.

The electrons interact with atoms in the sample, producing various signals that can be detected using specialized detectors (described in the following section) and that contain information about the sample's surface topography and composition [15,16].

Figure 3.6 shows a schematic illustration of a scanning electron microscope. At the upper part of the column in the electron gun, electrons are generated and then accelerated through the column with a designated accelerating voltage, typically in the range of 1 to 30 keV. Along the way, condenser lenses and apertures are utilized to control the convergence and the initial beam's diameter. The ultimate lens in the column is the objective lens, responsible for controlling the final electron beam's diameter and focusing the electron beam on the sample's surface positioned on a stage in the chamber. In a SEM, the beam's

diameter can vary from <1 nm up to 20 nm, depending on factors such as the electron gun type, the accelerating voltage, and the configuration of the lenses.

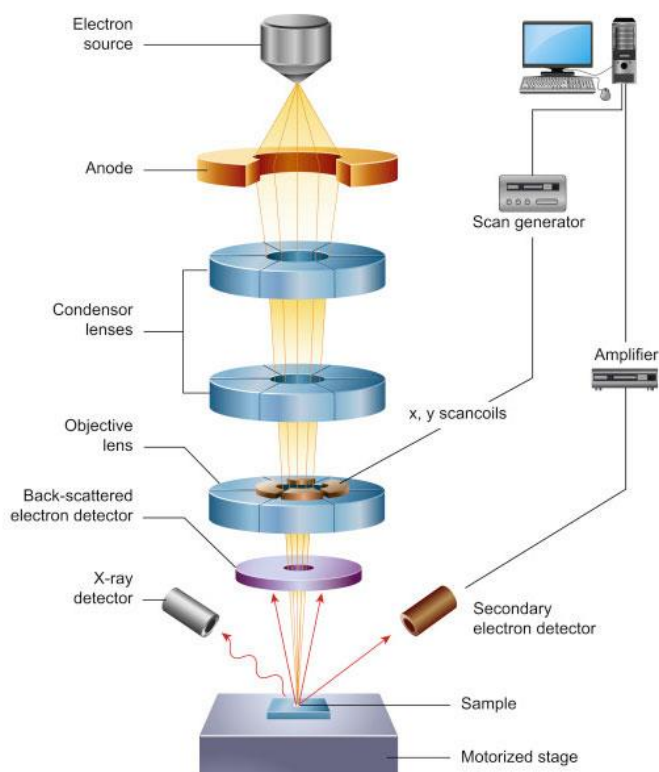


Figure 3.6: Schematic of a scanning electron microscope (With permission of the Nanoscience) [18].

The position of the electron beam on the sample is controlled by scan coils located above the objective lens. These coils enable the beam to be systematically scanned over sample surface in the X-Y plane. During the scanning process, the beam interacts with the sample, penetrating the material to a depth of a few micrometres [18,19]. The extent of this interaction volume is dependent on both the primary electron's accelerating voltage and atomic masses of the elements in the sample material.

Low-density samples exhibit an interaction volume resembling a tear-drop shape, **Figure 3.7**, while those composed of heavier elements display a hemispherical interaction volume. Increasing the accelerating voltage leads to a greater depth of penetration.

The interaction of electron beam upon striking the sample surface generates a variety of signals, including secondary electrons (SE), backscattered electrons (BSE), and characteristic X-rays. These signals are subsequently detected by respective detectors. In a SEM, the two most common detectors employed for high-resolution imaging are the secondary electron detector (SED) and the backscattered electron detector (BSD). To conduct surface composition microanalysis, energy dispersive X-ray spectroscopy (EDX) detectors are utilized.

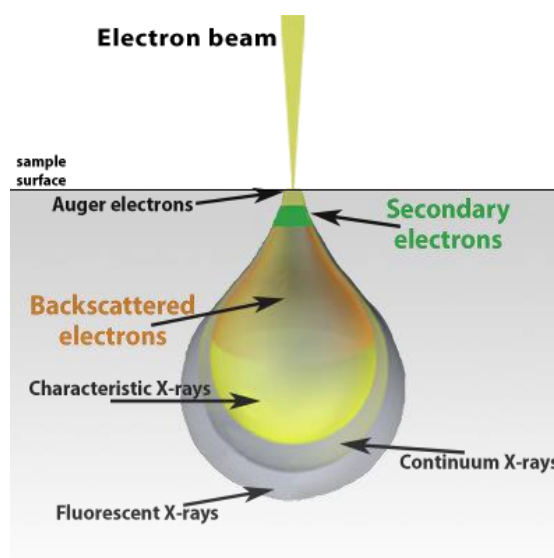


Figure 3.7: Schematic of electron beam interaction [19].

Secondary electrons are predominantly employed for creating topographical images since they are generated closer to the surface of the sample. These electrons are emitted as a result of inelastic scattering, **Figure 3.8**, or interactions that involve energy transfer from a primary beam electron to an atom in the sample. SEs typically have energies less than 50 eV. Images obtained using secondary electrons exhibit the highest lateral resolution, mainly because of the relatively small interaction volume, which is approximately equivalent to the beam diameter.

Elastic scattering at high angles ($> 90^\circ$) leads to the emission of BSEs above the sample surface, **Figure 3.8**. As the electron approaches the nucleus of an atom within the sample, the positive charge of the nucleus causes the fast electron to deflect, ultimately causing it to be remitted from the surface. The production of BSEs depends on the average atomic

number of scattering atom wherein heavier elements, possessing more positive charge, result in higher yield. Consequently, the contrast in images acquired with BSEs provides information on surface composition [19].

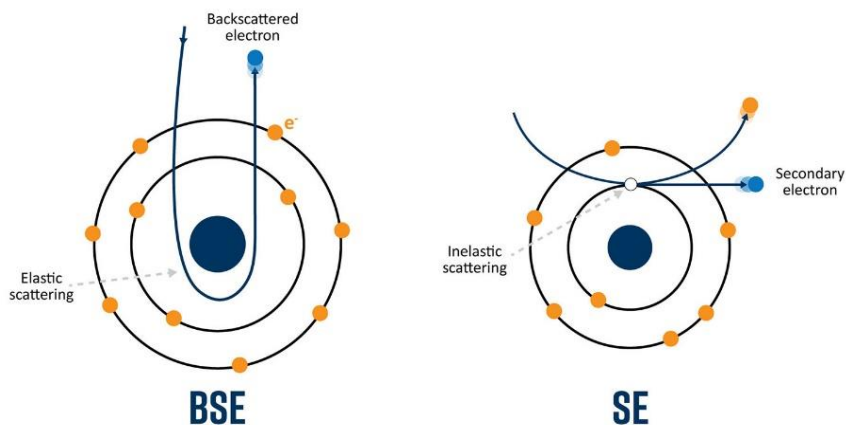


Figure 3.8: Schematic diagram of the generation of backscattered electrons (BSEs) vs. secondary electrons (SEs) (With permission of the Nanoscience) [18].

The scan generator, in conjunction with an external computer equipped with specialized software, coordinates the information (which includes the beam's X,Y position on the sample surface at each moment in time) with the intensity collected by the detector. This synchronization process enables the real-time display of a grayscale image, pixel-by-pixel. The signal-to-noise ratio can be adjusted depending on how long the electron beam dwells at each X,Y position. Magnification is determined by the size of the area that is scanned, with higher magnifications corresponding to progressively smaller scanned areas. Additionally, the number of pixels within a specific scanning area can be altered, affecting the apparent resolution [18].

The maximum resolution achievable in a SEM hinges on multiple factors including the electron beam diameter and interaction volume of the electron beam with the sample. Although it cannot deliver atomic-level resolution, some SEMs can achieve resolution better than 1 nm.

3.5.1.3 Field-emission scanning electron microscopy (FE-SEM)

The electron source plays a pivotal role in the functionality of a SEM as it has a substantial impact on its analytical performance. Termed the “electron gun”, this element must emit a bright and coherent stream of electrons, which can be adjusted and directed onto the sample by lenses within the column. SEMs generally employ three common types of electron emitters: tungsten filaments, solid-state hexaboride crystals, and field emission guns [19], as shown in **Figure 3.9**.

The tungsten filament comprises an inverted V-shaped wire of tungsten, approximately 100 μm long, which is heated resistively to generate electrons. This is the most basic type of electron source and was initially developed for the first generation of electron microscopes. Due to its cost-effectiveness, it continues to be the most widely used electron source to this day. The emission area of a tungsten filament is relatively large, which consequently leads to lower resolution.

In the field-emission gun scanning electron microscope (FEG-SEM), the function of the gun is to generate an exceptionally narrow beam of electrons with precisely controlled energy. It is termed a “field-emission” gun because an electric field induces the emission of high-energy electrons from a tungsten filament emitter, featuring a tip size as small as 10 nm. Consequently, this FEG-SEM provides superior spatial resolution, better reliability, improved signal-to-noise ratio, and an extended operational lifespan compared to earlier technologies [18,19].

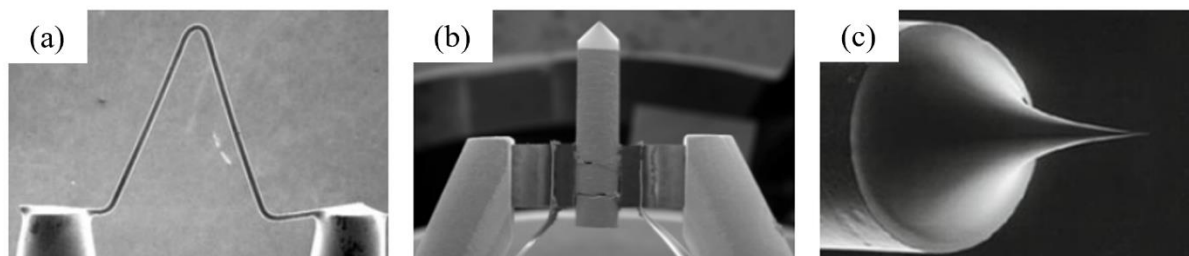


Figure 3.9: SEM images of (a) tungsten filament source, (b) solid-state crystal electron source, and (c) FEG electron source [18].

3.5.1.4 Focused-ion beam (FIB) milling

The focused ion beam, also known as FIB, is a scientific device resembling a SEM. However, while the SEM, which employs a focused beam of electrons to image the sample in the chamber, the FIB system takes advantage of a focused beam of ions instead. Furthermore, it is possible to integrate both electron and ion beam columns in the same system, offering to investigate the same features using either of the beams.

In the FIB system, a Ga ion (Ga^+) beam is employed to raster over the sample surface in a manner similar to the electron beam in a SEM, as illustrated in **Figure 3.10**. The high-energy ion beam allows the milling of small ditches in the sample at well-localized sites; thereby samples, sufficiently thin, can be cut out of the bulk material [15,20].

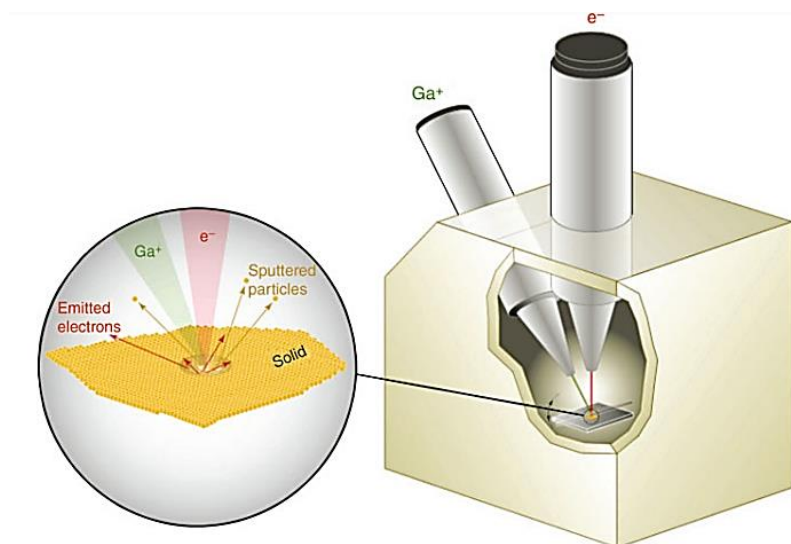


Figure 3.10: Schematic illustration of a dual-beam FIB/SEM instrument. Expanded view shows the electron and ion beam sample interactions [21].

In this study, surface imaging was performed using either a Hitachi SU8230 Regulus Ultra High-Resolution Field Emission SEM equipped with EDX or a Hitachi SU3500 Variable Pressure SEM combined with an Oxford Aztec X-Max50 SDD X-ray analyzer. EDX was carried out to elucidate the elemental composition of the surface. All SEM/EDX analyses were performed using an accelerating voltage of 5 keV to 10 keV with a spot intensity of 50-70%.

A LEO (Zeiss) 1540XB FIB/SEM was used to section samples using a Ga ion beam and to obtain cross-sectional images of surface films. Information on the porosity and oxide thickness can be obtained with this method.

3.5.2 Spectroscopy

3.5.2.1 Energy dispersive X-ray spectroscopy

Energy-dispersive X-ray spectroscopy (EDX) is a widely used technique for the identification and quantification of elemental compositions in a very small sample of material, even a few cubic micrometres.

Characteristic X-rays are emitted when an ionized atom relaxes to the ground state by filling a vacancy in the inner shell with an electron from an outer shell. The energy difference between these two shells is equivalent to the characteristic X-ray energy, which can serve as a unique fingerprint for identifying the specific element that it originated from. Characteristic X-rays that are produced through inelastic scattering allow for the precise identification of elements present in the sample. In addition to the characteristic X-ray peaks evident in EDX data, there is also a continuum (background) X-ray signal generated by the deceleration of incident electrons as they interact with the sample [16,18].

3.5.2.2 Laser Raman spectroscopy

When incident light strikes a sample, it excites the molecule from an initial energy state to a virtual E_{virt} state, as depicted in **Figure 3.11 (a)**. A virtual state is a very short-lived intermediate quantum state that lacks a precisely defined molecular energy value. Subsequently, from the virtual state, the molecule rapidly relaxes back to a vibrational level in the ground E_0 electronic state and emits a photon of light. When relaxation occurs, three possible situations can unfold.

First, the molecule undergoes excitation form, followed by relaxation to the same ground vibrational level (0), subsequently re-emitting a photon of light (green) with the energy equal to that of the incident photon. This process, recognized as Rayleigh scattering, is an elastic phenomenon wherein the frequency of the light remains unchanged.

The other two situations result in the inelastic scattering of the incident photon that alters its energy. If the molecule is excited by a photon from level 0 and then relaxes to level 1, the molecule acquires energy and reemits a photon of lesser energy (referred to as being red-shifted), corresponding to Stokes Raman scattering. The third possible situation occurs when the molecule is excited from level 1 and subsequently returns to level 0, thus losing its energy and re-emitting a photon of light with higher energy than the incident photon. This situation with the blue-shifted photon corresponds to anti-Stokes Raman scattering [22].

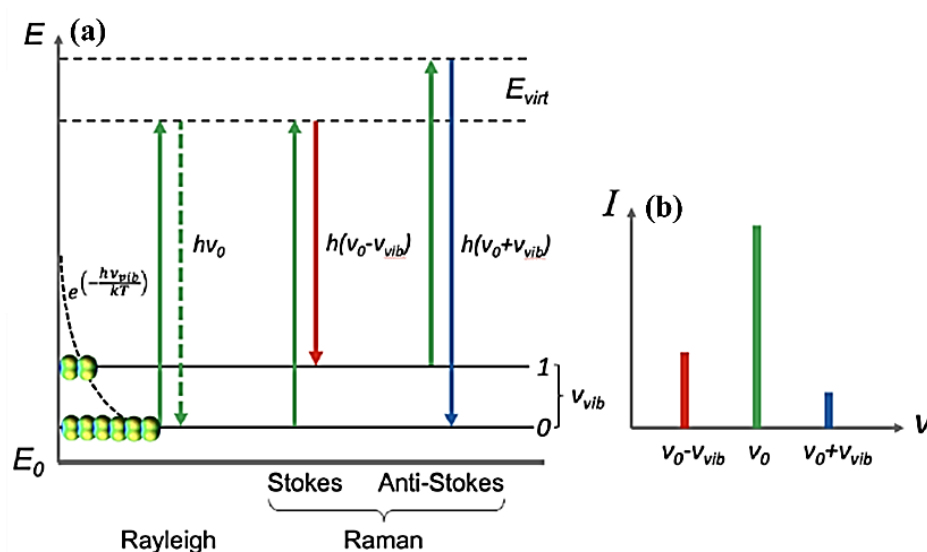


Figure 3.11: Schematic representation of (a) Rayleigh scattering (elastic), Stokes and anti-Stokes Raman scattering (inelastic) occurring during Raman spectroscopy and (b) intensity of Stokes Raman (red) scattering with regards to anti-Stokes Raman (blue) scattering (With permission of the Thermo Fisher scientific) [23].

At room temperature, the measurement of Raman spectra in the Stokes region has the most practical importance. Indeed, the intensities of spectral bands and, consequently, signal-to-noise ratios (S/N) in the Stokes region are notably higher than those in the anti-Stokes region, as shown in **Figure 3.11 (b)**.

A plot of Raman intensity versus the Raman shift, which is the difference between the frequencies of excitation light and Raman transitions, is known as a Raman spectrum.

In a Raman microscope, a laser excitation source and a spectrometer are combined with an optical (light) microscope, enabling non-destructive spectrochemical analysis of diverse materials and objects at the microscopic level. Additionally, a diffraction grating decomposes Raman scattering into its constituent spectral components, which are then focused onto the multi-element array detector.

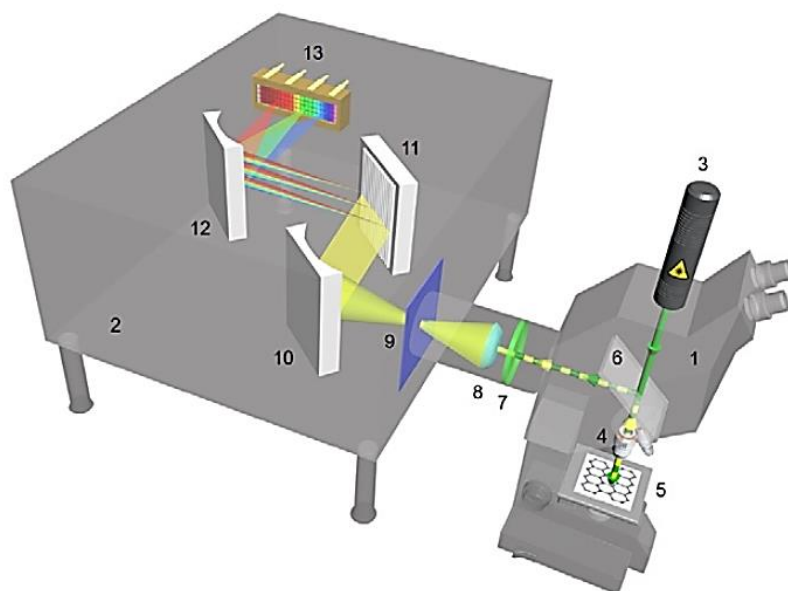


Figure 3.12: Schematic diagram of a dispersive Raman microscope: 1–optical microscope; 2–spectrograph; 3–laser source; 4–microscope objective; 5–sampling stage with a sample; 6–beam splitter or dichroic mirror; 7–Rayleigh filter; 8–microscope-to-spectrograph coupling optics; 9–spectrograph entrance aperture; 10–collimating mirror; 11–diffraction grating; 12–focusing mirror; 13–array detector (With permission of the Thermo Fisher scientific) [23].

While the appearance of the measured spectrum remains unaffected by the excitation wavelength, selecting an appropriate laser excitation wavelength is crucial for acquiring the most informative Raman spectrum of a given sample. According to Equation (3.4), the scattering intensity (I) is inversely proportional to the fourth power of the excitation wavelength (λ).

$$I \propto \frac{1}{\lambda^4} \quad (3.4)$$

Therefore, Raman spectroscopists prefer shorter laser wavelengths, such as blue (488 nm), green (514 and 532 nm), or red (633 nm), to obtain a stronger Raman signal and, consequently, achieve an improved S/N in the spectrum.

Raman spectroscopy presents unequivocal advantages for numerous applications, including:

- No sample preparation is required, or the sample preparation is rather trivial.
- The technique is nondestructive and saves the sample integrity.
- Since water is a weak Raman scatter and does not manifest much in Raman spectra, Raman spectroscopy proves to be well-suited for the study of analytes in aqueous solutions, e.g., biological compounds.

In fairness, it is important to acknowledge that Raman spectroscopy comes with recognized drawbacks. The major one is undoubtedly fluorescence interference. Also, stringent control over the laser power directed at the sample is necessary to prevent issues like local heating or photodecomposition.

Fluorescence only takes place when a molecule is excited up to a higher electronic state. Fluorescence can be notably diminished by using longer excitation wavelengths, such as visible (785 nm) or near-infrared (830 and 1064 nm), where the photon lacks sufficient energy to excite a molecule to higher electronic states [23].

In this study, the phases present on the oxidized Cu specimens before and after exposure to SH^- solutions were analyzed by laser Raman spectroscopy. Raman spectra were collected using a Renishaw InVia Reflex Raman spectrometer equipped with a He-Ne laser with a wavelength of 632.8 nm to excite Raman active vibrations. Spectra were recorded over the wavelength shift range 150 cm^{-1} to 900 cm^{-1} , with the laser used at 5% power to minimize any surface heating effects. All Raman spectra reported in this manuscript include the raw data only.

3.5.2.3 X-ray diffraction

X-ray diffraction (XRD) provides a rapid and non-destructive approach for identification and characterization of unknown materials.

X-rays which fall within the electromagnetic spectrum having wavelengths ranging from 0.01 to 10 nm, possess the rare ability to penetrate and undergo diffraction from internal atomic layers within crystals. This capability stems from the fact that their wavelengths are in the range of atomic dimensions of crystals that constitute most of the materials.

XRD analysis has not only advanced our understanding of the atomic arrangement within crystalline materials but has also played a crucial role in affirming purity of materials and identifying distinct phases.

Bragg's law serves as the foundation stone on which the structure of X-ray diffraction stands.

When a beam of X-rays impinges on a crystal face, it undergoes partial scattering by the atoms of the crystal. The fraction that is not scattered reaches the next atomic layer where another part is scattered, and the remainder passes across to the next layer, and so forth. Consequently, the diffraction pattern arises from the constructive and destructive interference of X-rays diffracted from each atomic plane. Constructive interaction occurs when the diffracted beams are in phase, while destructive interaction occurs when they are out of phase. The fundamental prerequisites for X-rays to diffract is the crystalline nature of the sample and that the outgoing angle of scattered X-rays is equal to the angle of incidence [24]. Bragg's law, expressed mathematically as Equation (3.5), defining the relationship between the wavelength of the X-ray beam (λ) and the angle of incidence (θ), calculates the angle where constructive interference from X-rays scattered by parallel planes of atoms will produce a diffraction peak, **Figure 3.13**.

$$n\lambda = 2d_{hkl} \sin \theta \quad (3.5)$$

where, n is an integer and d_{hkl} , the vector magnitude, is the distance between parallel planes of atoms and is a geometric function of the size and shape of the unit cell. Miller indices (hkl) are used to identify different planes of atoms.

In most diffractometers, the X-ray wavelength λ is fixed. Consequently, a family of planes produces a diffraction peak only at a specific angle 2θ .

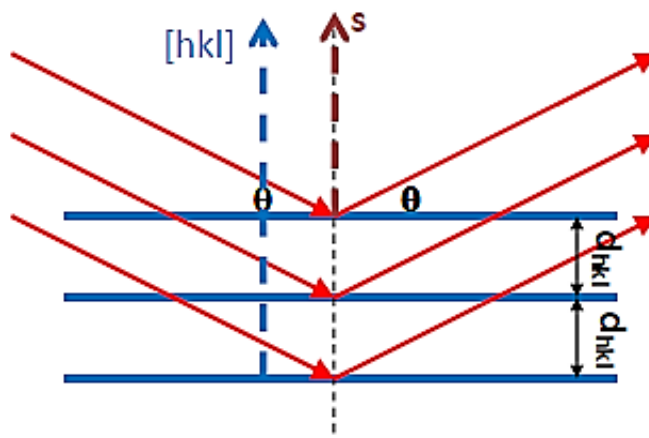


Figure 3.13: Schematic illustration of the constructive interference obeying Bragg's law ($[hkl]$, the plane normal, is the vector drawn from the origin of the unit cell to intersect the crystallographic plane (hkl) at a 90° angle. Additionally, the plane normal $[hkl]$ must be parallel to the diffraction vector (s)) [25].

Based on XRD measurements, one can measure the distance between the atomic layers of the crystal lattice, estimate bond lengths and angles, and verify the identity of the unknown materials by correlating their crystal lattice structure with that of standard reference materials.

The International Centre of Diffraction Data (ICDD), formerly known as the Joint Committee on Powder Diffraction Standards (JCPDS), maintains a database of diffraction patterns. To identify a particular phase both peak positions and relative intensities must fit.

A laboratory source of X-rays, as shown in **Figure 3.14**, comprises an evacuated tube housing a copper block anode bearing a metal target made of any of the metals such as molybdenum, tungsten, copper, rhodium, silver, or cobalt. The cathode is a tungsten filament. On passage of electric current through the filament, electrons are generated and move towards the anode under the highly accelerating voltage typically 30–150 kV. The accelerating electrons, upon striking the metal surface, knock out electrons from the inner shells, and the resulting vacancies are filled by electrons from the outer shells. This process leads to the emission of X-rays by metal atoms. The anode material determines the

wavelengths of the characteristic radiation. For most experiments, a single wavelength of characteristic radiation is selected using a filter or monochromator [25].

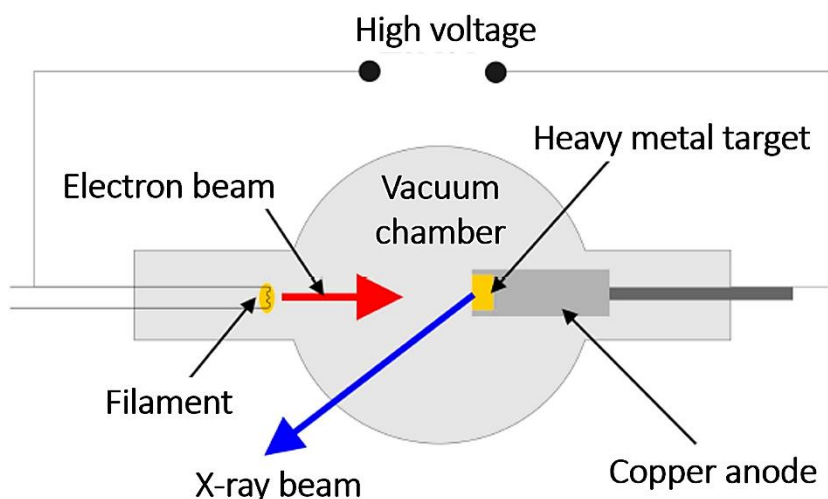


Figure 3.14: Schematic diagram of X-ray tube [25].

In practical terms, diffractometers can operate in a variety of modes, including a ω - 2θ mode (Bragg-Brentano geometry: $\omega=\theta$). In this configuration, the X-ray source remains stationary, while the sample is rotated at half the rate of the detector so as to maintain the θ - 2θ geometry, as shown in **Figure 3.15**. Diffraction will only occur from crystallites in which the plane normal $[hkl]$ is parallel to the diffraction vector (s), the vector that bisects the angle between the incident and diffracted beam [26].

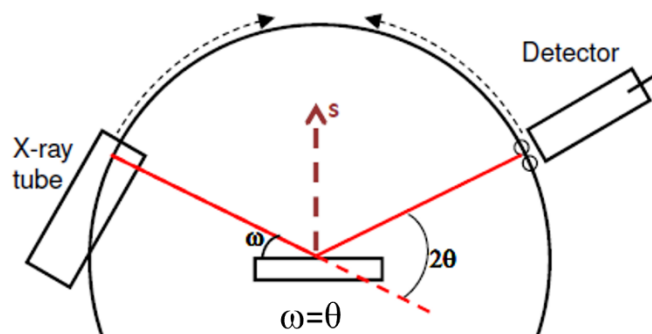


Figure 3.15: A schematic showing the Bragg-Brentano geometry in an XRD analysis [26].

In this research, all XRD spectra for powder samples were acquired using a Rigaku SmartLab X-ray diffractometer equipped with 2D HyPix-3000 detector and a Cu X-ray radiation source set at 40 kV. The detector scan range (2θ) was between 10 to 90°, with a scan speed of 3°/m.

3.6 References

- [1] L. Cederqvist, M. Johansson, N. Leskinen. U. Ronneteg, Design, production and initial state of the canister, TR-10-14, SKB, 2010.
- [2] P.G. Keech, P. Vo, S. Ramamurthy, J. Chen, R. Jacklin, D.W. Shoesmith, Design and development of copper coatings for long term storage of used nuclear fuel, *Corrosion Engineering, Science and Technology*, 49, 425–430, 2014.
- [3] R. Konečná, S. Fintová, Copper and copper alloys: casting, classification and characteristic microstructures in copper alloys - early applications and current performance - enhancing processes (ed Dr. Luca Collini), InTechOpen, 2012.
- [4] P.T. Kristiansen, F. Massel, L. Werme, C. Lilja, and L.C. Duda, Sulfidation of single-phase oxide on copper and as powder studied using soft X-Ray spectroscopy, *Journal of The Electrochemical Society*, 162, C785-C791, 2015.
- [5] K. Eckerman, A. Endo, Nuclear decay data for dosimetric calculations, *ICRP*, 38, 7-96, 2008.
- [6] R.P. Morco, J.M. Joseph, D.S. Hall, C. Medri, D.W. Shoesmith, J.C. Wren, Modelling of radiolytic production of HNO₃ relevant to corrosion of a used fuel container in deep geologic repository environments, *Corrosion Engineering, Science and Technology*, 52, 141-147, 2017.
- [7] M. Torres, L. Burdin, A.V. Rentería-Rodríguez, E.A. Franco-Urquiza, Degradation of epoxy-particles composites exposed to UV and gamma radiation, *Chemistry*, 5, 559–570, 2023.
- [8] B. Verlinden, P. Zsabka, K. Van Hecke, K. Verguts, L.C. Mihailescu, G. Modolo, M. Verwerft, K. Binnemans, T. Cardinaels, Dosimetry and methodology of gamma irradiation for degradation studies on solvent extraction systems, *Radiochimica Acta*, 109, 61–72, 2021.

- [9] E. McCafferty, Introduction to corrosion science, Springer Science & Business Media, 2010.
- [10] R. Francois, Environmental degradation in hydrocarbon fuel processing plant: issues and mitigation, *Advances in Clean Hydrocarbon Fuel Processing*, 437-462, 2011.
- [11] V. Climent, J.M. Feliu, Cyclic voltammetry, *Encyclopedia of Interfacial Chemistry*, 48-74, 2018.
- [12] G. Bontempelli, N. Dossi, R. Toniolo, Linear sweep and cyclic, Reference Module in Chemistry, Molecular Sciences and Chemical Engineering, 2016.
- [13] T. Martino, R. Partovi-Nia, J. Chen, Z. Qin, D.W. Shoesmith, Mechanisms of film growth on copper in aqueous solutions containing sulphide and chloride under voltammetric conditions, *Electrochimica Acta*, 127, 439–447, 2014.
- [14] O. Abollino, A. Giacomino, M. Malandrino, Voltammetry | Stripping voltammetry, *Encyclopedia of Analytical Science (Third Edition)*, 238-257, 2019.
- [15] A. Di Gianfrancesco, Technologies for chemical analyses, microstructural and inspection investigations, *Materials for Ultra-Supercritical and Advanced Ultra-Supercritical Power Plants*, 197-245, 2017.
- [16] S. Ebnesajjad, Surface and material characterization techniques, *Surface Treatment of Materials for Adhesive Bonding (Second Edition)*, 39-75, 2014.
- [17] G. Youssef, Applied mechanics of polymers - properties, processing, and behavior (First Edition), 273–299, 2022.
- [18] <https://www.nanoscience.com/techniques/scanning-electron-microscopy/>.
- [19] W. Zhou, R. Apkarian, Z.L. Wang, D. Joy, Fundamentals of scanning electron microscopy (SEM), scanning microscopy for nanotechnology, Springer, 1-40, 2007.
- [20] L.A. Giannuzzi, F.A. Stevie, Introduction to focused ion beams instrumentation, Springer, 2005.

- [21] C.A. Volkert, A.M. Minor, Focused ion beam microscopy and micromachining, MRS Bulletin, 389-399, 2007.
- [22] M. Cardona, Light scattering in solids, topics in applied physics, Springer-Verlag, 8, 1975.
- [23] Raman spectroscopy, microscopy and imaging, Thermo Fisher Scientific, 2023.
- [24] C. Hammond, The basics of crystallography and diffraction (Second edition), Oxford University Press, 2001.
- [25] B.D. Cullity, S.R. Stock, Elements of X-ray diffraction (Third Edition), Prentice Hall, 2001.
- [26] C. Suryanarayana, M.G. Norton, X-ray diffraction: a practical approach, Springer Science & Business Media, 2013.

4 Investigating the Electrochemical Behaviour of Copper in Alkaline Solution and the Effect of Electrochemically-grown Single-Phase Copper (I) Oxide on Bisulfide-induced Corrosion

4.1 Introduction

Once the UFC is buried underground in a DGR, environmental conditions will be oxidizing, due to the presence of either a small amount of oxygen trapped in the buffer material pores upon DGR closure or oxidants produced by gamma radiolysis [1,2]. The small amount of trapped oxygen in a Canadian DGR emplacement room once closed, based on the current design, will be 13 moles per container. Due to radioactive decay, which is responsible for an increase in temperature (around 90°C initially), the container will experience a warm and oxidizing environment. The uniformly distributed damage across the surface of each UFC due to reaction with oxygen will be maximum 298 µm. Nonetheless, this value is very conservative, because it assumes that all available oxygen will react with the copper to produce copper (I) species (while it is possible that some of the oxygen will react with copper (I), and consequently copper (II) will be formed, without consuming more Cu metal) and available oxygen will not be consumed by other reactions, such as oxidation of minerals in the rock and clay and biological processes in the DGR [3]. Following this period, once all available oxygen is totally consumed by scavenging mechanisms, repository conditions will evolve to anoxic. Upon establishment of anoxic conditions, bisulfide will be the only oxidant for copper. Although SH⁻ has not been detected in analyses of Canadian ground waters at the predicted DGR depth [4], it can be produced by SRB at spots far from the container in the compacted bentonite clay.

Pyrite (FeS₂, pK_{sp} at 25°C = 26.98) is a mineral that is found in bentonite specimens (at a level of less than 1 wt%), which makes it a potential source of SH⁻ in the DGR [5-8]. However, pyrite solubility is extremely low (~ 10⁻¹¹-10⁻¹² M), meaning that the concentration of bisulfide in equilibrium with pyrite is negligible [8]. Based on an earlier study, the sulfate concentration increases as time elapses in bentonite porewater, due to gypsum (CaSO₄) dissolution, a component of bentonite, so sulfate concentrations are considerable enough not to limit bisulfide production by SRB [9]. While the composition

of the groundwater in a Canadian DGR is unknown, since the NWMO has not chosen a site yet, it would be expected that chloride will be a dominant species, with a concentration between 0.001 and 5.6 M [4]. Furthermore, the groundwater composition will change when the water passes through the compacted bentonite clay which will surround the waste container. As a result of passing through bentonite clay to eventually reach the container, the groundwater pH will be in the range of 7 to 8, because of equilibrium with the calcite (CaCO_3) present in the bentonite [4]. The concentration of dissolved ions is expected to change slowly over time, although chloride anions will remain dominant.

At the time anoxic conditions are established, it is anticipated that the container surface will be covered by Cu_2O as a base layer, with various Cu (II) salts on top of that, e.g., $\text{CuCl}_2 \cdot 3\text{Cu}(\text{OH})_2$ as shown in **Figure 4.1** [10,11].

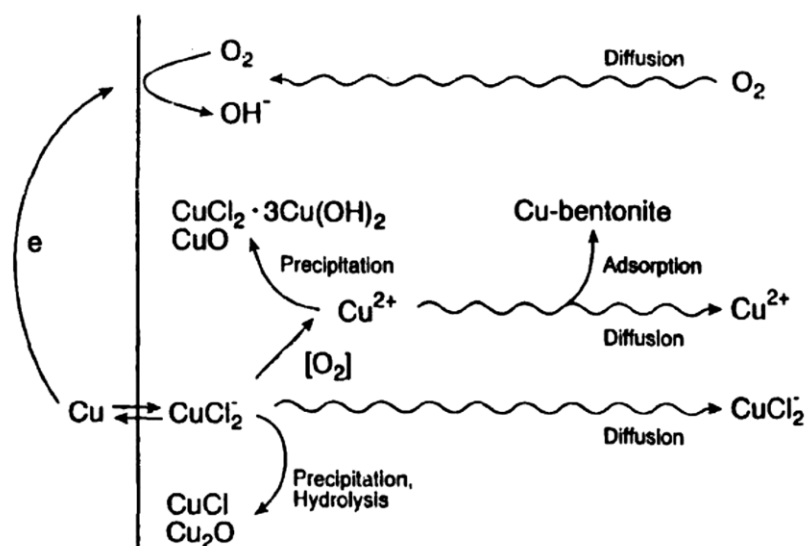


Figure 4.1: Proposed mechanism for copper corrosion in $[\text{Cl}^-]$ containing groundwater under oxic conditions (With permission of the Swedish Nuclear Fuel and Waste Management Company) [10].

The corrosion rate of a container under anoxic conditions can be influenced by the oxide films and corrosion products formed during the early stage of repository conditions. The degree to which an oxide film and/or corrosion product is able to affect the corrosion rate is dependent on its structure and the amount of surface that it covers.

Copper destabilization by bisulfide seems to be the only feasible long-term corrosion process for containers. Due to the initial period of oxic corrosion, when bisulfide-driven

corrosion begins the container surface will be covered by an oxide/hydroxide/Cu (II) salt that must be breached before bisulfide reaction with the copper substrate can happen [12]. Therefore, it is necessary to investigate the effect of dissolved bisulfide on oxidized copper surfaces.

The specific goals of this series of experiments are:

1. To form an oxide layer with known composition (Cu (I) oxides) like that expected to be produced during the initial oxidizing period in the repository, to determine the effects of Cu oxidation on the subsequent corrosion of Cu in aqueous bisulfide environments.
2. To study the conversion of copper oxide/hydroxide to copper sulfide in SH^- solutions of various concentrations.
3. To investigate the possibility of oxide-to-sulfide conversion through surface analysis.

4.2 Experimental

To investigate the effect of Cu oxidation on subsequent bisulfide-induced corrosion, firstly, an oxide layer (with known composition) was formed on the Cu surface, then this oxidized Cu specimen was exposed to solutions containing different concentrations of bisulfide, and the oxide-to-sulfide conversion was studied by means of surface analysis techniques.

4.2.1 Specimen preparation

O-free, P-doped copper provided by SKB, was used as a working electrode. The electrode preparation is explained in detail in section 3.1.

4.2.2 Solution preparation

To form copper oxides/hydroxide, the solution was prepared according to section 3.2.1.1. The grown oxides were then exposed to bisulfide solutions prepared as explained in section 3.3.1. The total bisulfide concentration was 5×10^{-5} and 10^{-4} M. All bisulfide solutions contained 0.1 M NaCl (assay $\geq 99.0\%$, Fisher chemical) as a supporting electrolyte.

4.2.3 Electrochemical cell design and instrumentation

All the details about the electrochemical cell design and instrumentation are described in section 3.2.1.2.

4.2.4 Electrochemical/corrosion experiments

Prior to each experiment, the copper electrode was cathodically cleaned at -0.85 V/SCE for 3 minutes to make naturally formed oxides from the surface defective. Similar experiments were done at two different locations: on the bench-top and in a glove-box. Prior to each experiment, the solution was sparged with a stream of ultra-pure Ar gas for a minimum of 30 minutes. Subsequently, during the bench-top experiments, which were conducted inside a Faraday cage to decrease electrical noise from external sources, solutions were continuously Ar-sparged, and for those experiments that were performed in the glove-box, after Ar-sparging, solutions were transferred into a glove-box filled with Ar and maintained in an anoxic condition to avoid contamination from atmospheric O_2 and to minimize SH^- oxidation.

4.2.4.1 Cyclic voltammetry

Voltammetric experiments were performed to investigate the mechanism of copper oxide/hydroxide formation. The potential was scanned from -1.3 to 0.5 V/SCE at two scan rates (1 and 2 mV/s) under both aerated and de-aerated conditions to find an appropriate potential at which to perform the oxidation.

4.2.4.2 Potentiostatic polarization

Freshly prepared specimens, after surface treatment, were oxidized at -0.3 V in 0.1 M NaOH for 30 minutes under de-aerated conditions. For the following part of this report (exposure to bisulfide-containing solutions), the specimens oxidized in this way will be denoted as oxidized specimens.

4.2.4.3 Corrosion potential measurements

Corrosion potentials (E_{corr}) were monitored once oxidized specimens were transferred to the second electrochemical cell containing bisulfide solution, under open-circuit

conditions, to investigate the effect of bisulfide on oxide films formed previously on the Cu specimens and their possible conversion to copper sulfide films upon exposure to solutions with different bisulfide concentrations.

4.2.4.4 Cathodic stripping voltammetry

Following E_{corr} measurements in SH^- solutions, the potential underwent scanning from the final E_{corr} value to -1.4 V/SCE at a rate of 1 mV/s. This process aimed to cathodically strip any oxide and sulfide films on the electrode surface. The selection of the lower potential limit was intended to minimize the initiation of H_2 evolution resulting from H_2O reduction. The appearance of cathodic peaks and the corresponding measured charges were then analyzed to determine the composition and quantity of the oxide and sulfide phases present.

4.2.5 Surface analyses

4.2.5.1 Laser Raman spectroscopy

Copper specimens oxidized at -0.3 V/SCE for 30 min in 0.1 M NaOH and oxidized Cu specimens exposed to 0.1 M NaCl containing different concentrations of bisulfide were prepared and then removed from the glove-box for characterization of the oxide/hydroxide and sulfide films formed on their surface using laser Raman spectroscopy.

4.2.5.2 Scanning electron microscopy

Surface imaging of oxidized specimens before and after exposure to bisulfide-containing solutions was performed using field emission SEM and conventional SEM equipped with an energy dispersive X-ray spectroscopy (EDX) analyzer to elucidate the elemental composition of the surface.

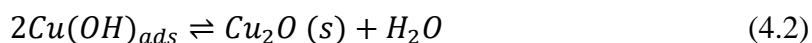
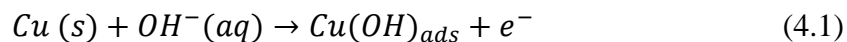
4.3 Results and Discussion

4.3.1 Oxidation of copper in alkaline solution

A suitable environment in which to prepare an oxidized copper layer with a certain composition is an alkaline solution. According to the Pourbaix diagram, Cu_2O is stable at $\text{pH} > 10$, while CuO is stable at $\text{pH} \geq 7$ but at more positive potentials than those associated with Cu_2O [13].

The voltammetric behaviour of Cu in 0.1 M NaOH (pH 12.9) was studied under both aerated and de-aerated conditions, as shown in **Figure 4.2**, to determine the proper conditions for growing an oxide film. Three different peaks can be distinguished, corresponding to Cu₂O, Cu(OH)₂ and CuO.

Peak A₁ shows the formation of a monolayer layer of Cu₂O via the reactions (4.1) and (4.2) [14]:

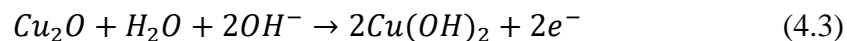


Shirkhanzaeh et al. [14] suggested that the formation of Cu(OH)_{ads} species happens along with the release of soluble Cu (I), which is directly formed from copper metal. This would be followed by growth and coalescence of Cu(OH)_{ads} species, which eventually forms a monolayer and inhibits the parallel dissolution reaction. A subsequent dehydration reaction follows, forming Cu₂O.

Also, Strehblow et al. [15] believed that, prior to film formation, for $E > \sim -0.8$ V/SCE, OH⁻ adsorption on the surface occurs, reaction (4.1), which leads to an irreversible surface reconstruction as OH⁻ is adsorbed–desorbed [15,16].

The formation of the Cu₂O layer, reaction (4.2), starts with the growth of small disk-like features, preferentially located at the terrace step edges, which eventually cover the whole surface [16,17].

Peak A₂, at more positive potentials, corresponds to the formation of an upper layer of Cu(OH)₂ by nucleation and growth from the solution. It was suggested by Shoosmith et al. [18] that the dissolved Cu (II) ions necessary for forming Cu(OH)₂ deposits will be produced either by the anodic dissolution of Cu₂O, which leads to a widening of the pores of the Cu₂O base layer or by metal dissolution through the pores of the Cu₂O layer [18], therefore the further oxidation of Cu⁰ and Cu₂O yielded a Cu₂O/CuO/Cu(OH)₂ layer, reactions (4.3)-(4.5):



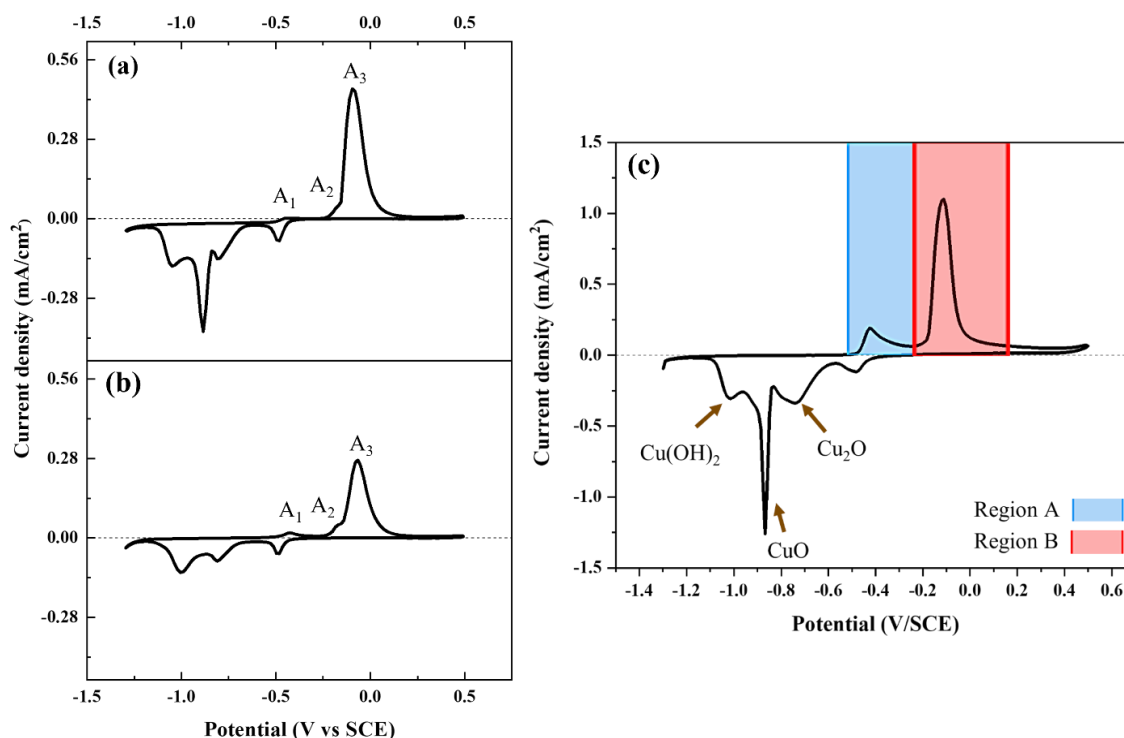
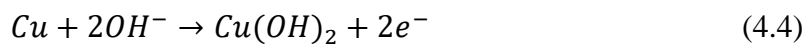


Figure 4.2: Cyclic voltammetry scans recorded on a Cu specimen immersed in 0.1 M NaOH (pH 13) solution under (a) aerated and (b) de-aerated conditions at 2 mV/s, (c) de-aerated conditions at 1 mV/s. Regions A and B represent different oxidation processes.

Peak A₃, on the forward scan, indicates the formation of a compact, partially passive mixed layer of CuO/Cu(OH)₂. The initially formed CuO at the base of pores in the Cu₂O continues to form at the Cu₂O/Cu(OH)₂ interface [19]:



As shown in **Figure 4.2 (c)**, the cathodic peaks on the negative-going scan can be attributed to the reduction of Cu₂O, CuO, and Cu(OH)₂ films, respectively, as described previously by Smith et al. [11]. It appears that the cathodic peak for Cu₂O was preceded by a small peak which can be related to either an adsorbed layer or a defective form of Cu₂O layer on the Cu surface.

The comparison between aerated and de-aerated conditions shows that the peak attributed to the formation of Cu_2O is smaller under aerated conditions than under de-aerated conditions. We can suggest that the presence of a significant amount of oxygen as oxidizing agent in aerated alkaline solution produces more OH^- ions (Equation (4.6)). According to Equation (4.3), hydrolysis by OH^- , and in unstirred solution (stirring can be induced by Ar-sparging in de-aerated solution), local supersaturation leads to formation and deposition of more $\text{Cu}(\text{OH})_2$ and subsequently formed CuO . On the forward scan, based on the peak area, which is relevant to the anodic charge, under aerated conditions, the final corrosion products are mostly comprised of Cu (II) oxides/hydroxides.



I chose to grow Cu_2O under both aerated and de-aerated conditions in an alkaline solution by applying a constant potential for a specific duration of time. Based on the literature [11], one would expect that potentiostatic oxidation of copper at -0.3 V/SCE (Region A shown in blue) for 30 minutes might lead to a single-phase Cu_2O layer. Either the extension of exposure time or choosing a potential in Region B (shown in red) can lead to the appearance of other phases, such as $\text{Cu}(\text{OH})_2$ and CuO , or a less compact Cu_2O layer.

To grow an oxide under optimal conditions, I grew it potentiostatically, under both aerated and de-aerated conditions. The potentiostatic current transient corresponding to the oxidation of copper under these conditions is shown in **Figure 4.3**.

Figure 4.3 shows that the current value under aerated conditions is mostly negative. This current represents the net current for the redox reaction, which is the sum of cathodic and anodic currents. The negative current value does not mean that an oxide film could not be formed on the surface, but it means that the cathodic reaction (O_2 reduction) is dominant under aerated conditions. As mentioned earlier, Cu_2O can be hydrolyzed by OH^- ions (Equation (4.6)) to $\text{Cu}(\text{OH})_2$. Therefore, since the goal was to form Cu_2O , de-aerated conditions were chosen over aerated conditions.

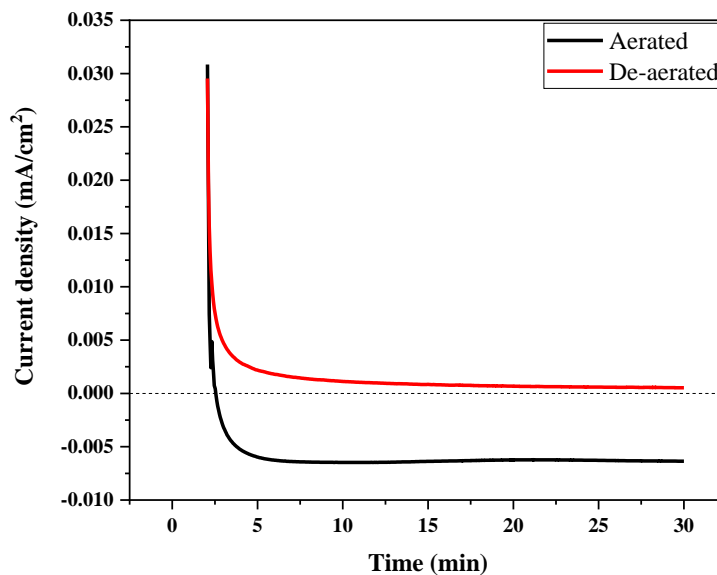


Figure 4.3: Current density-time plot recorded during potentiostatic oxidation of Cu at -0.3 V in 0.1 M NaOH solution for 30 min under aerated and de-aerated conditions.

To make sure that -0.3 V is the proper oxidation potential, various potentials in region A (-0.43 V, -0.40 V, and -0.3 V/SCE in **Figure 4.2 (c)**) were applied. The curves indicating the current density change and logarithm of current density (to show the differences clearly) for copper under de-aerated conditions at different applied potentials are given in **Figure 4.4**.

In all cases, as the oxide layer forms, the current density drops swiftly at the early stage. At -0.43 V/SCE, the current density appeared to be about to switch to a negative value at longer times. For the two more positive applied potentials, the current density approached a low, constant, potential-independent value at longer times. Integrating the current density–time transients yields a measure of the extent of film formation, assuming no dissolution as soluble Cu^{I} occurs [20].

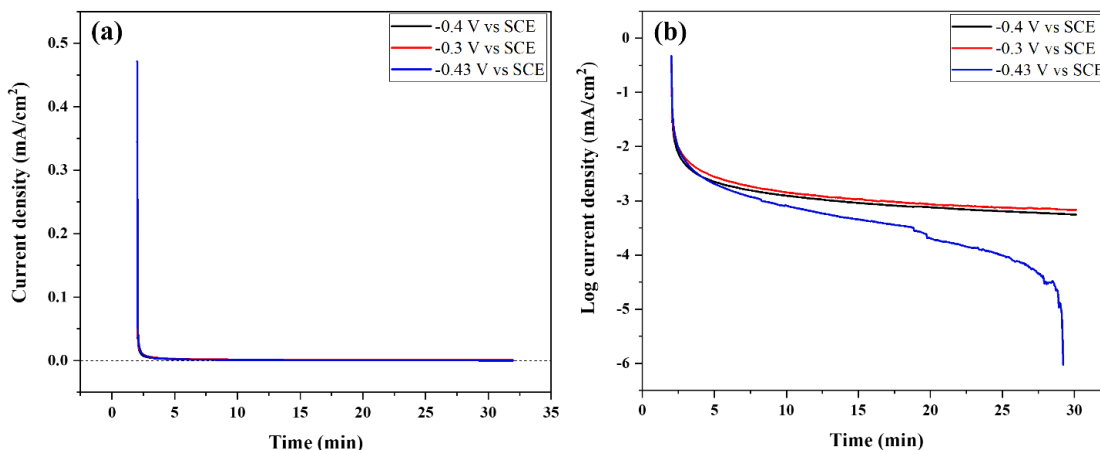


Figure 4.4: Plots recorded during potentiostatic oxidation at different potentials in de-aerated 0.1 M NaOH for 30 min: (a) i-time and (b) Log i-time.

Table 4.1 shows the charge densities for different applied potentials. Based on the results, the charge density for oxidation at an applied potential of -0.3 V is higher than at other potentials, so it could be expected that a thicker film would be formed by applying that potential.

The thickness of the oxide layer formed (δ) can be calculated using the charge densities in **Table 4.1** and Faraday's law, Equation (4.7),

$$\delta = \frac{q}{nF} \times V_m \quad (4.7)$$

where q is the volumetric charge density (C/m^3), V_m the molar volume of the oxide ($2.39 \times 10^{-5} m^3/mol$ for Cu_2O), n the number of exchanged electrons, and F the Faraday constant ($96485 C/mol$) [17]. Based on Equation (4.7), the average thickness of the Cu_2O layer formed on Cu after anodic polarization at -0.3 V/SCE for 30 min was around 10 nm.

Table 4.1: Absolute charge densities calculated by integration of the current density–time curves in **Figure 4.4 (b)**.

Applied Potential (V/SCE)	Charge density ($\mu\text{C}/\text{cm}^2$)
−0.30	4423
−0.40	3880
−0.43	3830

4.3.2 Exposure of oxidized Cu to bisulfide-containing solutions under two different conditions

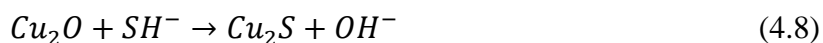
4.3.2.1 Glove-box experiments

To achieve the anoxic conditions, the first series of experiments was conducted inside a glove-box. **Figure 4.5** shows the variation of E_{corr} versus time recorded in 0.1 M NaCl containing different concentrations of bisulfide, on electrodes that were oxidized at −0.3 V (versus SCE) for 30 minutes in 0.1 M NaOH.

Regardless of bisulfide concentration, E_{corr} undergoes a transition from an initial potential which is 120 mV negative to the E_e for the Cu/Cu₂O redox couple. This value is close to the E_{corr} observed upon exposure of a clean, unoxidized copper electrode to de-aerated 0.1 M NaCl, which suggests the exposure of bare metal at the base of the pores [11]. This transition approaches a potential value close to E_e (Cu/Cu₂S) after 35 minutes for 0.1 M Cl[−] + 5 × 10^{−5} M SH[−] solution and 20 minutes for 0.1 M Cl[−] + 10^{−4} M SH[−]; this indicates surface redox conditions that have become dominated by the Cu/Cu₂S couple.

In terms of conversion of Cu (I) oxide to Cu (I) sulfide, there are two possible mechanisms:

1. Conversion through a chemical process:



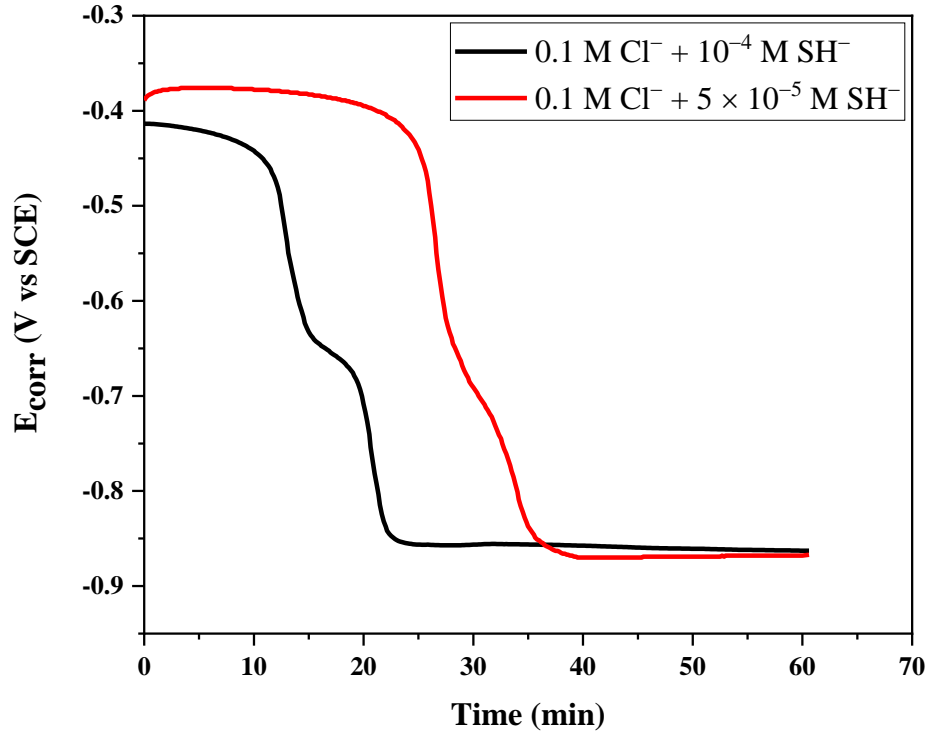
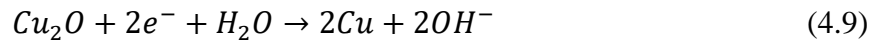
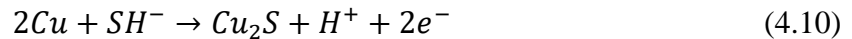


Figure 4.5: E_{corr} -time curves of oxidized Cu specimens exposed to 0.1 M NaCl solutions containing different concentrations of bisulfide inside the glove-box.

2. Conversion through a galvanically coupled process in which the cathodic reduction of Cu_2O ,



is coupled to the anodic formation of Cu_2S :



To confirm the presence of an oxide film on the oxidized Cu surface and the oxide-to-sulfide conversion, laser Raman spectroscopy was conducted (**Figure 4.6**).

Two broad peaks were observed, at 510 cm^{-1} and 610 cm^{-1} , indicating the presence of Cu_2O [21] on the surface of the oxidized specimen. The strong single peak at 300 cm^{-1} , which is related to Cu_2S [22], can be observed for oxidized specimens exposed to the different concentrations of bisulfide. The intensity of this signal increases with an increase in bisulfide concentration, and simultaneously the peaks associated with Cu_2O become

weaker but still are visible, consistent with the formation of sulfide on top of the oxide at the oxide/solution interface.

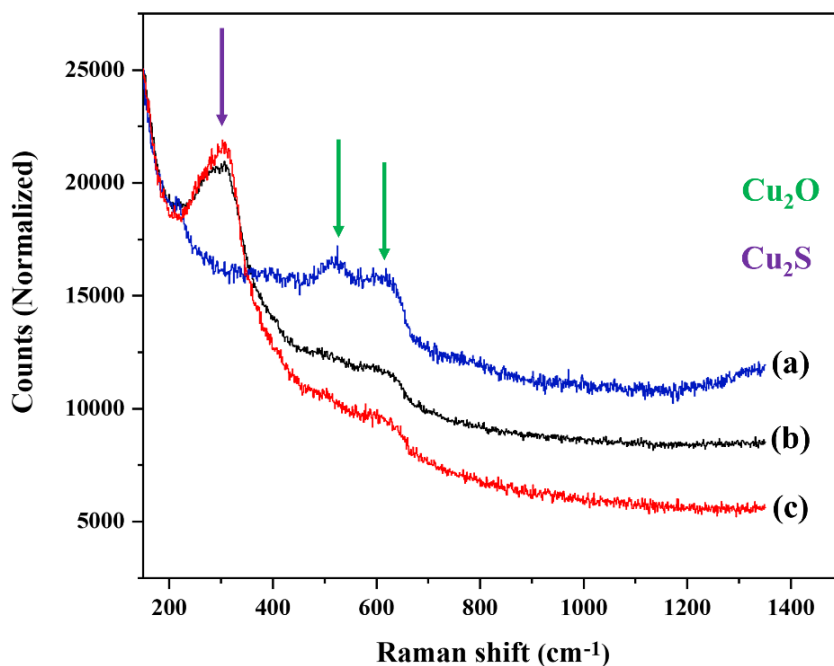


Figure 4.6: Raman Spectra collected on (a) an oxidized Cu specimen in 0.1 M NaOH (30 min, -0.3 V/SCE) and oxidized Cu specimens exposed to 0.1 M NaCl containing (b) 5×10^{-5} M SH^- and (c) 10^{-4} M SH^- inside the glove-box.

Figure 4.7 shows a series of SEM surface images for an oxide film grown potentiostatically at -0.3 V/SCE for 30 min in 0.1 M NaOH and films formed after exposing the oxidized Cu specimens to 0.1 M NaCl with various bisulfide concentrations.

The SEM micrograph indicates that a very thin, uniform layer of oxide was formed on the Cu specimen. This layer does not seem very dense and still the polishing lines can be observed. At 5×10^{-5} M SH^- , a thin nodular film can be inspected on the surface. When the concentration of bisulfide was increased to 10^{-4} M, a lamellar sulfide film, which consisted of various particles in a variety of sizes, oriented in preferential directions, was formed on the surface.

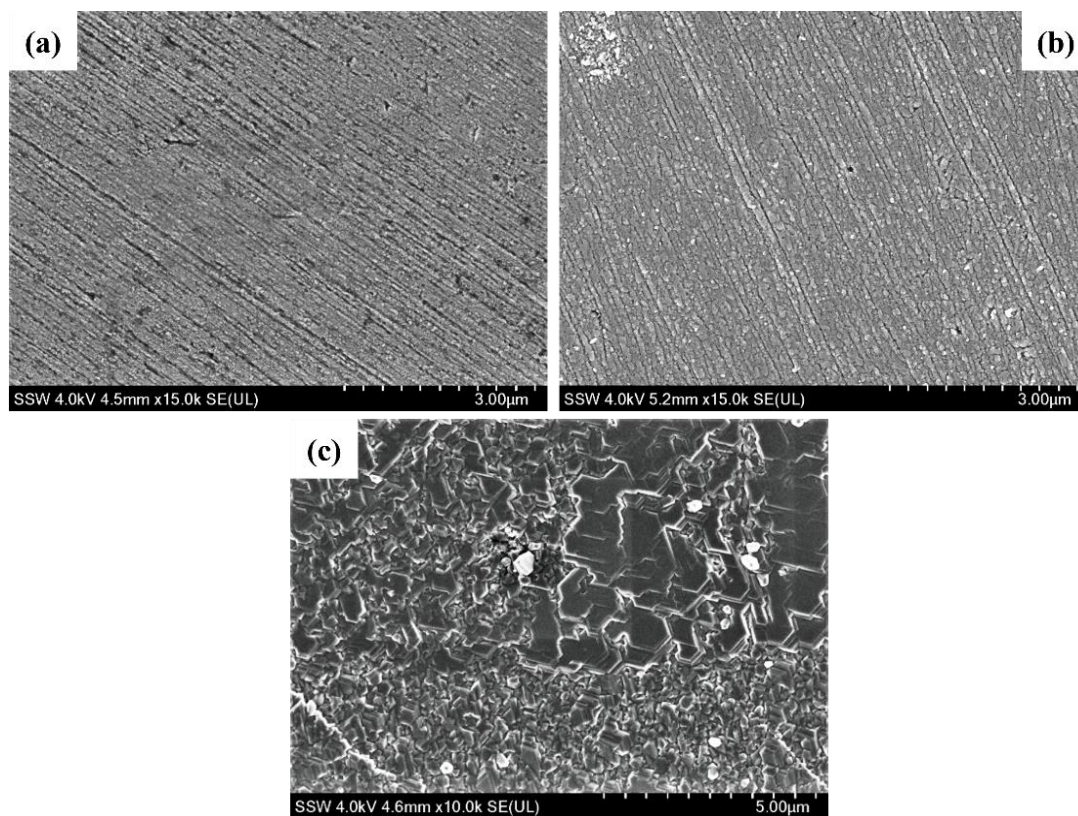


Figure 4.7: Morphologies of films on (a) a Cu specimen oxidized in 0.1 M NaOH and oxidized specimens exposed to 0.1 M NaCl containing (b) 5×10^{-5} M SH^- and (c) 10^{-4} M SH^- , inside the glove-box.

4.3.2.2 Ar-sparged solutions

4.3.2.2.1 Conversion of Cu_2O to Cu_2S at different SH^- concentrations

Figure 4.8 shows the changes in E_{corr} with time for oxidized specimens exposed to 0.1 M NaCl solutions containing 5×10^{-5} and 10^{-4} M SH^- , constantly sparged with Ar to provide de-aerated conditions during the experiment.

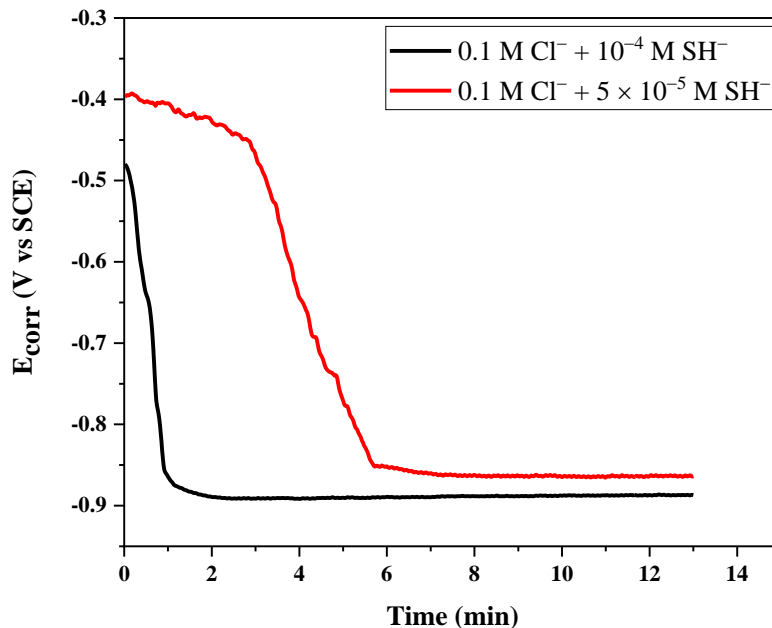


Figure 4.8: E_{corr} -time transients recorded on Cu electrodes, oxidized for 30 min at -0.3 V in Ar-sparged 0.1 M NaOH, on exposure to 0.1 M NaCl solution containing various bisulfide concentrations.

Figure 4.9 shows that the oxide-to-sulfide conversion can also be observed under these conditions, but the time required for this conversion is drastically shorter than that observed in the glove-box. Ar-sparging during the experiment facilitates the convection of SH^- ions toward the oxidized copper surface, and reaction between bisulfide ions and Cu_2O and Cu occurs faster, which can decrease the timeframe of the oxide-to-sulfide transition. The SEM/EDX performed on these specimens showed that a thin layer of oxide existed on the copper surface, but it was too thin to be detected by EDX.

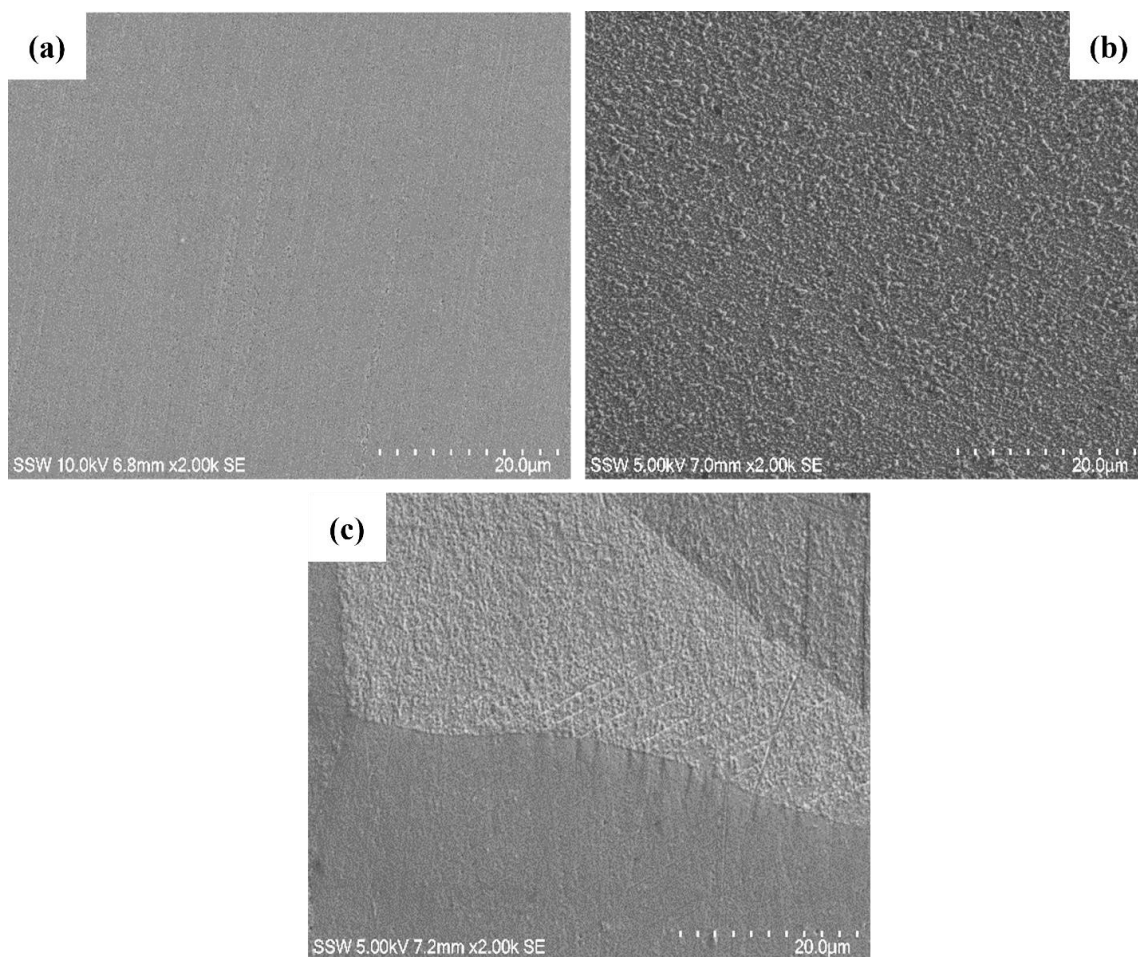


Figure 4.9: SEM micrographs of (a) the oxide layer formed on a Cu specimen in Ar-sparged 0.1 M NaOH, and sulfide layers on oxidized specimens exposed to 0.1 M NaCl containing, (b) 5×10^{-5} M SH^- and (c) 10^{-4} M SH^- .

A uniform nodular film was formed on the surface of a specimen exposed to 5×10^{-5} M SH^- and the presence of S on the surface was indicated by the EDX spectrum. In the case of the concentrated bisulfide solution, a non-uniform film could be seen on the surface. The base layer of this multilayer film had less elemental S, and some features grown on top of this layer in preferential directions were seen to have more S, as shown in **Figure 4.10** and **Table 4.2**.

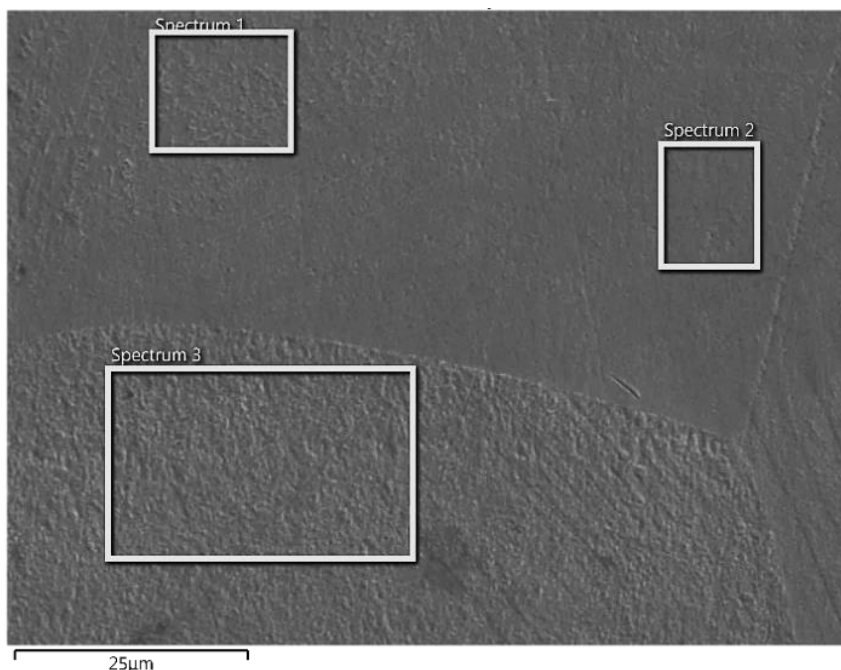


Figure 4.10: Selected regions on the oxidized Cu specimen exposed to Ar-sparged 0.1 M NaCl + 10^{-4} M SH^- solution for EDX.

Table 4.2: Elemental composition at the selected areas of the oxidized Cu specimen exposed to Ar-sparged 0.1 M NaCl + 10^{-4} M SH^- solution.

Element (wt %)	Spectrum 1	Spectrum 2	Spectrum 3
Cu	90.4	90.9	84.1
S	4.5	4.4	10.7
O	1.2	1.0	1.0
Others	3.9	3.7	4.2

4.3.2.2.2 Conversion of Cu_2O to Cu_2S at different periods of time

In this series of experiments, Cu specimens oxidized at -0.3 V/SCE for 30 min were transferred to an electrochemical cell containing 0.1 M Cl^- + 5×10^{-5} M SH^- , and E_{corr} monitored for various durations under Ar-sparged conditions, **Figure 4.11 (a)**. The initial E_{corr} values for the individual experiments were in the range -0.36 V/SCE to -0.4 V/SCE,

which is more negative than the potential for the Cu/Cu₂O equilibrium, suggesting some porosity in the Cu₂O layer. E_{corr} decreased slowly for a period that varied in duration for the three specimens before E_{corr} underwent a transition to -0.85V/SCE , a value close to the potential for the Cu/Cu₂S equilibrium at the specific concentration used in this experiment, demonstrating that the Cu surface was exposed to SH⁻ and E_{corr} controlled by the Cu/Cu₂S reaction.

After each period of immersion, cathodic stripping voltammetry (CSV) was performed to determine the nature and amounts of the phases present on the exposed surface, **Figure 4.11 (b)**. Also shown are CSVs recorded on a specimen exposed for only 10 s and one oxidized but not subsequently exposed to a SH⁻-containing solution. Prior to exposure to the SH⁻ solution, only a thin Cu₂O film, cathodically reduced in the range -0.4 V/SCE to -0.5 V/SCE , was present on the Cu surface. This reduction peak disappeared after a short SH⁻ exposure period and was replaced by a peak at potentials $< -1.0\text{ V/SCE}$, indicating that oxide-to-sulfide conversion had taken place [22,23].

The anodic charge densities accumulated during the oxidation step and the cathodic charge densities calculated by integrating the oxide and sulfide reduction peaks in the CSVs in **Figure 4.11 (b)** are shown in **Figure 4.12**. For the blank experiment, the difference between the oxidation charge and cathodic charge (which averaged $5\% \pm 1\%$ over three repeat runs) is a result of rinsing with Type-I water before transferring to the cell containing bisulfide solution. To verify this finding, a two-step blank experiment, including the oxide formation and cathodic stripping of the formed film, was performed in the same solution (0.1 M NaOH). The cathodic charge obtained from CSV was equal to the calculated anodic charge. Since the oxidation state of the Cu (Cu (I)) is the same in both the formed oxide (Cu₂O) and the Cu₂S conversion product, the charges obtained are directly comparable. Most of the oxide is converted to sulfide in the first 20 s, with the subsequent increase in total charge indicating that SH⁻ oxidation of the substrate Cu to Cu₂S begins before the conversion of Cu₂O is complete and continues after the conversion is complete. The continuous long-term growth of Cu₂S is consistent with the results of previous corrosion studies [24].

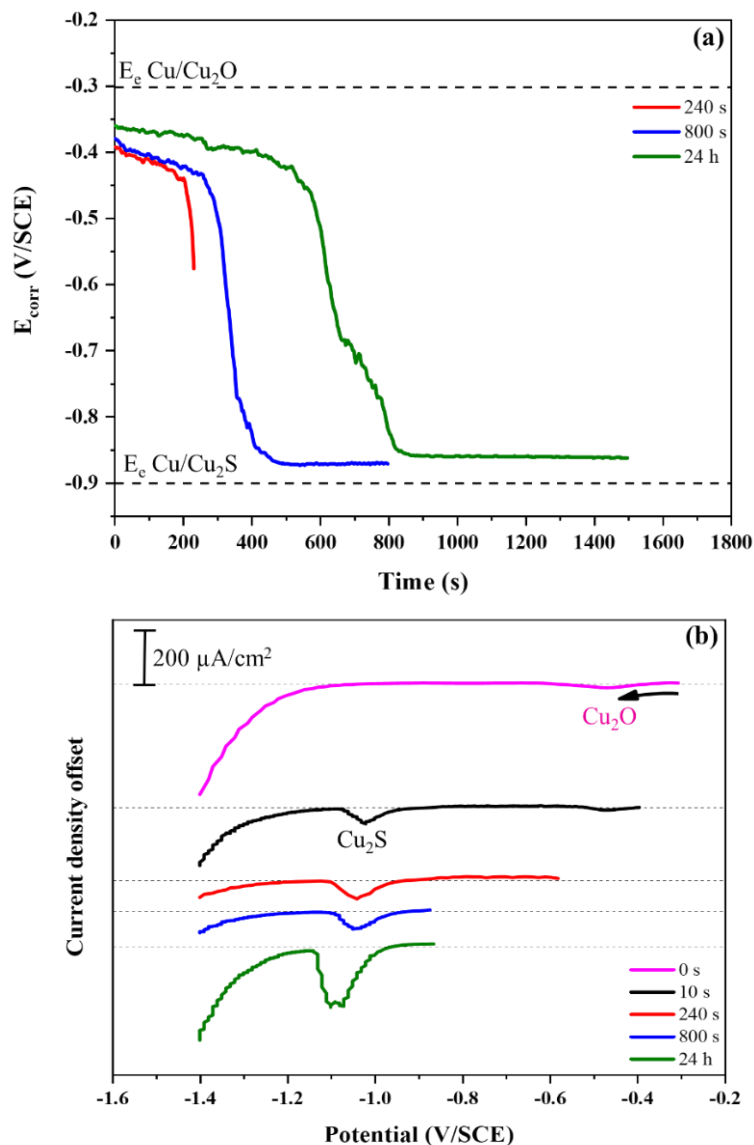


Figure 4.11: (a) E_{corr} recorded on Cu specimens oxidized at -0.3 V/SCE in 0.1 M NaOH after immersion in anaerobic solutions containing $0.1 \text{ M Cl}^- + 5 \times 10^{-5} \text{ M SH}^-$ (variations show the inherent irreproducibility of transition times and reproducibility of potentials) and (b) the respective CSVs, performed at a scan rate of 1 mV/s , after the surface was exposed to the bisulfide solution for different time periods, as indicated.

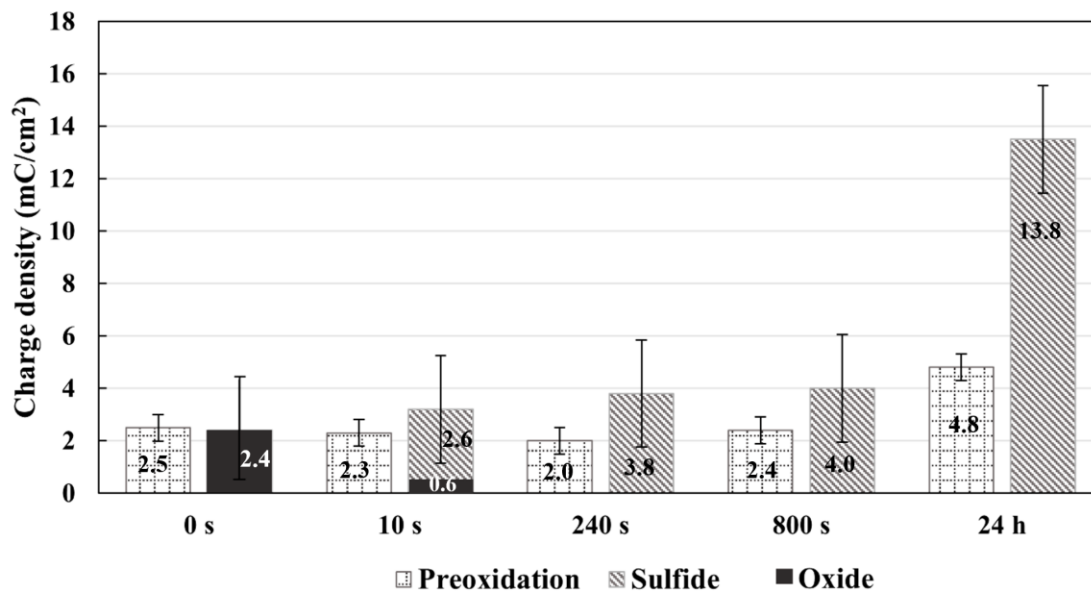


Figure 4.12: Anodic charge densities for specimens oxidized at -0.3 V/SCE in 0.1 M NaOH and the corresponding cathodic charges, with standard deviation, after immersion for different periods of time in a solution containing 0.1 M $\text{Cl}^- + 5 \times 10^{-5}$ M SH^- .

4.4 Conclusions

Our results show that the oxidation of copper in 0.1 M NaOH for 30 minutes under de-aerated conditions appears to result in the formation of a thin and uniform Cu_2O layer. On exposure to bisulfide, the oxide film is converted to Cu_2S at a rate dependent on bisulfide concentration and the conditions under which the experiment is conducted. Although Raman spectroscopy, SEM/EDX and CSV confirm that the oxide-to-sulfide reaction does occur, a layer of Cu_2O still exists adjacent to the Cu substrate.

4.5 References

- [1] F. King, L. Ahonen, C. Taxen, U. Vourinen, L. Werme, Copper corrosion under expected conditions in a deep geologic repository, TR-01-23, SKB, 2001.
- [2] R. Wu, R. Sandström, L.Z. Jin, Creep crack growth in phosphorus alloyed oxygen free copper, *Materials and Science Engineering:A*, 583, 151-160, 201.
- [3] D.S. Hall, T.E. Standish, M. Behazin, P.G. Keech, Corrosion of copper-coated used nuclear fuel containers due to oxygen trapped in a Canadian deep geological repository, *Corrosion Engineering, Science and Technology*, 53, 309–315, 2018.
- [4] J.R. Scully, M. Edwards, Review of the NWMO copper corrosion allowance, TR-2013-04, NWMO, 2013.
- [5] J.M. Smith, Z. Qin, F. King, L. Werme, D.W. Shoesmith, Sulfide film formation on copper under electrochemical and natural corrosion conditions, *Corrosion*, 63, 135–144, 2007.
- [6] J. Chen, Z. Qin, D.W. Shoesmith, Kinetics of corrosion film growth on copper in neutral chloride solutions containing small concentrations of sulfide, *Journal of the Electrochemical Society*, 157, 338–345, 2010.
- [7] J. Chen, Z. Qin, D.W. Shoesmith, Rate controlling reactions for copper corrosion in anaerobic aqueous sulphide solutions, *Corrosion Engineering, Science and Technology*, 46, 138–141, 2011.
- [8] F. King, A review of the properties of pyrite and the implications for corrosion of the copper canister, TR-13-19, SKB, 2013.
- [9] L. Duro, V. Montoya, E. Colàs, D. García, Groundwater equilibration and radionuclide solubility calculations, TR-2010-02, NWMO, 2010.

- [10] F. King, C. Lilja, K. Pedersen, P. Pitkänen, M. Vähänen, An update of the state-of-the-art report on the corrosion of copper under expected conditions in a deep geologic repository, TR-10-67, SKB, 2010.
- [11] J.M. Smith, Z. Qin, J.C. Wren, and D.W. Shoesmith, The influence of preoxidation on the corrosion of copper nuclear waste canisters in aqueous anoxic sulphide solutions, Materials Research Society symposia proceedings, 985, 2007.
- [12] T.E. Standish, D. Zagidulin, S. Ramamurthy, P.G. Keech, J.J. Noël, D.W. Shoesmith, Galvanic corrosion of copper-coated carbon steel for used nuclear fuel containers, Corrosion Engineering, Science and Technology, 52, 65-69, 2017.
- [13] M.A. Abdulhay, A. Al-Suhybani, Open circuit potential for copper electrode in 1 M NaCl solutions, Materialwissenschaft Und Werkstofftechnik, 23, 407-412, 1992.
- [14] M. Shirkhazadeh, G.E. Thompson, V. Ashworth, A study of the initial stages in oxidation of copper in alkaline solutions, Corrosion Science, 31, 293-298, 1990.
- [15] H.H. Strehblow, V. Maurice, P. Marcus, Initial and later stages of anodic oxide formation on Cu, chemical aspects, structure and electronic properties, Electrochimica Acta, 46, 3755-3766, 2001.
- [16] V. Maurice, P. Marcus, Current developments of nanoscale insight into corrosion protection by passive oxide films, Current Opinion in Solid State and Materials Science, 22, 156-167, 2018.
- [17] H. Chen, V. Maurice, L.H. Klein, L. Lapeire, K. Verbeken, H. Terryn, P. Marcus, Grain boundary passivation studied by in situ scanning tunneling microscopy on microcrystalline copper. Journal of Solid-State Electrochemistry, 19, 3501-3509, 2015.
- [18] D.W. Shoesmith, S. Sunder, M.G. Bailey, G.J. Wallace, F.W. Stanchell, Anodic oxidation of copper in alkaline solutions Part IV. Nature of the passivating film, Journal of Electroanalytical Chemistry and Interfacial Electrochemistry, 143, 153-165, 1983.

- [19] S.M. Abd El Haleem, B.G. Ateya, Cyclic voltammetry of copper in sodium hydroxide solutions, *Journal of Electroanalytical Chemistry*, 117, 309-319, 1981.
- [20] D.A. Palmer, Solubility measurements of crystalline Cu_2O in aqueous solution as a function of temperature and pH, *Journal of Solution Chemistry*, 40, 1067-1093, 2011.
- [21] H.Y. H. Chan, C.G. Takoudis, M.J. Weaver, Oxide film formation and oxygen adsorption on copper in aqueous media as probed by surface-enhanced Raman spectroscopy, *Journal of Physical Chemistry B*, 103, 357-365, 1999.
- [22] M. Guo, J. Chen, T. Martino, M. Biesinger, J.J. Noel, D.W. Shoesmith, The susceptibility of copper to pitting corrosion in borate-buffered aqueous solutions containing chloride and sulfide, *Journal of the Electrochemical Society*, 166, C550- C558, 2019.
- [23] T. Martino, R. Partovi-Nia, J. Chen, Z. Qin, D.W. Shoesmith, Mechanisms of film growth on copper in aqueous solutions containing sulphide and chloride under voltammetric conditions, *Electrochimica Acta*, 127, 439-447, 2014.
- [24] J. Chen, Z. Qin, D.W. Shoesmith, Long-term corrosion of copper in a dilute anaerobic sulfide solution, *Electrochimica Acta*, 56, 7854-7861, 2011.

5 Investigating the Electrochemical Behaviour and Surface Properties of the Electrochemically-grown Mixed Oxide in an Aqueous Bisulfide Solution

5.1 Introduction

The repository environment is anticipated to evolve from early warm and oxic conditions to later cold and anoxic conditions [1]. Likewise, degradation processes of the UFCs should transition from the initial oxygen-driven processes to those governed by the availability of bisulfide as oxidant. The timeframe over which the redox condition evolution will occur in the DGR is uncertain, and varying estimates have been given [2]. Recent field studies propose that the consumption of the O₂, trapped upon sealing of the DGR may conclude within the initial 10 to 100 years after container emplacement [3]. In contrast, the temperature evolution, influenced by container and DGR design, is more predictable. It is expected to transition from a high of 80 °C to 90 °C in the initial 100–200 years of emplacement to approximately 15 °C after several thousand years [4]. This transition may involve the conversion of (hydr)oxide-type corrosion products, accumulated during the oxic phase, to copper sulfide compounds [5].

Presently available information indicates that the maximum depth of container corrosion due to O₂ consumption will be limited to 298 μm, as calculated using mass balance, conservatively assuming all the trapped oxygen to be consumed in UFC corrosion and the corrosion product to be Cu₂O only [5]. Additionally, oxidants produced by H₂O radiolysis could result in a further 10–30 μm penetration of the Cu coating [6,7]. Chapter 4 focused on the influence of a single-layer Cu₂O deposit on subsequent bisulfide-induced corrosion. However, the research recognizes the importance of investigating the impact of mixed hydr(oxides) on the conversion process. This consideration arises from the fact that entrained O₂ could be also consumed in the oxidation of Cu (I) to Cu (II), leading to the formation of a multi-layer corrosion product consisting of Cu₂O/CuO/Cu(OH)₂. Numerous studies on Cu corrosion under gamma radiation, aiming to simulate radiation-induced

corrosion (RIC), have revealed that corrosion products formed on the Cu surface are a combination of Cu (I) oxide and Cu (II) hydr(oxide) [8-12].

The main objective of this chapter is:

To investigate the influence of electrochemically-grown dual-layer oxide ($\text{Cu}_2\text{O}/\text{CuO}$ and possibly $\text{Cu}(\text{OH})_2$) in alkaline solution on the bisulfide-induced corrosion of copper. This was done by measuring the corrosion potential, followed by cathodic stripping voltammetry to evaluate the extent to which the conversion processes take place after different immersion periods, and analyzing the surface corrosion products (films) to determine the film properties and the morphology of the corrosion damage using Raman spectroscopy, scanning electron microscopy (SEM) and energy dispersive X-ray (EDX) analyses.

5.2 Experimental

5.2.1 Specimen preparation

The working electrode used in this series of experiments was O-free, P-doped copper provided by SKB. For electrode preparation, see section 3.1.

5.2.2 Solution preparation

To form copper oxides and/or hydroxide, the solution was prepared according to section 3.2.1.1. The grown (hydr)oxides were then exposed to bisulfide solutions with a total $[\text{SH}^-]$ of 5×10^{-5} M, prepared as explained in section 3.3.1. All bisulfide solutions contained 0.1 M NaCl (assay $\geq 99.0\%$, Fisher chemical) as a supporting electrolyte.

5.2.3 Electrochemical cell design and instrumentation

All the details about the electrochemical cell design and instrumentation can be found in section 3.2.1.2.

5.2.4 Electrochemical/corrosion experiments

All experiments were conducted inside a Faraday cage to decrease electrical noise from external sources. Prior to each experiment, the solutions were sparged with a stream of

ultra-high purity Ar gas for 30 minutes, with sparging continued throughout the experiment. The Cu electrodes were cathodically cleaned at -850 mV/SCE for 3 minutes prior to each experiment.

5.2.4.1 Cyclic voltammetry

Voltammetric experiments were conducted to study the processes involved in the formation of copper (hydr)oxide. The potential was scanned from -1.3 to 0.5 V/SCE at a scan rate of 1 mV/s under de-aerated conditions to identify the appropriate potentials to be used in film growth experiments.

5.2.4.2 Potentiostatic polarization

Freshly prepared Cu specimens after surface treatment were oxidized at -0.22 V/SCE in 0.1 M NaOH for 30 minutes under de-aerated conditions to form oxides with favourable compositions. When used in subsequent experiments involving exposure to SH^- -containing solutions, these specimens are described as oxidized.

5.2.4.3 Corrosion potential measurements

Corrosion potentials (E_{corr}) were monitored on oxidized specimens after transfer to a second electrochemical cell containing SH^- solution, to investigate the effect of SH^- on the preformed oxide films.

5.2.4.4 Cathodic stripping voltammetry

After E_{corr} measurements of various durations in SH^- solutions, the potential was scanned from the final value of E_{corr} to -1.4 V/SCE at a scan rate of 1 mV/s to cathodically reduce oxide and sulfide films present on the electrode surface. From the potentials at which cathodic peaks appeared and the measured charges associated with them, the nature and amounts of the oxide and sulfide phases present were determined.

5.2.5 Surface analyses

5.2.5.1 Laser Raman spectroscopy

The phases present on the oxidized Cu specimens before and after exposure to SH^- solutions were analyzed by laser Raman spectroscopy. All Raman spectra reported in this thesis include the raw data only.

5.2.5.2 Scanning electron microscopy

Surface imaging was performed using a field emission SEM equipped with energy-dispersive X-ray spectroscopy (EDX). EDX was carried out to elucidate the elemental composition of the surface. A FIB/SEM was used to section specimens in order to obtain cross-sectional images of their surface films.

5.3 Results and Discussion

5.3.1 Voltammetric behaviour of Cu in de-aerated 0.1 M NaOH solution

As shown in **Chapter 4**, a cyclic voltammogram was recorded on Cu in an Ar-sparged solution (pH 12.9), **Figure 4.2 (c)** to determine the conditions required to grow different types of copper oxide.

Based on this voltammetric evidence, one would expect that applying a film growth potential in region A would result in the formation of a thin single-phase Cu (I) oxide layer, while applying a potential in region B, would lead to the formation of a much thicker duplex layer of Cu (I) and Cu (II) oxides or Cu (II) hydroxide on the Cu surface.

5.3.2 Formation of a duplex Cu_2O – CuO ($\text{Cu}(\text{OH})_2$) film

The oxide film formed on a UFC emplaced in a DGR is expected to be a combination of Cu (I) and Cu (II) products. Thus, to study an oxide film more closely, simulating those that will grow under the expected DGR conditions, Cu specimens were anodically polarized for 30 min at a number of more oxidizing potentials than that used to grow a Cu_2O film and then cathodically stripped to determine the phases formed. **Figure 5.1** shows CSVs recorded after oxidation at different potentials.

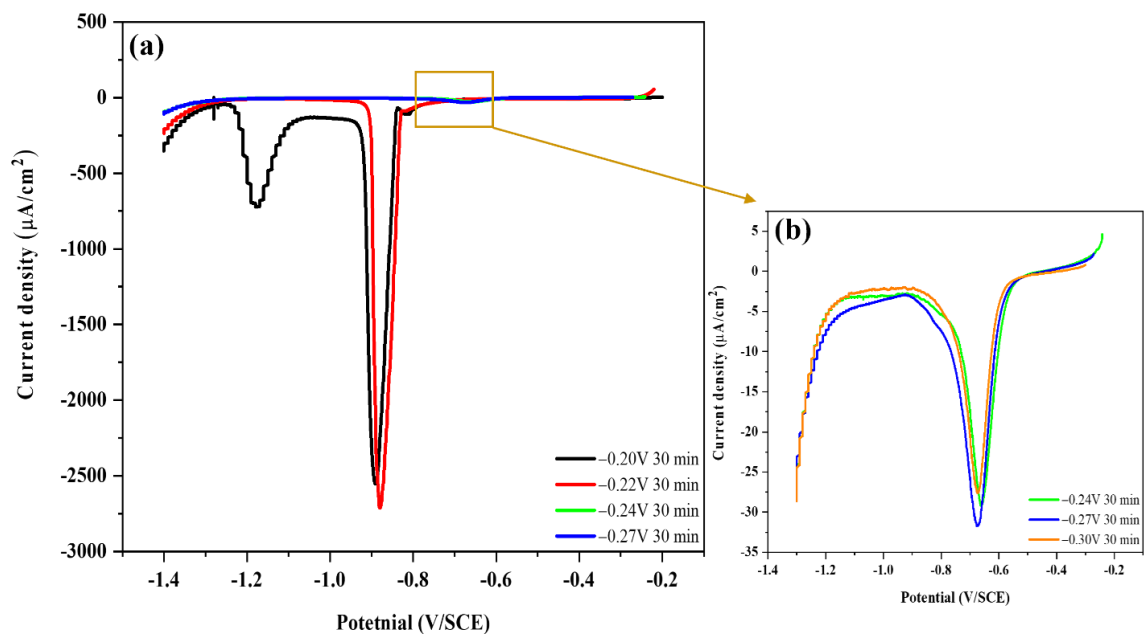


Figure 5.1: (a) Cathodic stripping voltammograms on Cu specimens after anodic polarization at different potentials in 0.1 M NaOH, (b) CSVs recorded after oxide growth at -0.24 , -0.27 and -0.3 V/SCE on an enhanced current density scale.

If the potential was set at either -0.3 V/SCE, -0.27 V/SCE or -0.24 V/SCE, only a single small reduction peak was observed, at ~ -0.67 V/SCE, **Figure 5.1 (b)**, consistent with the formation of a very thin layer of Cu_2O as observed in **Figure 4.9 (a)** and demonstrated in the Raman spectrum in **Figure 4.6 (a)**. Oxidation at -0.22 V/SCE led to an additional, much larger reduction peak at ~ -0.9 V/SCE, which suggests the presence of CuO , as indicated in the CV in **Figure 4.2 (c)** and proposed by Smith et al. [13]. After oxidation at -0.20 V/SCE, the observation of a third reduction peak at ~ -1.2 V/SCE indicates the formation of $\text{Cu}(\text{OH})_2$, based on **Figure 4.2 (c)** and the analysis of Smith et al. [13]. **Figure 5.1 (b)** shows a very small shoulder in the reduction current density in the potential region more negative than ~ -0.85 V/SCE, suggesting the onset of the formation of Cu (II) phases. This confirms the choice of -0.3 V/SCE as the most appropriate potential to form a single layer of Cu_2O .

The morphological properties of the multi-phase film formed at -0.22 V/SCE are shown in the SEM images of the surface and the cross-section in **Figure 5.2**.

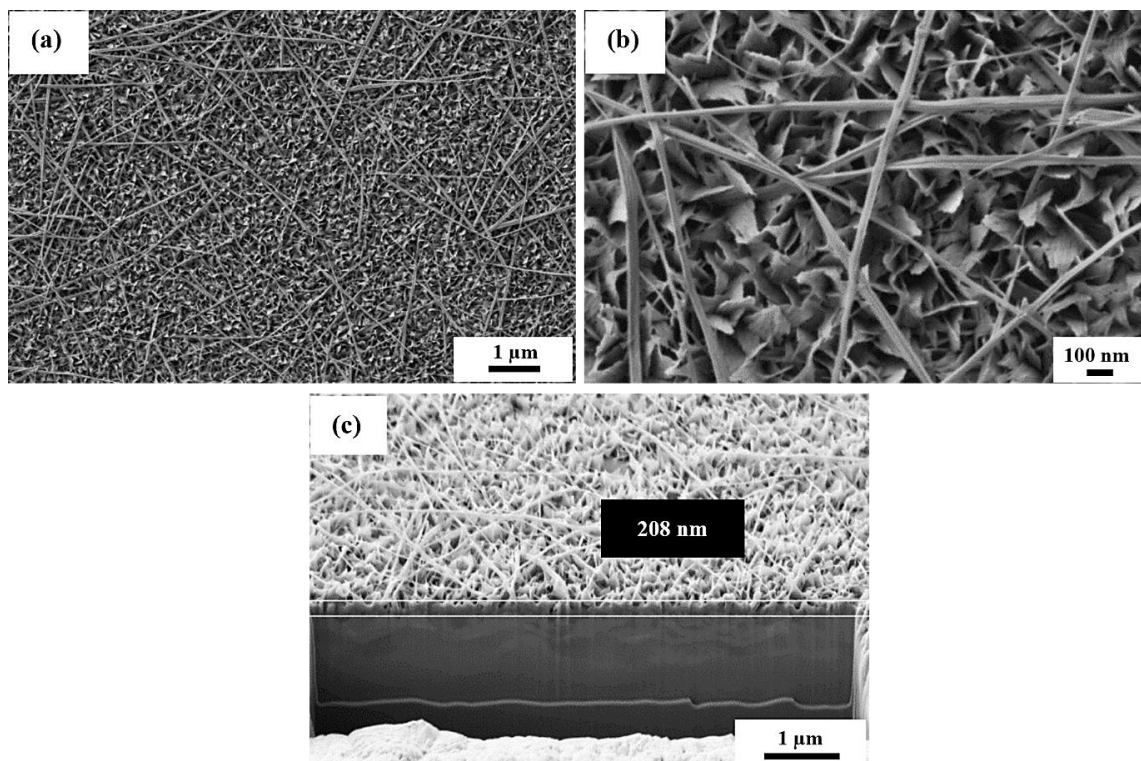


Figure 5.2: FE-SEM micrographs (a,b) showing the surface morphology of an oxide film anodically grown at -0.22 V/SCE in 0.1 M NaOH and (c) a FIB-cut cross-section of the film.

The surface images show a uniform coverage of 2-dimensional crystals with a sparse outer distribution of rod-like features. The cross-section shows a film thickness of ~ 208 nm, compared to the ~ 10 nm-thick layer of Cu_2O formed at -0.3 V/SCE. The Raman spectrum in **Figure 5.3** shows a series of peaks and shoulders indicating that the film was composed of a mixture of phases.

As shown in **Figure 4.6 (a)** and discussed in reference [14], Cu_2O yields peaks at 530 cm^{-1} and 623 cm^{-1} as well as a minor peak at 220 cm^{-1} . The dominance of the broad peak at $\sim 620\text{ cm}^{-1}$, compared to the shallow shoulder at $\sim 530\text{ cm}^{-1}$ and the sharp peak at 300 cm^{-1} followed by a small peak at 350 cm^{-1} , indicates the presence of CuO , which also exhibits a peak at $\sim 635\text{ cm}^{-1}$ [14,15]. Although not well defined, the shoulder in the region 400 to

550 cm^{-1} could contain a contribution from $\text{Cu}(\text{OH})_2$, which would yield a peak in the region 460-490 cm^{-1} [15].

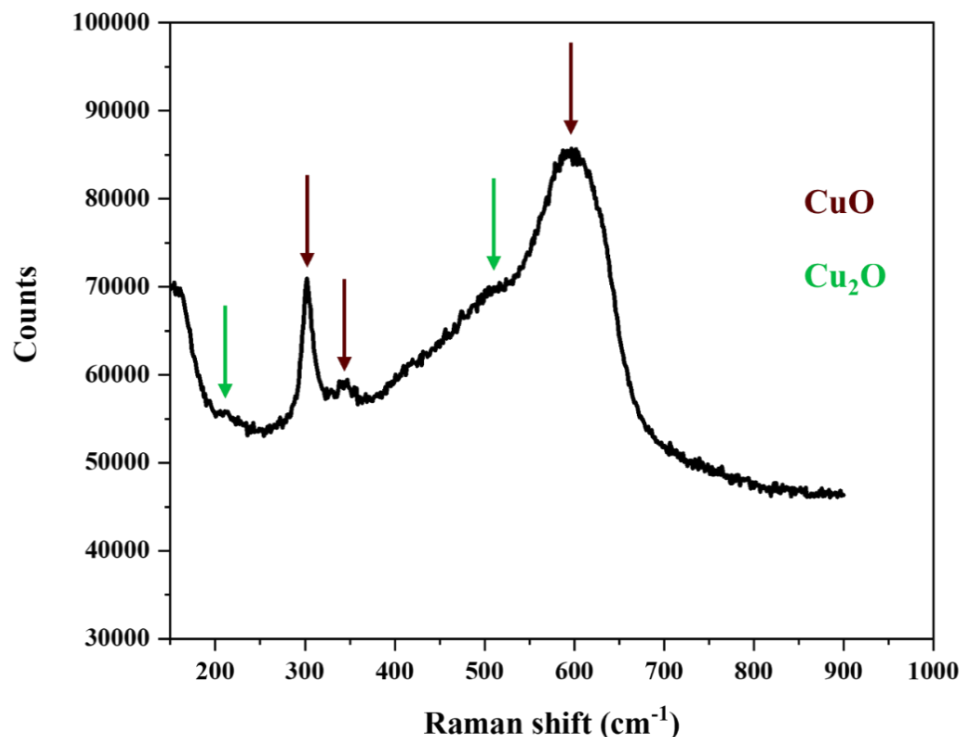


Figure 5.3: Raman spectrum recorded on a Cu specimen oxidized at -0.22 V/SCE in de-aerated 0.1 M NaOH.

It is feasible that such a weak signal could indicate that the disperse layer of rod-like crystals is $\text{Cu}(\text{OH})_2$ while the main body of the film is a mixture of Cu_2O and CuO . The size of the reduction peak at ~ -0.9 V/SCE in the CSV (**Figure 5.1 (a)**) suggests that CuO may be the dominant phase present, although it is also feasible that further formation of Cu_2O is promoted by reaction (5.1).



5.3.3 Conversion of $\text{Cu}_2\text{O}/\text{CuO}/\text{Cu}(\text{OH})_2$ to Cu_2S

The specimens oxidized in 0.1 M NaOH solution at -0.22 V/SCE were exposed to a 0.1 M $\text{Cl}^- + 5 \times 10^{-5}$ M SH^- solution for a series of exposure times. **Figure 5.4 (a)** shows E_{corr}

time plots for specimens exposed for 30 min and 24 h (only the first 300 min of exposure is shown here since there was no significant change over the subsequent exposure period), which exhibit a series of stages (A to D).

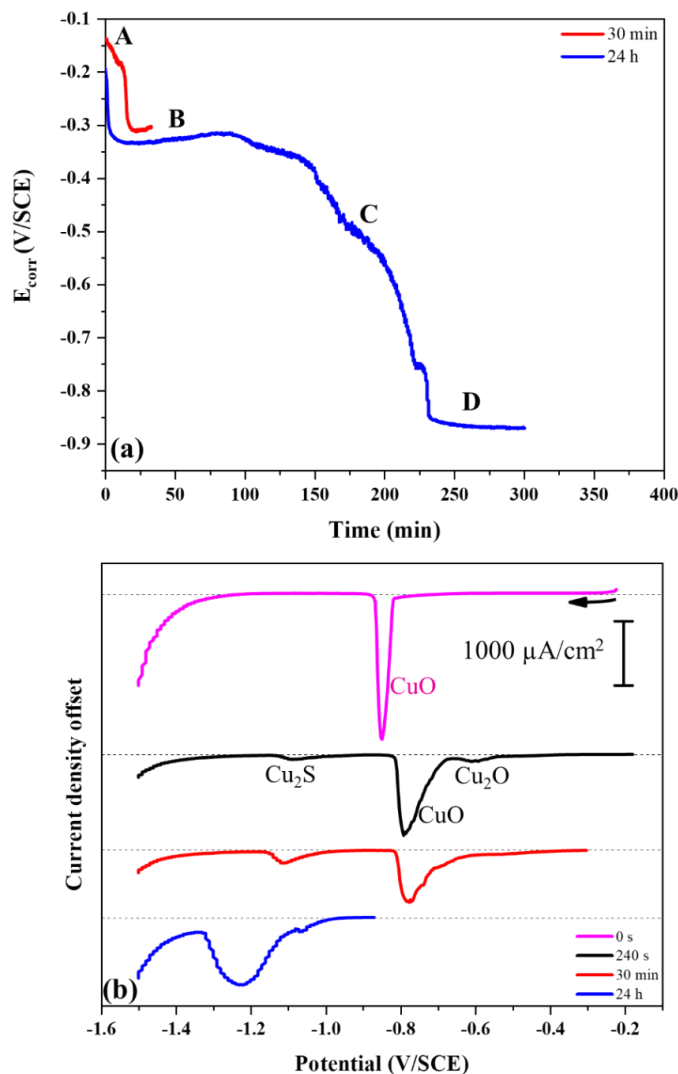


Figure 5.4: (a) E_{corr} recorded on Cu specimens oxidized at -0.22 V/SCE in 0.1 M NaOH after immersion in an anaerobic 0.1 M $\text{Cl}^- + 5 \times 10^{-5}$ M SH^- solution; and (b) the respective CVs performed at a scan rate of 1 mV/s after the surface was exposed to the bisulfide for different time periods, as indicated.

The initial E_{corr} in region A was 100 to 200 mV more positive than that registered when only a thin Cu_2O layer was present, **Figure 4.11 (a)**. Prior to SH^- addition, consistent with

the CSVs shown in **Figure 5.1**, a single peak attributable to the reduction of CuO and possibly Cu₂O was observed in the CSV. This high E_{corr} in region A suggests that the Cu₂O/CuO film formed at -0.22 V/SCE was initially more protective and/or more oxidized than that formed at -0.3 V/SCE. Although the time required varied from ~ 2 min to ~ 20 min, E_{corr} decreased to -0.35 V/SCE from -0.3 V/SCE, which was still ~ 100 mV more positive than observed after oxidation at the lower potential.

A CSV recorded when E_{corr} had first decreased into region B (after 4 min of exposure) shows that the reduction of the Cu₂O/CuO film occurred at a less negative potential, indicating a more reactive surface film. It is presently unclear what caused this shift in reduction potential, but it was likely due to a SH⁻-induced change in the state of the surface film, indicated by the transition in E_{corr} from region A to region B, which rendered it more readily reducible. It is also noticeable that the reduction peak in **Figure 5.4 (b)** is wider and less well-defined. The observation of a small reduction peak at -1.05 V/SCE confirms that the formation of Cu₂S commenced in region B. At longer times in region B (after 30 min) the CSV shows that the Cu₂O/CuO film became even easier to reduce, as the extent of Cu₂S formation increased, as indicated by the increase in the reduction peak current density at -1.12 V/SCE.

Once E_{corr} decreased into region D, a broad peak was observed in the CSV, confirming the presence of a significant amount of Cu₂S. This major broad reduction peak, preceded by a small shoulder, is characteristic for the reduction of a thin Cu₂S layer formed directly on the Cu surface, with a thicker layer of Cu₂S deposited on the outer oxide surface [16]. In the present series of experiments, no change in behaviour in region C was captured. Previously, the stabilization of E_{corr} in this potential region was attributed to SH⁻-induced porosity of the oxide film that enabled SH⁻ to penetrate to the Cu surface and initiate galvanic corrosion via the coupling of reactions (5.2) and (5.3) [13]. This claim remains to be confirmed.

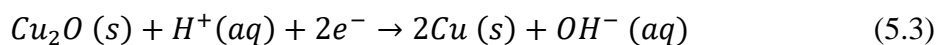
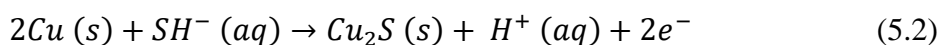


Figure 5.5 presents the anodic charges passed to create the oxide for each test run and the total amount of oxide and sulfide reduced during the CSV, expressed as charges obtained by integration of the reduction peaks in the CSVs.

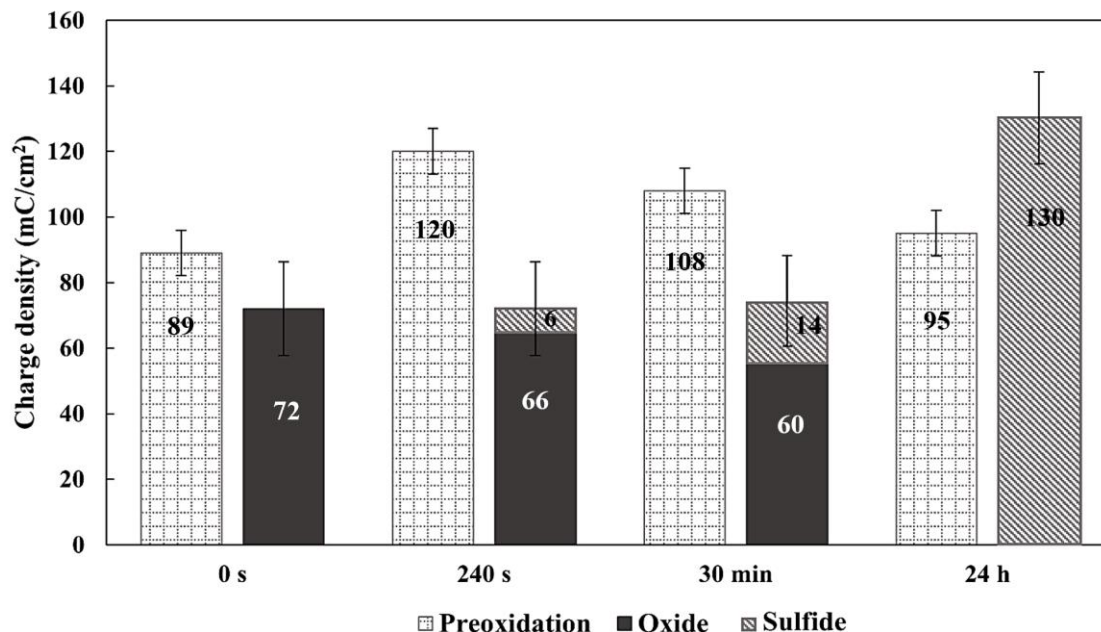


Figure 5.5: Anodic charge densities for specimens oxidized at -0.22 V/SCE in 0.1 M NaOH and the corresponding cathodic charges, with standard deviation, after immersion for different periods of time in a solution containing 0.1 M $\text{Cl}^- + 5 \times 10^{-5}$ M SH^- .

The blank experiment was repeated under different conditions to determine the reason for the decrease in the cathodic charge compared to the corresponding anodic charge. Obtained results show that the 20% decrease in the total cathodic charge vs. the anodic charge for the blank specimen could be attributed to the presence of oxide/hydroxide species on the surface that could not be reduced in the CSV; the effect of rinsing with Type-I water was not noticeable here. Despite the differing amounts of anodic charge for sulfidized grown oxides at 240 s and 30 min, the same amount of cathodic charge (sum total of oxide and sulfide reduction) was measured from CSVs. It could be expected that oxidation produced a reproducible base layer of Cu_2O and CuO with most of the anodic charge beyond that level going to the growth of irreducible species on the surface, which likely includes poorly connected $\text{Cu}(\text{OH})_2$ species. The total amount of reducible Cu_2S after 24 h of immersion

can be determined in the CSV, but whether or not there was any residual oxide on the surface cannot, since the poor electrical connection between residual oxide/hydroxide and Cu substrate prevents it from being measured by CSV. Therefore, other complementary techniques are required to prove the presence of residual oxide on the surface.

Over the first 30-min period, the sum total reduction charge for oxide and sulfide did not change significantly, suggesting that only oxide-to-sulfide conversion was occurring. However, over the much longer exposure period of 24 h, during which E_{corr} was in region D for the large majority of the exposure period, the charge for Cu_2S reduction was almost 1.5 times higher than that for creating the original oxide (considering 20% decrease in the cathodic charge for irreducible species), which is evidence that substantial oxidation of the Cu substrate, reaction 5.2, had occurred, in addition to oxide-to-sulfide conversion, reactions (5.2)-(5.4).

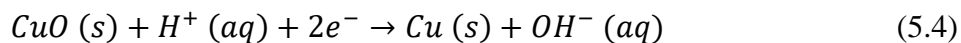


Figure 5.6 shows SEM micrographs of the surface and the cross-section of a specimen exposed to a $0.1 \text{ M Cl}^- + 5 \times 10^{-5} \text{ M SH}^-$ solution for 45 min (region B in **Figure 5.4 (a)**), and **Figure 5.7** shows the corresponding EDX maps for Cu, O and S.

The crystalline nanowires formed during the oxidation (and thought to be $\text{Cu}(\text{OH})_2$, **Figure 5.2**) appear to have remained mostly unconverted, as does the majority of the underlying $\text{Cu}_2\text{O}/\text{CuO}$ layer. The film thickness remained in the 100 to 300 nm range, as observed for the formed oxide film (**Figure 5.2**), confirming that no substantial additional Cu_2S formation had occurred.

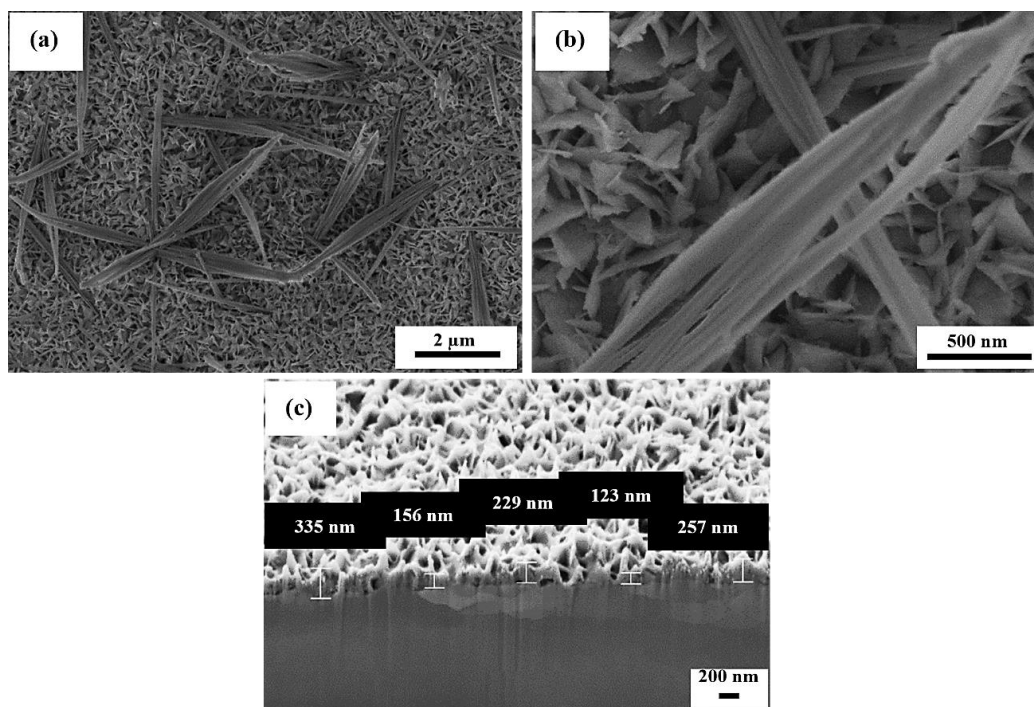


Figure 5.6: SEM micrographs (a,b) showing the surface morphology of an oxide film grown at -0.22 V/SCE in 0.1 M NaOH after 45 min exposure (stage B in E_{corr} plot vs. time, **Figure 5.4 (a)**) to a solution containing 0.1 M Cl^- + 5×10^{-5} M SH^- : (c) a FIB-cut cross-section of the film.

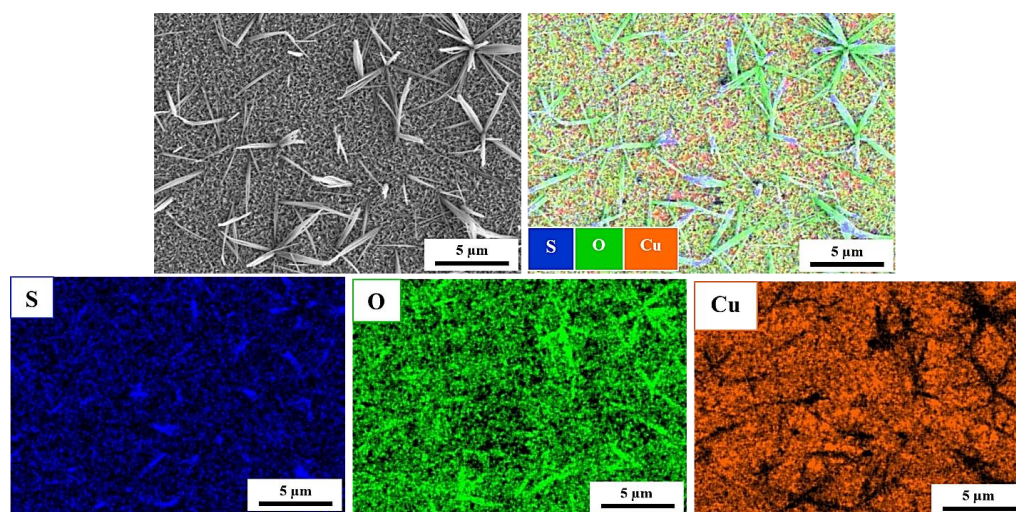


Figure 5.7: SEM micrograph and respective EDX maps of an oxide film grown at -0.22 V/SCE in 0.1 M NaOH after 45 min exposure (stage B in E_{corr} plot vs. time, **Figure 5.4 (a)**) to a solution containing 0.1 M Cl^- + 5×10^{-5} M SH^- .

The EDX map for S, **Figure 5.7**, shows that the base layer of oxide experienced some apparently localized conversion to Cu_2S , consistent with the observation of only a small reduction peak at -1.0 V/SCE in the CSV after exposure in region B over such a period. It is also possible that the scattered locations exhibiting strong sulfur (S) EDX signals are associated with the locations of nanowires, which may indicate that their original growth during oxidation occurred at more porous locations in the surface $\text{Cu}_2\text{O}/\text{CuO}$ layer. This would have allowed SH^- access to the Cu surface, leading to the direct formation of Cu_2S by reaction with Cu. That minimal conversion of oxide to sulfide occurred is confirmed by the elemental atomic percentages listed in **Table 5.1**, with the approximately equal Cu and O percentages consistent with the dominant presence of CuO .

Table 5.1: Atomic percentage of different elements corresponding to **Figure 5.7**

Element	Composition [at. %]
Oxygen	47.1
Sulfur	0.8
Copper	52.1

Figure 5.8 and **Figure 5.9** show a similar set of SEM images of the surface and cross section of a specimen exposed to the SH^- solution for 24 h; i.e., well into region D (as defined in **Figure 5.4 (a)**).

The surface and cross-sectional images show a widely dispersed deposit with an irregular morphology on top of a base layer which was thicker and more porous than that present on the oxidized surface prior to exposure to the SH^- solution. The EDX maps suggest a significantly higher amount of S than observed after the short exposure, with the atomic percentages, **Table 5.2**, confirming this was the case. The high atomic percentage of Cu is consistent with the presence of Cu_2S , with the significant O percentage confirming that oxide-to-sulfide conversion was incomplete.

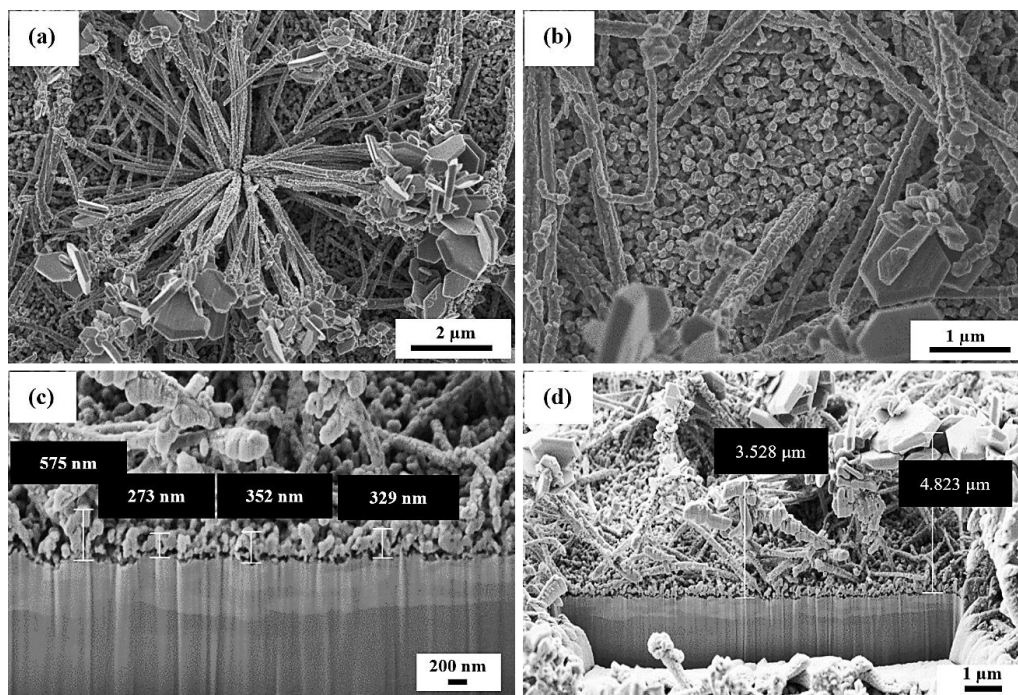


Figure 5.8: FE-SEM micrographs (a,b) showing the surface morphology of an oxide grown at -0.22 V/SCE in 0.1 M NaOH after 24 h exposure (stage D in E_{corr} plot vs. time, **Figure 5.4 (a)**) to solution containing 0.1 M $\text{Cl}^- + 5 \times 10^{-5}$ M SH^- and (c,d) a FIB-cut cross-section of the film.

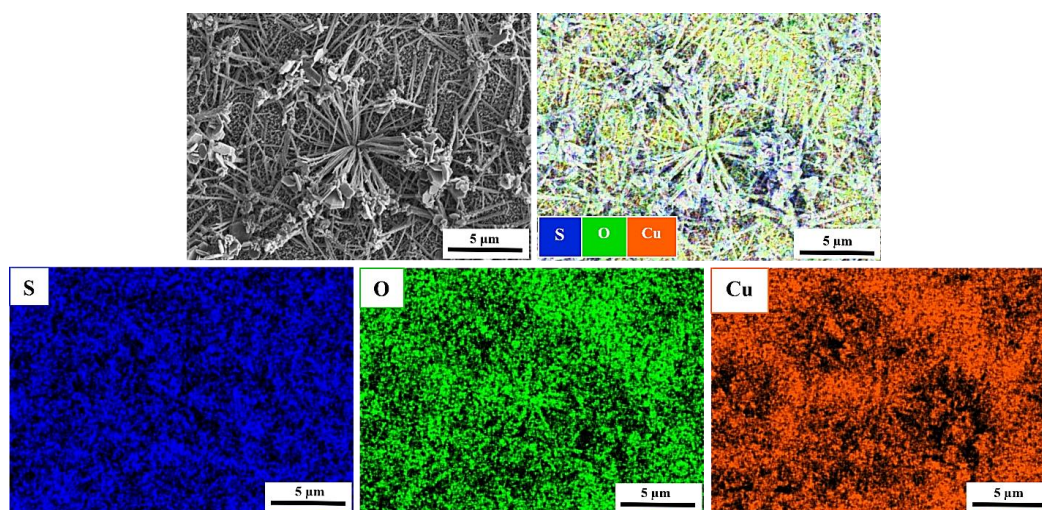


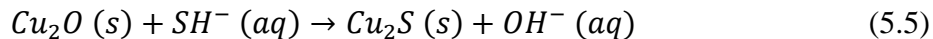
Figure 5.9: FE-SEM micrograph and respective EDX maps of an oxide grown at -0.22 V/SCE in 0.1 M NaOH after long-term exposure (stage D in E_{corr} plot vs. time, **Figure 5.4 (a)**) to solution containing 0.1 M $\text{Cl}^- + 5 \times 10^{-5}$ M SH^- .

Table 5.1: Atomic percentage of different elements corresponding to **Figure 5.9**

Element	Composition [at. %]
Oxygen	10.0
Sulfur	20.2
Copper	69.8

Inspection of the SEM images, **Figure 5.8** and **Figure 5.9**, shows that the majority of nanowire structures (thought to be $\text{Cu}(\text{OH})_2$) remained unconverted, although the presence of hexagonal crystals (indication of sulfide crystals by EDS analysis in **Figure 5.9**) at the tips of such structures suggest conversion may have been underway at locations where the $[\text{SH}^-]$ was not depleted by reaction with the $\text{Cu}_2\text{O}/\text{CuO}$ sublayer and with the Cu substrate. Given that Cu_2S at these locations, like the irreducible oxide species, would have been in poor electrical contact with the Cu surface, it is likely they were not detected in CSV experiments. This would lead to an underestimation of the amount of Cu_2S present on the surface. Comparison of the Raman spectra recorded on a oxidized specimen and on specimens exposed for either a short period (45 min; region B in **Figure 5.4 (a)**) or a long period (24 h; region D in **Figure 5.4 (a)**), **Figure 5.10**, confirms that extensive conversion of the $\text{Cu}_2\text{O}/\text{CuO}$ surface layer occurred. Since Raman scattering is relatively insensitive to $\text{Cu}(\text{OH})_2$, its remaining presence in the nanowire structures could not be confirmed.

The data presented demonstrate that when only a thin layer of Cu_2O was present on the Cu surface, its conversion to Cu_2S occurred rapidly, a process that could be attributed to either the chemical conversion reaction (5.5), as previously claimed by Smith et al. [13], or the electrochemical reaction, facilitated by a thin, conductive oxide layer.



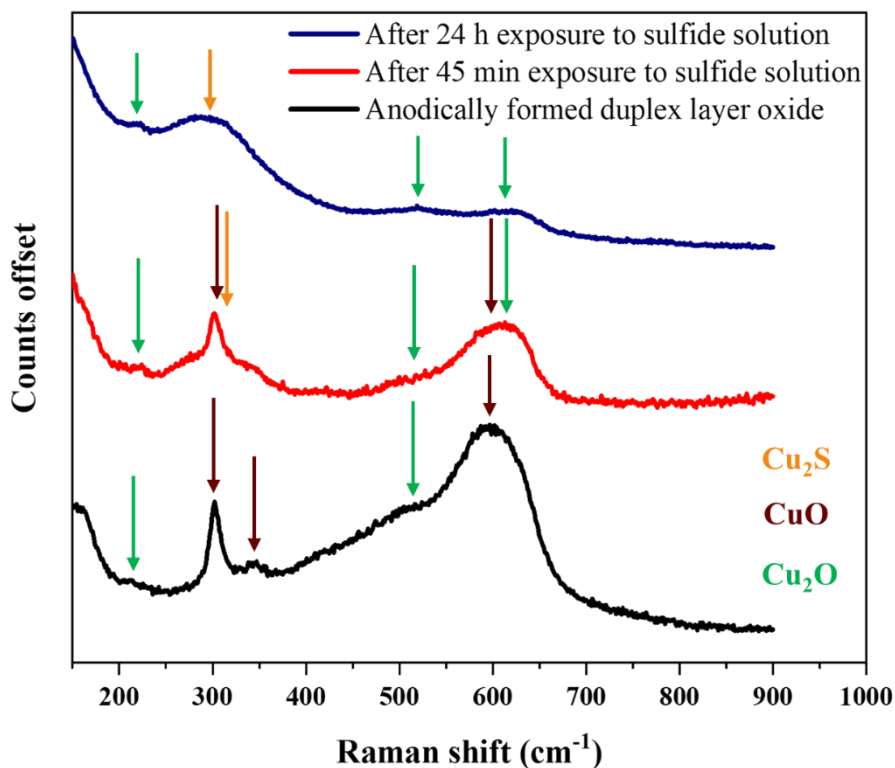
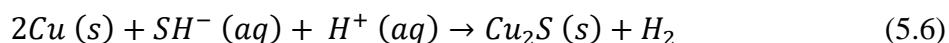


Figure 5.10: Raman spectra recorded on a Cu surface that was oxidized at -0.22 V/SCE in 0.1 M NaOH before and after exposure to a solution containing 0.1 M $\text{Cl}^- + 5 \times 10^{-5}$ M SH^- for different periods.

However, when a mixed oxide/hydroxide ($\text{Cu}_2\text{O}/\text{CuO}/\text{Cu}(\text{OH})_2$) layer was present, complete conversion to Cu_2S was not achieved after 24 h of exposure to a solution containing 5×10^{-5} M SH^- . Initially, while the potential was in region A (**Figure 5.4 (a)**), oxide-to-sulfide conversion, probably mostly Cu_2O to Cu_2S in the base layer, proceeded relatively easily. The penetration of SH^- to the Cu surface at a later stage could have initiated the galvanic coupling of CuO reduction (reactions (5.3) and (5.4) or reaction (5.1)) to Cu oxidation and Cu_2S formation (reactions (5.2), (5.5), and (5.6)).



When the E_{corr} was in region B, where it stayed for an extended period, it is possible that a galvanic process, required to convert Cu^{II} (in CuO) to Cu^{I} in Cu_2S , was accompanied by the chemical conversion of Cu_2O to Cu_2S (reaction (5.5)). Eventually, this combination of

conversion processes could lead to the more extensive conversion of the $\text{Cu}_2\text{O}/\text{CuO}$ layer to Cu_2S and consequently the exposure of a larger surface area of the Cu substrate. This would have further accelerated the galvanic process, possibly accounting for the slight arrest in E_{corr} in region C (**Figure 5.4 (a)**) and allowed the corrosion of the Cu substrate to Cu_2S via reaction 5.6. Whether or not the comproportionation reaction (reaction 5.1) was involved in the conversion of Cu (II) to Cu (I) remains unresolved.

Finally, the disperse outer layer of nanowires, which are assumed to be composed of $\text{Cu}(\text{OH})_2$, appears to have remained predominantly unconverted. This may reflect the possibility that this deposit was in poor electrical contact with the sublayers of $\text{Cu}_2\text{O}/\text{CuO}/\text{Cu}_2\text{S}$ and the Cu substrate, which would have inhibited the electron transfer process required to convert the Cu (II) to Cu (I). The accumulation of hexagonal crystals at the tips of the nanowires suggests some conversion may have occurred. However, the formation of these crystals could be more plausibly attributed to the deposition of $\text{Cu}(\text{SH})_2^-$ and Cu_3S_3 species known to be released from a Cu surface corroding in a SH^- solution [17]. **Figure 5.11** shows an attempt to schematically illustrate the various stages of the overall conversion process.

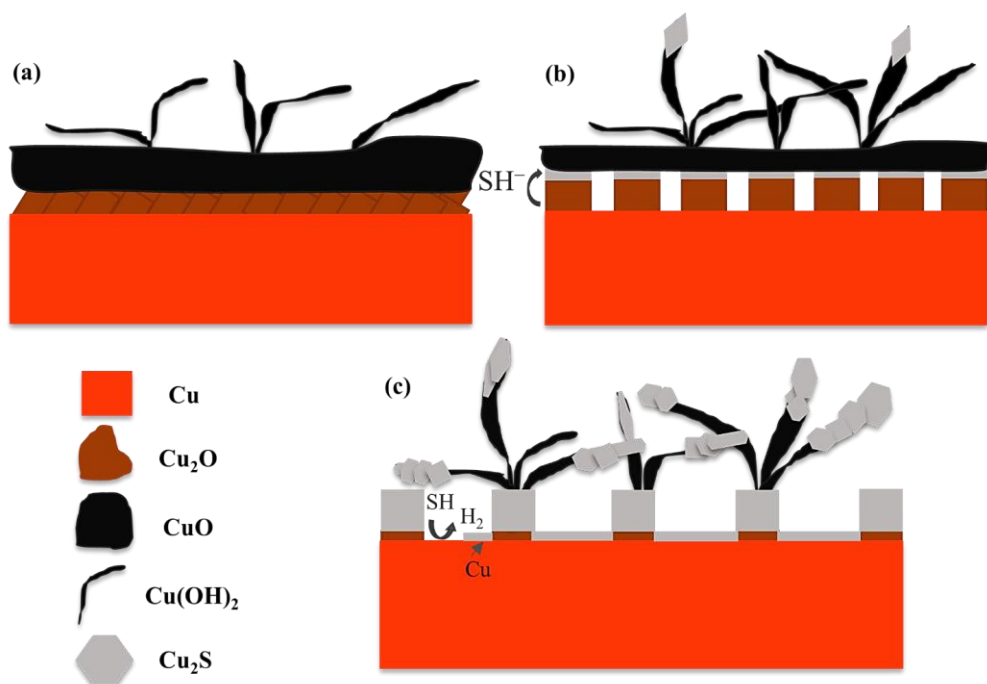


Figure 5.11: Schematic illustration of the stages of conversion of a Cu₂O/CuO/Cu(OH)₂ film on a Cu surface to Cu₂S in a chloride solution containing 5×10^{-5} M SH⁻: (a) the Cu₂O/CuO/Cu(OH)₂ layer before exposure to the SH⁻ solution; (b) the partially converted film after a short exposure period with E_{corr} in region B (**Figure 5.4 (a)**); (c) the film after an extended period of exposure to the SH⁻ solution with E_{corr} in region D (**Figure 5.4 (a)**).

5.4 Conclusions

Cu specimens were oxidized electrochemically. Subsequently, the conversion of the resulting oxide/hydroxide films to chalcocite (Cu₂S) in a chloride solution containing bisulfide was monitored through the measurement of E_{corr} and CSV. Thin Cu₂O films exhibited rapid conversion to Cu₂S, via the electrochemical pathways in the presence of SH⁻ ions. This underscores the importance of the structure and the thickness of Cu₂O in determining the efficiency of the conversion process. The conversion of thicker duplex films composed of Cu₂O, CuO, and presumably Cu(OH)₂, was notably slower and incomplete over the longest exposure period of 24 h. This conversion process entailed a combination of chemical conversion (Cu₂O to Cu₂S) and a galvanic process involving oxide reduction (CuO to Cu (I)) coupled to Cu oxidation (Cu to Cu₂S). Remarkably, the

small amounts of $\text{Cu}(\text{OH})_2$ present did not undergo conversion to Cu_2S within the 24 h timeframe. As these conversion processes led to an increasing exposure of the underlying Cu substrate, the corrosion process eventually became dominated by the direct oxidation of Cu to Cu_2S .

5.5 References

- [1] T. Standish, J. Chen, R. Jacklin, P. Jakupi, S. Ramamurthy, D. Zagidulin, P. Keech, D.W. Shoosmith, Corrosion of copper-coated steel high level nuclear waste containers under permanent disposal conditions, *Electrochimica Acta*, 211, 331–342, 2016.
- [2] F. King, D.S. Hall, P.G. Keech, Nature of the near-field environment in a deep geological repository and the implications for the corrosion behaviour of the container, *Corrosion Engineering, Science and Technology*, 52, 25–30, 2017.
- [3] H. Müller, B. Garitte, T. Vogt, S. Köhler, T. Sakaki, H. Weber, T. Spillmann, M. Hertrich, J. Becker, N. Giroud, V. Cloet, N. Diomidis, T. Vietor, Implementation of the full-scale emplacement (FE) experiment at the Mont Terri rock laboratory, *Swiss Journal of Geosciences*, 110, 287–306, 2017.
- [4] A. Hedin, J. Johansson, C. Lilja, P. Sellin, B. Kalinowski, M. Björck, I. Puigdomenech, F. King, Supplementary information on canister integrity issues, TR-19-15, SKB, 2019.
- [5] D.S. Hall, M. Behazin, W.J. Binns, P.G. Keech, An evaluation of corrosion processes affecting copper-coated nuclear waste containers in a deep geological repository, *Progress in Materials Science*, 118, 100766, 2021.
- [6] D.S. Hall, T.E. Standish, M. Behazin, P.G. Keech, Corrosion of copper-coated used nuclear fuel containers due to oxygen trapped in a Canadian deep geological repository, *Corrosion Engineering, Science and Technology*, 53, 309-315, 2018.
- [7] F. King, M. Behazin, A review of the effect of irradiation on the corrosion of copper-coated used fuel containers *Corrosion and Materials Degradation*, 2, 678-707, 2021.
- [8] K. Bessho, Y. Oki, N. Akimune, H. Matsumura, K. Masumoto, S. Sekimoto, N. Osada, N. Kinoshita, H. Monjushiro, S. Shibata, Corrosion of copper in water and colloid formation under intense radiation field, *Journal of Radioanalytical and Nuclear Chemistry*, 303, 1117-1121, 2015.

- [9] Jean, Arielle M., "Evolution of Cu₂O morphology during copper corrosion in the presence of gamma-radiation" M.Sc., The University of Western Ontario, Electronic Thesis and Dissertation Repository, 4593, 2017.
- [10] J. Khatouri, M. Mostafavi, J. Amblard, J. Belloni, Radiation-induced copper aggregates and oligomers, *Chemical Physics Letters*, 191, 351-356, 1992.
- [11] A. Björkbacka, H. Saman, C. Leygraf, M. Jonsson, Radiation induced corrosion of copper in anoxic aqueous solution, *Electrochemical and Solid-State Letters*, 15, C5-C7, 2012.
- [12] A. Björkbacka, C.M. Johnson, C. Leygraf, M. Jonsson, Role of the oxide layer in radiation-induced corrosion of copper in anoxic water. *The Journal of Physical Chemistry C*, 120, 11450-11455, 2016.
- [13] J.M. Smith, J.C. Wren, M. Odziemkowski, D.W. Shoesmith, The electrochemical response of preoxidized copper in aqueous sulfide solutions, *Journal of the Electrochemical Society*, 154, C431, 2007.
- [14] G. Niaura, Surface-enhanced Raman spectroscopic observation of two kinds of adsorbed OH⁻ ions at copper electrode, *Electrochimica Acta*, 45, 3507-3519, 2000.
- [15] J.C. Hamilton, J.C. Farmer, R.J. Anderson, In situ Raman spectroscopy of anodic films formed on copper and silver in sodium hydroxide solution, *Journal of the Electrochemical Society*, 133, 739-745, 1986.
- [16] T. Martino, R. Partovi-Nia, J. Chen, Z. Qin, D.W. Shoesmith, Mechanisms of film growth on copper in aqueous solutions containing sulphide and chloride under voltammetric conditions, *Electrochimica Acta*, 127, 439-447, 2014.
- [17] J. Chen, Z. Qin, T. Martino, D.W. Shoesmith, Non-uniform film growth and micro/macro-galvanic corrosion of copper in aqueous sulphide solutions containing chloride, *Corrosion Science*, 114, 72-78, 2017.

6 Assessment of the Electrochemical Behaviour and Surface Properties of Hydrothermally-grown Mixed Oxide in the Presence of Bisulfide-containing Solution

6.1 Introduction

In a DGR, in the early oxic period, the formation of oxides/hydroxides (and oxychlorides such as atacamite ($\text{Cu}_2\text{Cl}(\text{OH})_3$) in saline groundwaters) is expected, but once oxygen is consumed and anoxic conditions are established, corrosion will be driven by bisulfide produced remotely by the action of SBR.

The nature of naturally-grown copper oxide on the UFC surface within a DGR would be diverse. Factors like container surface temperature, bentonite porewater composition and pH, and irradiation dose will influence the oxide structure, spanning from nanometre to micrometre scale, with varying levels of porosity and compactness [1]. In bentonite porewater at its natural pH of approximately 8.6, the stable forms of Cu hydr(oxide) are either Cu_2O or CuO , depending on the redox potential. Although $\text{Cu}(\text{OH})_2$ is frequently observed in short-term experiments, CuO is more stable than the corresponding hydroxide. In the moderately alkaline range, Cu_2O will be slightly soluble as dissolved Cu^+ , and CuO as dissolved HCuO_2^- [1-3].

Localized corrosion typically occurs on passive metals as the ultra-thin passive film (commonly an oxide) is chemically or mechanically damaged. In a defect-free or "perfect" material, this form of corrosion is generally triggered when the surface is exposed to an environment containing aggressive chemical species, such as chloride or bisulfide, leading to local film breakdown and the exposure of potentially anodic sites on the metal surface. If areas adjacent to this site can support cathodic reactions, galvanic coupling of the two sites can lead to a rapidly propagating pit that could swiftly perforate the metal wall thickness and ultimately cause structural failure [4-6].

In previous assessments of Cu performance within a Canadian DGR, there was compelling evidence suggesting that the conditions necessary for localized corrosion processes, such

as pitting or crevice corrosion, are unlikely to occur in a post-closure oxic period [7-11] since the chemical environment in a Canadian DGR is highly unlikely to meet the necessary conditions for passive film growth. The presence of a passive film is a prerequisite for the occurrence of processes like pitting and crevice corrosion [12-16].

Roshan Daljeet et al. [18] investigated the propensity of copper to undergo active dissolution through immersion in solutions containing various combinations and concentrations of Cl^- , SO_4^{2-} , and HCO_3^- ions at different temperatures. Based on electrochemical behaviour, active dissolution was found to be the preferred corrosion process in most scenarios. However, approximately 40–50 μm of surface roughening was observed in Cl^- solutions in corrosion experiments, which was attributed to the preferential active dissolution of different grains [17]. Preferential grain reactivity is expected to be dependent on the purity and crystallinity of the copper. In an analysis of the damage expected under oxic DGR conditions an allowance of up to 100 μm was conservatively assigned for this roughening process. This aligns with estimates used in other programs.

Under anoxic conditions, in situations with low bisulfide concentrations or under stagnant conditions, it has been shown by Martino et al. [19,20] that porous copper sulfide films form, allowing bisulfide penetration and ongoing active corrosion. More compact copper sulfide films, capable of blocking incoming bisulfide, form only at higher concentrations well beyond those anticipated in a DGR.

The key points are that passivation involves the formation of a duplex film comprising Cu_2O and a Cu (II) layer (either CuO or $\text{Cu}(\text{OH})_2$), with the Cu (II) layer responsible for passivity. Despite CuO being the thermodynamically stable species, the kinetic preference favours the formation of $\text{Cu}(\text{OH})_2$ [1].

The nature of the film present on a container surface prior to the establishment of anoxic conditions in a DGR will be determined by oxidation during transportation and emplacement and corrosion during the early oxic period present immediately after closure and sealing of the DGR. This will determine the nature of the reactions occurring once anoxic conditions are established and corrosion becomes supported by reaction with SH^- .

The goals of the research described in this chapter were:

1. To investigate the effects of oxidation processes (in this case films grown hydrothermally) on the subsequent bisulfide-induced corrosion of Cu.
2. To determine the nature of the oxide-to-sulfide conversion reactions once exposure to a SH^- -containing solution occurs.
3. To understand the mechanism of the conversion reactions, identify the associated corrosion products, and determine their influence on the distribution of corrosion damage on the Cu surface.

6.2 Experimental

6.2.1 Specimen preparation

All experiments were performed with O-free, P-doped wrought Cu provided by the Swedish Nuclear Fuel and Waste Management Company (SKB). Specimens were prepared as described in section 3.1.

6.2.2 Solution preparation

To form an oxide layer on a copper specimen, the specimens were immersed in specific solutions for a specific time as described in section 3.2.2.1. The hydrothermally-grown oxides were then exposed to bisulfide solutions containing a $[\text{SH}^-]$ of either 10^{-4} or 2×10^{-4} M, prepared as described in section 3.3.1. All bisulfide solutions contained a supporting electrolyte of 0.1 M NaCl (with an assay of $\geq 99.0\%$, Fisher Chemical).

6.2.3 Electrochemical cell design and instrumentation

See section 3.2.1.2.

6.2.4 Electrochemical/corrosion experiments

All experiments were carried out in a three-compartment electrochemical cell within a Faraday cage to reduce interference from external electrical sources. Before each experiment, solutions containing SH^- were purged with ultra-high purity Ar gas for 30 minutes, and sparging was maintained throughout the experiment.

6.2.4.1 Corrosion potential measurements

Corrosion potentials (E_{corr}) were recorded on oxidized specimens after transfer to an electrochemical cell containing a SH^- solution, to study the influence of SH^- on the grown oxide films.

6.2.4.2 Cathodic stripping voltammetry

After measuring E_{corr} in SH^- solutions for different durations, the potential was scanned from the final E_{corr} value to -1.4 V/SCE at a scan rate of 10 mV/min to cathodically reduce oxide and sulfide films formed on the electrode surface. The potentials at which cathodic peaks were observed were used to determine the type of oxide and sulfide phases present [21].

6.2.5 Surface analyses

6.2.5.1 Laser Raman spectroscopy

The surface of each oxidized Cu specimen was analyzed, both before and after exposure to the SH^- solutions, using laser Raman spectroscopy. The details are described in section 3.5.2.2.

6.2.5.2 Scanning electron microscopy

Surface imaging was conducted using a field emission SEM with energy dispersive X-ray spectroscopy (EDX) to determine the physical morphology and elemental composition of the surface phases. Additionally, a FIB/SEM was employed to section specimens, allowing for the acquisition of cross-sectional images of surface films. The details are described in sections 3.5.1.2 and 3.5.1.4.

6.3 Results and Discussion

6.3.1 Characterization of hydrothermally-grown mixed oxide

SEM images (**Figure 6.1**) reveal that the film was composed of small clusters on the surface, suggesting that the oxide growth rate was uneven.

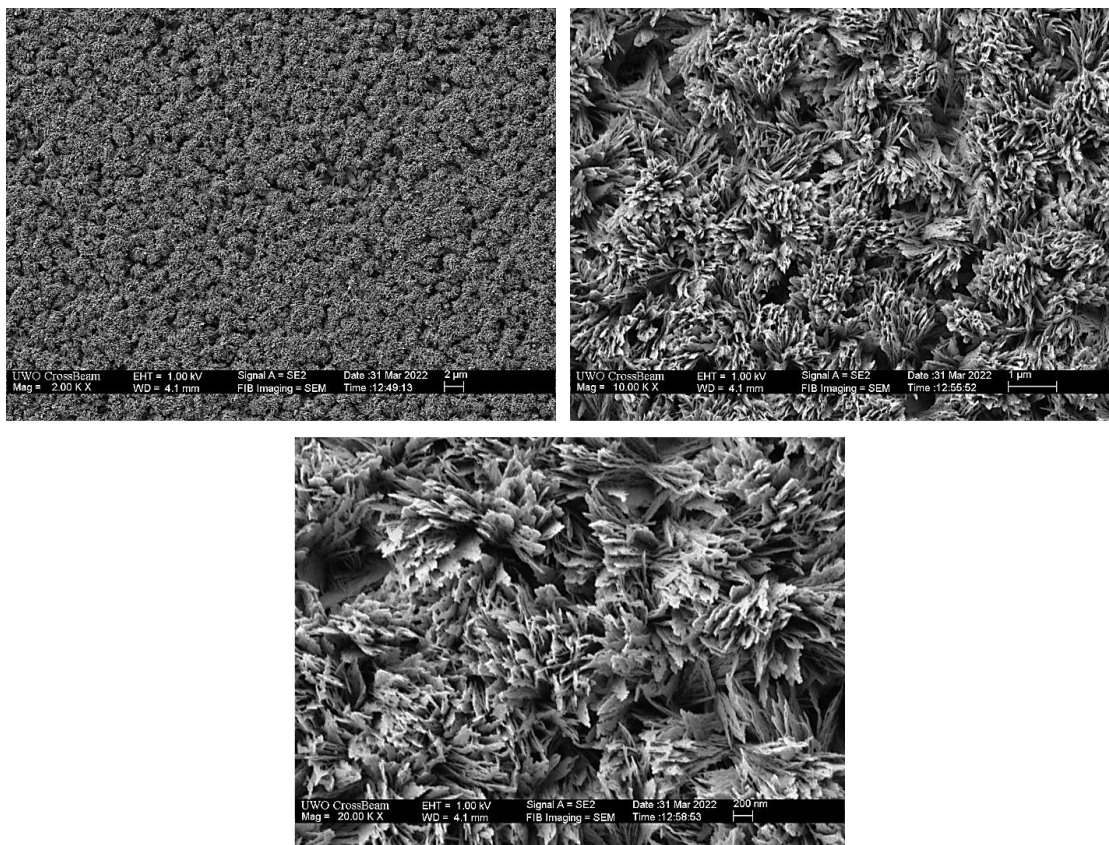


Figure 6.1: SEM images of hydrothermally-grown copper oxide on SKB copper.

The oxide film composition was analyzed using Raman spectroscopy. The Raman spectrum shown in **Figure 6.2**, exhibited strong signals for CuO at 298, 347 and 591 cm^{-1} [22-24]. Compared to the mixed oxide layer grown electrochemically in **Chapter 5**, the characteristic peaks for Cu_2O (peak at 218 cm^{-1} and the doublet peak in the range of 400 to 600 cm^{-1}) are not easily detectable, suggesting the formation of a thick layer of CuO film on top of the Cu_2O layer.

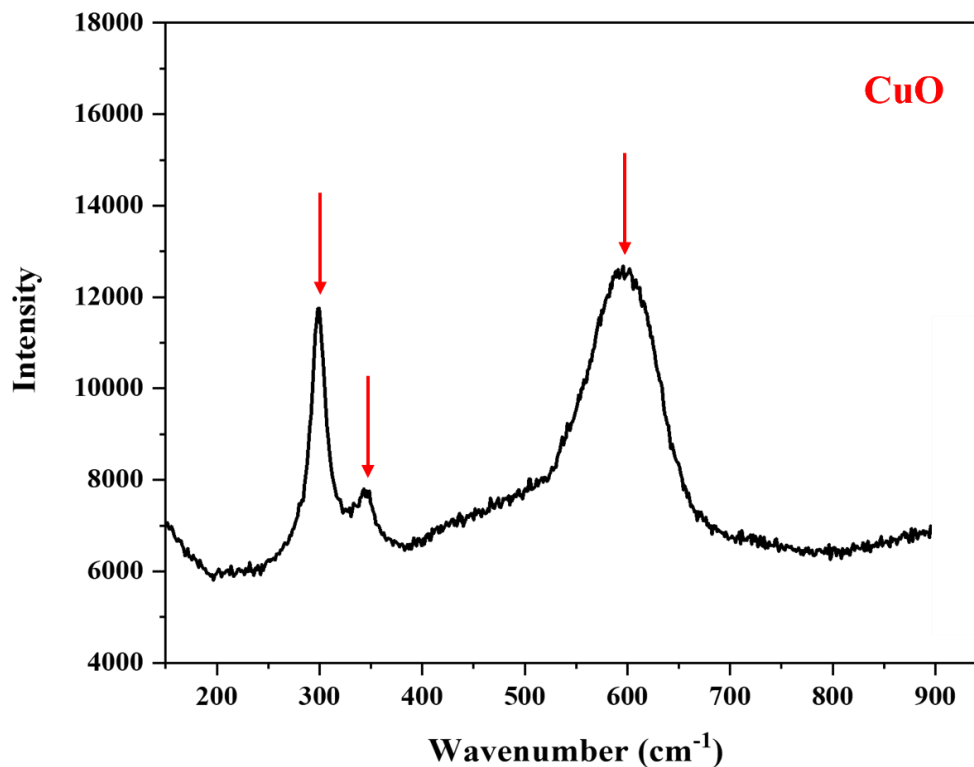


Figure 6.2: Raman spectrum of hydrothermally-grown copper oxide

To gain insights into the film morphology and thickness, SEM/FIB coupled with EDX was employed on the oxidized Cu specimens. As can be seen in **Figure 6.3** and **Table 6.1**, the FIB/SEM images revealed the oxide film structure consisting of an extremely porous inner layer (average thickness: 326 nm) covered by an outer layer with an average thickness of 1.5 μm . The outer CuO deposit grew in clusters, which would be consistent with deposition at porous locations in a thin base layer which presumably is Cu_2O . **Figure 6.3 (c)** clearly shows the outer CuO film was also porous. The total thickness of the formed oxide layer was determined to be 1.8 μm (calculated as an average of the measurements in **Figures 6.3 (a)** and **6.3 (b)**). EDX results on the cross-section of the film confirmed the composition of the outer layer as CuO. No localized penetrations into the metal were observed at the Cu/film interface in the SEM/FIB images (**Figure 6.3 (c)**). To reveal the extent of corrosion damage to the Cu substrate, the oxide films were removed using a pickling solution (Ar-sparged 9.1 wt% HClO_4 + 3.5 g/L $\text{C}_6\text{H}_{12}\text{N}_4$ inhibitor).

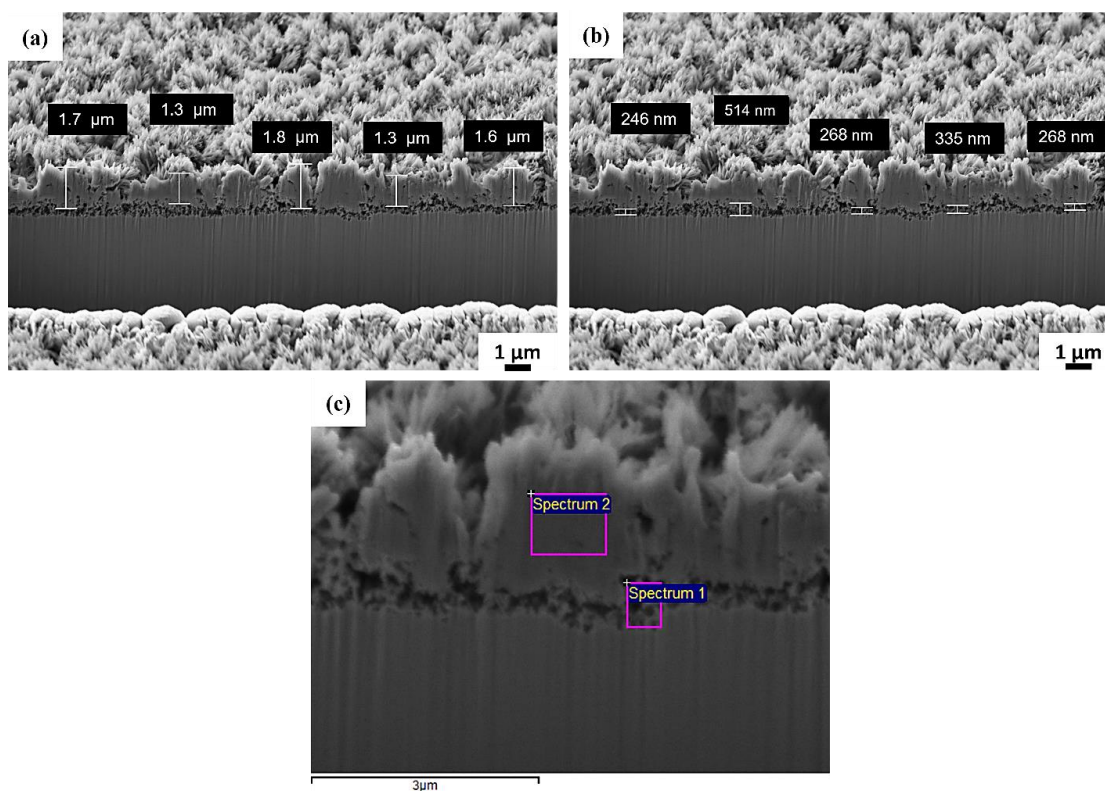


Figure 6.3: SEM/FIB cross-sections of hydrothermally-grown copper oxide (a) outer layer, (b) inner layer, and (c) EDX selected spots.

Table 6.1: Atomic percentage of different elements corresponding to **Figure 6.3**

Spectrum	C	O	Cu	Al	Si	Ga
Spectrum 1	4.2	10.8	82.5	-	1.2	1.3
Spectrum 2	3.3	46.4	45.7	1.0	3.6	-

The SEM images in **Figure 6.4** display the surface of the oxidized specimen after film removal. The top row images, along with elemental data from EDX (**Table 6.2**), show that while the deposited CuO layer is efficiently removed, incomplete removal of what appears to be the Cu₂O base layer is observed, with notable detection of oxygen in certain areas (region 2) on the surface. In the bottom row, the presence of holes suggests a small number of locally corroded sites formed during oxide growth.

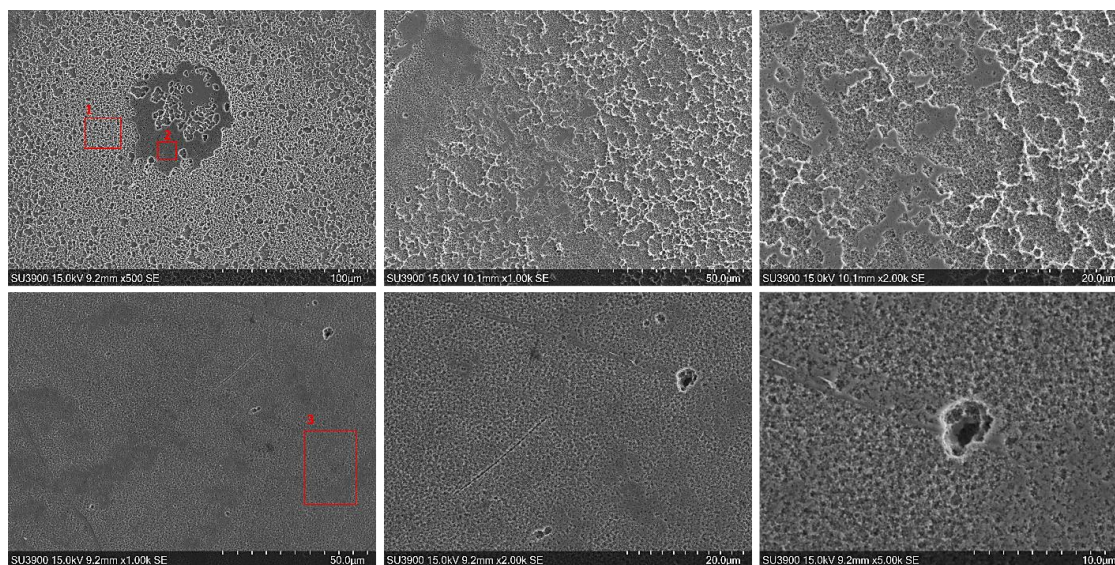


Figure 6.4: SEM images on the surface of an oxidized Cu specimen after film removal via a chemical method (Red boxes show the selected regions for EDX).

Table 6.2: Composition (wt. %) at selected regions shown in **Figure 6.4**

Spectrum Label	Cu	O	Si	C
Spectrum 1	91.4	0.5	-	8.1
Spectrum 2	69.6	22.1	0.3	8.0
Spectrum 3	92.3	0.4	-	7.3

The hydrothermal formation of an oxide film on Cu specimens was monitored over an exposure period of 3 days under open circuit conditions, **Figure 6.5**. The potential initially decreased slightly before steadily increasing from ~ -0.156 to ~ -0.13 V/SCE and becoming steadily noisier as film growth progressed. An observed positive shift in E_{corr} must involve either a decrease in anodic kinetics (Cu oxidation) or a decrease in cathodic kinetics (ClO_3^- reduction). Both would occur as a consequence of the development of a partially protective oxide deposit. The slow and relatively small increase leading to a thick CuO film would be consistent with the growth of the porous film, and the increase in noise the irregular variations in anodic and cathodic reaction rates.

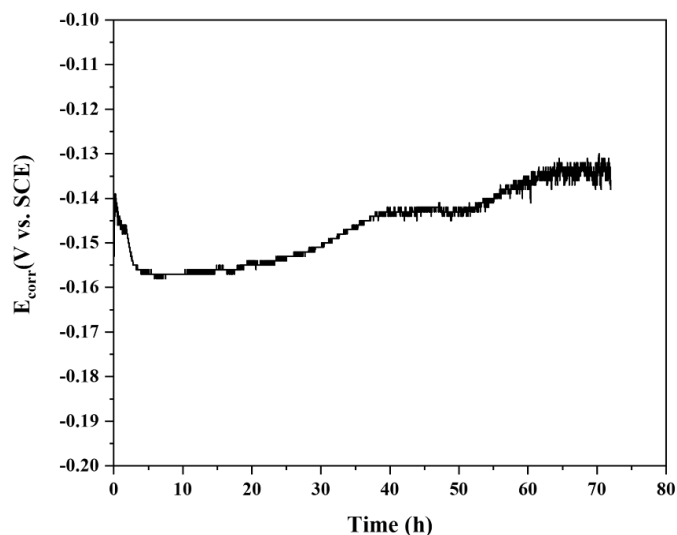


Figure 6.5: E_{corr} recorded on Cu during the growth of oxide in 0.57 M KClO_3 and 0.1 M Na_2CO_3 solution at 50 °C.

6.3.2 Characterization of sulfidized grown oxide

Oxidized specimens were exposed to a solution containing 0.1 M Cl^- + 10^{-4} M SH^- for different periods of time, and E_{corr} was monitored, shown in **Figure 6.6**.

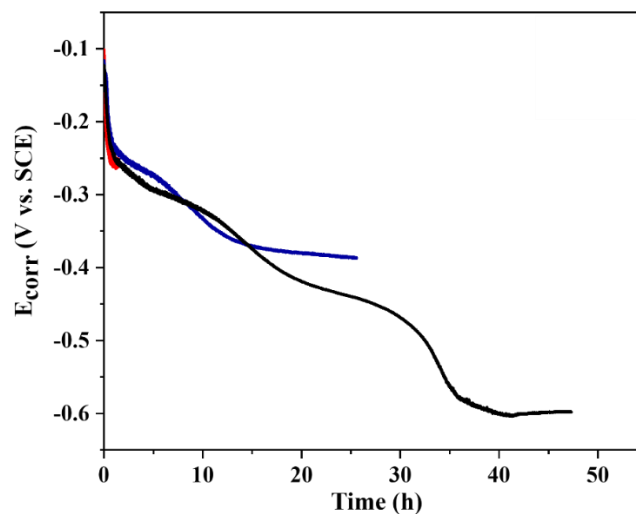


Figure 6.6: E_{corr} of oxidized Cu in 0.1 M NaCl + 10^{-4} M Na_2S .

The initial E_{corr} closely resembled that observed during the growth of the oxide (**Figure 6.5**), indicating the presence of Cu (II)-containing species on the surface, close to the

equilibrium potentials of the redox couples of Cu/Cu(OH)₂ and Cu/CuO. Prolonged exposure to the bisulfide solution resulted in a shift in potential towards more negative values, signifying a change in the redox properties of the surface. The E_{corr} first stabilized around -0.35 V/SCE which is close to the equilibrium potential of Cu/Cu₂O, as validated in our recent study on the electrochemically-grown oxide. A distinct steady-state plateau at approximately -0.65 V/SCE was observed, contrasting with the absence of such a feature when forming the dual-layer oxide electrochemically. Findings from previous work, particularly by Teague et al. [25], suggest that this plateau aligns with the exposure of the Cu substrate to the incoming solution passing through an existing porous layer.

To better understand the underlying processes beneath the surface film and to gain insight into film morphology and film thickness, surface examination using SEM/FIB coupled with EDX was conducted on the oxidized specimens after different immersion times in 0.1 M NaCl + 10^{-4} M Na₂S solution (at specific potentials).

Figure 6.7 shows the SEM/FIB images from the surface and a cross-section of the film formed on the oxidized specimen after reaching $E_{\text{corr}} \sim -260$ mV in 0.1 M NaCl + 10^{-4} M Na₂S solution.

In the context of the sulfidization process, the surface morphology of the specimen at a potential of -0.26 V/SCE reveals notable changes. The outer layer's structure becomes more porous, exhibiting small holes on the surface. Examining SEM images of the cross-section across these holes indicates the growth of these holes toward the copper substrate, showcasing a dynamic evolution. Additionally, the EDX map taken at the cross-section, shown in **Figure 6.8**, offers proof of a sulfide film forming on top of the oxide layer after 1 hour of exposure, with no indication of SH⁻ reaching the Cu surface to initiate Cu corrosion. The observed pits in this figure did not resemble those caused by exposure to the bisulfide-containing solution, as they were filled with oxide. It is highly likely that they formed during the hydrothermal treatment. The topmost layer was coated with platinum for FIB-cutting to prevent the thin film from collapsing.

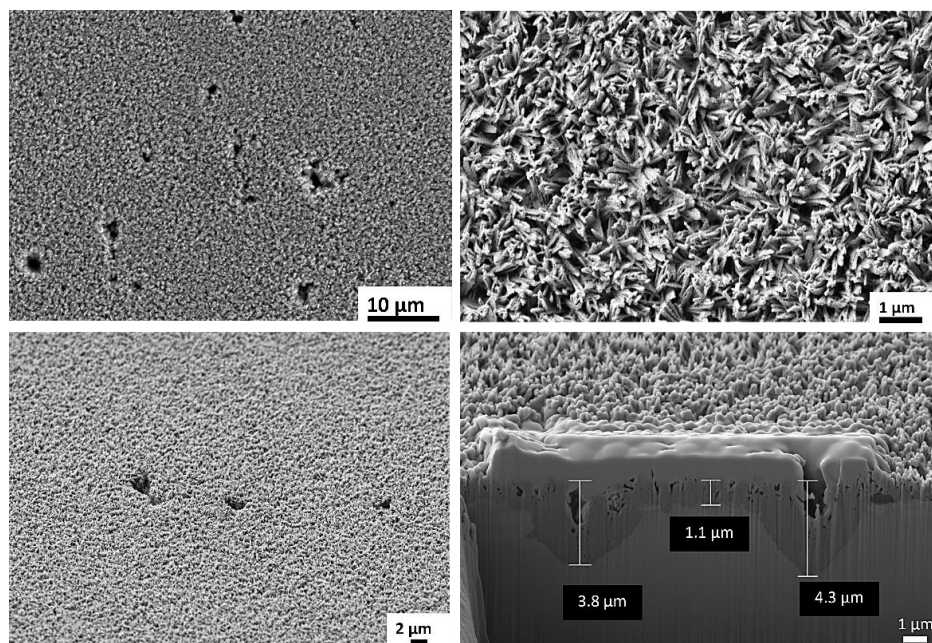


Figure 6.7: SEM images and FIB cross-section on oxidized Cu after 1 h-exposure to 0.1 M NaCl + 10^{-4} M Na₂S (E_{corr} : -260 mV).

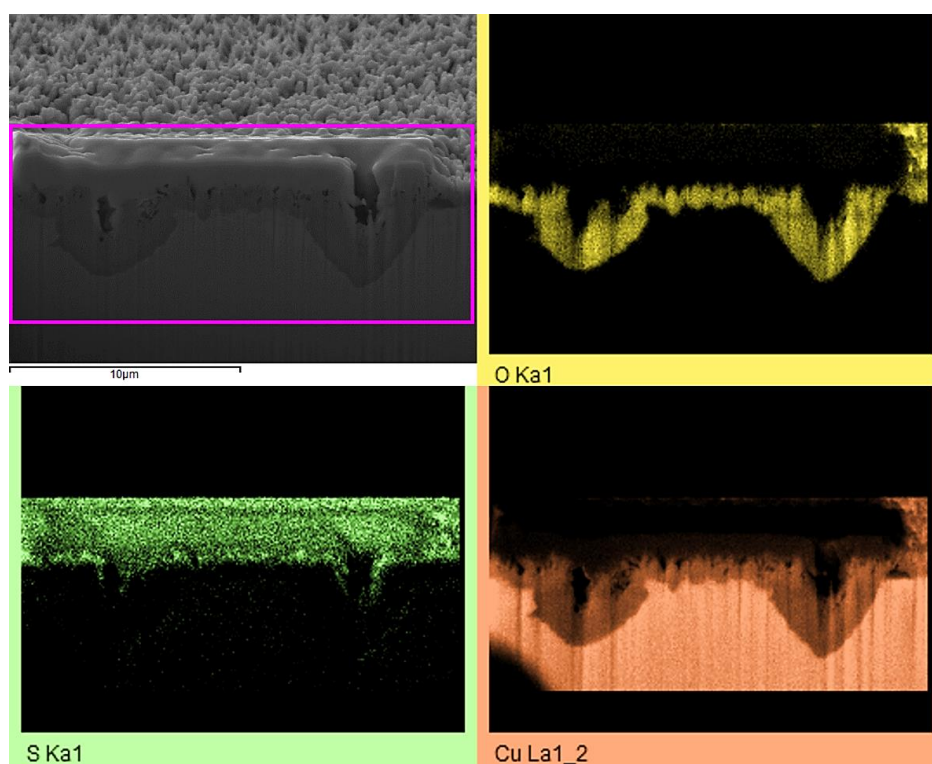


Figure 6.8: EDX maps of a FIB cross-section on oxidized Cu after exposure to 0.1 M NaCl + 10^{-4} M Na₂S (E_{corr} : -260 mV).

Figure 6.9 shows the Raman spectra obtained on oxidized Cu after exposure to 0.1 M NaCl + 10^{-4} M Na₂S at different E_{corr} .

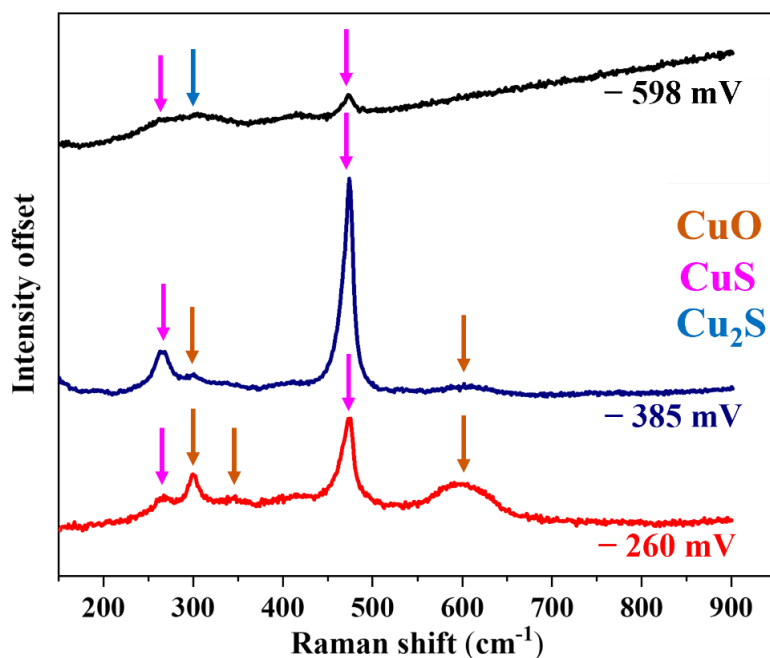


Figure 6.9: Raman spectra obtained on oxidized Cu after exposure to 0.1 M NaCl + 10^{-4} M Na₂S at different E_{corr} , as indicated on the figure.

Analyzing the Raman results at $E_{\text{corr}} \sim -260$ mV/SCE, the predominant corrosion products identified were CuO with characteristic peaks at 298, 345, and 597 cm^{-1} [24,26,27] and CuS [28-30] with peaks at 263 and 475 cm^{-1} . Notably, despite previous evidence supporting the existence of an inner layer of Cu₂O, no discernible peaks corresponding to Cu₂O were detected on this particular specimen.

Therefore, the alteration in the shape of the outer CuO layer and its conversion into CuS during the initial brief exposure period suggested that this change occurred rapidly through the deposit (as shown in **Figure 6.8**), due to the exceptionally large surface area of the hydrothermally-formed CuO clusters, which are very fine, as seen in **Figure 6.3 (c)**, even though E_{corr} had only reached -260 mV/SCE. This notably large surface area might also be the reason behind the robust and distinct Raman peaks observed for CuS (as illustrated in **Figure 6.9**).

SEM images captured on the top surface of the sulfidized specimen at the concluding corrosion potential of -385 mV/SCE (after 26 h immersion), shown in **Figure 6.10**, reveal notable changes in the surface morphology. The size of the pores on the surface increased, and the film no longer exhibited a flaky structure. Instead, the surface film appeared more compact than the specimen exposed to 0.1 M NaCl + 10^{-4} M Na₂S solution for only 1 hour (-260 mV/SCE). This evolution in surface characteristics over the extended exposure time suggests that conversion of copper oxide to copper sulfide has a significant role in the dynamic corrosion process.

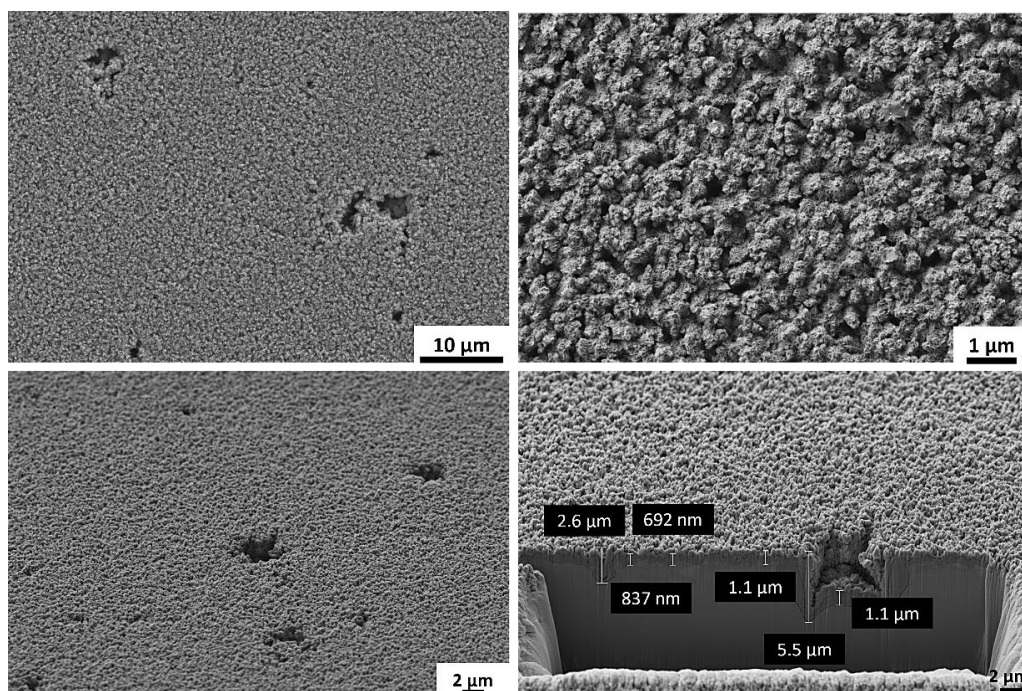


Figure 6.10: SEM images and FIB cross-section on oxidized Cu after exposure to 0.1 M NaCl + 10^{-4} M Na₂S (E_{corr} : -385 mV).

The FIB/SEM image reveals intricate details across one of the pores, providing a deeper understanding of the corrosion process. Specifically, the image illustrates the growth of holes beneath the film, offering insights into both the depth of the holes and the length of their openings. This observation is crucial for characterizing the extent and dimensions of the corrosive features formed during the exposure.

The EDX map analysis for different elements at the cross-section of the film formed on oxidized Cu after exposure to 0.1 M NaCl + 10^{-4} M Na₂S at $E_{\text{corr}} \sim -385$ mV (**Figure 6.11**) reveals the continued presence of an oxide layer beneath the sulfide film, extending toward the bottom of the observed holes. Meanwhile, the Raman spectrum of the corrosion product film, shown in **Figure 6.9**, provides further insights into the chemical composition. The characteristic peaks for CuS at 263 and 474 cm^{-1} became more pronounced, indicating an increased prevalence of copper sulfide in the corrosion product. Although signals for CuO at 298 and 598 cm^{-1} were still present, they appeared less strong compared to those observed at the less negative potential (-260 mV), suggesting that as the potential shifts to more negative potentials, the oxide-to-sulfide conversion reactions become more dominant.

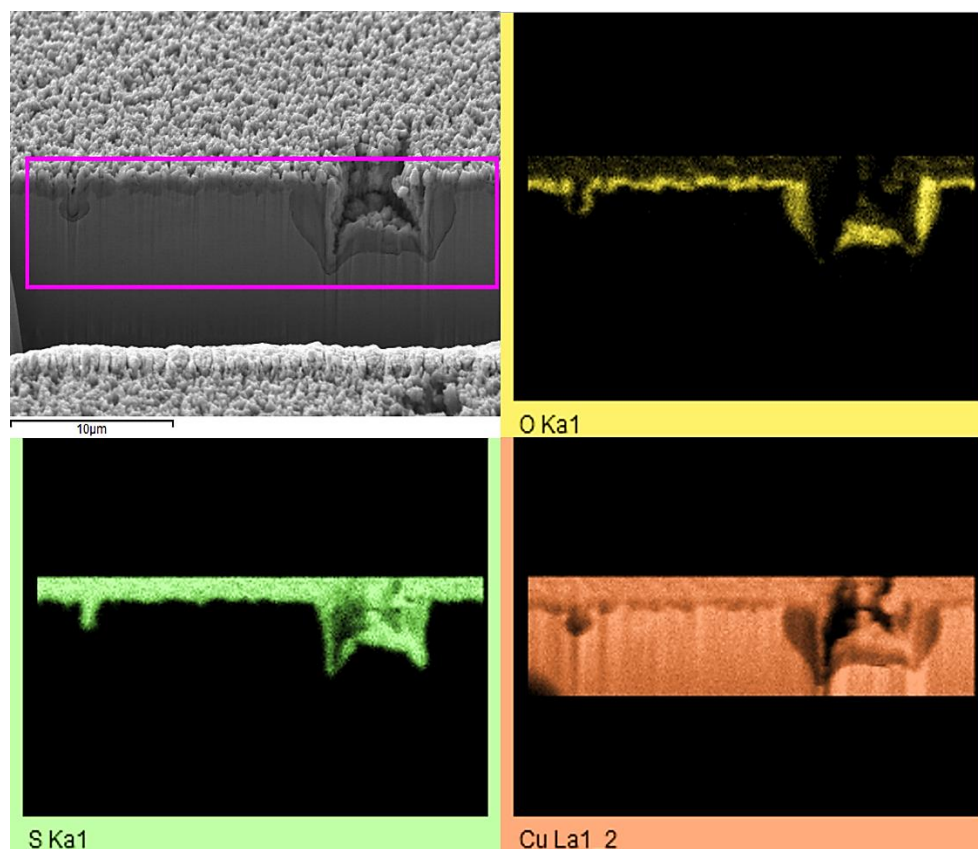


Figure 6.11: EDX maps of FIB cross-section on oxidized Cu after exposure to 0.1 M NaCl + 10^{-4} M Na₂S (E_{corr} : -385 mV).

The presence of a residual oxide layer implies that the conversion of CuO to CuS slowed considerably once the SH^- ions reached the denser base of the clusters. The thickness of the remaining oxide layer was too large for it to be composed of just the Cu_2O barrier layer. Another possibility is that within this range of potential, the reaction between SH^- and Cu could potentially initiate, as the bisulfide ions had reached the copper surface in certain locations. However, the Raman analysis (**Figure 6.9**) did not reveal any Cu_2S , the anticipated product of the reaction between SH^- and Cu. The presence of a thick CuS film slowed the transport of SH^- ions to reactive sites down, resulting in a low concentration of SH^- at the Cu surface. This low concentration restricted the rate at which the remaining surface oxide, as depicted in **Figure 6.10**, converted to copper sulfide.

As can be seen in **Figure 6.12**, the SEM images captured from the sulfidized specimen at the potential ~ -598 mV/SCE, corresponding to the most stable plateau, reveal some peculiar features on the surface.

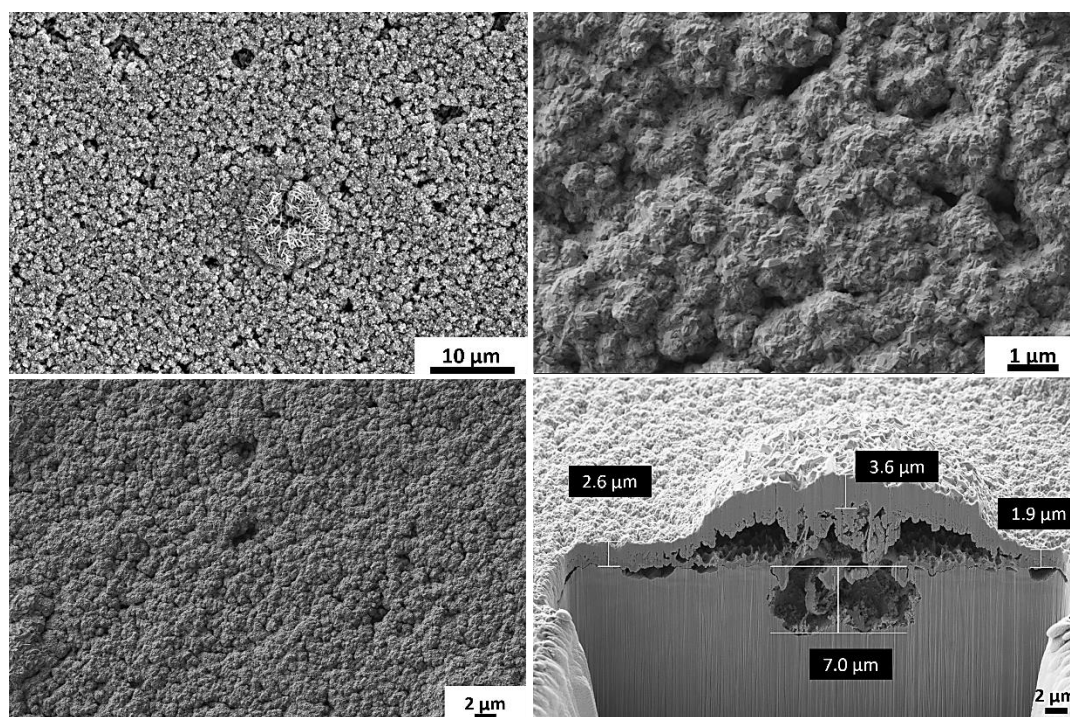


Figure 6.12: SEM images and FIB cross-section on oxidized Cu after exposure to 0.1 M $\text{NaCl} + 10^{-4}$ M Na_2S (E_{corr} : -598 mV).

The clusters are still visible in **Figure 6.12**, showing some crystallinity development expected for Cu_2S formation. In comparison to the initial hydrothermally-grown oxide film shown in **Figure 6.7**, this film appeared more compact but still retained its porous nature. Despite the outer layer exhibiting a more compact structure, numerous bumps were apparent across the surface. Further investigation by creating a trench across one of these bumps exposed a preferential dissolution of the substrate beneath this specific bump. This localized dissolution suggests a non-uniform corrosion pattern, emphasizing the influence of grown oxide structure not only on conversion of oxide-to-sulfide but also on the corrosion behaviour of Cu.

A specific feature observed in the SEM images involves a hole with its opening covered by a protective film. The EDX map analysis (**Figure 6.13**) indicates that this film is composed of sulfide, while a trace of oxygen suggests the presence of a residual oxide layer.

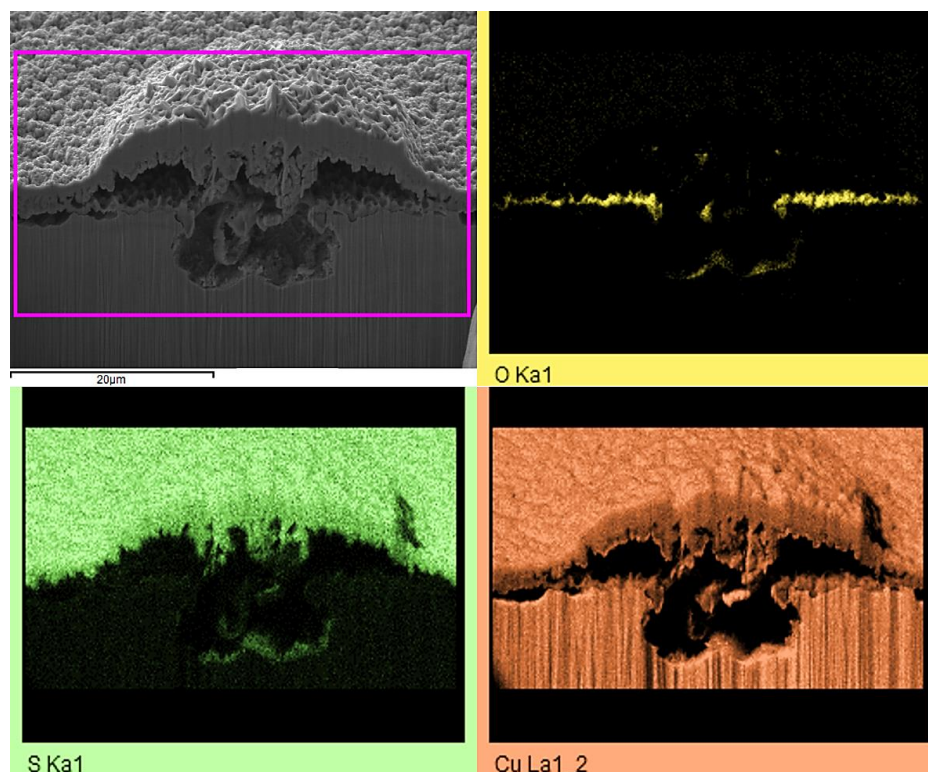


Figure 6.13: EDX maps of FIB cross-section on oxidized Cu after exposure to 0.1 M $\text{NaCl} + 10^{-4}$ M Na_2S (E_{corr} : -598 mV).

This oxide layer acts as a porous membrane, enabling the bisulfide solution to permeate through and react with the underlying Cu metal. The formation of sulfide-containing species at the bottom of the holes is confirmed by the EDX map. Raman spectrum analysis (**Figure 6.9**) reveals that, at potential ~ -598 mV, the composition of the corrosion product is a mixture of Cu_2S with a weak peak at 300 cm^{-1} and CuS with characteristic peaks at 263 and 474 cm^{-1} . The reduced intensity of the CuS Raman peaks might signify the accumulation of Cu_2S alongside the CuS . By the time E_{corr} had decreased to -598 mV, Raman spectroscopy no longer detected any oxide presence (**Figure 6.9**), yet EDX analyses (**Figure 6.13**) validated the existence of a thin oxide layer at the Cu/film interface.

At this potential, the deposition of Cu_2S within the pre-existing CuS layer (assuming it had not converted into Cu_2S) resulted in stress buildup, causing the film to buckle, particularly over a corroded void formed during hydrothermal growth (**Figure 6.12**). Since the volume of the sulfide film is greater than that of the oxide layer (due to the larger S anion), the existence of a stress build-up was expected. The expansion in volume, along with the accumulation of sulfide by the corrosion of the Cu substrate, explains the overall thickening of the film from its initial size of $1\text{-}2\text{ }\mu\text{m}$ (as depicted in **Figure 6.3**) to $2\text{-}4\text{ }\mu\text{m}$ by the time E_{corr} decreases to -598 mV. The EDX analysis (as shown in **Figure 6.13**) reveals remnants of oxide lingering on the Cu surface, both inside and outside the corroded void. The accumulation of stress resulted in a separation at the interface between the oxide and sulfide layers, and potentially at the oxide/Cu interface as well. This phenomenon was most evident in the EDX map for Cu.

The following set of experiments was conducted on the oxidized specimen subjected to sulfidization in $0.1\text{ M NaCl} + 10^{-4}\text{ M Na}_2\text{S}$ solution at a potential approximately -760 mV/SCE , a value in close proximity to the equilibrium potential of the $\text{Cu/Cu}_2\text{S}$ redox couple, as illustrated in **Figure 6.14**. Our earlier research [31] and work done by Bojinov et al. [32] demonstrated that the oxide layer was nearly converted into Cu_2S , yet a residual layer of oxide, Cu_2O , persisted on the surface.

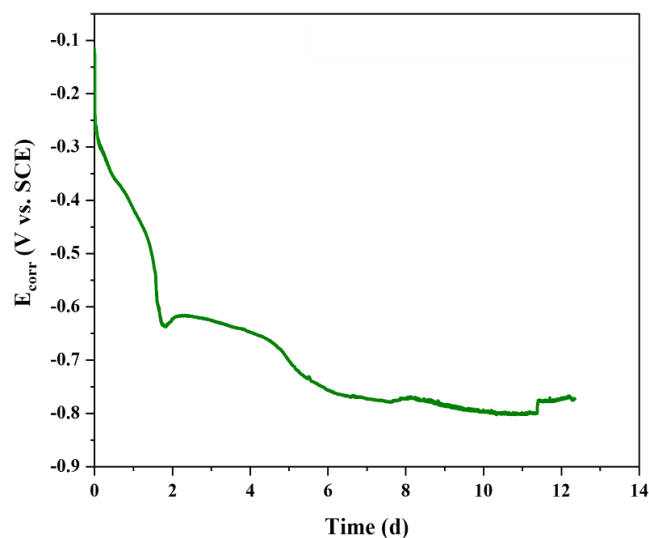


Figure 6.14: E_{corr} of oxidized Cu in 0.1 M NaCl + 10^{-4} M Na₂S.

The outcome derived from the Raman spectrum of the sulfidized specimen at $E_{\text{corr}} \sim -760$ mV/SCE, as shown in **Figure 6.15**, aligns well with previous findings [31]. The corrosion product primarily consisted of Cu₂S with a peak at 300 cm^{-1} , with the additional detection of a layer of Cu₂O with peaks at 218, 523, and 623 cm^{-1} [24,33,34]. There is no Raman indication of CuO, although it is possible that the corrosion product still be a combination of Cu (I) and Cu (II) oxides.

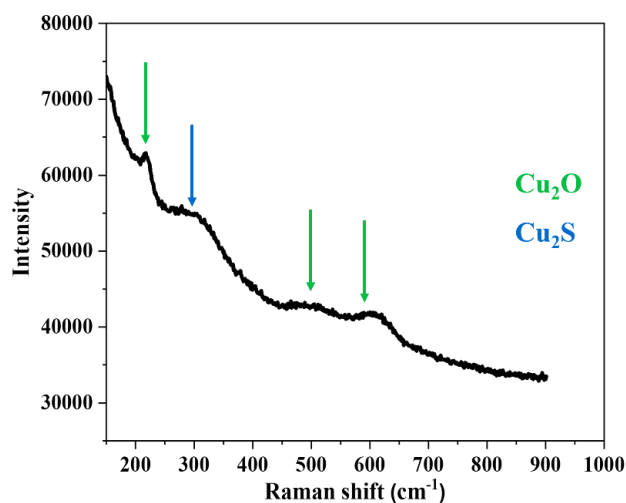


Figure 6.15: Raman Spectrum obtained on oxidized Cu after exposure to 0.1 M NaCl + 10^{-4} M Na₂S at -760 mV.

The SEM images of the surface film, **Figure 6.16**, confirm the stress development leading to the buckling and detachment of the film from the Cu substrate, indicating the increasing prominence of Cu substrate corrosion. This is evident from the crystalline nature of the predominantly Cu_2S film formed. The stratified nature of the surface layer might stem from the initial conversion of oxide, resulting in an inner porous structure, while the outer crystalline structure could be attributed to the deposition of Cu_2S . Beneath the porous layer, there is a stratum of re-deposited Cu resulting from the cutting process through a void, an unavoidable artificial effect.

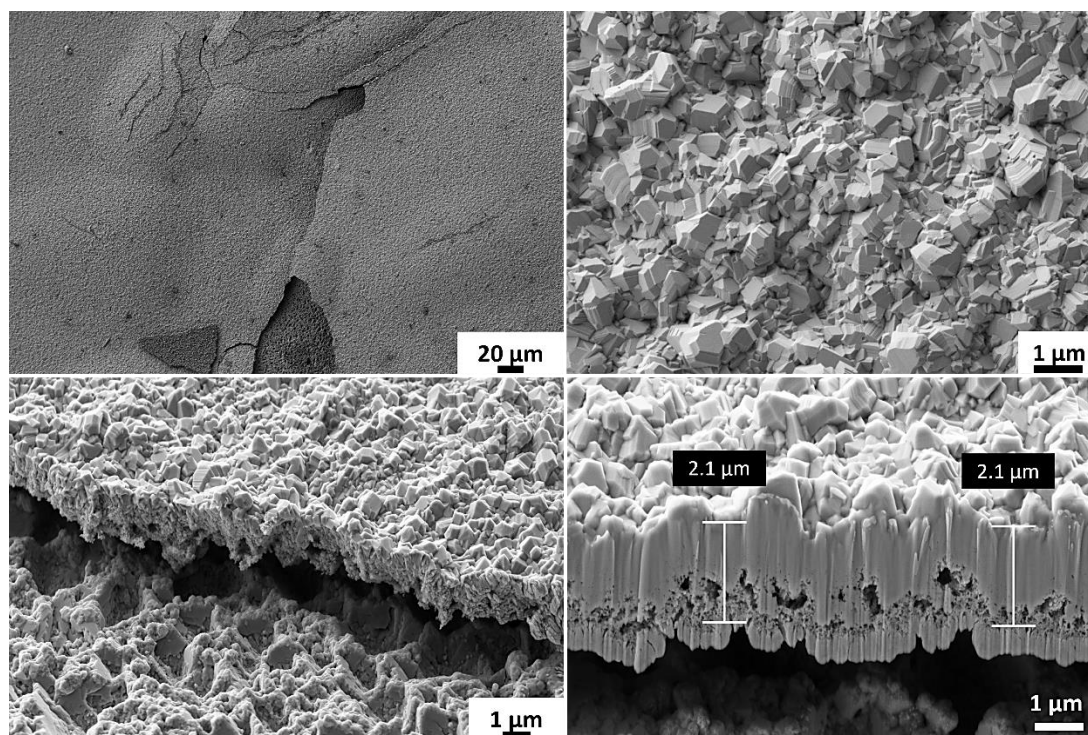


Figure 6.16: SEM images and FIB cross-section on oxidized Cu after exposure to 0.1 M $\text{NaCl} + 10^{-4}$ M Na_2S (E_{corr} : -760 mV).

Considering Raman results at different potentials, **Figure 6.9** and **Figure 6.15**, the likelihood is that at less negative potentials (-260 and -385 mV), the oxide film was mainly converted to CuS . As the corrosion potential shifted to more negative potentials (-600 mV), the converted film was composed of CuS and Cu_2S . At the potential (-760 mV), Cu_2S became the stable compound. Based on SEM/FIB images, **Figures 6.7**, **6.10**, **6.12**, and **6.16**, in the region where the primary corrosion product formed at the film/solution

interface was CuS, the film structure appeared more porous than that in the region dominated by Cu₂S in which the film was more compact, leading to a more pronounced growth of holes beneath the film.

To elucidate the composition of the corrosion product formed following exposure to 0.1 M NaCl + 2×10^{-4} M Na₂S solution for different durations (at each selected potential), linear sweep voltammetry was conducted at a scan rate of 10 mV/min after the corrosion potential was monitored, **Figure 6.17**. The utility of CSV lies in the distinct potential separation of cathodic reduction peaks for the sulfide film and the oxide film, allowing for their differentiation via this method. The rationale behind conducting this series of experiments in a solution with a higher concentration of bisulfide was to expedite the time required to reach specific potentials.

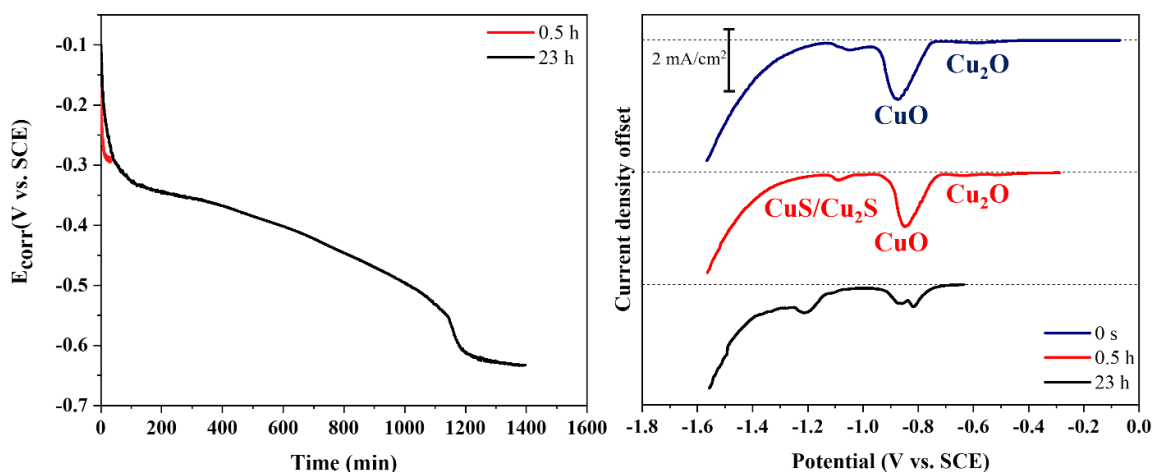


Figure 6.17: Oxidized Cu in 0.1 M NaCl + 2×10^{-4} M Na₂S: E_{corr} (left) and cathodic stripping voltammograms (right) recorded after immersion for various periods.

The initial plot (blue), recorded upon exposure of the specimen to 0.1 M NaCl + 2×10^{-4} M Na₂S solution, indicates that the film primarily consisted of CuO/Cu₂O. A small cathodic reduction peak at -1.2 V/SCE corresponds to the sulfide peak, manifesting due to the low scan rate, the scan took nearly 2 h for this potential range. When the electrode reached a potential of around -0.28 V/SCE, the conversion of oxide to sulfide became apparent, yet both Cu (I)- and Cu (II)-containing species persisted on the surface. Notably, the CSV revealed a more distinct peak for Cu₂O, consistent with observations in **Chapter 5**. As the

potential approached the establishment of another steady-state plateau (-0.65 V/SCE), the reduction peak for the sulfide film intensified, while conversely, the size of the reduction peaks for Cu oxide diminished.

6.3.3 Mechanistic understanding of localized corrosion

In this study, the initiation of localized corrosion occurred during hydrothermal growth of an oxide film, prior to the sulfide exposure. Initially (1 h-exposure at -260 mV), the oxide layer was much thicker than the sulfide layer. However, over a 26 h-exposure period (at -385 mV), the copper sulfide layer consistently grew, while the oxide layer's thickness decreased. The sulfide layer could grow either through the conversion of the oxide layer or by precipitation, as copper ions diffused through the porous oxide layer and reacted with bisulfide ions. As the sulfide film composition shifted from CuS to Cu₂S at longer times (at -589 mV), the film became more compact, leading to localized corrosion progressing downwards due to the galvanic effect between the underlying Cu metal and the conductive copper sulfide layer. Moreover, the oxide layer, which began detaching from the Cu metal, did not impede the progress of localized corrosion. At -760 mV, the film delaminated completely from the Cu surface, but a layer of porous oxide was still detected unconverted beneath the sulfide film, possibly due to poor electrical contact between the oxide film and the Cu.

6.4 Conclusions

In this study, a dual-layer copper oxide (Cu₂O/CuO) was effectively formed via a hydrothermal method. As the corrosion potential shifted towards more negative potentials, localized corrosion initiated on sulfidized pre-oxidized samples, resulting in the propagation of corrosion and eventual delamination of the corrosion product from the surface. Furthermore, the conversion of oxide to sulfide led to the formation of a compact layer on the surface, primarily composed of CuS at less negative potentials and Cu₂S at more negative potentials.

6.5 References

- [1] F. King, Corrosion of copper in alkaline chloride environments, TR-02-25, SKB, 2022.
- [2] D.W. Shoesmith, T.E. Rummery, D. Owen, W. Lee, Anodic oxidation of copper in alkaline solutions 2-The open-circuit potential behavior of electrochemically formed cupric hydroxide films, *Electrochimica Acta*, 22, 1403–1409. 1977.
- [3] L.D. Burke, M.J.G. Ahern, T.G. Ryan, An investigation of the anodic behavior of copper and its anodically produced oxides in aqueous solutions of high pH, *Journal of the Electrochemical Society*, 137, 553–561. 1990.
- [4] S. Gao, B. Brown, D. Young, M. Singer, Formation of iron oxide and iron sulfide at high temperature and their effects on corrosion, *Corrosion Science*, 135, 167–176, 2018.
- [5] W. Zhang, B. Brown, D. Young, G. Bota, S. Nestic, M. Singer, Pitting mechanism of mild steel in marginally sour environments – Part I: A parametric study based on formation of protective layers, *Corrosion Science*, 183, 109305, 2021.
- [6] W. Zhang, B. Brown, D. Young, M. Singer, Pitting mechanism of mild steel in marginally sour environments – Part II: Pit initiation based on the oxidation of the chemisorbed iron sulfide layers, *Corrosion Science*, 184, 109337, 2021.
- [7] F. King, M. Kolar, Lifetime predictions for nuclear waste disposal containers, *Corrosion*, 75, 309–323, 2018.
- [8] Postclosure Safety assessment of a used fuel repository in sedimentary rock, TR-2013-07, NWMO, 2013.
- [9] J.R. Scully, M. Edwards, Review of the NWMO copper corrosion allowance, TR-2013-04, NWMO, 2013.
- [10] Postclosure Safety assessment of a used fuel repository in crystalline rock, TR-2017-02, NWMO, 2017.

- [11] J.R. Scully, D. Feron, H. Hanninen, Peer review of the NWMO copper corrosion program, TR-2016-11, NWMO, 2016.
- [12] Z. Qin, R. Daljeet, M. Ai, N. Farhangi, J.J. Noël, S. Ramamurthy, The active/passive conditions for copper corrosion under nuclear waste repository environment. *Corrosion Engineering, Science and Technology*, 52, 45–49, 2017.
- [13] J. Chen, Z. Qin, D.W. Shoesmith, Long-term corrosion of copper in a dilute anaerobic sulfide solution, *Electrochimica Acta*, 56, 7854–7861, 2011.
- [14] T. Martino, J. Chen, M. Guo, S. Ramamurthy, D.W. Shoesmith, J.J. Noël, Comments on E. Huttunen-Saarivirta et al., “Kinetic properties of the passive film on copper in the presence of sulfate-reducing bacteria” [*Journal of the Electrochemical Society*, 165, C450, 2018], *Journal of the Electrochemical Society*, 166, Y13–Y16, 1990.
- [15] Supplementary information on canister integrity issues, TR-19-15, 135, SKB, 2019.
- [16] D.S. Hall, T.E. Standish, M. Behazin, P.G. Keech, Corrosion of copper-coated used nuclear fuel containers due to oxygen trapped in a Canadian deep geological repository, *Corrosion Engineering, Science and Technology*, 53, 309-315, 2018.
- [17] Daljeet, Roshan J., "Analysis and differentiation of uniform and localized corrosion of Cu", The University of Western Ontario, Electronic Thesis and Dissertation Repository, 8036, 2021.
- [18] D.S. Hall, M. Behazin, W.J. Binns, P.G. Keech, An evaluation of corrosion processes affecting copper-coated nuclear waste containers in a deep geological repository, *Progress in Materials Science*, 118, 100766, 2021.
- [19] T. Martino, J. Chen, Z. Qin, D.W. Shoesmith, The kinetics of film growth and their influence on the susceptibility to pitting of copper in aqueous sulphide solutions, *Corrosion Engineering, Science and Technology*, 52, 61–64, 2017.

- [20] T. Martino, R. Partovi-Nia, J. Chen, Z. Qin, D.W. Shoesmith, Mechanisms of film growth on copper in aqueous solutions containing sulphide and chloride under voltammetric conditions, *Electrochimica Acta*, 127, 439–447, 2014.
- [21] N.U. Obeyesekere, Pitting corrosion, Trends in Oil and Gas Corrosion Research and Technologies, In Woodhead Publishing Series in Energy, 215-248, 2017.
- [22] J.M. Smith, J.C. Wren, M. Odziemkowski, D.W. Shoesmith, The electrochemical response of preoxidized copper in aqueous sulfide solutions, *Journal of the Electrochemical Society*, 154, C431, 2007.
- [23] T. Yu, X. Zhao, Z.N. Shen, Y.H. Wu, W.H. Su, Investigation of individual CuO nanorods by polarized micro-Raman scattering, *Journal of Crystal Growth*, 268, 590-595, 2004.
- [24] F. Perez-Robles, F.J. Garcia-Rodriguez, S. Jimenez-Sandoval, J. Gonzalez-Hernandez, Raman study of copper and iron oxide particles embedded in an SiO₂ matrix, *Journal of Raman Spectroscopy*, 30, 1099-1104, 1999.
- [25] Y. Deng, A.D. Handoko, Y. Du, S. Xi, B.S. Yeo, In situ Raman spectroscopy of copper and copper oxide surfaces during electrochemical oxygen evolution reaction, *ACS Catalysis*, 6, 2473–2481, 2016.
- [26] M. Teague, S. Li, H. Cong, Interfacial corrosion of copper and the formation of copper hydroxychloride, Honors Research Projects, 696, 2018.
- [27] J. Chrzanowski, J.C. Irwin, Raman scattering from cupric oxide, *Solid State Communications*, 70, 11-14, 1989.
- [28] J.C. Irwin, T. Wei, J. Franck, Raman scattering investigation of Cu₁₈O, *Journal of Physics: Condensed Matter*, 3, 299-306, 1991.
- [29] G. Parker, G. Hope, R. Woods, Raman spectroscopic identification of surface species in the leaching of chalcopyrite. *Electrochemistry in Mineral Processing VI*. F.M. Doyle,

G.H. Kelsall, R. Woods, Editors PV2003-18, The Electrochemical Society Proceeding Series, Pennington, NJ, 181, 2003.

[30] T.P. Mernagh, A.G. Trudu, A laser Raman microprobe study of some geologically important sulphide minerals, *Chemical Geology*, 103, 113-127, 1993.

[31] N.R. De Tacconi, K.L. Rajeshwar, O. Reynaldo, Study of copper sulfide film formation by voltammetry combined with electrochemical quartz crystal microgravimetry/coulometry and optical spectroscopy, *The Journal of Physical Chemistry*, 100, 18234-18239, 1996.

[32] E. Salehi Alaei, M. Guo, J. Chen, M. Behazin, E. Bergendal, C. Lilja, D.W. Shoesmith, J.J. Noël, The transition from used fuel container corrosion under oxic conditions to corrosion in an anoxic environment, *Materials and Corrosion*, 74, 1690-1706, 2023.

[33] M. Bojinov, T. Ikalainen, Z. Que, T. Saario, Effect of sulfide on de-passivation and re-passivation of copper in borate buffer solution, *Corrosion Science*, 218, 111201, 2023.

[34] H.H. Chan, C.G. Takoudis, M.J. Weaver, Electrochemical control of gas phase oxidation and reduction of copper by surface-enhanced Raman spectroscopy, *Electrochemical and Solid-State Letters*, 2, 189-191, 1999.

[35] H.H. Chan, C.G. Takoudis, M.J. Weaver, Oxide formation and oxygen adsorption on copper in aqueous media as probed by surface-enhanced Raman spectroscopy, *Journal of Physical Chemistry B*, 103, 357-365, 1999.

7 Assessment of the Electrochemical Behaviour and Surface Properties of Radiolytically-formed Mixed Oxide in the Presence of Bisulfide-containing Solution

7.1 Introduction

In the DGR, the used fuel container will experience a sustained exposure to ionizing radiation, particularly γ -radiation, emanating from the decay of radionuclides in the used fuel [1]. The γ -radiation dose rate at the external copper layer is estimated by Morco et al. to be 2.3 Gy/h after 10 years of emplacement, gradually decreasing to a level of 0.2 Gy/h after 100 years [2,3].

When γ -radiation interacts with Cu metal, the transferred energy rapidly transforms into heat without causing significant chemical alterations [4-7]. However, in the presence of water or humid air in contact with the Cu, γ -radiation can induce decomposition of the molecules in the environment, leading to the formation of redox-active (H_2O_2 , $\text{HO}\cdot$, O_2 , H_2 , $\text{H}\cdot$ and e^-_{aq}) and acidic species (primarily nitric acid (HNO_3)) [8,9].

In the presence of a continuous γ -radiation flux, the concentrations of radiolysis species eventually stabilize, reaching a pseudo-steady state, typically on a micro- to millisecond timescale [4,10]. This can have an impact on the corrosion kinetics of metals as the oxidants become uniformly distributed in the solution [9]. The steady-state concentrations of radiolysis products are influenced by factors such as the radiation dose rate, solution pH, and the presence of radical scavengers like O_2 and Cl^- [3,11].

From a corrosion perspective, the crucial radiolysis products are the stable molecular species such as H_2O_2 , O_2 , H^+ , $\text{NO}_3^-/\text{NO}_2^-$, and, in highly saline ground waters, intermediate chloride radiolysis products like ClO and Cl_2 . Their importance is attributed to the different timescales of the various reactions occurring; while the more reactive radical species have only short lifetimes, the stable molecular products reach an equilibrium concentration in homogeneous solutions, which makes them important in corrosion processes [3].

The primary oxidant responsible for Cu corrosion in the presence of radiation is a subject of debate [12,13]. While higher dissolution rates have been attributed to radiolytically-produced radical species like HO• or, more recently, radiolytically produced O₂, [13-15] evidence supports the dominant influence of radiolytically-produced H₂O₂. H₂O₂ has been identified as the main oxidant in radiolytic processes over O₂, for both kinetic and thermodynamic reasons [4,12,16-18].

Recent investigations on radiation-induced corrosion of copper indicate that this process is significant in anoxic water at radiation doses similar to those expected in a deep repository [16-19]. Surface characterization revealed Cu₂O as the major oxidation product, and local corrosion features exhibited spatial periodicity (non-uniformity). These studies demonstrate that the primary pathway for the reaction between H₂O₂ and Cu and its oxides involves the catalytic decomposition of H₂O₂, rather than the oxidation of the solids [15,19].

Earlier research indicates that the corrosion rate tends to rise when a pre-oxidized layer is present on the copper surface. Furthermore, H₂O₂, a stable oxidative aqueous radiolysis product, primarily undergoes catalytic decomposition on oxide surfaces, suggesting it does not directly contribute to copper oxidation. This result contradicts the studies that implicate the direct role of H₂O₂ in corrosion [14,20,21].

Research on gamma radiation-induced corrosion of copper in moist air has been conducted with dose rates ranging from 0.1 to 0.7 kGy/h and total radiation doses of 107–510 kGy. These studies, conducted at relative humidities of 40–100% and temperatures of 90–150 °C, revealed the presence of cuprite (Cu₂O) and tenorite (CuO) on the copper surfaces [19,22,23].

The study by Bjorkbacka et al. [19] investigated the impact of gamma radiation on copper corrosion in de-aerated pure water with a pH around 7. Gamma irradiation was conducted over 168 hours using a Cs-137 gamma source, yielding dose rates of 0.37 or 0.77 kGy/h. Results indicate increased corrosion in irradiated specimens compared to unirradiated reference specimens, supported by higher copper concentrations in the water post-irradiation. Surface analysis revealed localized corrosion features, which were tentatively

attributed to anodic reactions in circular centres and cathodic reactions in surrounding areas.

Another study by Bjorkbacka et al. [20] examined the influence of a copper oxide layer on copper cubes exposed to γ -radiation in de-aerated pure water. Irradiations were conducted at ambient temperature and pH 5.5, with total radiation doses reflecting those expected on the outer canister surface within the first 100 years (about 100 kGy). Bjorkbacka et al. claimed that radiation-induced corrosion is markedly more pronounced on pre-oxidized copper than on polished copper. The proposed mechanism suggests the hydroxyl radical ($\text{HO}\cdot$) as the primary oxidative species fueling the corrosion process.

Soroka et al. [13] claimed that copper corrosion induced by exposure to H_2O_2 is primarily driven by molecular oxygen, which arises from the catalytic decomposition of H_2O_2 on the oxide surface. These findings, along with earlier observations [14], suggest that molecular oxygen is likewise the principal oxidant involved in radiation-induced corrosion of copper.

The long-term exposure (up to 360 days) study conducted by Ibrahim et al. [24] led to two distinct corrosion features: general corrosion covering most of the surface, observed as copper-coloured areas, and more extensively corroded patches, which appeared as purple/blue locations. XPS analyses indicated that after 7 days of exposure, the outermost surface layer (approximately 7 nm in thickness) consisted of a mixture of Cu (I) and Cu (II), with Cu (II) mainly present as $\text{Cu}(\text{OH})_2$. Subsequent analyses after exposure for 90, 180, and 300 days showed that CuO became the dominant phase in the top few nanometers of both the generally corroded areas and the more extensively corroded patches.

7.2 Experimental

7.2.1 Specimen preparation

Coupons were cut from O-free, P-doped wrought copper blocks provided by the SKB. Experiments were conducted in triplicate using three Cu specimens subjected to irradiation, and a reference specimen, treated identically to the irradiated specimens but without irradiation.

7.2.2 Solution preparation

To promote oxide growth, solutions were prepared as described in section 3.2.3.1. Subsequently, the designated volume of the test solution (either 400 or 500 μL) was applied to the surface of each coupon using a micro-pipette. The initial pH of 9.0 was selected because the solubilities of both Cu (I) and Cu (II) species are at a minimum at that value.

The radiolytically-grown oxides were then exposed to bisulfide solutions with a $[\text{SH}^-]$ concentration of 5×10^{-5} M, as detailed in section 3.3.1. Each bisulfide solution contained a 0.1 M NaCl supporting electrolyte.

7.2.3 Specimen irradiation

The specimens were placed in custom-designed holders to ensure consistent radiation exposure across all vials during the 24, 48, and 70 h-irradiation periods in a cobalt-60 (^{60}Co) gamma-irradiation cell. For the radiation experiments in this thesis, the absorbed radiation dose rate was 1.1 kGy/h. Following irradiation, individual vials were periodically removed from the chamber. Each coupon was then removed from the vial, rinsed with Type-I water, dried using Ar gas, and stored in a glove box for subsequent electrochemical and surface analyses. Solution samples were also collected with a plastic pipette for pH measurement.

7.2.4 Electrochemical cell design and instrumentation

See section 3.2.1.2.

7.2.5 Electrochemical/corrosion experiments

All tests were conducted within a Faraday cage to minimize disruptions from external electrical sources. Prior to each experiment, solutions containing bisulfide underwent a 30-minute purging process with ultra-high purity Ar gas, which continued throughout the duration of the experiment.

7.2.5.1 Corrosion potential measurements

Corrosion potentials (E_{corr}) were measured after transferring the oxidized specimens to an electrochemical cell containing SH^- solutions.

7.2.5.2 Cathodic stripping voltammetry

Following the measurement of E_{corr} in the bisulfide solution, the potential was scanned from the last recorded E_{corr} value to -1.4 V/SCE at a scan rate of 10 mV/min to cathodically reduce the oxide and sulfide films present on the electrode surface. The emergence of cathodic peaks at specific potentials was utilized to identify the types of oxide and sulfide phases present.

7.2.6 Surface analyses

7.2.6.1 Laser Raman spectroscopy

Raman spectroscopy was utilized to analyze the composition of the film formed on the surface of the coupons, both before and after exposure to SH^- solutions. The details are described in section 3.5.2.2.

7.2.6.2 Optical Microscopy

Optical microscopy was used to observe the details of the formation of thin hydroxide/oxide and sulfide films on the specimen surfaces. For more details, see section 3.5.1.1.

7.2.6.3 Scanning electron microscopy

The surface topography and morphology of the coupons were examined using SEM coupled with energy dispersive X-ray spectroscopy (EDX) used to determine the elemental composition of the surface. FIB/SEM was employed to investigate the film/substrate interface and the cross-sectional morphology of the films and to observe film thicknesses and porosity. More details are described in sections 3.5.1.2 and 3.5.1.4.

7.3 Results and Discussion

7.3.1 Characterization of radiolytically-grown oxide film

7.3.1.1 In 400 μL aerated pure water (pH_0 9)

Optical microscopy offers the capability to observe the entire surface at any given time and to identify the presence of deposited layers based on specific colours associated with different compounds. This provides insights into the copper oxidation state and the anion involved in the complex. Cupric hydroxide ($\text{Cu}(\text{OH})_2$), typically bluish-green, is known to exhibit polymorphism, often appearing as fibrous or colloidal structures [4,25-28]. Cu_2O can vary from yellow to deep red depending on crystal size, with smaller crystals exhibiting a yellow hue due to quantum confinement effects [29-32]. By contrast, CuO appears black in colour [33].

Copper specimens were periodically extracted from the irradiation chamber and subsequently stored in a glove box for further surface analysis. The optical images from irradiated specimens after different exposure periods are shown in **Figure 7.1**.

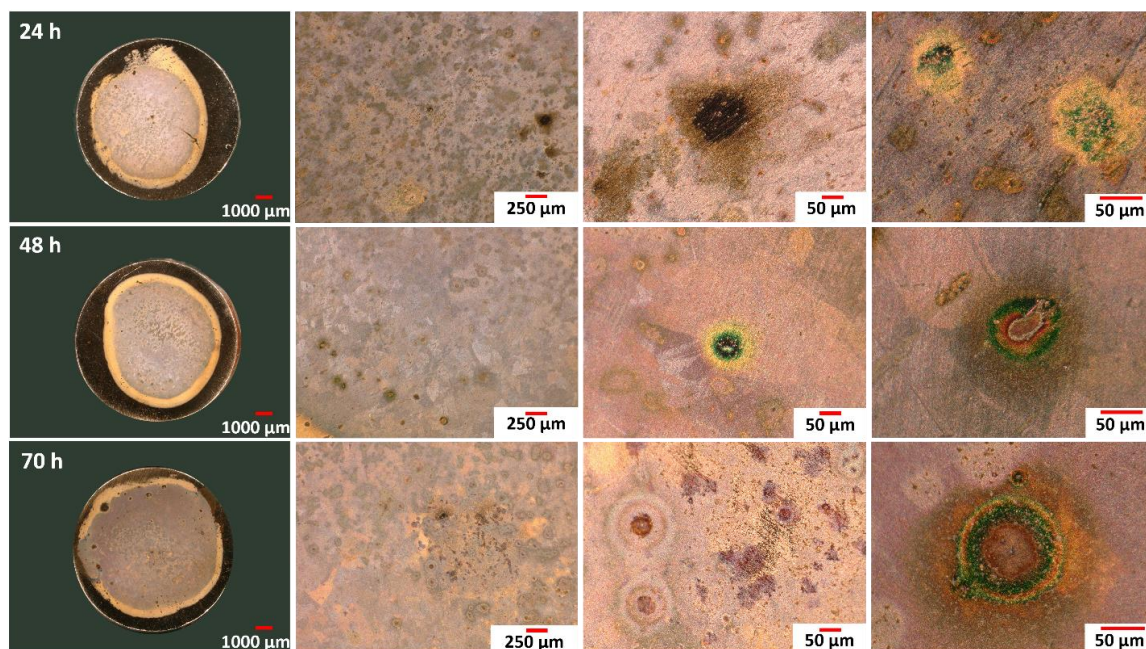


Figure 7.1: Optical images during copper corrosion after exposure to 400 μL of aerated pure water (pH_0 9) in the presence of γ -radiation.

Figure 7.1 shows optical images of Cu surfaces after exposure to irradiated aerated water for various times. The surface of the 24 h-irradiated specimen displayed a predominantly light purple film covering its centre, transitioning into a yellowish ring around the outer edge. Circular features [19,20], ranging in colour from light brown to dark yellow, were evident across the surface, and the grinding lines due to surface preparation remained visible at higher magnifications. Additionally, some of these circular features appeared to contain a green compound, although their shape was not precisely circular, exhibiting a tendency towards circularity.

At low magnification, the 48 h-irradiated specimen exhibited a surface pattern similar to that of the 24 h-irradiated specimen. However, significant differences included a more uniform oxide layer, with less noticeable grinding lines. The colour of the oxide film appeared more purple and light blue, with the presence of concentric waves and an increased contribution of a green compound within the circular features. Additionally, the size of the circular features was larger than those of the 24 h-irradiated specimen.

After 70 h of irradiation, the oxide film extended across most of the surface. More purple, blue, and pink concentric waves were visible across the surface. Some parts of the surface appeared to have increased thickness compared to the 48 h-irradiated specimen, as grinding lines were no longer detectable. The contribution of a green-coloured compound within the circular features remained observable.

SEM was used to provide detailed information on the film morphology at higher resolution, with the elemental composition of selected locations analyzed using EDX. **Figure 7.2** shows SEM images of locations selected for EDX analysis on the Cu surface, both in the absence and presence of irradiation.

Figure 7.2 (a) displays SEM images of the non-irradiated specimen, revealing the presence of only a thin oxide layer on the surface, as evidenced by the visible grinding lines. Additionally, small black particles identified as silicon (Si) residues from the grinding process using SiC paper were observed. The EDX analysis recorded at the location marked 1, **Table 7.1**, shows the presence of a small amount of oxygen (O) (0.3 wt%), confirming the presence of a thin oxide.

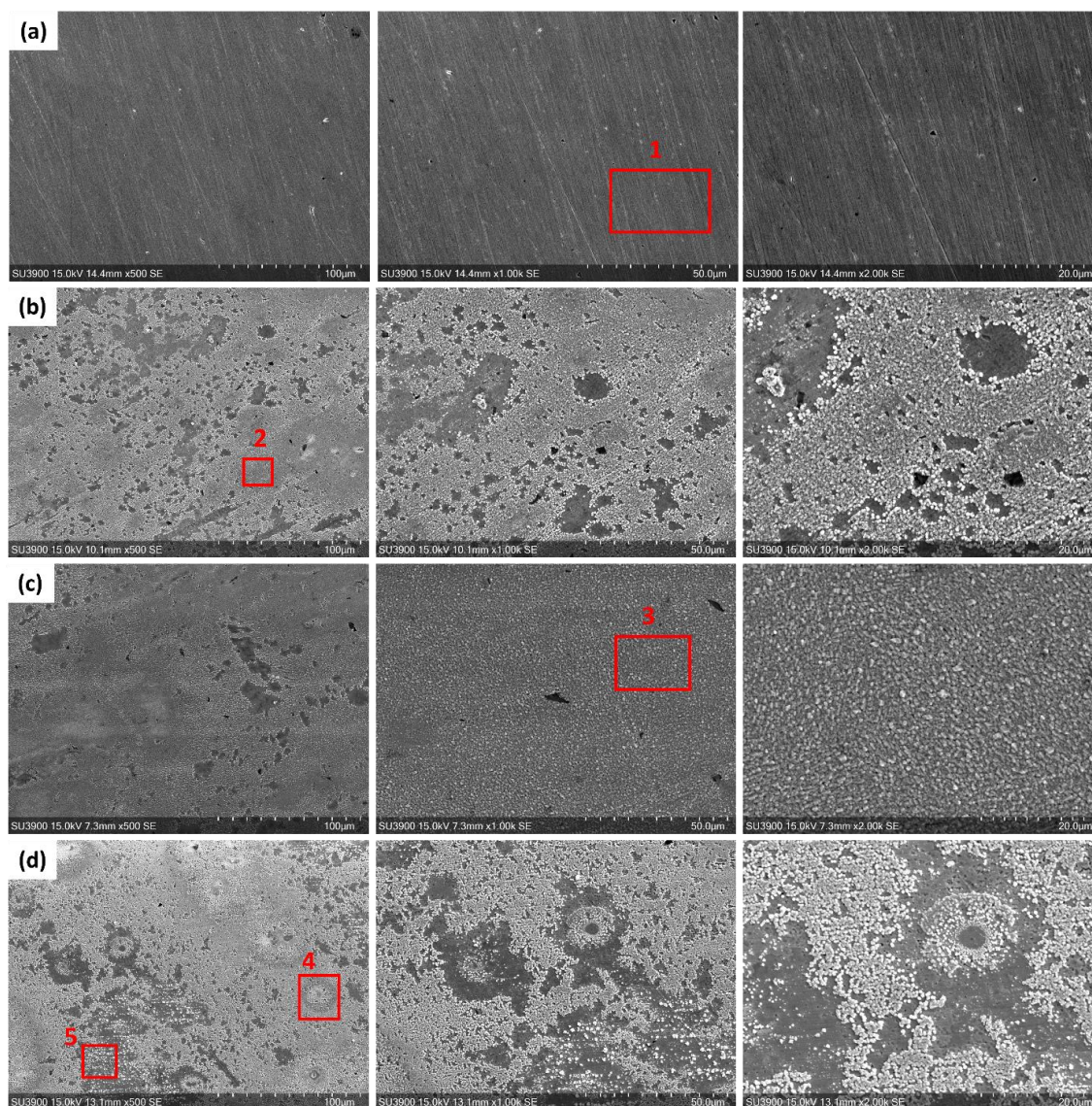


Figure 7.2: SEM images of the copper surface in 400 μL of aerated pure water solutions ($\text{pH}_0 = 9$) in the absence (a) and presence of γ -radiation (b) 24 h, (c) 48 h, and (d) 70 h (Red boxes show the selected locations for EDX).

After 24 h of radiation exposure, **Figure 7.2 (b)**, the surface was mostly covered with patches of fine particulates. This film did not provide perfect coverage, and Si particles were still visible on the surface. The EDX analysis (region 2) revealed an increase in O content to 7.1 wt%, confirming the formation of an O-containing deposit, along with 0.2 wt% chlorine (Cl). The source of Cl detected on the surface is uncertain but consistent with findings by Ibrahim et al. [24].

Table 7.1: Composition (wt. %) of the surface oxides (shown in **Figure 7.2**) formed during corrosion in the absence and presence of γ -radiation in aerated pure water (400 μ L).

Spectrum Label	Cu	O	C	Cl	Si
Spectrum 1	93.2	0.3	6.5	-	-
Spectrum 2	86.3	7.1	6.4	0.2	-
Spectrum 3	84.6	9.0	6.2	0.2	-
Spectrum 4	82.7	8.4	8.6	0.3	-
Spectrum 5	87.2	3.4	9.2	0.1	0.1

SEM images after 48 h of exposure, as depicted in **Figure 7.2 (c)**, show an increased film coverage and larger particle size than seen during the 24 h-exposure. Although Si particles were still visible on the surface, indicating a thin film, there was a notable improvement in coverage. EDX analysis in region 3 (**Table 7.1**) shows a higher O content on the surface, confirming the formation of an oxide/hydroxide film. Also, a small amount of Cl persisted.

Raman spectroscopy was employed to analyze the composition of the oxide film on both the non-irradiated and irradiated specimens after 70 h of exposure to 400 μ L of solution, shown in **Figure 7.3**.

Pure Cu_2O and $\text{Cu}(\text{OH})_2$ exhibit similar Raman characteristic peaks, albeit with minor differences in peak intensity. Cu_2O displays a sharp peak at 218 cm^{-1} , along with peaks at 523 cm^{-1} and 623 cm^{-1} , with the latter being more intense than the former. In contrast, $\text{Cu}(\text{OH})_2$ shows a weak or negligible peak at 218 cm^{-1} , and a 523 cm^{-1} peak that is more intense than the 623 cm^{-1} peak. Consequently, a combination of $\text{Cu}(\text{OH})_2$ and Cu_2O would yield spectra with peaks at 218 cm^{-1} , 523 cm^{-1} , and 623 cm^{-1} , with the intensities of the 523 cm^{-1} and 623 cm^{-1} peaks being similar [8].

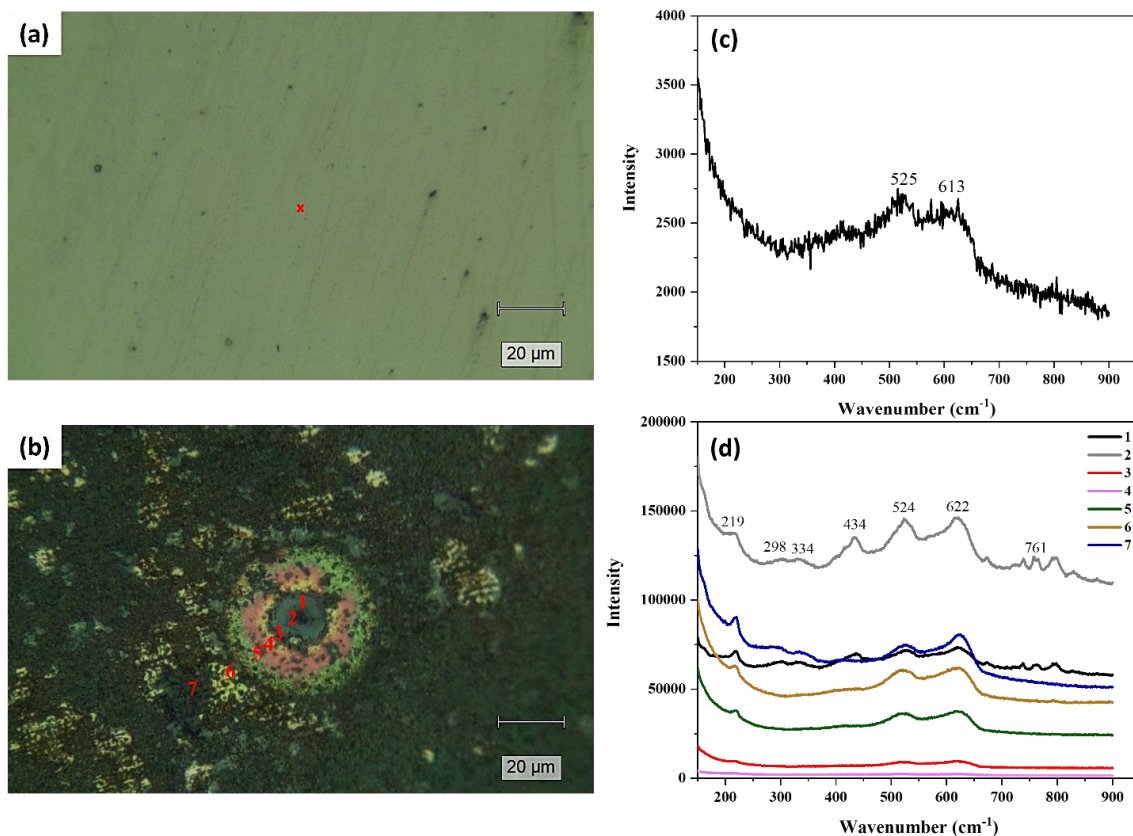


Figure 7.3: Image and Raman spectrum (a,c) of a Cu surface corroded for 70 h in 400 μL of aerated pure water in the absence of γ -radiation and image and Raman spectra (b,d) of a Cu surface corroded for 70 h in 400 μL of aerated pure water in the presence of γ -radiation (Selected locations are shown with red x and numbers).

After 70 hours, **Figures 7.3 (a)** and **7.3 (c)**, the surface of the non-irradiated specimen appeared to be predominantly covered by $\text{Cu}(\text{OH})_2$, as indicated by characteristic peaks at 525 cm^{-1} (more intense) and 613 cm^{-1} . Since both Cu_2O and $\text{Cu}(\text{OH})_2$ yield similar peaks, the presence of Cu_2O is also possible. For the 70 h-irradiated specimen, **Figures 7.3 (b)** and **7.3 (d)**, analyzing various locations provided insights into the composition gradient from the inner to outer waves in the concentric wave patterns. Moving outward, the intensity of peaks at 298 cm^{-1} , 334 cm^{-1} , 434 cm^{-1} , and 761 cm^{-1} decreased. Spectra 1 and 2 displayed the above characteristic peaks, which could be indicative of malachite ($\text{Cu}_2(\text{CO}_3)(\text{OH})_2$) [8,34]. In an aerated environment, $\text{CO}_2(\text{g})$ would be present in the

solution and react with water to produce H_2CO_3 , which can lower the initial pH to around 6.0-6.5. After 70 h of irradiation, pH measurement confirmed a decrease from 9 to 6.5.

Although radiolytically-produced nitrate is also expected to be present in the solution, Raman spectra show no indication of its presence. This is consistent with the formation of green malachite, $\text{Cu}_2(\text{CO}_3)(\text{OH})_2$, at locations 1 and 2, since this phase is favoured thermodynamically over the growth of a basic copper nitrate complex ($\Delta G^\circ_f(\text{Cu}_2(\text{CO}_3)(\text{OH})_2) = -903.3 \text{ kJ/mol}$, $\Delta G^\circ_f \text{Cu}_2(\text{NO}_3)(\text{OH})_3 = -653.2 \text{ kJ/mol}$) [35,36].

Spectra 3, 4, 5, and 6 (**Figure 7.3** and **Table 7.1**) suggest a combination of Cu_2O and $\text{Cu}(\text{OH})_2$, with similar intensities of peaks at 524 cm^{-1} and 622 cm^{-1} . Spectrum 7, obtained from a spot outside the feature, exhibited peaks possibly associated with CuO , such as those at 298 cm^{-1} and 334 cm^{-1} [37]. In areas with minimal coverage (not shown here), a more yellowish film resembling the composition of the non-irradiated specimen was observed.

7.3.1.2 In 500 μL aerated pure water (pH₀ 9)

Under DGR conditions, minimal amounts of water will be present on the Cu surface under stagnant conditions. Various solution parameters, such as the thickness of the surface water layer, its pH, and ionic content, can affect oxide formation [8]. To investigate the impact of a limited depth of water on oxide formation, a Cu specimen was subjected to gamma-radiation (1.1 kGy/h) for 70 h in a 500 μL solution.

The SEM images in **Figure 7.4**, including BSE and SE images, coupled with images of FIB-cut cross sections show the surface topography and film thickness.

The SEM images reveal distinctive features of the radiolytically-grown oxide, characterized by localized patterns, such as concentric waves, and scattered, apparently corroded patches. The visible grinding lines confirm that the general surface is covered by a thin oxide layer. The images also show that the distribution of corrosion products is non-uniform, with thicker regions covered with larger granular particles. The cross-sections show a two-layer structure with a general thickness of $\sim 385 \text{ nm}$ and a secondary thicker deposit in some areas which can achieve a thickness of 781 nm.

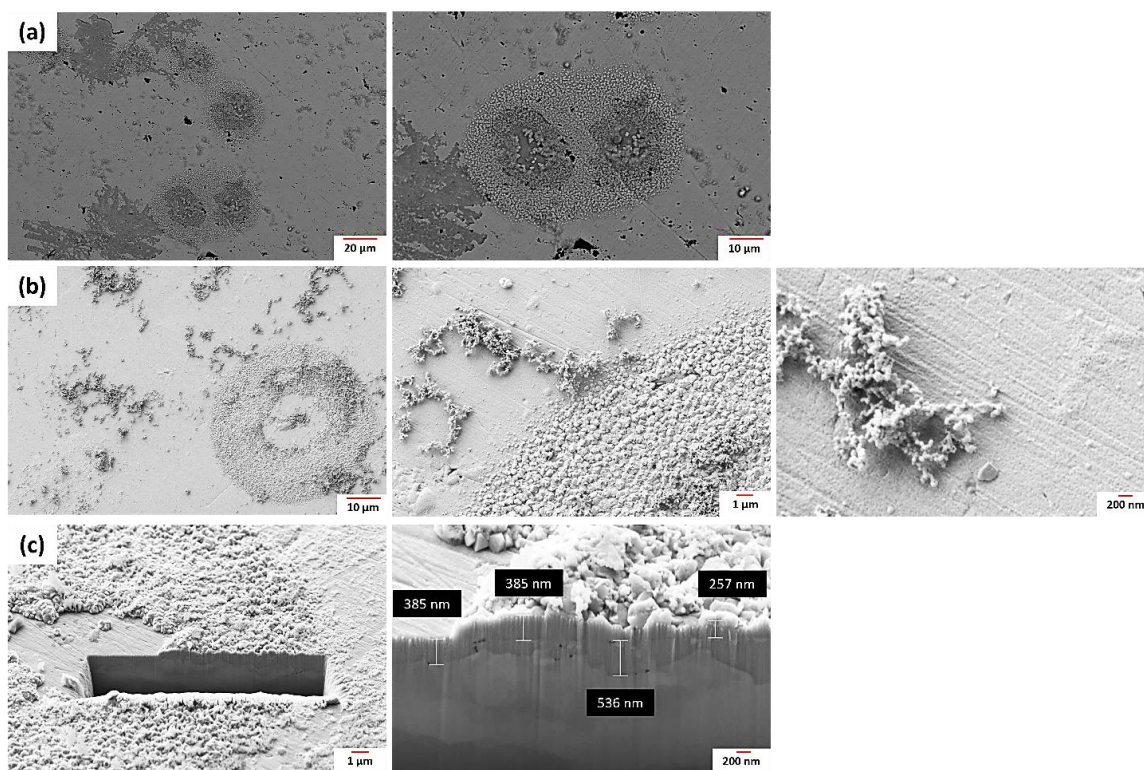


Figure 7.4: SEM images (a) BSE and (b) SE of the surface and (c) the metal-oxide cross-section (cut using focused Ga-ion beam) after 70 h corrosion in 500 μL aerated pure water solution in the presence of γ -radiation.

The EDX map depicted in **Figure 7.5** illustrates the distribution of O on the surface. O was predominantly concentrated within the circular features and nano-particulate patches. The SEM images in **Figure 7.4** (c) indicate the presence of a thin layer on areas without a particulate deposit, although it is difficult to detect by EDX.

The Raman spectrum of the surface covered by only a thin layer, **Figure 7.6** (top row), reveals that the surface layer of the 70 h-irradiated specimen in 500 μL solution predominantly consists of $\text{Cu}(\text{OH})_2$ due to the peaks that appear at 430, 524, and 615 cm^{-1} . Moreover, the Raman spectra (bottom row) obtained from various locations within the circular features indicate a multi-layer film composition comprising Cu (I) and Cu (II)-containing species. The central region is primarily composed of Cu_2O , with characteristic peaks at 218, 410, 523, and 624 cm^{-1} [37-39] while towards the outer regions, the presence of Cu (II)-containing species, became more apparent as indicated by more pronounced

peaks at 293 and 336 cm^{-1} for CuO and peaks at 523 and 624 cm^{-1} with equal intensity for $\text{Cu}(\text{OH})_2$.

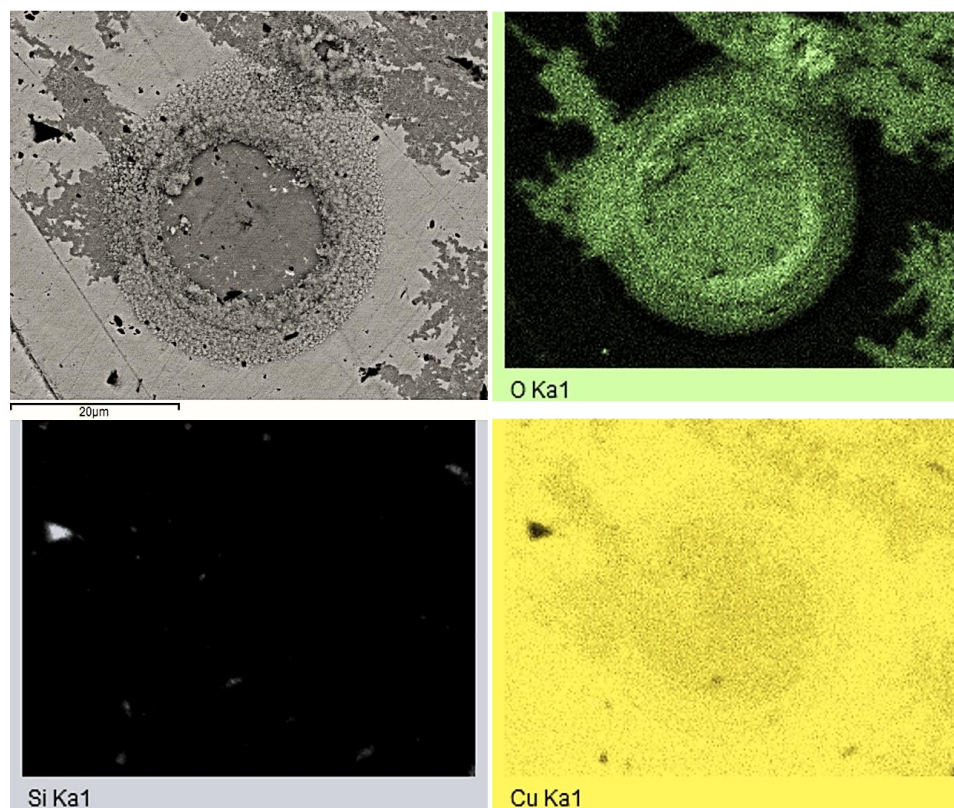


Figure 7.5: EDX map of a circular feature and the surrounding colloidal patches on a Cu surface after 70 h-corrosion in $500\ \mu\text{L}$ of aerated pure water ($\text{pH}_0\ 9$) in the presence of γ -radiation.

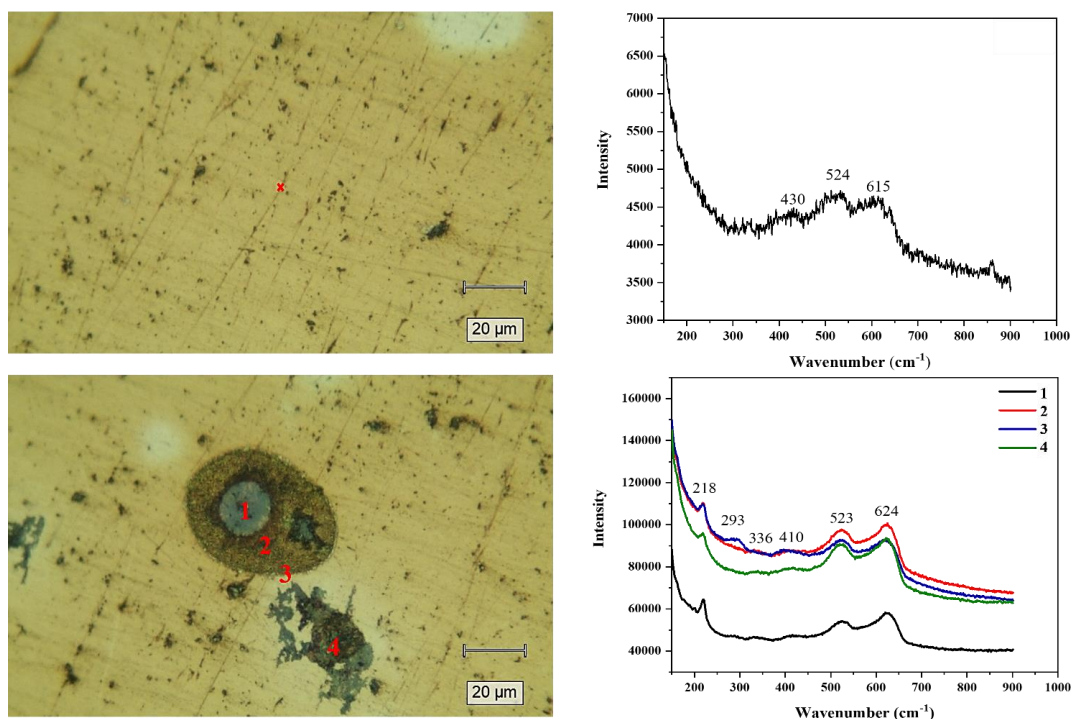


Figure 7.6: Images and Raman spectra of the base layer (top row) and a circular feature (bottom row) on the surface oxide after 70 h-corrosion in 500 μL of aerated pure water (pH_0 9) in the presence of γ -radiation (Selected locations are shown with red x and numbers).

7.3.2 Characterization of the sulfidized grown oxide

7.3.2.1 Radially-grown oxide in 400 μL aerated pure water (pH_0 9)

The specimens with a grown oxide were subsequently immersed in a solution containing 0.1 M Cl^- + 5×10^{-5} M SH^- for 20 h. Optical images of the exposed surfaces are shown in **Figure 7.7**.

After exposure to a bisulfide-containing solution, the 24 h-irradiated specimen displayed a uniform film around the perimeter and a more intricate film in the central region. The prevalent colour hues observed were light blue, light gray, and dark blue/purple. Upon closer examination, circular features were noted on the surface. While their shape and number density remained consistent with those of the oxidized specimen, there was a noticeable change in colour.

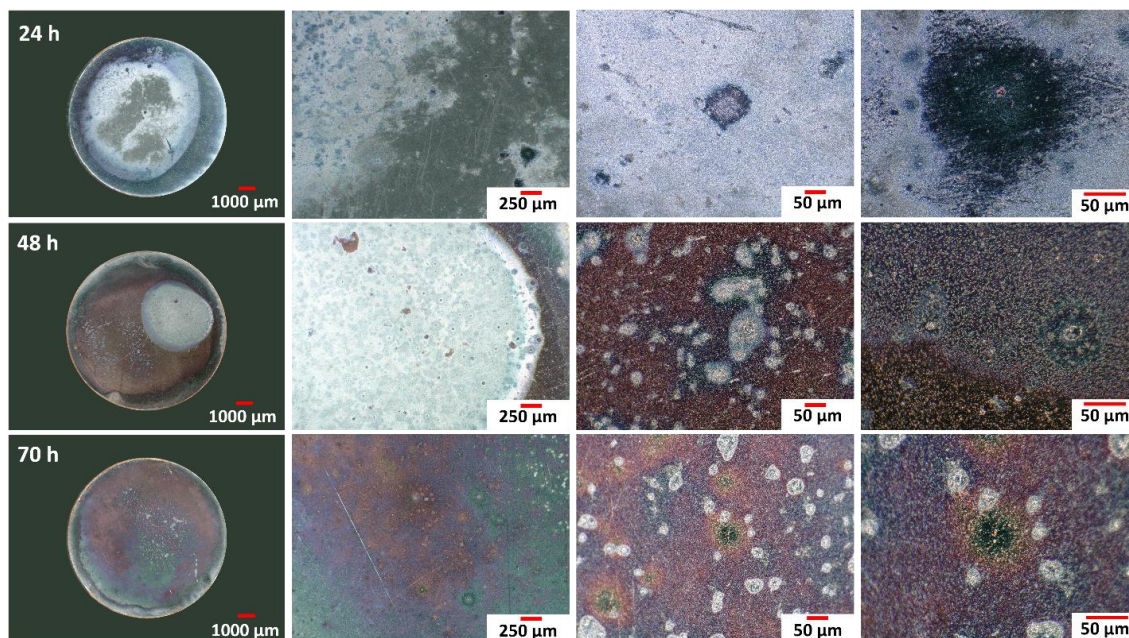


Figure 7.7: Optical images of the grown oxide in 400 μL of pure water in the presence of γ -radiation; 24 h, 48 h, and 70 h after 20 h-immersion in a 0.1 M $\text{Cl}^- + 5 \times 10^{-5}$ M SH^- solution.

A variety of colours were observed on the 48 h-irradiated specimen, including dark brown, light blue, and dark purple, indicating a possible non-uniformity in the composition of the surface film. Various structural features ranging from ovals to circles are evident across the surface. Following the exposure of the 70 h-irradiated specimen to bisulfide-containing solution, the surface film appeared more homogeneous, with predominant colours being blue, purple, and orange in some areas. Notably, features containing green compounds appeared unchanged or showed minimal alteration (also observed in 24 h- and 48 h-irradiated specimens). Colour changes were more pronounced at the edges of the specimens compared to the centre in all cases.

The SEM images, **Figure 7.8**, offered a morphological comparison between the non-irradiated specimen and those exposed to radiation following a 20 h-immersion in the bisulfide solution. Additionally, EDX analysis, **Table 7.2**, on various spots provided insights into the elemental composition.

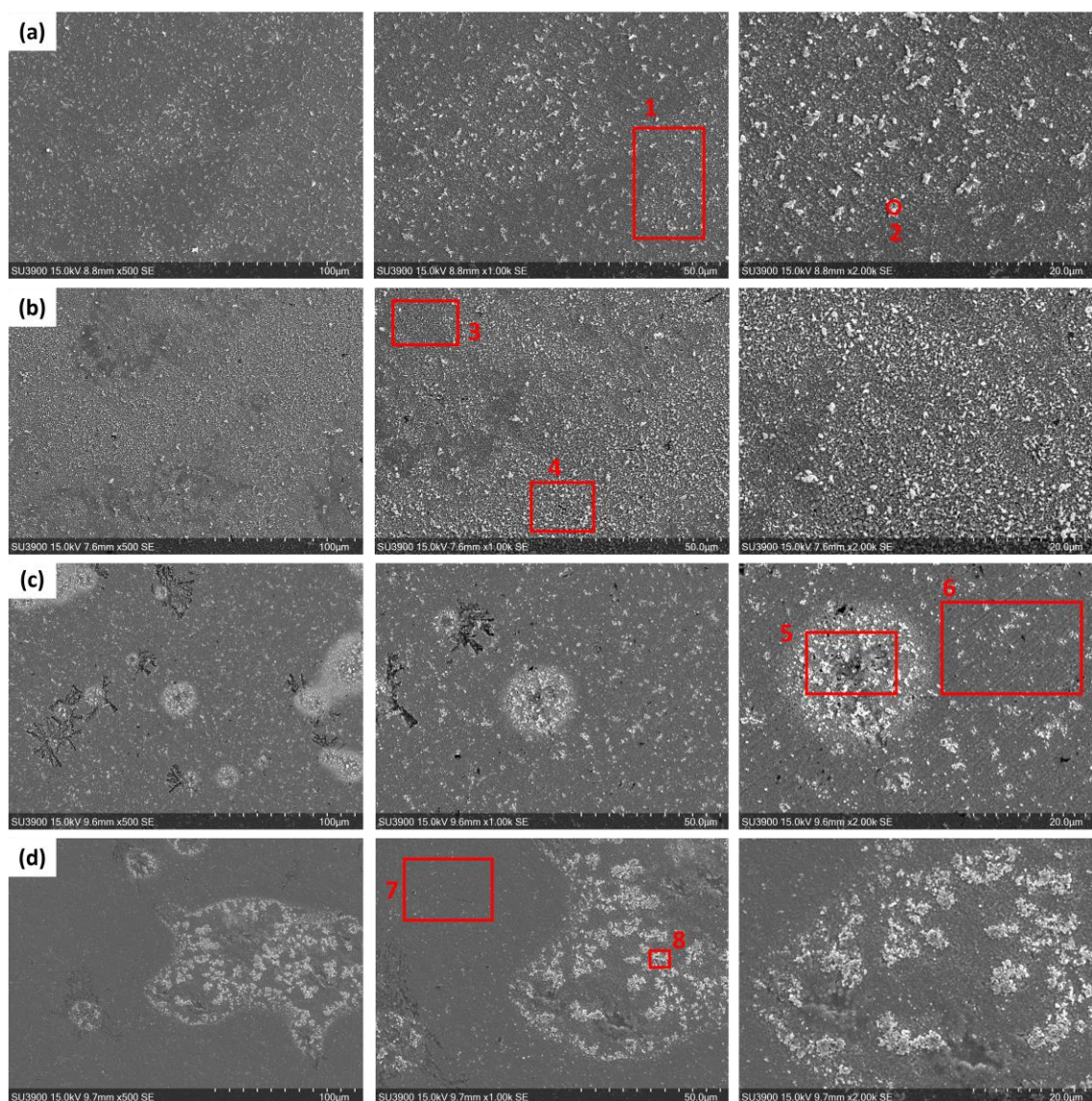


Figure 7.8: SEM images of the grown oxide in 400 μL of pure water in the absence of γ -radiation (a) and in the presence of γ -radiation (b) 24 h, (c) 48 h, and (d) 70 h after 20 h-immersion in a 0.1 M $\text{Cl}^- + 5 \times 10^{-5}$ M SH^- solution (Red boxes show the selected locations for EDX).

Upon exposure of the non-irradiated specimen to the bisulfide solution, the surface morphology of the specimen, **Figure 7.8 (a)**, shows a sparse distribution of fine particles. The EDX analysis of the general surface (location 1, **Figure 7.8 (a)**) shows a dominant S signal but a detectable O signal also. Since the density of particles was sparse, this dominance suggests that a general but incomplete conversion of oxide to sulfide had

occurred. EDX analysis on a particle indicates the S signal is enhanced and no O detected confirming the particles are Cu sulfide.

Table 7.2: Composition (wt. %) of the surface films (shown in **Figure 7.8**) after 20 h-immersion in a 0.1 M $\text{Cl}^- + 5 \times 10^{-5}$ M SH^- solution.

Spectrum Label	Cu	O	S	C	Si
Spectrum 1	85.9	0.5	5.0	8.6	-
Spectrum 2	81.0	-	8.8	10.2	-
Spectrum 3	81.6	1.2	10.4	6.8	-
Spectrum 4	80.0	1.1	11.8	7.1	-
Spectrum 5	89.5	0.3	3.7	6.3	0.2
Spectrum 6	81.5	0.5	9.9	7.5	0.6
Spectrum 7	86.7	-	4.7	8.6	-
Spectrum 8	78.9	0.4	10.6	9.9	0.2

Figure 7.8 (b) depicts the surface of the 24 h-irradiated specimen following a 20 h-exposure to a bisulfide solution. In contrast to the non-irradiated specimen, the irradiated surface exhibited a higher density of granular particles, suggesting either/or both a more extensive conversion of oxide to sulfide and/or a more extensive corrosion of the Cu substrate to Cu_2S at faults or pores in the surface oxide formed during irradiation. The more general formation of copper sulfide on this irradiated surface is confirmed by the EDX analyses of areas with apparently lower (location 3, **Figure 7.8 (b)**) and higher (location 4, **Figure 7.8 (b)**) densities of patches and the accompanying increases in the amount of S detected by EDX (**Table 7.2**).

A similar, more extensive formation of sulfide is observed on specimens subjected to more extended periods of irradiation, **Figures 7.8 (c)**, **Figure 7.8 (d)**, and **Table 7.2**. Comparison

of the S levels in areas 5 and 6 (**Figure 7.8 (c)**) and 7 and 8 (**Figure 7.8 (d)**) on specimens irradiated for 48 and 70 h, respectively demonstrate that sulfide formation was more extensive in the patches (often circular) within which corrosion damage during irradiation occurred more extensively, **Figures 7.2 and 7.3**, to produce a more porous, and hence less protective $\text{Cu}_2\text{O}/\text{Cu}(\text{OH})_2/\text{Cu}_2(\text{CO}_3)(\text{OH})_2$ deposit. These observations suggest that oxide-to-sulfide conversion may dominate on the general oxide-covered surface. The more extensive formation of sulfide particles in the areas more extensively corroded during irradiation suggests a more extensive corrosion of the Cu substrate in these less protected areas of the surface.

Raman spectroscopy was conducted on the specimen irradiated for 70 h followed by a 20 h-immersion in a solution containing $0.1 \text{ M Cl}^- + 5 \times 10^{-5} \text{ M SH}^-$. Various spectra, **Figure 7.9**, obtained from different locations, revealed differing intensities of the characteristic peak for sulfide at 300 cm^{-1} [40]. Additionally, peaks at 520 and 621 cm^{-1} suggested the presence of oxide (Cu_2O) on the surface [8]. The low intensity at location 1 suggests this location was an exposed Cu site. The evolution in colour from black to green, accompanied by the increasing relative intensity of the peak for Cu_2S , suggests the surface was covered by an oxide in the core, surrounded by Cu_2S on the surface remote from the central location.

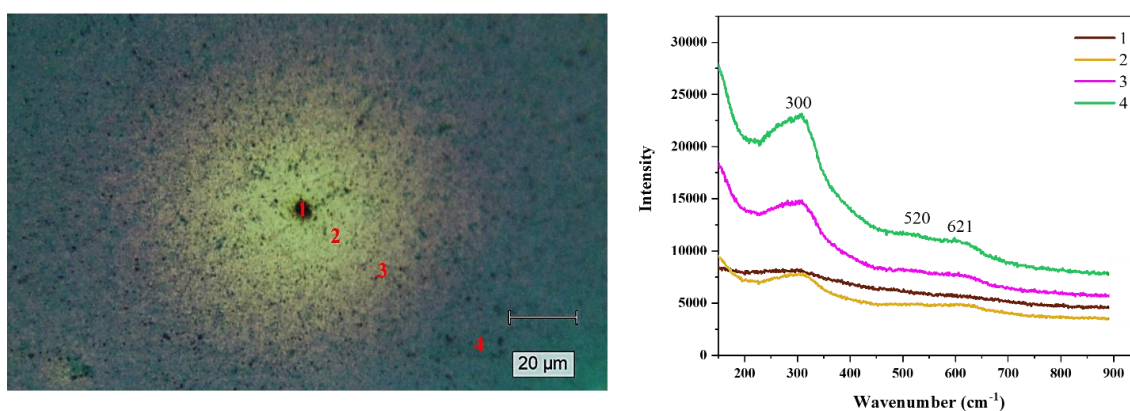


Figure 7.9: Optical image and Raman spectra recorded at selected locations on the grown oxide (70 h-radiation in $400 \mu\text{L}$ pure water) after 20 h-immersion in a $0.1 \text{ M Cl}^- + 5 \times 10^{-5} \text{ M SH}^-$ solution (Selected locations are shown with red numbers).

7.3.2.2 Radiolytically-grown oxide in 500 μL aerated pure water (pH 9)

The effect of bisulfide ions on the conversion of radiolytically-grown oxide was investigated by measuring E_{corr} over the exposure period, **Figure 7.10**. A 70 h-irradiated specimen was immersed in a solution containing $0.1 \text{ M Cl}^- + 5 \times 10^{-5} \text{ M SH}^-$. Initially, E_{corr} exhibited a value near -0.14 V/SCE , close to the equilibrium potentials of $\text{Cu}/\text{Cu}(\text{OH})_2$ and Cu/CuO [40]. However, immersion in the bisulfide-containing solution caused a shift in the E_{corr} , which eventually achieved a value close to -0.85 V/SCE after partial arrests around -0.3 V/SCE and -0.7 V/SCE . The final steady-state value was approaching the E_{corr} at which the dominant reaction would be the corrosion of Cu to Cu_2S , as mentioned in previous chapters [40,41].

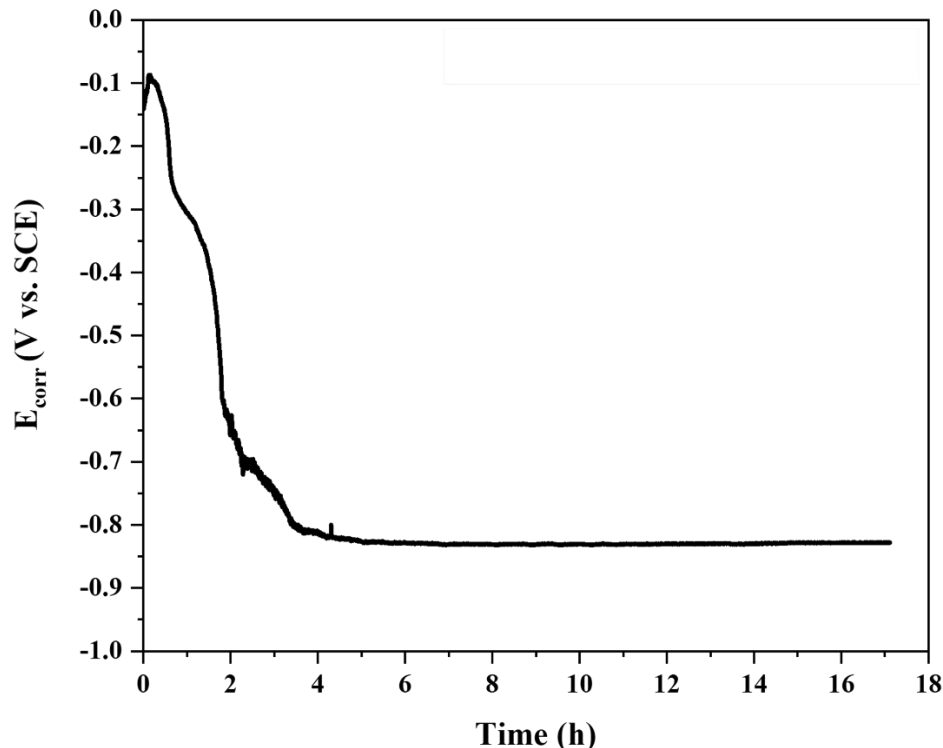


Figure 7.10: E_{corr} measurement as a function of time for a grown oxide (70 h-radiation in 500 μL pure water) after immersion in a $0.1 \text{ M Cl}^- + 5 \times 10^{-5} \text{ M SH}^-$ solution.

Cathodic stripping voltammetry (CSV) was used to investigate the evolution of the oxide-to-sulfide conversion reaction, **Figure 7.11**.

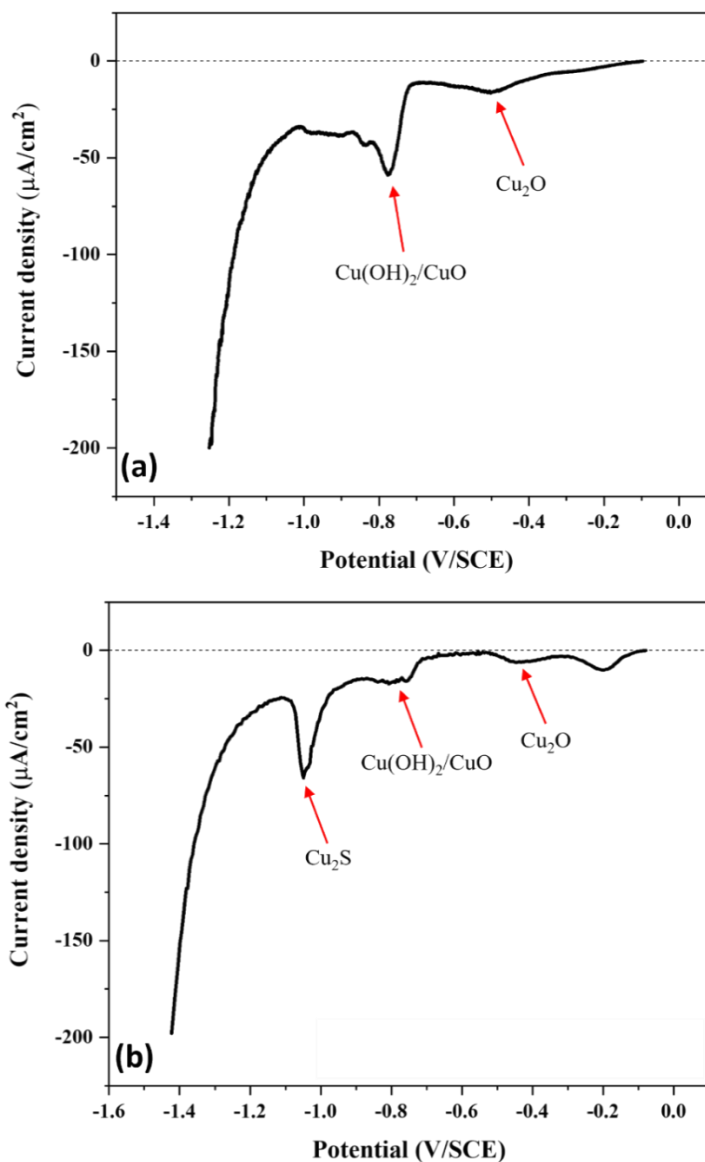


Figure 7.11: Cathodic stripping voltammograms of grown oxide (70 h-radiation in 500 μL pure water) after transfer to a (a) 0.1 M Cl^- , and (b) 0.1 M $\text{Cl}^- + 5 \times 10^{-5}$ M SH^- solution at 10 mV/min.

Figure 7.11 (a) shows the CSV recorded on a specimen with a grown oxide/hydroxide/malachite film in a solution containing only 0.1 M Cl^- . Three distinct peaks were observed at a scan rate of 10 mV/min. The first peak occurred around -0.45 V/SCE, and corresponds to the reduction of Cu_2O , as mentioned in **Chapter 4**. Two additional peaks around -0.8 and -0.85 V/SCE suggest the presence of Cu (II) oxide and

Cu (II) hydroxide on the surface [40, 41]. This indicates that the radiolytically-formed oxide consists of a mixture of Cu (I) and Cu (II)-containing species, consistent with the Raman analyses (**Figure 7.3**). A different CSV was observed in a $0.1 \text{ M Cl}^- + 5 \times 10^{-5} \text{ M SH}^-$ solution. Since the extended time required to complete the CSV was nearly 2 h, a detectable amount of $\text{Cu}_2\text{O}/\text{Cu}(\text{OH})_2/\text{Cu}(\text{CO}_3)(\text{OH})_2$ was converted to Cu_2S , as indicated by the observance of peak between -1.0 V/SCE and -1.1 V/SCE shown previously in **Chapter 5** to be due to the reduction of Cu_2S . That partial conversion of the grown film to Cu_2S had occurred was indicated by the decrease in the charges associated with the reduction of the Cu (I)/Cu (II) phase originally present. The additional peak at a more positive potential, along with the reduction peak for Cu_2O , is presently unassigned but is at a potential at which Cu(I) oxide would be reduced.

SEM images of the surface and cross-section of the sulfidized 70 h-irradiated specimen in $0.1 \text{ M Cl}^- + 5 \times 10^{-5} \text{ M SH}^-$ solution after 20 h, **Figure 7.12**, revealed a thin base layer with an average thickness of 86 nm. The EDX analysis, **Table 3**, showed 0.4 wt% O and 3.5 wt% S in this layer. The accumulated particulates on the surface, with an average thickness of 818 nm, exhibited 0 wt% O and 10.9 wt% S. Notably, circular features observed on the radiolytically formed oxides in $400 \mu\text{L}$ were absent in this case.

As can be seen in **Figure 7.13**, Raman spectroscopy conducted on various locations on the sulfidized 70 h-irradiated specimen after a 20h-immersion in $0.1 \text{ M Cl}^- + 5 \times 10^{-5} \text{ M SH}^-$ solution reveal that the surface was predominantly covered by a sulfide film, Cu_2S (main peak at 301 cm^{-1}) [42], with the remainder mostly consisting of Cu_2O species showing peaks at 218, 520, and 610 cm^{-1} [37,38]. The intensity of Raman characteristic peaks for the sulfide film varied across the surface, indicating spatial heterogeneity.

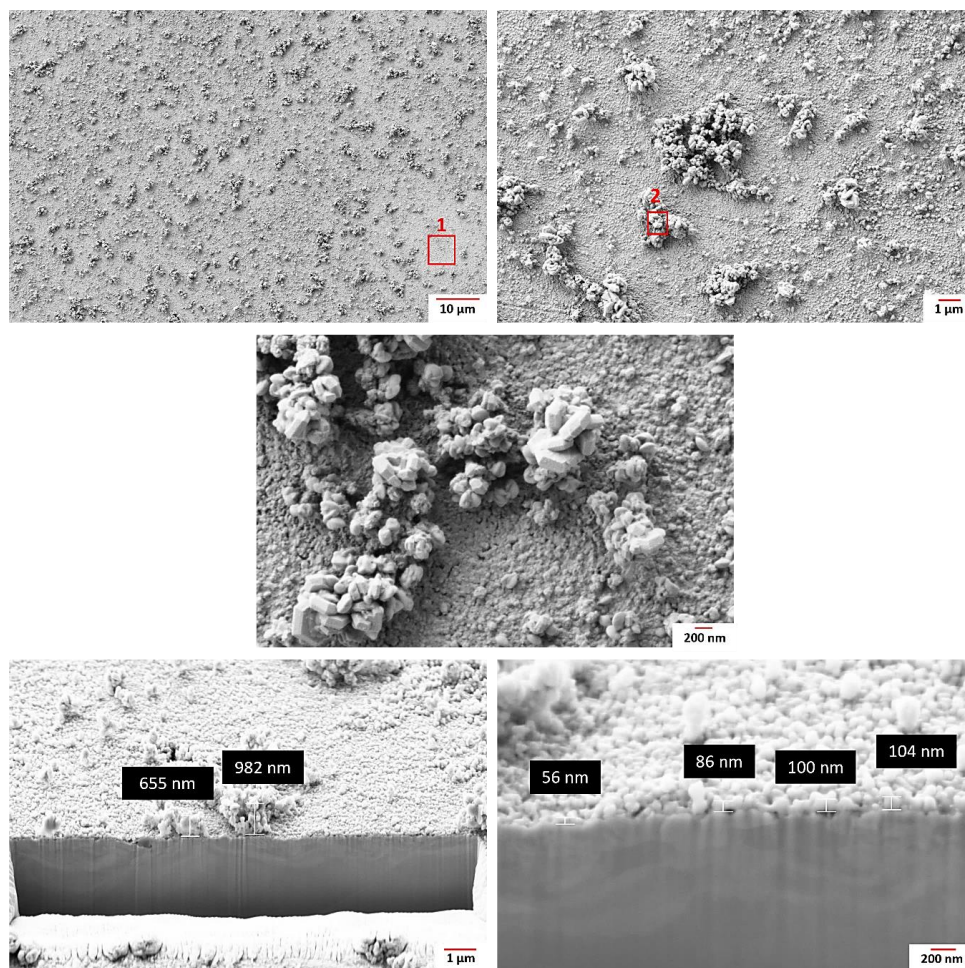


Figure 7.12: SEM images (top and middle rows) and FIB cross-sections (bottom row) of the grown oxide corroded for 70 h in a 500 μL of pure water in the presence of γ -radiation after immersion in a 0.1 M $\text{Cl}^- + 5 \times 10^{-5}$ M SH^- solution (Red boxes show the selected locations for EDX).

Table 7.3: Composition (wt. %) of the surface films (shown in **Figure 7.12**) after 20 h-immersion in a 0.1 M $\text{Cl}^- + 5 \times 10^{-5}$ M SH^- solution.

Spectrum Label	Cu	O	S	C
Spectrum 1	93.2	0.4	3.5	2.9
Spectrum 2	84.4	-	10.9	4.7

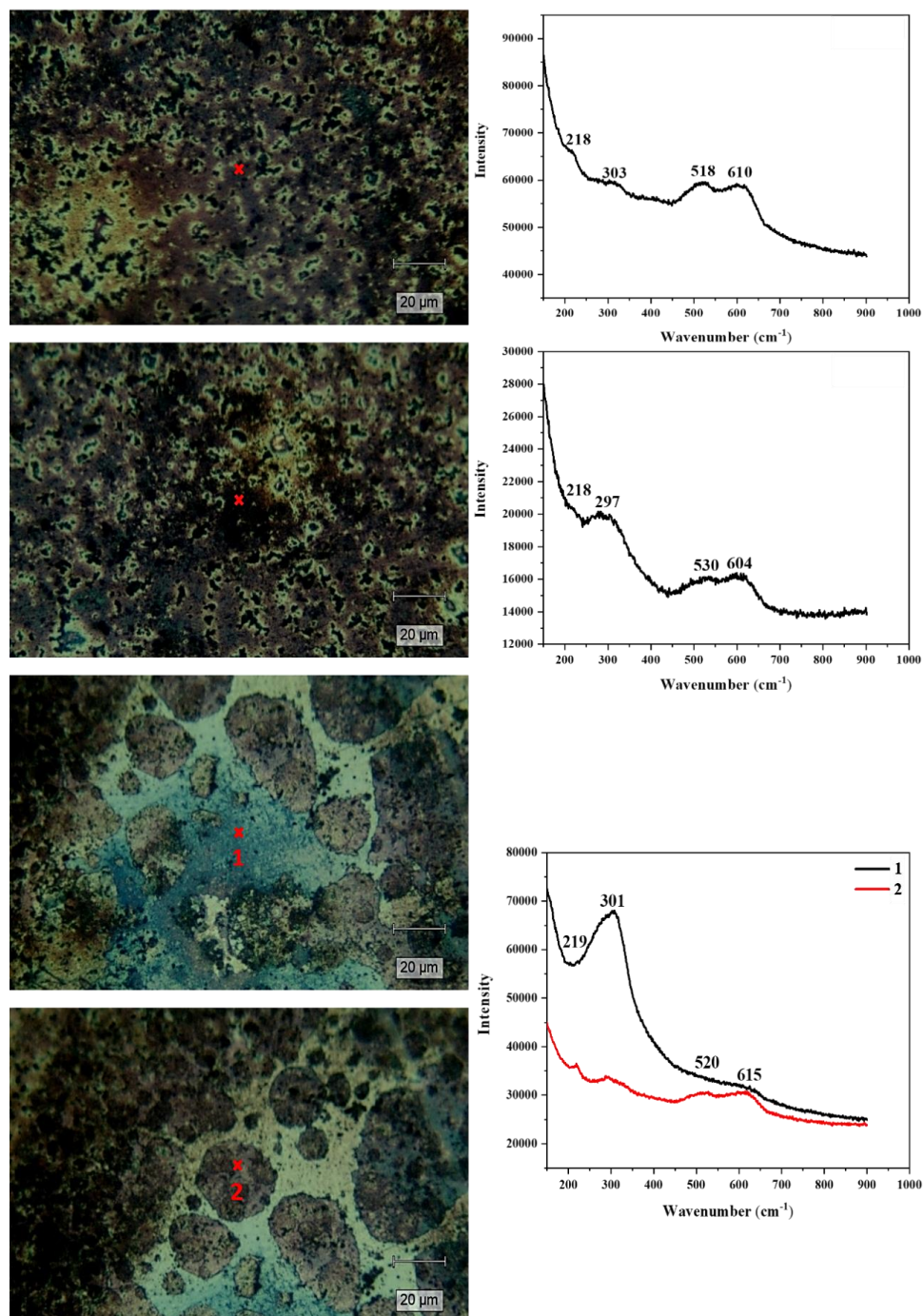
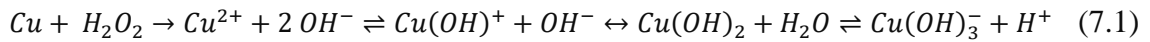


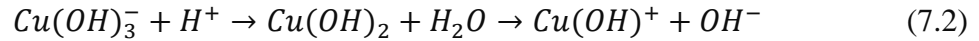
Figure 7.13: Images and Raman spectra of selected spots on the grown oxide (70 h-radiation in 500 μL pure water) after 20 h-immersion in a 0.1 M Cl^- + 5×10^{-5} M SH^- solution (x and the red numbers show the selected locations for Raman).

7.3.3 Mechanistic understanding

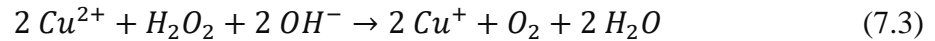
Grandy [8] outlined a potential mechanism for oxide growth under irradiation, which can be applied to this study. She proposed three stages for oxide formation. In the initial stage, the minimum solubility of cupric ions due to a pH of 9 was noted [26]. However, during corrosion, pH fluctuations occurred over time and location, affecting the predominant cupric ion species in solution based on hydroxide ion and cupric ion concentrations. Initially, copper oxidized to Cu^{2+} in the presence of H_2O_2 , generating hydroxide ions (Equation 7.1).



The subsequent diffusion of $\text{Cu}(\text{OH})_3^-$ and H^+ from the metal surface shifts hydrolysis equilibria, favoring the formation of $\text{Cu}(\text{OH})_2$ and $\text{Cu}(\text{OH})^+$ through Equation 7.2.



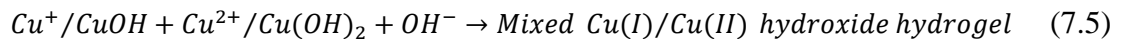
In the second stage, the corrosion process led to the development of a mixed Cu (I) and Cu (II) hydroxide hydrogel network, visibly observed as $\text{Cu}(\text{OH})_2$ hydrogel patches on the surface. Accumulation of Cu^{2+} and colloid particles occurred alongside H_2O_2 oxidation coupled with Cu^{2+} reduction (Equation 7.3).



The limited solubility of Cu^+ quickly established its solubility equilibrium (Equation 7.4).

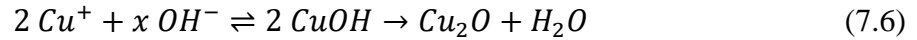


CuOH became integrated into the solid hydrogel network, forming a mixed Cu (I)/Cu (II) hydroxide hydrogel (Equation 7.5).

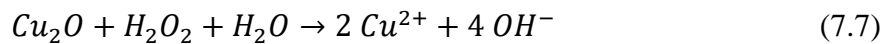


The acceleration of cupric to cuprous ion reduction by H_2O_2 bolstered the cyclic feedback loop between $\text{Cu}(\text{OH})_2$ production and consumption, facilitating swift CuOH formation.

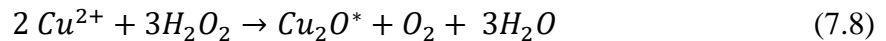
In stage 3, the process commenced as CuOH reached its supersaturation limit within the hydrogel, prompting the precipitation of Cu₂O (Equation 7.6).



Once Cu₂O crystals appeared on the surface, they underwent redox-assisted Ostwald ripening [43-45]. With the low solubility of Cu⁺, oxidation followed by dissolution as Cu²⁺ prevailed over Cu⁺ dissolution, aiding the Ostwald ripening phenomenon. Initially, Cu₂O oxidized to Cu²⁺ (Equation 7.7), then dissolved into and diffused through the solution.



The net reduction and reprecipitation of Cu₂O constituents occurred on larger crystals of lower average free energy (indicated by a * Equation (7.8)).



In the presence of radiation, redox reactions between copper species readily coupled with H₂O₂ redox reactions. In closed systems, Ostwald ripening led to the growth of large crystals at the expense of small crystals.

Grandy [8] suggested that during Ostwald ripening, crystals may form in Liesegang band patterns if there is a directional preference for the diffusion of solution species. These patterns typically emerge when diffusion occurs through slow transport media such as gel layers [46-49]. Grandy [8] claimed that in the context of copper corrosion, Cu²⁺ diffusion through the Cu(OH)₂ hydrogel layer covering the surface during Cu₂O Ostwald ripening occurred slowly, leading to the appearance of Liesegang band patterns in the oxide layer. As a result, the circular Liesegang bands observed during copper corrosion were not correlated with the underlying grain structure but were rather a consequence of Cu²⁺ diffusion through the hydrogel's mobile phase, occurring uniformly in all directions from the initiation point.

Grandy [8] highlighted that the rationale behind the impact of solution volume could be directly linked to the duration of stage 1, which hinges on the rate at which Cu²⁺

accumulates in solution, reaches the solubility limit of $\text{Cu}(\text{OH})_2$, and initiates precipitation. In solutions with a small volume, Cu^{2+} accumulation occurs rapidly, leading to a brief stage 1. Conversely, stage 1 is prolonged in solutions with a larger volume where it takes more time to reach Cu^{2+} saturation. Consequently, the concentration of Cu^{2+} plays a crucial role in determining the size of Cu_2O crystals, with lower Cu^{2+} levels in larger solution volumes resulting in smaller crystals. Moreover, larger solution volumes contribute to increased metal loss.

7.4 Conclusions

In this investigation, a combined Cu (I) and Cu (II) hydr(oxide) film was formed on a wrought Cu specimen using gamma-radiation in aerated pure water (pH_0 9) with varying volumes. Based on SEM images, it was observed that the film formed on the surface in a 500 μL solution appeared thinner compared to that in a solution with a volume of 400 μL . Notably, both cases exhibited concentric wave features, which were absent in the non-irradiated specimen. E_{corr} , CSV, and SEM/EDX results revealed that the irradiated specimens with the oxide film formed on the surface following exposure to bisulfide-containing solutions, were converted to copper sulfide. This behavior closely resembled that of an oxide created electrochemically, although the starting point was at a more positive potential value, indicating the presence of Cu (II)-containing species on the surface. At E_{corr} of approximately -0.85 V/SCE, the only compounds detected on the surface were Cu_2O and Cu_2S . Moreover, the presence of CO_2 as a dissolved gas in the solution (Type-I water) led to the contribution of H_2CO_3 to film formation as malachite ($\text{Cu}_2(\text{CO}_3)(\text{OH})_2$), which exhibited a green color and was confirmed with Raman.

7.5 References

- [1] F. King, L. Ahonen, C. Taxen, U. Vuorinen, L. Werme, Copper corrosion under expected conditions in a deep geologic repository, TR-01-23, SKB, 2001.
- [2] R.P. Morco, "Gamma-radiolysis kinetics and its role in the overall dynamics of materials degradation", Doctor of Philosophy, The University of Western Ontario, Electronic Thesis and Dissertation Repository, 7248, 2020.
- [3] R.P. Morco, J.M. Joseph, D.S. Hall, C. Medri, D.W. Shoesmith, J.C. Wren, Modelling of radiolytic production of HNO₃ relevant to corrosion of a used fuel container in deep geologic repository environments, *Corrosion Engineering, Science and Technology*, 52, 141-147, 2017.
- [4] J.M. Joseph, B.S. Choi, P. Yakabuskie, J.C. Wren, A Combined experimental and model analysis on the effect of pH and O₂(aq) on gamma-radiolytically produced H₂ and H₂O₂, *Radiation Physics and Chemistry*, 77, 1009-1020, 2008.
- [5] J.W.T. Spinks, R.J. Woods, An introduction to radiation chemistry, 2nd edn, (Wiley, 1976).
- [6] Farhataziz, M.A.J. Rodgers, Radiation chemistry: principles and applications, (VCH Publishers, 1987).
- [7] J.H. O'Donnell, Principles of radiation chemistry, American Elsevier, 1970.
- [8] Grandy, Lindsay J., "Effects of gamma-radiation on the evolution of copper corrosion dynamics in deep geological repository solution environments", The University of Western Ontario, Electronic Thesis and Dissertation Repository. 8257, 2021.
- [9] Jean, Arielle M., "Evolution of Cu₂O morphology during copper corrosion in the presence of gamma-radiation", The University of Western Ontario, Electronic Thesis and Dissertation Repository. 4593, 2017.

- [10] P. Yakabuskie, J. Joseph, J. Wren, The effect of interfacial mass transfer on steady-state water radiolysis, *Radiation Physics and Chemistry*, 79, 777-785, 2010.
- [11] P.A. Yakabuskie, J.M. Joseph, C.R. Stuart, J.C. Wren, Long-term γ -radiolysis kinetics of NO_3^- and NO_2^- solutions, *The Journal of Physical Chemistry A*, 115, 4270-4278, 2011.
- [12] K. Daub, X. Zhang, J.J. Noël, J.C. Wren, Effects of γ -radiation versus H_2O_2 on carbon steel corrosion, *Electrochimica Acta*, 55, 2767-2776, 2010.
- [13] I. Soroka, N. Chae, M. Jonsson, On the mechanism of γ -radiation-induced corrosion of copper in water, *Corrosion Science*, 182, 109279, 2021.
- [14] A. Björkbacka, M. Yang, C. Gasparrini, C. Leygraf, M. Jonsson, Kinetics and mechanisms of reactions between H_2O_2 and copper and copper oxides, *Dalton Transactions*, 44, 16045-16051, 2015.
- [15] A. Björkbacka, S. Hosseinpour, M. Johnson, C. Leygraf, M. Jonsson, Radiation induced corrosion of copper for spent nuclear fuel storage, *Radiation Physics and Chemistry*, 92, 80-86, 2013.
- [16] K. Bessho, Y. Oki, N. Akimune, H. Matsumura, K. Masumoto, S. Sekimoto, N. Osada, N. Kinoshita, H. Monjushiro, S. Shibata, Corrosion of copper in water and colloid formation under intense radiation field, *Journal of Radioanalytical and Nuclear Chemistry*, 303, 1117-1121, 2015.
- [17] Q.W. Knapp, J.C. Wren, Film formation on type-316L stainless steel as a function of potential: probing the role of gamma-radiation, *Electrochimica Acta*, 80, 90-99, 2012.
- [18] M. Behazin, J.J. Noël, J.C. Wren, Combined effects of pH and γ -irradiation on the corrosion of Co-Cr alloy stellite-6. *Electrochimica Acta*, 134, 399-410, 2014.
- [19] A. Björkbacka, S. Hosseinpour, C. Leygraf, M. Jonsson, Radiation induced corrosion of copper in anoxic aqueous solution, *Electrochemical and Solid-State Letters*, 15, C5-C7, 2012.

- [20] A. Björkbacka, C.M. Johnson, C. Leygraf, M. Jonsson, Role of the oxide layer in radiation-induced corrosion of copper in anoxic water, *The Journal of Physical Chemistry C*, 120, 11450–11455, 2016.
- [21] A. Hiroki, J.A. LaVerne, Decomposition of hydrogen peroxide at water-ceramic oxide interfaces, *The Journal of Physical Chemistry B*, 109, 3364–3370, 2006.
- [22] D.T. Reed, R.A. Van Konynenburg, Corrosion of copper-based materials in irradiated moist air systems, *Materials Research Society Symposium Proceedings*, 212, 1991.
- [23] D.T. Reed, V. Swayambunathan, B.S. Tani, R.A. Van Konynenburg, Corrosion product identification and relative rates of corrosion of candidate metals in an irradiated air-steam environment, *Materials Research Society Symposium Proceedings*, 176, 1990.
- [24] B. Ibrahim, D. Zagidulin, M. Behazin, S. Ramamurthy, J.C. Wren, D.W. Shoesmith, The corrosion of copper in irradiated and unirradiated humid air, *Corrosion Science*, 141, 53–62, 2018.
- [25] N.N. Greenwood, A. Earnshaw, *Chemistry of the elements*, 2nd edn, Butterworth-Heinemann, 1997.
- [26] K.J. Powell, P.L. Brown, R.H. Byrne, T. Gajda, G. Hefter, S. Sjöberg, H. Wanner, Chemical speciation of environmentally significant metals with inorganic ligands. Part 2: The Cu^{2+} - OH^- , Cl^- , CO_3^{2-} , SO_4^{2-} , and PO_4^{3-} Systems. *Pure and Applied Chemistry*, 79, 895-950, 2007.
- [27] Z.D. Draganic, I.G. Draganic, *The radiation chemistry of water*, Academic Press: New York, 1971.
- [28] J.C. Wren, Steady-state radiolysis: effects of dissolved additives, *ACS Symposium Series: Nuclear Energy and the Environment*, 1046, 271-295, 2010.
- [29] N.D. Zoubov, C. Vanleughenaghe, M. Pourbaix, Copper in atlas of electrochemical equilibria in aqueous solutions, Section 14.1, 384-392 (NACE International Cebelcor, 1974).

- [30] C. Leygraf, T. Chang, G. Herting, I. Odnevall Wallinder, The origin and evolution of copper patina colour, *Corrosion Science*, 157, 337-346, 2019.
- [31] P.A. Korzhavyi, B. Johansson, Thermodynamic properties of copper compounds with oxygen and hydrogen from first principles, SKB, 2010.
- [32] I.L. Soroka, A. Shchukarev, M. Jonsson, N.V. Tarakina, P.A. Korzhavyi, Cuprous hydroxide in a solid form: Does it exist? *Dalton Transactions*, 42, 9585-9594, 2013.
- [33] D. Nunes, A. Pimentel, L. Santos, P. Barquinha, L. Pereira, E. Fortunato, R. Martins, Structural, optical, and electronic properties of metal oxide nanostructures in metal oxide nanostructures (eds Daniela Nunes et al.), Elsevier, Chapter 3, 59-102, 2019.
- [34] R.L. Frost, W.N. Martens, L. Rintoul, E. Mahmutagic, J.T. Kloprogge, Raman spectroscopic study of azurite and malachite at 298 and 77 K, *Journal of Raman Spectroscopy*, 33, 252-259, 2002.
- [35] L. Dörner, C. Cancellieri, B. Rheingans, M. Walter, R. Kägi, P. Schmutz, M.V. Kovalenko, L.P.H. Jeurgens, Cost-effective sol-gel synthesis of porous CuO nanoparticle aggregates with tunable specific surface area, *Scientific Reports*, 9, 11758, 2019.
- [36] S. Kondrat, P. Smith, P. Wells, P. Chater, J. Carter, D. Morgan, E.M. Fiordaliso, J. Wagner, T. Davies, L. Lu, J. Bartley, S. Taylor, M. Spencer, C. Kiely, G. Kelly, C. Park, M. Rosseinsky, G. Hutchings, Stable amorphous georgeite as a precursor to a high-activity catalyst, *Nature*, 531, 83-87, 2016.
- [37] Y. Deng, A.D. Handoko, Y. Du, S. Xi, B.S. Yeo, In situ Raman spectroscopy of copper and copper oxide surfaces during electrochemical oxygen evolution reaction: identification of Cu^{III} oxides as catalytically active species, *ACS Catalysis*, 6, 2473-2481, 2016.
- [38] F. Texier, L. Servant, J.L. Bruneel, F. Argoul, In situ probing of interfacial processes in the electrodeposition of copper by confocal Raman microspectroscopy, *Journal of Electroanalytical Chemistry*, 446, 189-203, 1998.

- [39] H.Y.H. Chan, C.G. Takoudis, M.J. Weaver, Oxide formation and oxygen adsorption on copper in aqueous media as probed by surface-enhanced Raman spectroscopy. *Journal of Physical Chemistry B*, 103, 357-365, 1999.
- [40] E. Salehi Alaei, M. Guo, J. Chen, M. Behazin, E. Bergendal, C. Lilja, D.W. Shoesmith, J.J. Noël, The transition from used fuel container corrosion under oxic conditions to corrosion in an anoxic environment, *Materials and Corrosion*, 74, 1690-1706, 2023.
- [41] J.M. Smith, J.C. Wren, M. Odziemkowski, D.W. Shoesmith, The electrochemical response of preoxidized copper in aqueous sulfide solutions, *Journal of the Electrochemical Society*, 154, C431, 2007.
- [42] G. Parker, G. Hope, R. Woods, Raman spectroscopic identification of surface species in the leaching of chalcopyrite, *Electrochemistry in Mineral Processing VI*. Doyle, F.M., Kelsall, G.H., Woods, R., Editors PV2003-18, The Electrochemical Society Proceeding Series, Pennington, NJ, 181, 2003.
- [43] J.H. Yao, K.R. Elder, H. Guo, M. Grant, Theory and simulation of Ostwald ripening, *Physical Review B*, 47, 14110-14125, 1993.
- [44] I.M. Lifshitz, V.V. Slyozov, The Kinetics of precipitation from supersaturated solid solutions, *Journal of Physics and Chemistry of Solids*, 19, 35-50, 1961.
- [45] Shin, Y. G. "Nonlinear dynamics of carbon steel corrosion under gamma radiation", Doctor of Philosophy, The University of Western Ontario, Electronic Thesis and Dissertation Repository, 7339, 2020.
- [46] D. Papineau, Chemically oscillating reactions in the formation of botryoidal malachite, *American Mineralogist*, 105, 447-454, 2020.
- [47] K.H. Stern, The Liesegang phenomenon, *Chemical Reviews*, 54, 79-99, 1954.
- [48] S. Sadek, R. Sultan, Liesegang patterns in nature: A diverse scenery across the sciences, *Precipitation Patterns in Reaction-Diffusion Systems*, 661, 1-43, 2010.

[49] D. Smith, On Ostwald's supersaturation theory of rhythmic precipitation (Liesegang's Rings), *The Journal of Chemical Physics*, 81, 3102-3115, 1984.

8 Investigating the Role of Cu in the Conversion of Copper Oxide to Copper Sulfide

8.1 Introduction

The exposure environment within a DGR will undergo a transition from warm and oxidizing to cool and anoxic, with the time required being challenging to predict [1,2]. Initially, atmospheric O₂, sealed within the repository along with heat generated by radioactive decay, will lead to warm, dry, and oxidizing conditions. However, dissolved O₂ will gradually be depleted due to various processes, such as corrosion of the container, oxidation of dissolved copper corrosion products, and reactions with microbes and redox-sensitive materials present in the clay backfill [3].

The corrosion products formed during the aerated period may include cuprite (Cu₂O), tenorite (CuO), paratacamite (Cu₂Cl(OH)₃), due to high chloride content in deep groundwaters at Canadian sites, and malachite (Cu₂CO₃(OH)₂) in the presence of increased carbonate concentrations [4].

As O₂ is consumed and radioactive decay leads to a decrease in heat production, conditions at the surface of the container will transition from warm and oxidizing to cool and anoxic, and bisulfide will become the principal oxidant during the long-term corrosion of copper [5-7].

In a repository bisulfide can originate from various sources, including the dissolution of sulfide minerals like pyrite (FeS₂) in the rock and bentonite buffer materials, with the most significant source being the remote production of bisulfide in groundwaters due to the action of SRB [8].

Bisulfide-induced copper corrosion is constrained by several factors, including a low bisulfide concentration ($< 10^{-6}$ mol/L), a low flux (10^{-11} to 10^{-10} mol/(m²·s)), and a low rate of transport of remotely produced bisulfide through the compacted buffer materials to the container surface [6,7,9].

When dissolved bisulfide reaches the container surfaces, they will already be covered by corrosion products from the initial oxic phase [4]. Eiselstein et al. [10] discovered that the protective oxide film formed under aerated conditions was rapidly destroyed once bisulfide was introduced. This loss in protection was evident through a shift in the corrosion potential to less noble values and an increase in corrosion rate. EDX analysis revealed a thick porous outer layer of Cu_2S containing various impurities. The destabilization of copper by bisulfide is the viable long-term corrosion process for copper waste containers, but penetration/conversion of the oxide already present on the container surface will be required before bisulfide can react with the underlying copper.

X-ray absorption spectroscopy [11-13] and X-ray photoelectron spectroscopy [14-17] have provided compelling evidence that copper exists in the monovalent state in all copper sulfides. However, the copper corrosion products formed during the aerated phase of the repository are likely to include divalent copper compounds, along with monovalent copper. Consequently, reduction of Cu (II) to Cu (I) must occur when bisulfide ions react with the oxides. Despite this understanding, the detailed mechanism(s) of this reduction process remain unclear.

Ma et al. [18] investigated the sulfidation of CuO nanoparticles (NPs) in water by inorganic sulfide. Characterization techniques including X-ray absorption spectroscopy, X-ray diffraction, and transmission electron microscopy revealed the transformation of CuO into various copper sulfide (Cu_xS_y) species, including crystalline CuS (covellite) and amorphous Cu_xS_y species, with the reduction of Cu (II) to Cu (I) coupled with sulfide oxidation to sulfate, leading to the formation of copper sulfate hydroxide species. The extent of sulfidation depended on the sulfide to CuO molar concentration ratio, with incomplete sulfidation observed after 7 days, even at the highest S/Cu molar ratio of 2.16.

Galtayries and Bonnelle [19] investigated the gas-phase interaction between H_2S and Cu, Cu_2O , and CuO surfaces using X-ray photoelectron spectroscopy and ion scattering spectroscopy. Their findings revealed that Cu (II) species were reduced to Cu (I) and that adsorbed S^{2-} was oxidized to sulfate-like species. Barbour et al. [20] found no visible or

measurable sign of sulfidation in CuO samples exposed for 5.5 h at 24°C in air with 65% humidity containing 600 ppb H₂S.

Hollmark et al. [12,13] observed that in studies of sulfidation of copper oxides in water solutions, CuO did not show markedly more resistance to sulfidation than Cu₂O. Despite not determining the sulfidation rate, there was no noticeable difference between the two oxides over the exposure period employed (12 h), suggesting similar sulfidation mechanisms.

Prolonged exposure of CuO formed electrochemically on a Cu coupon to a synchrotron beam appeared to reduce the Cu (II) contribution in the X-ray absorption spectrum. The observation of a reduced Cu (II) contribution in the X-ray absorption spectrum raised the possibility of a radiation-induced comproportionation reaction (Equation 8.1), where Cu (II) is reduced by Cu to form Cu (I). This suggests that Cu may act as an electron donor for the reduction of Cu (II) during sulfidation, different than the proposal by Galtayries and Bonnelle [19] for the gas phase reaction.



In **Chapters 4, 5, 6, and 7**, results demonstrating the effects of copper oxidation on the subsequent corrosion process in aqueous bisulfide were presented. The purpose of the research described in this chapter is to investigate whether the Cu substrate is involved in the conversion of an initially present oxide layer. To achieve this, the reaction of Cu (I)/Cu (II) oxides with bisulfide has been studied in the absence of a Cu substrate and compared to the reaction of Cu metal with bisulfide.

8.2 Experimental

Commercially available Cu₂O and CuO powders were characterized and then exposed to 0.1 M NaCl solutions containing different concentrations of bisulfide for various immersion periods. Subsequently, the composition of the resulting products was determined.

8.2.1 Specimen preparation

The Cu (I) oxide (cuprous oxide) (Cu_2O , 95.0% assay), Cu (II) oxide (cupric oxide) (CuO , 99.0% assay), and copper powders were purchased from J.T. Baker, Sigma-Aldrich. The powders were used as received.

8.2.2 Solution preparation

Solutions were prepared with reagent-grade sodium chloride (NaCl , 99.0% assay), sodium sulfide ($\text{Na}_2\text{S}\cdot 9\text{H}_2\text{O}$, 98.0% assay), and Type-I water, based on the procedure described in section 3.3.1. Pristine powders were exposed to solutions containing 0.1 M NaCl , as well as 5×10^{-5} and 5×10^{-3} M Na_2S . To maintain a de-aerated environment, required to minimize sulfide oxidation, the solution was sparged with ultrapure Ar for 30 min prior to each experiment and then continuously throughout the immersion experiment.

8.2.3 Cell design

4 g of either CuO , Cu_2O , or mixed Cu/CuO (1:1 ratio) powders was exposed to 250 mL of the bisulfide solution for different durations of immersion using a specific cell setup as shown in **Figure 8.1**.

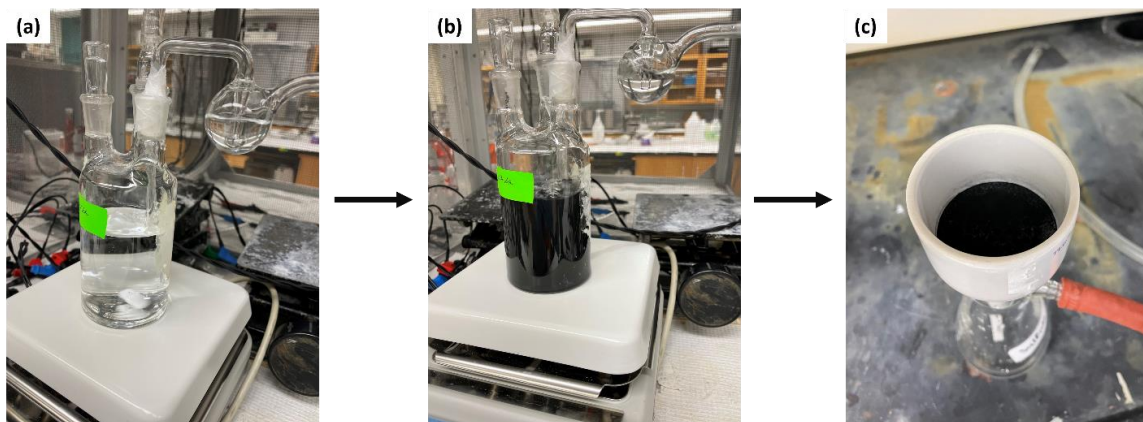


Figure 8.1: Cell used in the immersion tests; (a) pre-purging with Ar gas, (b) adding powder to the bisulfide solution (continuously stirring), and (c) retrieving the resulting powder

The powder samples were stirred constantly to ensure that all particles came into continuous contact with the bisulfide solution. After a specific exposure time, the remaining powder was retrieved from the solution by running it through a filter paper (GE Healthcare (Whatman™), circle, diameter 55 mm) using a vacuum pump. After drying, the retrieved powder, of which there was less than the initial reactant powder, was stored in a glove-box for subsequent analysis.

8.2.4 Analytical characterization

8.2.4.1 X-ray Diffraction

Powder X-ray diffraction was first used to identify the composition of the pristine and sulfidized copper oxide powders. Diffraction patterns of these materials were collected using A Rigaku SmartLab X-ray diffractometer, operating in the Bragg configuration using Cu K α radiation (40 kV, 45 mA) at an incident angle of 10° or 20° to 95° at a scan speed of 3.00°/min.

8.3 Results and Discussion

8.3.1 Characterization of the pristine Cu₂O and CuO powders

The XRD patterns recorded on the pristine CuO and Cu₂O powders are shown in **Figure 8.2**. The diffraction pattern for CuO, shown in **Figure 8.2 (a)**, has main peaks at $2\theta^\circ = 35.55^\circ, 35.57^\circ, 38.41^\circ,$ and 38.73° , which correspond to diffraction from the (002), (-111), (111), and (200) planes of CuO, respectively [21]. Additionally, the diffraction pattern of Cu₂O (**Figure 8.2 (b)**) exhibits main peaks at $2\theta^\circ = 29.51^\circ, 36.37^\circ, 42.26^\circ, 61.36^\circ, 73.64^\circ,$ and 77.38° which correspond to diffraction from the (110), (111), (200), (220), (311), and (222) planes of Cu₂O, respectively [22]. The XRD results confirmed that the initially used powders contained no detectable impurity phases.

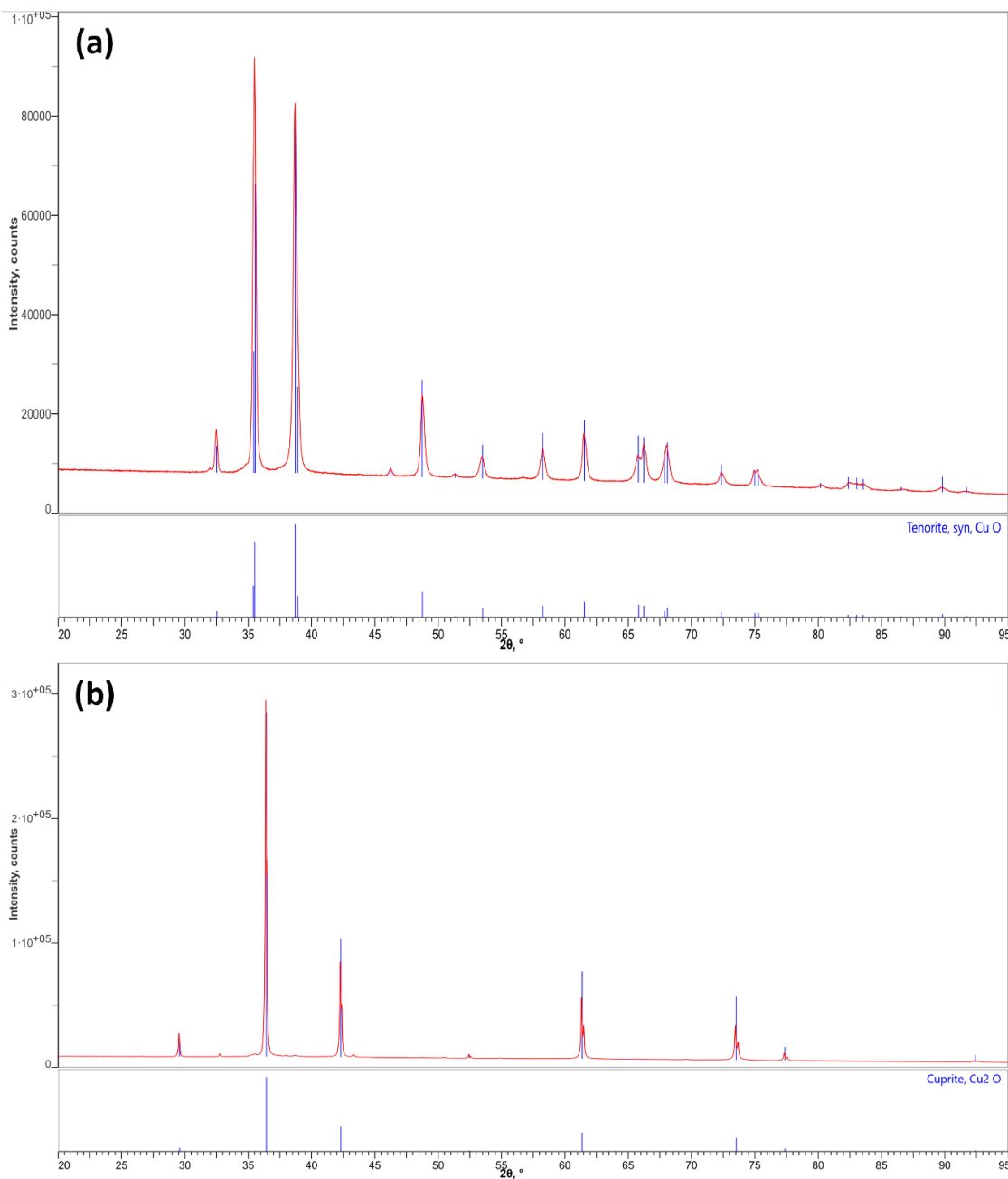


Figure 8.2: XRD patterns (Red) of the pristine (a) CuO powder and (b) Cu₂O powder, together with standards (Blue) obtained from the Rigaku SmartLab XRD database.

8.3.2 Characterization of the sulfidized Cu₂O, CuO, and mixed Cu/CuO powders

To investigate the potential conversion of CuO powder to copper sulfide in bisulfide-containing solution, the same amount of CuO powder was exposed to $0.1 \text{ M Cl}^- + 5 \times 10^{-5}$

M SH⁻ for different immersion times. The XRD patterns recorded on the CuO powder exposed to bisulfide solution for 30 min, 1 h, 2 h, 5 h, and 24 h are shown in **Figure 8.3**.

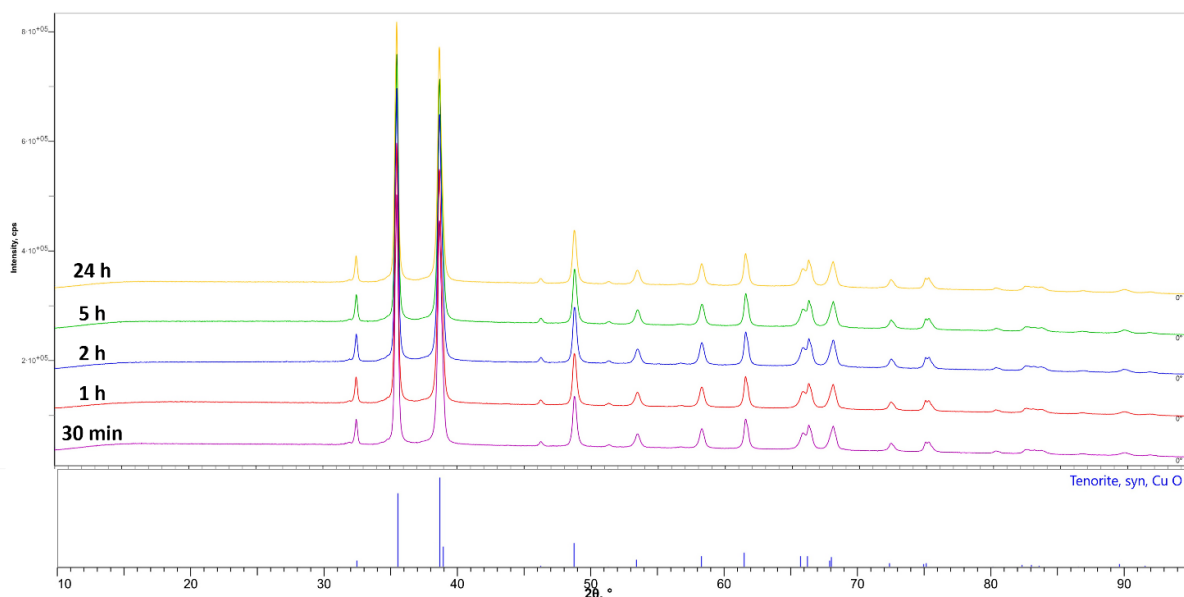


Figure 8.3: XRD patterns collected on CuO powder exposed to 0.1 M Cl⁻ + 5 × 10⁻⁵ M SH⁻ solutions for different durations of immersion, together with standard obtained from the Rigaku SmartLab XRD database.

According to the measured XRD patterns, no conversion reaction occurred in the presence of bisulfide ions on the timescale of the immersion test.

The role of copper metal in the conversion of Cu (II) oxide to copper sulfide in the bisulfide solution was studied by adding the mixed Cu/CuO powder (1:1 ratio) to bisulfide solutions (0.1 M Cl⁻ + 5 × 10⁻⁵ M SH⁻) for different immersion times. **Figure 8.4** shows the XRD patterns recorded on mixed Cu/CuO powder after 30 min, 1 h, 2 h, 5 h, and 24 h immersion in the bisulfide solutions. As can be seen in **Figure 8.4 (b)**, comparison of the standards to the measured patterns of sulfidized Cu/CuO after 1 h indicates that, although conversion of oxide to sulfide did not take place in the presence of sulfide, the comproportionation reaction between Cu and CuO particles led to the formation of Cu₂O. The main peaks for Cu₂O can be detected at 2θ° = 29.51°, 36.37°, 42.26°, 61.36°, 73.64°, while the diffraction pattern for Cu has main peaks at 2θ° = 43.27°, 50.41°, and 74.14° which correspond to

diffraction from the (111), (200), and (220) planes of Cu, respectively [22]. The intensity of the mentioned peaks increased as the immersion time increased to 2 h.

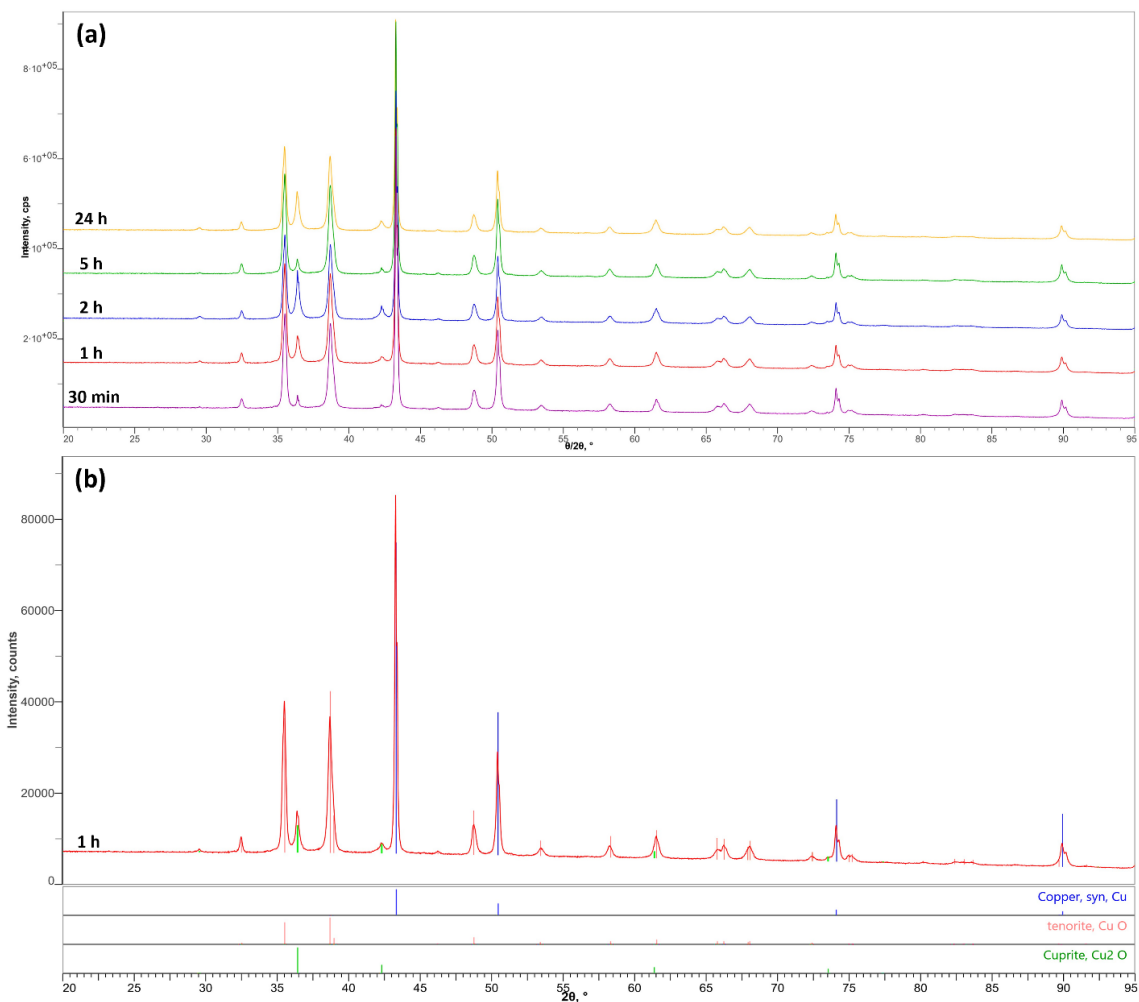


Figure 8.4: XRD patterns of (a) a mixed Cu/CuO powder (1:1 ratio) exposed to bisulfide solutions ($0.1 \text{ M Cl}^- + 5 \times 10^{-5} \text{ M SH}^-$) for different immersion times, together with (b) standards obtained from the Rigaku SmartLab XRD database fitted to the selected pattern for sulfidized Cu/CuO powder after 1 h.

The conversion of copper (I) oxide to sulfide was investigated by adding the Cu_2O powder to $0.1 \text{ M Cl}^- + 5 \times 10^{-5} \text{ M SH}^-$ solutions for different immersion times. The XRD patterns collected on Cu_2O powder in bisulfide solutions after 2 h- and 24 h-immersion are presented in **Figure 8.5**.

The results show that although the Cu atom was monovalent in the Cu_2O structure, there was no change in the Cu_2O powder's XRD pattern in the presence of sulfide after 24 h immersion.

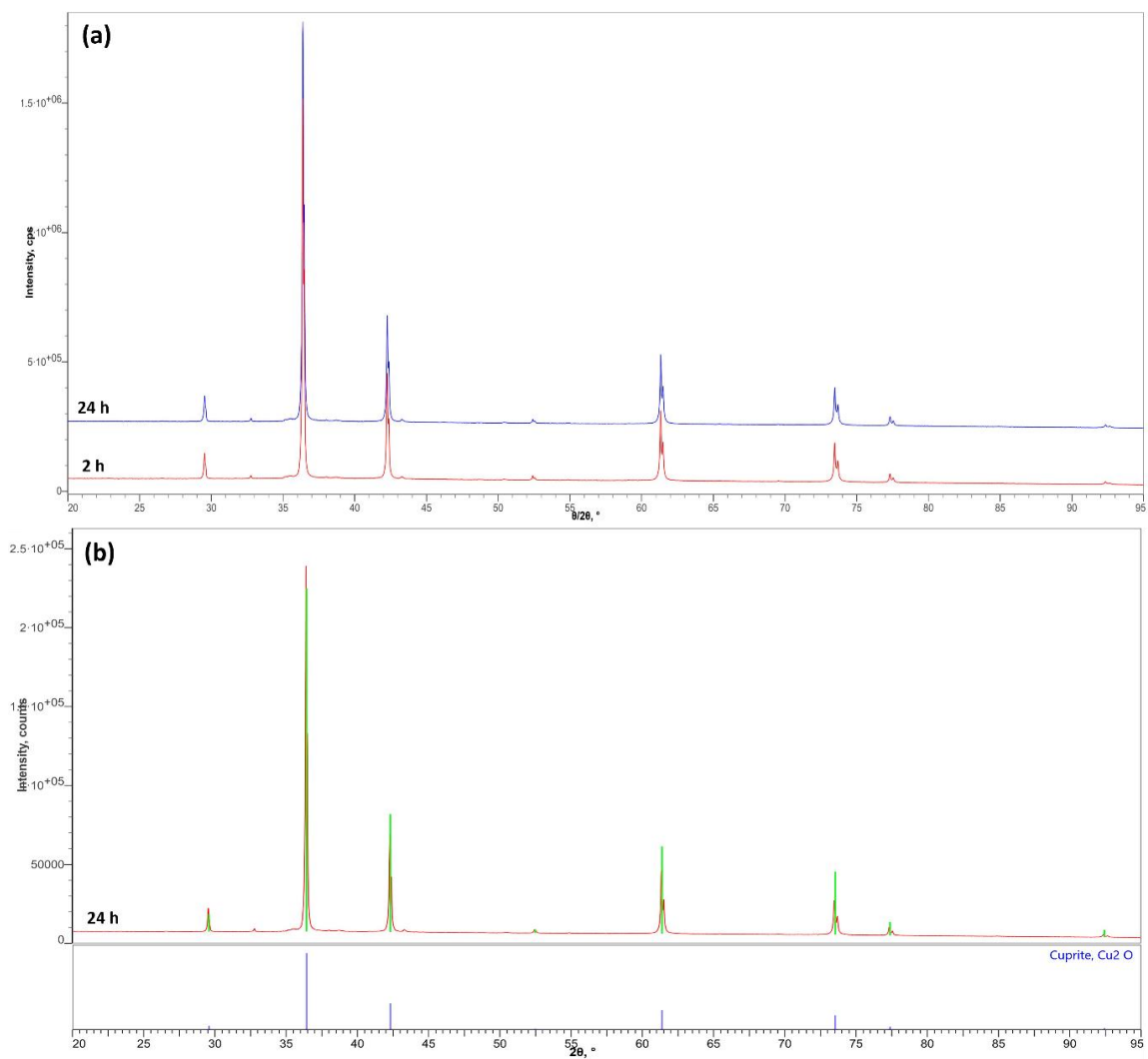


Figure 8.5: XRD patterns collected on (a) a Cu_2O powder exposed to $0.1 \text{ M Cl}^- + 5 \times 10^{-5} \text{ M SH}^-$ solutions for different durations of immersion, together with (b) standard obtained from the Rigaku SmartLab XRD database fitted to the selected pattern for sulfidized Cu_2O powder after 24 h.

In an attempt to accelerate the conversion process, the concentration of bisulfide was increased to $5 \times 10^{-3} \text{ M}$. The XRD pattern obtained after a 24 h-immersion of CuO powder

in $0.1 \text{ M Cl}^- + 5 \times 10^{-3} \text{ M SH}^-$ solution is shown in **Figure 8.6** and compared to standard patterns.

Upon bisulfide addition, although a new phase emerged in the sulfidized CuO powder due to minor peaks in the XRD pattern, the predominant phase remained CuO. Besides CuO, copper sulfate hydroxide, brochantite ($\text{Cu}_4(\text{SO}_4)(\text{OH})_6$), was also detected with main peaks at $2\theta^\circ = 35.61^\circ, 22.78^\circ, 16.54^\circ, 13.88^\circ, 33.44^\circ$ [23]. The presence of sulfate minerals suggests oxidation of some of the sulfide to sulfate in the sulfidation process, potentially during drying. Because dissolved oxygen was removed prior to the sulfidation process, Cu (II) likely served as the oxidant for sulfide oxidation, leading to Cu (I) formation. This reduction of Cu (II) to Cu (I) by sulfide has been previously observed by Luther et al. [24].

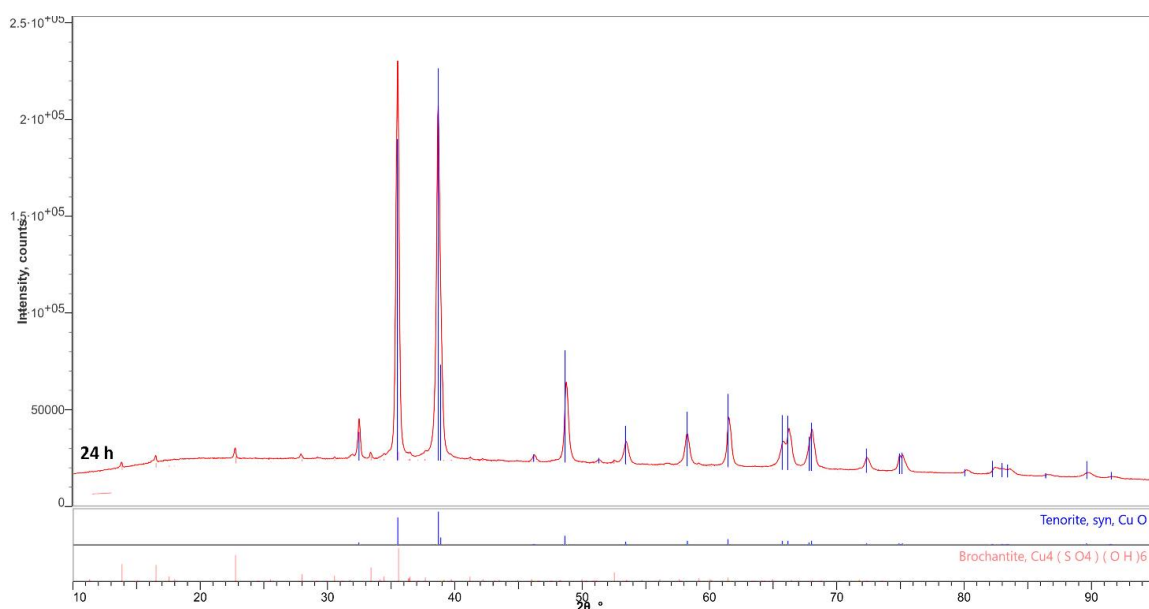


Figure 8.6: XRD pattern collected on CuO powder exposed to $0.1 \text{ M Cl}^- + 5 \times 10^{-3} \text{ M SH}^-$ solution for 24 h, together with standards obtained from the Rigaku SmartLab XRD database.

8.4 Conclusions

This chapter presents an initial exploration of the immersion testing of copper oxide powder in bisulfide solution. However, further investigation is required if the role of copper

in the conversion of copper oxide to copper sulfide is to be elucidated. The immersion test of copper oxide powders yielded the following results:

Regardless of the composition of the copper oxide, exposure of the powder to a chloride solution containing bisulfide ($0.1 \text{ M Cl}^- + 5 \times 10^{-5} \text{ M SH}^-$) did not yield any observable conversion to copper sulfide over the duration of the immersion period. The exposure of mixed Cu and CuO powders to a bisulfide solution led to the formation of Cu_2O , suggesting the potential occurrence of the comproportionation reaction. These findings obtained from the immersion of copper oxide powders in bisulfide solution lend support to a hypothesis that the chemical conversion is slower compared to the electrochemical reaction in the presence of copper metal, as detailed in **Chapters 4, 5, 6, and 7**. Moreover, an increase in bisulfide concentration resulted in the formation of copper sulfate hydroxide, brochantite.

8.5 References

- [1] F. King, M. Kolar, A numerical model for the corrosion of copper nuclear fuel waste containers, MRS Online Proceedings Library (OPL), 412, 555–562, 1995.
- [2] H. Müller, B. Garitte, T. Vogt, S. Köhler, T. Sakaki, H. Weber, T. Spillmann, M. Hertrich, J. Becker, N. Giroud, V. Cloet, N. Diomidis, T. Vietor, Implementation of the full-scale emplacement (FE) experiment at the Mont Terri rock laboratory, Mont Terri Rock Laboratory, 20 Years: Two Decades of Research and Experimentation on Claystones for Geological Disposal of Radioactive Waste, 110, 287–306, 2017.
- [3] F. King, M. Kolar, Report No.06819-REP-01200-10041-R00, Ontario Power Generation: Nuclear Waste Management Division 2000.
- [4] P.T. Kristiansen, F. Massel, L. Werme, C. Lilja, L.-C. Duda, Sulfidation of single-phase oxide on copper and as powder studied using soft X-Ray spectroscopy, Journal of The Electrochemical Society, 162, C785-C791, 2015.
- [5] F. King, Proceedings of the international conference on deep geologic disposal of radioactive waste, Canadian Nuclear Society, 9-35, 1996.
- [6] A. Gordon, H. Pahverk, E. Börjesson, L. Sjögren, O. Karlsson, H. Bergqvist, F. Lindberg, A. Johansson, Corrosion morphology of copper in anoxic sulphide environments, TR-18-14, SKB, 2018.
- [7] F. King, J. Chen, Z. Qin, D. Shoesmith, C. Lilja, Sulphide-transport control of the corrosion of copper canisters, Corrosion Engineering, Science and Technology, 52, 210–216, 2017.
- [8] H. Drake, I. Geoconsulting, Investigation of sulphide production in core-drilled boreholes in Äspö Hard Rock Laboratory. Boreholes KA3110A, KA3385A and KA3105A, TR-13-12, SKB, 2014.
- [9] E.P. Kremer, Durability of the Canadian used fuel container, Corrosion Engineering, Science and Technology, 52, 173–177, 2017.

- [10] L.E. Eiselstein, B.C. Syrett, S.S. Wing, R.D. Caligiuri, The accelerated corrosion of Cu Ni alloys in sulphide-polluted seawater: Mechanism no. 2, *Corrosion Science*, 23, 223-239, 1983.
- [11] H.M. Hollmark, P.G. Keech, J.R. Vegelius, P. Kristiansen, L. Werme, L.-C. Duda, Sulfidation of oxidized copper studied by soft X-ray spectroscopy, *MRS Online Proceedings Library (OPL)*, 1475, 2012.
- [12] H.M. Hollmark, J. Vegelius, P. Kristiansen, L. Werme, L.-C. Duda, Exposure of oxidized copper surfaces to aqueous Na₂S solution studied with soft X-Ray spectroscopy, *Journal of the Electrochemical Society*, 158, C1, 2011.
- [13] H.M. Hollmark, P.G. Keech, J.R. Vegelius, L. Werme, L.-C. Duda, X-ray absorption spectroscopy of electrochemically oxidized Cu exposed to Na₂S, *Corrosion Science*, 54, 85-89, 2012.
- [14] J.C.W. Folmer, F. Jelinek, The valence of copper in sulphides and selenides: An X-ray photoelectron spectroscopy study, *Journal of the Less Common Metals*, 76, 153-162, 1980.
- [15] J.C.W. Folmer, F. Jelinek, G.H.M. Calis, The electronic structure of pyrites, particularly CuS₂ and Fe_{1-x}Cu_xSe₂: An XPS and Mössbauer study, *Journal of Solid-State Chemistry*, 72, 137-144, 1988.
- [16] S.W. Goh, A.N. Buckley, R.N. Lamb, Copper(II) sulfide?, *Minerals Engineering*, 19, 204-208, 2006.
- [17] S.W. Goh, A.N. Buckley, R.N. Lamb, R.A. Rosenberg, D. Moran, The oxidation states of copper and iron in mineral sulfides, and the oxides formed on initial exposure of chalcopyrite and bornite to air, *Geochimica et Cosmochimica Acta*, 70, 2210-2228, 2006.
- [18] R. Ma, J. Stegemeier, C. Levard, C.W. Noack, G.E. Brown, G.V. Lowry, Sulfidation of copper oxide nanoparticles and properties of resulting copper sulfide, *Environmental Science: Nano*, 4, 347-357, 2014.

- [19] A. Galtayries, J-P. Bonnelle, XPS and ISS studies on the interaction of H₂S with polycrystalline Cu, Cu₂O and CuO surfaces, *Surface and interface analysis*, 23, 171-179, 1995.
- [20] J.C. Barbour, J.W. Braithwaite, A.F. Wright, *Nuclear Instruments and Methods in Physics Research Section B: Beam Interactions with Materials and Atoms*, 175, 382-387, 2001.
- [21] M. Bin Mobarak, M.S. Hossain, F. Chowdhury, S. Ahmed, Synthesis and characterization of CuO nanoparticles utilizing waste fish scale and exploitation of XRD peak profile analysis for approximating the structural parameters, *Arabian Journal of Chemistry*, 15, 104117, 2022.
- [22] N.H. Lam, R.P. Smith, N. Le, C.T.T. Thuy, M.S. Tamboli, A.M. Tamboli, S. Alshehri, M.M. Ghoneim, N.T.N. Truong, J.H. Jung, Evaluation of the structural deviation of Cu/Cu₂O nanocomposite using the X-ray diffraction analysis methods, *Crystals*, 12, 566, 2022.
- [23] S. Merlino, N. Perchiazzi, D. Franco, Brochantite, Cu₄SO₄(OH)₆: OD character, polytypism and crystal structures, *European Journal of Mineralogy*, 15, 267-275, 2003.
- [24] G.W. Luther, S.M. Theberge, T.F. Rozan, D. Rickard, C.C. Rowlands, A. Oldroyd, Aqueous copper sulfide clusters as intermediates during copper sulfide formation, *Environmental Science and Technology*, 36, 394-402, 2002.

9 Summary and Future Work

9.1 Summary

The primary goal of this research was to study the conversion of copper oxide to copper sulfide on wrought copper, as the DGR conditions evolve from oxic to anoxic. In particular, this thesis was focused on the effect of different types of copper oxide/hydroxide, created via different methods, with known composition and thickness, on the subsequent bisulfide-induced corrosion of Cu. The main focus was on developing a better understanding of the mechanisms through which the different types of copper oxide/hydroxide could convert to copper sulfide, thereby estimating the amount of corrosion damage to Cu containers more accurately.

Chapter 4 aimed to determine the optimal conditions for growing Cu (I) oxide anodically in a 0.1 M NaOH solution and to examine how different conditions and bisulfide concentrations affect the conversion of copper oxide to copper sulfide. The primary focus of this chapter was to investigate the kinetics of the oxide-to-sulfide conversion in 0.1 M NaCl solutions with bisulfide concentrations of 5×10^{-5} and 10^{-4} M. The findings indicated that when copper was oxidized in a 0.1 M NaOH solution at -0.3 V/SCE for 30 min under de-aerated conditions, a thin and uniform layer of Cu_2O was formed. Upon contact with bisulfide, the oxide layer transformed to Cu_2S at a rate influenced by the bisulfide concentration and experimental conditions. Although Raman spectroscopy, SEM/EDX, and CSV confirmed the occurrence of the oxide-to-sulfide reaction, a residual layer of Cu_2O adjacent to the copper substrate was still detected afterward.

In **Chapter 5**, the influence of a dual-layer oxide ($\text{Cu}_2\text{O}/\text{CuO}$), grown electrochemically at -0.22 V/SCE in 0.1 M NaOH solution, on the bisulfide-induced corrosion of copper was examined. The extent of conversion processes occurring after varying immersion periods was assessed by measuring the corrosion potential and using cathodic stripping voltammetry. Additionally, the surface corrosion deposits were analyzed to understand the properties and morphology of the resulting corrosion damage. The duplex films, composed of Cu_2O , CuO , and possibly $\text{Cu}(\text{OH})_2$, exhibited slower and incomplete conversion, even after 24 h of exposure to 0.1 M NaCl + 5×10^{-5} M Na_2S . The conversion of duplex films

involved both chemical conversion (Cu_2O to Cu_2S) and a galvanic process wherein oxide reduction (CuO to Cu (I)) coupled with Cu oxidation (Cu to Cu_2S). Even after 24 h, $\text{Cu}(\text{OH})_2$ remained unconverted to Cu_2S . As a consequence of the conversion process exposing the underlying Cu substrate, the corrosion process eventually transitioned to being driven primarily by the direct oxidation of Cu to Cu_2S .

The study in **Chapter 6** was to investigate how hydrothermally-grown copper oxide ($\text{Cu}_2\text{O}/\text{CuO}$), which possessed a structure distinct from that of electrochemically-grown oxide, affected bisulfide-induced corrosion. The experiments involved measuring the corrosion potential under varying bisulfide concentrations (10^{-4} and 2×10^{-4} M) and analyzing the properties of surface corrosion products to assess film characteristics and corrosion damage. The hydrothermal process effectively produced a dual-layer copper oxide ($\text{Cu}_2\text{O}/\text{CuO}$). With the corrosion potential shifting to more negative values, localized corrosion occurred during oxide growth, eventually causing the corrosion product to delaminate from the surface. The oxide-to-sulfide conversion resulted in the development of a dense surface layer, primarily comprising CuS at less negative potentials and Cu_2S at more negative potentials.

The goal of **Chapter 7** was to form corrosion products analogous to those formed during the initial oxic period of the repository and to determine whether such films can subsequently inhibit the reaction of copper with bisulfide. Gamma radiation was used to create a combined Cu (I) and Cu (II) oxide film on wrought Cu samples in aerated pure water at varying solution volume (400 and 500 μL). Surface morphologies of corrosion products and corrosion damage were examined using SEM/EDX/FIB. The comparison between different types of copper oxide enabled us to better understand the effect of the nature of the oxide film on the bisulfide-induced corrosion and to consider all the possible scenarios. SEM images revealed a thinner film formation in 500 μL solution than that in 400 μL solution, with both showing concentric wave features absent in non-irradiated samples. Results from E_{corr} , CSV, and SEM/EDX indicated conversion of copper oxide to copper sulfide upon exposure of the oxide-coated metal to bisulfide-containing solutions, similar to electrochemically formed oxide behaviour but with a more positive starting potential indicative of Cu (II)-containing species. At E_{corr} of around -0.85 V/SCE, only

Cu₂O and Cu₂S compounds were detected on the surface. Additionally, the presence of CO₂ in Type-I water led to a contribution from H₂CO₃ in the film formation, resulting in green-coloured malachite, as confirmed via Raman spectroscopy.

The goal of **Chapter 8** was to explore whether copper had an important role in the conversion of copper oxide to copper sulfide. By subjecting Cu (I) and Cu (II) oxide powders to bisulfide-containing solutions, the reaction between bisulfide and copper oxides in the absence of Cu metal was replicated. However, in some cases, Cu powder was also included alongside Cu (II) oxide. Regardless of the powder composition, the immersion experiments showed no conversion of copper oxide powder to copper sulfide when exposed to a chloride solution containing bisulfide (5×10^{-5} M). However, when mixed copper and copper oxide powders were exposed to a bisulfide solution, the formation of Cu₂O indicated the potential comproportionation reaction. These findings suggested that the chemical conversion process was slower than the electrochemical reaction in the presence of copper metal. Additionally, higher bisulfide concentrations led to the formation of copper sulfate hydroxide, brochantite.

Overall, the current study shed light on the complex interplay between oxide formation and subsequent bisulfide-induced corrosion in DGR environments.

Our results have shown that regardless of the composition and nature of the oxide film, either a single-phase oxide film or a dual layer of combined copper oxides, the grown oxide film on the Cu surface was partially converted to a copper sulfide film via chemical conversion and/or galvanically-coupled processes. Moreover, an unreacted remnant of the oxide layer was detected on the surface, surviving for longer than the duration of our experiments. This remnant oxide was non-protective and permitted direct corrosion of Cu by bisulfide species arriving at the metal surface. Oxide films were grown either electrochemically, radiolytically, or hydrothermally. The electrochemically-grown oxides, upon exposure to bisulfide solutions, underwent quick conversion to copper sulfide (Cu₂S) as shown by the corrosion potential (E_{corr}) measurements and cathodic stripping voltammetry (CSV) at different immersion times. The same results were observed for the radiolytically-grown oxide with a multi-layer structure composed of Cu (I) and Cu (II)

oxides. The thickness of the two mentioned oxides was on the nanometre scale. Hydrothermally-grown oxides were thicker than the electrochemically- and radiolytically-grown oxides. The results of CSVs showed that some parts of the oxide film and the sulfide film formed on top of the oxide film could not be cathodically stripped from the surface and remained in the form of a defective film, and that direct corrosion of Cu occurred, driven by bisulfide species reaching the metal surface. This suggests that conversion of oxide to sulfide films is fastest when an electrochemical pathway is available, and much slower if it must depend on the chemical pathway. The regions of the oxide which were not connected electrically to the surface could only undergo chemical conversion. The results obtained from immersion of copper oxide powder in bisulfide solution support the idea that the chemical conversion is not as quick as the electrochemical reaction in the presence of copper metal.

9.2 Future Work

In a DGR, the salinity of groundwater could facilitate the formation of paratacamite ($\text{Cu}_2\text{Cl}(\text{OH})_3$) as another potential corrosion product during the aerobic phase. Further investigations are necessary to understand the formation of paratacamite and to explore the influence of chloride ions on the properties of the grown oxide film (paratacamite) and its subsequent conversion to sulfide. Additionally, the kinetics of the conversion reaction in the presence of various types of copper oxide, each with distinct thicknesses and structures, warrants examination. Electrochemical experiments conducted at rotating disc electrodes offer a means to study these kinetics by controlling mass transport to and from the electrode surface. Moreover, it is crucial to study the corrosion of oxidized copper in dense clay buffer materials since DGR containers will be surrounded by compacted clay. For the radiolytically-grown oxide in pure water, conducting solution analysis is essential as a complementary technique to enhance understanding of film formation at each stage of oxide formation. Furthermore, emphasis should be placed on investigating the interface between the developed oxide and the Cu substrate in hydrothermally-grown oxide to assess the potential occurrence of localized corrosion during oxide growth. Finally, for powder immersion experiments, extending immersion durations to several days or months at various bisulfide concentrations is necessary. Exploring different ratios of S/Cu is vital as

they influence the conversion of copper oxide to copper sulfide. Modifications in the filtration method post-immersion testing, such as filtering within an anaerobic chamber, are required to minimize oxygen exposure.

Curriculum Vitae

EDUCATION

2019-2024 **PhD Candidate in Electrochemistry and Corrosion Studies,**

Chemistry, University of Western Ontario, London, Ontario

Advisor: Dr. James J. Noël

2014-2017 **M.Sc. in Materials Engineering-Characterization and Selection of Engineering Materials,**

School of Metallurgy and Materials Engineering, University of Tehran, Tehran, Iran

Advisors: Dr. R. Naderi Mahmoudi, Dr. B. Ramezanzadeh

GPA: (17.82/20)

2008-2013 **B.Sc. in Materials Engineering-Extractive Metallurgy,**

School of Metallurgy and Materials Engineering, Iran University of Science and Technology (IUST), Tehran, Iran

Advisor: Dr. M. Soltanieh

GPA: (15.86/20)

SCHOLARSHIP/AWARD

- 2019 • **Christian Sivertz Scholarship**, Department of Chemistry, Western University, Canada
- 2023 • **2023 CNS Travel Grant**, Canadian Nuclear Society, Canada

PUBLICATIONS

1. Salehi, Elham, Reza Naderi Mahmoudi, and Bahram Ramezanzadeh. "Synthesis and characterization of an effective organic/inorganic hybrid green corrosion inhibitive complex based on zinc acetate/*Urtica Dioica*." *APPLIED SURFACE SCIENCE* 396, no. February (2016): 1499-1514

2. Salehi, Elham, Reza Naderi Mahmoudi, and Bahram Ramezanzadeh. "Improvement in the protective performance of epoxy ester coating through inclusion of an effective hybrid green corrosion inhibitive pigment." *Journal of the Taiwan Institute of Chemical Engineers* 81, no. December (2017): 391-405
3. Elham Salehi Alaei, Mengnan Guo, Jian Chen, Mehran Behazin, Erik Bergendal, Christina Lilja, David W. Shoesmith, and James J. Noël, "The transition from used fuel container under oxic conditions to corrosion in an anoxic environment", *Materials and Corrosion*, September (2023): 1690-1706, <https://doi.org/10.1002/maco.202313757>

TEACHING EXPERIENCES

- Teaching Assistant, First Year Chemistry Lab (1301A), Fall 2019 and Fall 2020
- Teaching Assistant, Third Year Instrumental Analysis Lab (3372G), Winter 2019

LEADERSHIP EXPERIENCE

- Mentoring, guiding, and supporting junior grad researchers/summer students in the laboratory

CONFERENCE/MEETING PRESENTATIONS

- | | |
|---------------|-----------------------------------------------------------------------------------------------------------------------------------------------------------------------------------------------------------------------|
| December 2020 | <ul style="list-style-type: none"> • Electrochemical Society Student Symposium Annual Event, Canada <p>Oral Presentation</p> |
| January 2021 | <ul style="list-style-type: none"> • The Environmental Impact of Engineered Materials Degradation in Porous Consolidated Media, Canada <p>Oral Presentation</p> |
| July 2021 | <ul style="list-style-type: none"> • NACE Southern Ontario Student Section 11th Annual Symposium, Canada <p>Oral Presentation: Best oral presentation award-3rd place</p> |
| November 2021 | <ul style="list-style-type: none"> • 24th Chemistry and Biochemistry Graduate Research Conference, Canada <p>Oral Presentation</p> |
| June 2022 | <ul style="list-style-type: none"> • 105th Canadian Chemistry Conference and Exhibition (CCCE 2022), Canada <p>Oral Presentation</p> |

- August 2022

 - **NACE Southern Ontario Student Section 12th Annual Symposium, Canada**

Oral Presentation: Best oral presentation award-3rd place
- November 2022

 - **The Environmental Impact of Engineered Materials Degradation in Porous Consolidated Media, ORF & Alliance Meeting, Canada**

Oral Presentation
- March 2023

 - **NSERC-NWMO Alliance and ORF Program Meeting, Canada**

Oral Presentation
- June 2023

 - **Canadian Chemistry Conference and Exhibition (CSC 2023), Canada**

Poster Presentation
- August 2023

 - **5th Canadian Conference on Waste Management, Decommissioning and Environmental Restoration, Canada**

Poster Presentation
- September 2023

 - **ORF Northwest Ontario Event, Canada**

Poster Presentation

ACADEMIC ACTIVITIES

- 2021-June 2023

 - **University of Western Ontario ECS Student Chapter, Vice-president**
- 2021-2022

 - **Graduate Education Committee Member of Chemistry department**
- April-Sep 2023

 - **Society of Graduate Students (SOGS), Councillor**

VOLUNTEERING ACTIVITIES

- November 2019

 - **Fall Preview Day Open House, Department of Chemistry, Western University, Canada**
- December 2019

 - **Outreach event for students from secondary schools, Department of Chemistry, Western University, Canada**

- February 2023 • **CAGIA (Canadian Association for Girls in Science, a STEM club for girls aged 7 to 16)**, Department of Chemistry, Western University, Canada
- September 2023 • **Ignace and Area Youth Gathering (Chemistry demo, Exhibitor booth, and Presentation)**, Ignace, Canada